

Single-Zone Cylinder Pressure
Modeling and Estimation
for Heat Release Analysis
of SI Engines

Markus Klein

Linköping 2007

Linköping Studies in Science and Technology. Dissertations
No. 1124

**Single-Zone Cylinder Pressure Modeling and Estimation
for Heat Release Analysis of SI Engines**

Copyright © 2007 Markus Klein

markus.s.klein@gmail.com
http://www.fs.isy.liu.se/
Department of Electrical Engineering,
Linköping University,
SE-581 83 Linköping,
Sweden.

ISBN 978-91-85831-12-8

ISSN 0345-7524

Printed by Liu-Tryck, Linköping, Sweden 2007

To Sofia, Ebba, Samuel and Nora

ABSTRACT

Cylinder pressure modeling and heat release analysis are today important and standard tools for engineers and researchers, when developing and tuning new engines. Being able to accurately model and extract information from the cylinder pressure is important for the interpretation and validity of the result.

The first part of the thesis treats single-zone cylinder pressure modeling, where the specific heat ratio model constitutes a key part. This model component is therefore investigated more thoroughly. For the purpose of reference, the specific heat ratio is calculated for burned and unburned gases, assuming that the unburned mixture is frozen and that the burned mixture is at chemical equilibrium. Use of the reference model in heat release analysis is too time consuming and therefore a set of simpler models, both existing and newly developed, are compared to the reference model.

A two-zone mean temperature model and the Vibe function are used to parameterize the mass fraction burned. The mass fraction burned is used to interpolate the specific heats for the unburned and burned mixture, and to form the specific heat ratio, which renders a cylinder pressure modeling error in the same order as the measurement noise, and fifteen times smaller than the model originally suggested in Gatowski et al. (1984). The computational time is increased with 40 % compared to the original setting, but reduced by a factor 70 compared to precomputed tables from the full equilibrium program. The specific heats for the unburned mixture are captured within 0.2 % by linear functions,

and the specific heats for the burned mixture are captured within 1 % by higher-order polynomials for the major operating range of a spark ignited (SI) engine.

In the second part, four methods for compression ratio estimation based on cylinder pressure traces are developed and evaluated for both simulated and experimental cycles. Three methods rely upon a model of polytropic compression for the cylinder pressure. It is shown that they give a good estimate of the compression ratio at low compression ratios, although the estimates are biased. A method based on a variable projection algorithm with a logarithmic norm of the cylinder pressure yields the smallest confidence intervals and shortest computational time for these three methods. This method is recommended when computational time is an important issue. The polytropic pressure model lacks information about heat transfer and therefore the estimation bias increases with the compression ratio. The fourth method includes heat transfer, crevice effects, and a commonly used heat release model for firing cycles. This method estimates the compression ratio more accurately in terms of bias and variance. The method is more computationally demanding and thus recommended when estimation accuracy is the most important property. In order to estimate the compression ratio as accurately as possible, motored cycles with as high initial pressure as possible should be used.

The objective in part 3 is to develop an estimation tool for heat release analysis that is accurate, systematic and efficient. Two methods that incorporate prior knowledge of the parameter nominal value and uncertainty in a systematic manner are presented and evaluated. Method 1 is based on using a singular value decomposition of the estimated hessian, to reduce the number of estimated parameters one-by-one. Then the suggested number of parameters to use is found as the one minimizing the Akaike final prediction error. Method 2 uses a regularization technique to include the prior knowledge in the criterion function.

Method 2 gives more accurate estimates than method 1. For method 2, prior knowledge with individually set parameter uncertainties yields more accurate and robust estimates. Once a choice of parameter uncertainty has been done, no user interaction is needed. Method 2 is then formulated for three different versions, which differ in how they determine how strong the regularization should be. The quickest version is based on ad-hoc tuning and should be used when computational time is important. Another version is more accurate and flexible to changing operating conditions, but is more computationally demanding.

SVENSKT REFERAT

Den svenska titeln på avhandlingen är "En-zons-modellering och estimering för analys av frigjord värme i bensinmotorer¹".

Förbränningsmotorer har varit den primära maskinen för att generera arbete i fordon i mer än hundra år, och kommer att vara högentresant även i fortsättningen främst p.g.a. bränslets höga energidensitet. Emissionskrav från främst lagstiftare, prestandakrav såsom effekt och bränsleförbrukning från potentiella kunder, samt den konkurrens som ges av nya teknologier såsom bränsleceller fortsätter att driva teknikutvecklingen av förbränningsmotorer framåt.

Teknikutvecklingen möjliggörs av att ingenjörer och forskare har mött dessa krav genom t.ex. grundforskning på förbränningsprocessen, nya eller förbättrade komponenter i motorsystemet och nya teknologier såsom variabla ventiltider och variabelt kompressionsförhållande. De två sistnämnda är exempel på teknologier som direkt påverkar tryckutvecklingen i cylindern, där det är viktigt att få noggrann kunskap om hur förbränningsprocessen fortlöper och hur bränslets kemiska energi frigörs som värme och sedan omvandlas till mekaniskt arbete. Detta kallas analys av frigjord värme och kopplar direkt till motorns emissioner, effekt och bränsleförbrukning.

En analys av frigjord värme möjliggörs av att man: 1) kan mäta cylindertrycket under förbränningsprocessen; 2) har matematiska modeller för hur cylindertrycket utvecklas som funktion av kolvrörelsen och förbränningsprocessen; samt 3) har metodik för att beräkna den

¹Egentligen tändstiftsmotorer

frigjorda värmen genom att anpassa den valda modellen till cylindertrycksmätningen.

Sensorerna för att mäta trycket i cylindern har den senaste tiden blivit både noggrannare och robustare mot den extrema miljö och de snabba tryck- och temperaturförändringar som sensorn utsätts för under varje cykel. Idag används cylindertryckssensorer enbart i labb- och testmiljö, mest beroende på att sensorn är relativt dyr, men det pågår en teknikutveckling av sensorerna som siktar på att de i framtida fordon även skall sitta i produktionsmotorer.

Matematiska modeller av cylindertrycksutvecklingen och metoder för att beräkna den frigjorda värmen behandlas i denna avhandling.

Avhandlingens innehåll och kunskapsbidrag

Avhandlingen består av tre delar och det sammanhållande temat är cylindertryck. Den första delen behandlar en-zons-modellering av cylindertrycksutvecklingen, där blandningen av luft och bränsle i cylindern behandlas som homogen. Detta antagande möjliggör en kort beräkningstid för den matematiska modellen. Ett bidrag i avhandlingen är identifiering av den viktigaste modellkomponenten i en allmänt vedertagen en-zons-modell samt en modellförbättring för denna komponent.

I den andra delen studeras kompressionsförhållandet, vilket är förhållandet mellan största och minsta cylindervolym under kolvens rörelse. Denna storhet är direkt kopplad motorns verkningsgrad och bränsleförbrukning. Avsnittet beskriver och utvärderar metoder för att bestämma kompressionsförhållandet i en motor utgående från cylindertrycksmätningar. Dessa metoder appliceras och utvärderas på en av Saab Automobile utvecklad prototypmotor med variabelt kompressionsförhållande.

När man beräknar parametrar i matematiska modeller där parametrarna har fysikalisk tolkning, såsom temperatur, har användaren ofta förkunskap och erfarenhet om vilka värden dessa bör anta. Den tredje delen utvecklar ett verktyg för hur användaren kan väga in sådan förkunskap när parametrarnas värden beräknas utgående från cylindertrycksmätningar och den valda matematiska modellen. Särskilt en av metoderna ger en bra kompromiss mellan användarens förkunskap och mätdata. Detta verktyg kan användas för analys av frigjord värme och motorkalibrering, som ett diagnosverktyg och som ett analysverktyg för framtida motordesigner.

ACKNOWLEDGMENTS

This work has been carried out at the department of Electrical Engineering, division of Vehicular Systems at Linköpings Universitet, Sweden. It was financially funded by the Swedish Agency for Innovation Systems (VINNOVA) through the excellence center ISIS (Information Systems for Industrial control and Supervision), and by the Swedish Foundation for Strategic Research SSF through the research center MOVII. Their support is gratefully acknowledged.

My time as a PhD student has broaden my mind and been enjoyable and I would thank all my colleagues, former and present, at Vehicular Systems since your are all jointly the cause of that.

I would also like to thank my supervisors Dr. Lars Eriksson and Professor Lars Nielsen for their guidance and for letting me join the research group of Vehicular Systems. Dr. Eriksson has inspired me greatly through interesting discussions and through his true enthusiasm for engine research. I have enjoyed working with you. My co-authors Prof. Lars Nielsen, Ylva Nilsson and Dr. Jan Åslund are also acknowledged for fruitful collaborations. They have, as well as Dr. Ingemar Andersson, Dr. Per Andersson, Dr. Gunnar Cedersund, Dr. Erik Frisk, Martin Gunnarsson, Per Öberg and many others, contributed to my research by insightful discussions and creative efforts. Martin Gunnarsson is also acknowledged for keeping the engine lab running, as well as Carolina Fröberg for making administrative stuff work smoothly. Dr. Erik Frisk

deserves an extra mention since he has constantly been within range of my questions and he has always helped out without hesitation.

Dr. Lars Eriksson has proof-read the entire thesis, while Dr. Erik Frisk, Dr. Jan Åslund and Per Öberg have proof-read parts of it. I am very grateful for the time and effort you have put into my work. Dr. Ingemar Andersson has inspired me to finish the thesis, and Professor Lars Nielsen has helped me to stay focused during the final writing of the thesis.

To all the people who have hosted me during the middle part of my PhD studies, among those Andrej Perkovic and Maria Asplund, Dan and Tottis Lawesson, Fredrik Gustavsson and Louise Gustavsson-Ristenvik, Pontus Svensson, Mathias and Sara Tyskeng, and especially Jan Bruggård, I wish to direct my sincere gratitude for rooming me but also for making sure I had an enjoyable stay. The year I shared house with Ingemar and Janne is a memory for life.

The support from my family, my in-law family and all my friends has been invaluable.

This work would never have been accomplished without the indefatigable love, support and encouragement of Sofia. Finally I would like to thank Nora, Samuel, Ebba and Sofia, whom I love more than life itself, for all the joy and adventures you bring along.

Linköping, July 2007
Markus Klein

CONTENTS

1	Introduction	1
1.1	Outline	3
1.2	Contributions	6
1.3	Publications	6
I	Modeling	9
2	An overview of single-zone heat-release models	11
2.1	Model basis and assumptions	12
2.2	Rassweiler-Withrow model	15
2.3	Apparent heat release model	18
2.4	Matekunas pressure ratio	20
2.5	Gatowski et al. model	20
2.6	Comparison of heat release traces	24
2.7	Summary	26
3	Heat-release model components	27
3.1	Pressure sensor model	27
3.1.1	Parameter initialization – pressure offset Δp . . .	28
3.1.2	Parameter initialization – pressure gain K_p . . .	28
3.1.3	Crank angle phasing	29
3.1.4	Parameter initialization – crank angle offset $\Delta\theta$.	30
3.2	Cylinder volume and area models	31

3.2.1	Parameter initialization – clearance volume V_c	32
3.3	Temperature models	32
3.3.1	Single-zone temperature model	33
3.3.2	Parameter initialization – cylinder pressure at IVC p_{IVC}	33
3.3.3	Parameter initialization – mean charge temperature at IVC T_{IVC}	33
3.4	Crevice model	35
3.4.1	Parameter initialization – crevice volume V_{cr}	36
3.4.2	Parameter initialization – cylinder mean wall temperature T_w	36
3.5	Combustion model	37
3.5.1	Vibe function	37
3.5.2	Parameter initialization – energy released Q_{in}	38
3.5.3	Parameter initialization – angle-related parameters $\{\theta_{ig}, \Delta\theta_d, \Delta\theta_b\}$	39
3.6	Engine heat transfer	39
3.6.1	Parameter initialization – $\{C_1, C_2\}$	42
3.7	Thermodynamic properties	42
3.7.1	Parameter initialization – γ_{300} and b	42
3.8	Summary of single-zone heat-release models	43
3.9	Sensitivity in pressure to parameter initialization	45
4	A specific heat ratio model for single-zone heat release models	49
4.1	Outline	50
4.2	Chemical equilibrium	50
4.3	Existing models of γ	52
4.3.1	Linear model in T	52
4.3.2	Segmented linear model in T	52
4.3.3	Polynomial model in p and T	53
4.4	Unburned mixture	54
4.4.1	Modeling λ -dependence with fixed slope, b	57
4.5	Burned mixture	58
4.6	Partially burned mixture	63
4.6.1	Reference model	63
4.6.2	Grouping of γ -models	64
4.6.3	Evaluation criteria	67
4.6.4	Evaluation covering one operating point	68
4.6.5	Evaluation covering all operating points	72
4.6.6	Influence of γ -models on heat release parameters	76
4.6.7	Influence of air-fuel ratio λ	77
4.6.8	Influence of residual gas	79
4.6.9	Summary for partially burned mixture	82

4.7	Summary and conclusions	83
-----	-----------------------------------	----

II Compression Ratio Estimation 85

5	Compression ratio estimation – with focus on motored cycles	87
5.1	Outline	88
5.2	Cylinder pressure modeling	89
5.2.1	Polytropic model	89
5.2.2	Standard model	90
5.2.3	Cylinder pressure referencing	90
5.3	Estimation methods	91
5.3.1	Method 1 – Sublinear approach	91
5.3.2	Method 2 – Variable projection	92
5.3.3	Method 3 – Levenberg-Marquardt and polytropic model	93
5.3.4	Method 4 – Levenberg-Marquardt and standard model	94
5.3.5	Summary of methods	94
5.4	Simulation results	95
5.4.1	Simulated engine data	95
5.4.2	Results and evaluation for motored cycles at OP2	96
5.4.3	Results and evaluation for motored cycles at all OP	98
5.4.4	Sensitivity analysis at OP2	101
5.4.5	Results and evaluation for fired cycles at OP2	103
5.5	Experimental results	103
5.5.1	Experimental engine data	103
5.5.2	Results and evaluation for OP2	105
5.5.3	Results and evaluation for all OP	108
5.6	Conclusions	112

III Prior Knowledge based Heat Release Analysis 115

6	Using prior knowledge for single-zone heat release analysis	117
6.1	Outline	119
6.2	Cylinder pressure modeling	120
6.2.1	Standard model	120
6.2.2	Cylinder pressure parameters	120
6.3	Problem illustration	120
6.4	Estimation methods	123

6.4.1	Method 1 – SVD-based parameter reduction . . .	124
6.4.2	Method 2 – Regularization using prior knowledge	130
6.4.3	How to determine the prior knowledge?	139
6.4.4	Summarizing comparison of methods 1 and 2 . . .	141
7	Results and evaluation for motored cycles	143
7.1	Simulation results – motored cycles	143
7.1.1	Simulated engine data	143
7.1.2	Parameter prior knowledge	144
7.1.3	Method 1– Results and evaluation	146
7.1.4	Method 2– Results and evaluation	157
7.1.5	Summary for simulation results	169
7.2	Experimental results – motored cycles	174
7.2.1	Experimental engine data	174
7.2.2	Parameter prior knowledge	175
7.2.3	Method 1– Results and evaluation	175
7.2.4	Method 2– Results and evaluation	176
7.3	Summary of results for motored cycles	184
8	Results and evaluation for fired cycles	187
8.1	Simulation results – fired cycles	187
8.1.1	Simulated engine data	187
8.1.2	Parameter prior knowledge	188
8.1.3	Method 1– Results and evaluation	189
8.1.4	Method 2– Results and evaluation	193
8.1.5	Summary for simulation results	208
8.2	Experimental results – fired cycles	209
8.2.1	Experimental engine data	209
8.2.2	Parameter prior knowledge	209
8.2.3	Method 1– Results and evaluation	211
8.2.4	Method 2– Results and evaluation	213
8.3	Summary of results for fired cycles	220
8.4	Future Work	221
9	Summary and conclusions	223
9.1	A specific heat ratio model for single-zone heat release models	223
9.2	Compression ratio estimation	224
9.3	Prior knowledge based heat release analysis	226
	Bibliography	229

A	A specific heat ratio model – further details	237
A.1	Temperature models	237
A.1.1	Single-zone temperature model	237
A.1.2	Two-zone mean temperature model	238
A.2	SAAB 2.3L NA – Geometric data	239
A.3	Parameters in single-zone model	240
A.4	Crevice energy term	242
A.5	Simple residual gas model	245
A.6	Fuel composition sensitivity of γ	246
A.6.1	Burned mixture – Hydrocarbons	246
A.6.2	Burned mixture – Alcohols	247
A.6.3	Unburned mixtures	250
A.6.4	Partially burned mixture – influence on cylinder pressure	250
A.7	Thermodynamic properties for burned mixture	253
A.8	Thermodynamic properties for partially burned mixture	254
B	Compression ratio estimation – further details	263
B.1	Taylor expansions for sublinear approach	263
B.2	Variable Projection Algorithm	264
B.3	SVC – Geometric data	265
B.4	Parameters in single-zone model	265
C	Prior knowledge approach – further details	267
C.1	Levenberg-Marquardt method	267
C.1.1	Minimizing prediction errors using a local optimizer	268
C.2	Linear example	272
C.2.1	Linear example for methods 1 and 2	274
C.3	Motivation for M2:3+	275
C.4	L850 – Geometric data	279
C.5	Parameters in single-zone model – motored cycles	279
C.6	Parameters in single-zone model – fired cycles	279
C.7	Complementary results for prior knowledge approach	282
D	Notation	289
D.1	Parameters	289
D.1.1	Heat transfer	289
D.1.2	Engine geometry	290
D.1.3	Engine cycle	290
D.1.4	Thermodynamics and combustion	291
D.1.5	Parameter estimation	292
D.2	Abbreviations	293
D.3	Evaluation criteria	294

INTRODUCTION

Internal combustion engines have been the primary machine for generating work in mobile applications for more than a century, they are also continuing to be of high interest due to the high energy density of the fuels and their possibility to give good total fuel consumption. Continuous improvements and refinements are made to meet the increasing performance demands from customers and legislators, where both emissions and total system economy are important.

Emission regulations from the legislators provide a hard limit on the design—they must be met. Today the state-of-the-art technology for achieving low emissions from combustion engines, is the gasoline engine equipped with a three-way catalyst (TWC). Regulations for diesel engines are also continuously being made stricter to reach those of the gasoline engine with a TWC.

Development and competition between manufacturers strives to meet the needs of customers and deliver products with better performance both with respect to power and fuel consumption. Emerging technologies like the gas turbine and now the fuel cell pose possibilities and give a healthy competition, which also drives the technology development of combustion engines forward.

Engineers have met the challenges posed by stricter emission regulations through for example fundamental research on combustion, adding new components to more complex systems, as well as optimization of total system performance. Engine systems are becoming increasingly complex as new technologies are developed, but systematic methods are

also required to handle and integrate these technologies. Some examples of promising techniques for spark ignited (SI) engines are variable valve actuation and variable compression ratio. Both of these exemplify technologies that control the development of the in-cylinder process directly and where it is of importance to get accurate knowledge about the combustion process. The combustion process and other in-cylinder processes are directly reflected in the measured cylinder pressure, and used as a standard tool for tuning and optimizing engine performance. This is of course also important for conventional engines.

In-cylinder pressure modeling and estimation

The in-cylinder pressure is important since it contains information about the work production in the combustion chamber and thus gives important insight into the control and tuning of the engine. Being able to accurately model and extract information from the cylinder pressure is important for the interpretation and validity of the result. Researchers and engineers strive to extract as much information as possible from the combustion chamber through the in-cylinder pressure and models of different complexity exist for interpretation of the cylinder pressures. Here the focus is on single-zone models that treats the in-cylinder contents as a single zone and single fluid. These models can describe the cylinder pressure well and have a low computational complexity, which is also an important parameter when analyzing engine data.

Due to the short time scales of the process a sequence of measurements on an engine gives huge amounts of data. These large sets of data have to be analyzed efficiently, systematically, and with good accuracy. In-cylinder pressure analysis, the most efficient models are the single zone models, and the accuracy of these is the topic of the thesis. The foundation for the analysis of the model is the first law of thermodynamics where the relation between work, volume, pressure and temperature is described through the ratio of specific heats. Analyses that have been performed show that the specific heat ratio is of high importance for the model and therefore this model component is studied in great detail. Therefore, the first part of the thesis is on single-zone heat release modeling, where the specific heat ratio model constitutes a key part.

In-cylinder pressure models in general have a number of parameters, that have to be determined. For an accurate in-cylinder pressure analysis it is necessary, but not sufficient as will be shown later in the thesis, that the difference between the measured and modeled data is small. To minimize this difference, in a given measure, requires that the parameters are estimated, and this is the estimation problem.

Whenever the parameters in a physical model have a physical mean-

ing, the user usually has an expectation or prior knowledge of either what values the parameters should have, or at least the range in which they should be in. The user might even know which parameters that are most certain. These are examples of information that come from our prior knowledge. In the third part of the thesis it is shown how such information can be incorporated in the estimation problem.

Compression ratio estimation

The theme in the thesis is cylinder pressure and the second part treats compression ratio estimation based on measured cylinder pressure data. This particular problem is directly motivated by the variable compression engine, where the compression ratio can be changed continuously to eliminate an important design trade-off made in conventional engines. High compression ratios give good engine efficiency but at high loads a high compression ratio can result in engine destruction through engine knock. In such an engine the compression ratio is changed continuously to get the best performance from the engine. When the engine is driven at low loads a high compression ratio is selected for good efficiency and at high loads a low compression ratio is used to reduce engine knock. Compression ratio estimation is studied for several reasons where the most important is for diagnostic purposes. A too high compression ratio can lead to engine destruction while a too low compression ratio gives a too high fuel consumption.

Four different methods for compression ratio estimation are proposed and evaluated. The research was motivated by the variable compression engine, but the methods are generally applicable and can also be used on conventional engines to get a better value of the compression ratio from experimental data.

1.1 Outline

An outline of the thesis in terms of short summaries of each chapter is given below and indicates the scope of each chapter. The notation used is summarized in appendix D, where the parameters are given in appendix D.1, and the abbreviations are summarized in appendix D.2. In the thesis various evaluation criteria are used, and they are summarized in appendix D.3.

Chapter 2: An overview of single-zone heat-release models

This chapter serves as an introduction to single-zone heat release modeling. First the basis and assumptions made for single-zone heat release modeling are given. Based on these, four well-known heat release mod-

els are presented. These are compared with respect to their computed heat release trace given a cylinder pressure trace.

Chapter 3: Heat-release model components

The model components used in the most descriptive single-zone heat release model in chapter 2, the Gatowski et al. (1984) model, are described. The model components of the other three heat release models form a subset of these. For each model component, a method to initialize the model component parameters is given. The sensitivity in cylinder pressure for each of these parameters is then investigated. The chapter ends with a summary of the equations, parameters, inputs and outputs of the Gatowski et al. model.

Chapter 4: A specific heat ratio model for single-zone heat release models

An accurate specific heat ratio model is important for an accurate heat release analysis. This since the specific heat ratio couples the systems energy to other thermodynamic quantities. This chapter therefore investigates models of the specific heat ratio for the single-zone heat release model developed by Gatowski et al. (1984). The objective is to find a model accurate enough to only introduce a cylinder pressure modeling error in the order of the cylinder pressure measurement noise, while keeping the computational complexity at a minimum. Based on assumptions of frozen mixture for the unburned mixture and chemical equilibrium for the burned mixture, the specific heat ratio is calculated using a full equilibrium program for an unburned and a burned air-fuel mixture, and compared to already existing and newly proposed models of γ . It is assumed that a general single-zone heat release model can be used as a reference model.

The evaluation is performed in terms of modeling error in γ and in cylinder pressure. The impact each γ -model has on the heat release, in terms of estimated heat release parameters in the Vibe function is illustrated. The influence of fuel composition, air-fuel ratio and residual gas content is also investigated.

Large parts of the material in this chapter and in appendix A have previously been published in Klein and Eriksson (2004c) and Klein and Eriksson (2004a). Appendix A contains further details and argumentation that support the development of the specific heat ratio models, and gives a background and a thorough explanation of some of the details in the models.

Chapter 5: Compression ratio estimation – with focus on motored cycles

The purpose of this chapter is to estimate the compression ratio given a cylinder pressure trace, in order to diagnose the compression ratio if it e.g. gets stuck at a too high or too low ratio. Four methods for compression ratio estimation based on cylinder pressure traces are developed and evaluated for both simulated and experimental cycles. A sensitivity analysis of how the methods perform when subjected to parameter deviations in crank angle phasing, cylinder pressure bias and heat transfer is also made.

In appendix B further details and argumentation on compression ratio estimation for motored cycles are given, and it serves as a complement to this chapter. Chapter 5 together with appendix B is an edited version of Klein et al. (2006), which itself is based on Klein et al. (2004) and Klein and Eriksson (2005b).

Chapter 6–8: Using prior knowledge for single-zone heat release analysis

Two methods that take parameter prior knowledge into account, when performing parameter estimation on the Gatowski et al. model, are presented. The application in mind is a tool for cylinder pressure estimation that is accurate, systematic and efficient. The methods are described in detail, and it is shown how to incorporate the prior knowledge in a systematic manner. Guidelines of how to determine the prior knowledge for a specific application are then given. The performance of the two methods is evaluated for both simulated and experimentally measured cylinder pressure traces. These evaluations are made in chapter 7: Results and evaluation for motored cycles and in chapter 8: Results and evaluation for fired cycles. Appendix C contains further details and argumentation that support the development and evaluation of the two parameter estimation methods.

Experimental and simulated engine data

During the project different engines have been available in the Vehicular Systems engine laboratory. Therefore the simulated and experimental data used in the chapters are from different engines.

Chapters 2–4 use a naturally aspirated 2.3L engine from SAAB, and its geometry is given in appendix A.2. In chapter 5 the SAAB Variable Compression (SVC) engine is used, with the geometry given in appendix B.3. The results for chapters 6–8 are based on data from a turbocharged 2.0L SAAB engine, see appendix C.4.

1.2 Contributions

The following list summarizes the main contributions of this thesis:

- The interrelation between models in the single-zone heat release model family is shown. A method for finding nominal values for all parameters therein is suggested.
- It is shown that the specific heat ratio model is the most important component in cylinder pressure modeling.
- The importance of using the cylinder pressure error as a measure of how well a specific heat ratio model performs is pinpointed.
- A new specific heat ratio model to be used primarily in single-zone heat release models. This model can easily be incorporated with the Gatowski et al.-model, and reduces the modeling error to be of the same order as the cylinder pressure measurement noise.
- Four methods for estimating the compression ratio index, given a cylinder pressure trace are proposed. One method is recommended for its accuracy, while another is preferable when computational efficiency is important.
- Two methods of using prior knowledge applied to the in-cylinder pressure estimation problem are presented and evaluated. For the second method, it is shown that prior knowledge with individually set parameter uncertainties yields more accurate and robust estimates.

1.3 Publications

In the research work leading to this thesis, the author has published a licentiate thesis and the following papers:

Journal papers:

- M. Klein, L. Eriksson, and Y. Nilsson (2003). Compression estimation from simulated and measured cylinder pressure. *SAE 2002 Transactions Journal of Engines, 2002-01-0843*, 111(3), 2003.
- M. Klein and L. Eriksson (2005a). A specific heat ratio model for single-zone heat release models. *SAE 2004 Transactions Journal of Engines, 2004-01-1464*, 2005.
- M. Klein, L. Eriksson and J. Åslund (2006). Compression ratio estimation based on cylinder pressure data. *Control Engineering Practice*, 14(3):197–211.

Conference papers:

- M. Klein, L. Eriksson and Y. Nilsson (2002). Compression estimation from simulated and measured cylinder pressure. *Electronic engine controls*, SP-1703, SAE Technical Paper 2002-01-0843. SAE World Congress, Detroit, USA, 2002.
- M. Klein and L. Eriksson (2002). Models, methods and performance when estimating the compression ratio based on the cylinder pressure. Fourth conference on Computer Science and Systems Engineering in Linköping (CCSSE), 2002.
- M. Klein and L. Eriksson (2004c). A specific heat ratio model for single-zone heat release models. *Modeling of SI engines*, SP-1830, SAE Technical Paper 2004-01-1464. SAE World Congress, Detroit, USA, 2004.
- M. Klein, L. Eriksson and J. Åslund (2004). Compression ratio estimation based on cylinder pressure data. In proceedings of IFAC symposium on Advances in Automotive Control, Salerno, Italy, 2004.
- M. Klein (2004). A specific heat ratio model and compression ratio estimation. Licentiate thesis, Vehicular Systems, Linköping University, 2004. LiU-TEK-LIC-2004:33, Thesis No. 1104.
- M. Klein and L. Eriksson (2004b). A comparison of specific heat ratio models for cylinder pressure modeling. Fifth conference on Computer Science and Systems Engineering in Linköping (CCSSE), 2004.
- M. Klein and L. Eriksson (2005b). Utilizing cylinder pressure data for compression ratio estimation. IFAC World Congress, Prague, Czech Republic, 2005.

The following conference papers have also been produced by the author during the project, but they are not explicitly included in the thesis:

- M. Klein and L. Nielsen (2000). Evaluating some Gain Scheduling Strategies in Diagnosis of a Tank System. In proceedings of IFAC symposium on Fault Detection, Supervision and Safety for Technical Processes, Budapest, Hungary, 2000.
- M. Klein and L. Eriksson (2006). Methods for cylinder pressure based compression ratio estimation. *Electronic Engine Control*, SP-2003, SAE Technical paper 2006-01-0185. SAE World Congress, Detroit, USA, 2006.

Part I

Modeling

AN OVERVIEW OF SINGLE-ZONE HEAT-RELEASE MODELS

When analyzing the internal combustion engine the in-cylinder pressure has always been an important experimental diagnostic, due to its direct relation to the combustion and work producing processes (Chun and Heywood, 1987; Cheung and Heywood, 1993). The in-cylinder pressure reflects the combustion process, the piston work produced on the gas, heat transfer to the chamber walls, as well as mass flows in and out of crevice regions between the piston, rings and cylinder liner.

Thus, when an accurate knowledge of how the combustion process propagates through the combustion chamber is desired, each of these processes must be related to the cylinder pressure, so the combustion process can be distinguished. The reduction of the effects of volume change, heat transfer, and mass loss on the cylinder pressure is called *heat-release analysis* and is done within the framework of the first law of thermodynamics. In particular during the closed part of the engine cycle when the intake and exhaust valves are closed. The most common approach is to regard the cylinder contents as a *single zone*, whose thermodynamic state and properties are modeled as being uniform throughout the cylinder and represented by average values. No spatial variations are considered, and the model is therefore referred to as zero-dimensional. Models for heat transfer and crevice effects can easily be included in this framework. Another approach is to do a more detailed thermodynamic analysis by using a multi-zone model, where the cylinder is divided into a number of zones, differing in composition and properties. Each zone being uniform in composition and temper-

ature, and the pressure is the same for all zones, see for e.g. (Nilsson and Eriksson, 2001).

The goal of this chapter is to show the *structure* of different *single-zone heat-release model families* and how they are derived. The discussion of details in the model components are postponed to chapter 3, since they might distract the readers attention from the general structure of the model family. Chapter 3 gives a more thorough description of the model components.

Single-zone models for analyzing the heat-release rate and simulating the cylinder pressure are closely connected; they share the same basic balance equation and can be interpreted as each others inverse. They are both described by a first order ordinary differential equation that has to be solved. In heat release models a pressure trace is given as input and the heat release is the output, while in pressure models a heat release trace is the input and pressure is the output. For a given heat-release model an equivalent pressure model is obtained by reordering the terms in the ordinary differential equation. Since they are so closely connected it is beneficial to discuss them together.

2.1 Model basis and assumptions

The basis for the majority of the heat-release models is the first law of thermodynamics; the energy conservation equation. For an open system it can be stated as

$$dU = \delta Q - \delta W + \sum_i h_i dm_i, \quad (2.1)$$

where dU is the change in internal energy of the mass in the system, δQ is the heat transported to the system, δW is the work produced by the system and $\sum_i h_i dm_i$ is the enthalpy flux across the system boundary. Possible mass flows dm_i are: 1) flows in and out of the valves; 2) direct injection of fuel into the cylinder; 3) flows in and out of crevice regions; 4) piston ring blow-by. The mass flow dm_i is positive for a mass flow into the system and h_i is the mass specific enthalpy of flow i . Note that h_i is evaluated at conditions given by the zone the mass element leaves.

As mentioned earlier, single-zone models is our focus at the moment, so we will now look into those in more detail. Some commonly made assumptions for the single-zone models are:

- the cylinder contents and the state is uniform throughout the entire chamber.
- the combustion is modeled as a release of heat.

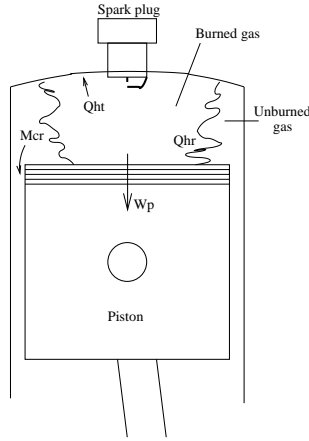


Figure 2.1: Schematic of the combustion process in the cylinder, that defines the sign convention used in the pressure and heat-release models.

- the heat released from the combustion occurs uniformly in the chamber.
- the gas mixture is an ideal gas.

Consider the combustion chamber to be an open system (single zone), with the cylinder head, cylinder wall and piston crown as boundary. Figure 2.1 shows a schematic of the combustion chamber, where the sign conventions used in pressure and heat-release models are defined. The change in heat dQ consists of the released chemical energy from the fuel dQ_{ch} , which is a heat adding process, and the heat transfer to the chamber walls dQ_{ht} , which is a heat removing process. The heat transport is therefore represented by $dQ = dQ_{ch} - dQ_{ht}$. Note that the heat transfer cools the gases at most times, but in some instances it heats the air-fuel mixture. The only work considered is the work done by the fluid on the piston W_p and it is considered positive, therefore $dW = dW_p$. The first law of thermodynamics (2.1) can then be rewritten as

$$dQ_{ch} = dU_s + dW_p - \sum_i h_i dm_i + dQ_{ht}. \quad (2.2)$$

The piston work dW_p is assumed to be reversible and can be written as $dW_p = pdV$. For an ideal gas, the change in sensible energy dU_s is a function of mean charge temperature T only, thus:

$$U_s = m_{tot}u(T), \quad (2.3)$$

which in its differentiated form becomes:

$$dU_s = m_{tot}c_v(T)dT + u(T)dm_{tot}, \quad (2.4)$$

where m_{tot} is the charge mass, and $c_v = \left(\frac{\partial u}{\partial T}\right)_V$ is the mass specific heat at constant volume. The mean temperature is found from the ideal gas law as $T = \frac{pV}{m_{tot}R}$, and its differentiated form is

$$dT = \frac{1}{m_{tot}R}(Vdp + pdV - RTdm_{tot}), \quad (2.5)$$

assuming R to be constant. For reading convenience, the dependence of T in c_p , c_v and γ is often left out in the following equations. Equation (2.2) can now be rewritten as

$$dQ_{ch} = \frac{c_v}{R}V dp + \frac{c_v + R}{R}p dV + (u - c_v T)dm_{tot} - \sum_i h_i dm_i + dQ_{ht}, \quad (2.6)$$

using equations (2.4) and (2.5). The specific heat ratio is defined as $\gamma = \frac{c_p}{c_v}$ and with the assumption of an ideal gas the mass specific gas constant R can be written as $R = c_p - c_v$, yielding that the mass specific heat at constant volume is given by

$$c_v = \frac{R}{\gamma - 1}. \quad (2.7)$$

The mass specific heat is the amount of energy that must be added or removed from the mixture to change its temperature by 1 K at a given temperature and pressure. It relates internal energy with the thermodynamic state variables p and T , and is therefore an important part of the heat release modeling. Inserting (2.7) into (2.6) results in

$$dQ_{ch} = \frac{1}{\gamma - 1}V dp + \frac{\gamma}{\gamma - 1}p dV + \left(u - \frac{RT}{\gamma - 1}\right)dm_{tot} - \sum_i h_i dm_i + dQ_{ht}. \quad (2.8)$$

From this equation, four different single-zone models with various levels of complexity will be derived. To begin with the isentropic relation is derived, then the polytropic model is formulated and this model forms the basis for calculating the mass fraction burned with the Rassweiler-Withrow method (Rassweiler and Withrow, 1938). Secondly, a model for computing the apparent heat release first proposed in Krieger and Borman (1967) will be derived. Thirdly, the pressure ratio developed by Matekunas (1983) is shortly summarized. Finally, a model including heat transfer and crevice effects (Gatowski et al., 1984) will be given.

The isentropic process and isentropic relation

In many situations real processes are compared to ideal processes and as comparison the isentropic process is normally used. From the isentropic process an isentropic relation can be found by integrating the first law of thermodynamics (2.8). The assumptions are:

- No mass transfer: Crevice effects and leakages to the crankcase (often called blow-by) are non-existent, i.e. $dm_{tot} = dm_i = 0$.
- Neither heat transfer nor heat release:
 - Heat transfer is not explicitly accounted for, i.e. $\bar{d}Q_{ht} = 0$, and thus $\bar{d}Q = \bar{d}Q_{ch} - \bar{d}Q_{ht} = \bar{d}Q_{ch}$.
 - Using the fact that there is no release of chemical energy during the compression phase prior to the combustion or during the expansion phase after the combustion, therefore $\bar{d}Q = 0$ for these regions.
- The specific heat ratio γ is constant.

The first two assumptions yield that (2.8) can be expressed as:

$$dp = -\frac{\gamma p}{V}dV. \quad (2.9)$$

From (2.9) and the last assumption above the *isentropic relation* is found by integrating as

$$pV^\gamma = C = \text{constant} \quad (2.10)$$

by noting that γ is considered to be constant.

2.2 Rassweiler-Withrow model

The Rassweiler-Withrow method was originally presented in 1938 and many still use the method for determining the mass fraction burned, due to its simplicity and it being computationally efficient. The mass fraction burned $x_b(\theta) = \frac{m_b(\theta)}{m_{tot}}$ is the burned mass $m_b(\theta)$ normalized by the total charge mass m_{tot} , and it can be seen as a normalized version of the accumulated heat-release trace $Q_{ch}(\theta)$ such that it assumes values in the interval $[0, 1]$. The relation between the mass fraction burned and the amount of heat released can be justified by noting that the energy released from a system is proportional to the mass of fuel that is burned. The input to the method is a pressure trace $p(\theta_j)$ where the crank angle θ at each sample j is known (or equivalently; the volume is known at each sample) and the output is the mass fraction burned trace $x_{b,RW}(\theta_j)$.

A cornerstone for the method is the fact that pressure and volume data during compression and expansion can be approximated by the polytropic relation

$$pV^n = \text{constant}. \quad (2.11)$$

This expression comes from the isentropic relation (2.10) but γ is exchanged for a constant exponent $n \in [1.25, 1.35]$. This has been shown to give a good fit to experimental data for both compression and expansion processes in an engine (Lancaster et al., 1975). The exponent n is termed the polytropic index. It differs from γ since some of the effects of heat transfer are included implicitly in n . It is comparable to the average value of γ_u for the unburned mixture during the compression phase, prior to combustion. But due to heat transfer to the cylinder walls, index n is greater than γ_b for the burned mixture during expansion (Heywood, 1988, p.385).

When considering combustion where $dQ = dQ_{ch} \neq 0$, equation (2.8) can be rewritten as

$$dp = \frac{n-1}{V} dQ - \frac{np}{V} dV = dp_c + dp_v, \quad (2.12)$$

where dp_c is the pressure change due to combustion, and dp_v is the pressure change due to volume change, compare dp in (2.9). In the Rassweiler-Withrow method (Rassweiler and Withrow, 1938), the actual pressure change $\Delta p = p_{j+1} - p_j$ during the interval $\Delta\theta = \theta_{j+1} - \theta_j$, is assumed to be made up of a pressure rise due to combustion Δp_c , and a pressure rise due to volume change Δp_v ,

$$\Delta p = \Delta p_c + \Delta p_v, \quad (2.13)$$

which is justified by (2.12). The pressure change due to volume change during the interval $\Delta\theta$ is approximated by the polytropic relation (2.11), which gives

$$\Delta p_v(j) = p_{j+1,v} - p_j = p_j \left(\left(\frac{V_j}{V_{j+1}} \right)^n - 1 \right). \quad (2.14)$$

Applying $\Delta\theta = \theta_{j+1} - \theta_j$, (2.13) and (2.14) yields the pressure change due to combustion as

$$\Delta p_c(j) = p_{j+1} - p_j \left(\frac{V_j}{V_{j+1}} \right)^n. \quad (2.15)$$

By assuming that the pressure rise due to combustion in the interval $\Delta\theta$ is proportional to the mass of mixture that burns, the mass fraction burned at the end of the j 'th interval thus becomes

$$x_{b,RW}(j) = \frac{m_b(j)}{m_b(\text{total})} = \frac{\sum_{k=0}^j \Delta p_c(k)}{\sum_{k=0}^M \Delta p_c(k)}, \quad (2.16)$$

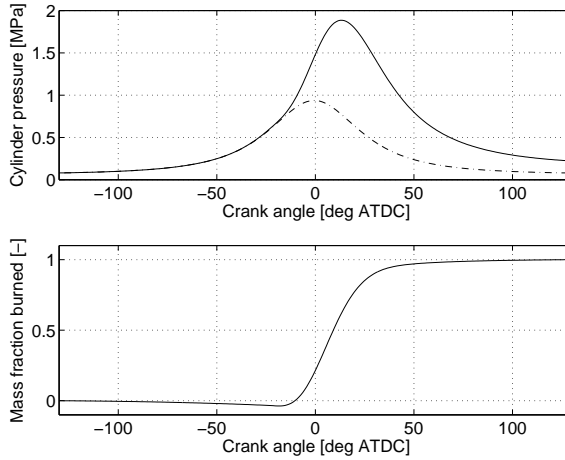


Figure 2.2: Top: Fired pressure trace (solid) and motored pressure trace (dash-dotted). Bottom: Calculated mass fraction burned profile using the Rassweiler-Withrow method.

where M is the total number of crank angle intervals and $\Delta p_c(k)$ is found from (2.15). The result from a mass fraction burned analysis is shown in figure 2.2, where the mass fraction burned profile is plotted together with the corresponding pressure trace. In the upper plot two cylinder pressure traces, one from a fired cycle (solid) and one from a motored cycle (dash-dotted) are displayed. When the pressure rise from the combustion becomes visible, i.e. it rises above the motored pressure, the mass fraction burned profile starts to increase above zero. The mass fraction burned profile increases monotonously as the combustion propagates through the combustion chamber. Equations (2.15)-(2.16) form the classical Rassweiler-Withrow mass fraction burned method.

If instead a heat-release trace is sought, the pressure change due to combustion in (2.12), $dp_c = \frac{n-1}{V} dQ$, can be rewritten and approximated by

$$\Delta Q_{RW}(j) = \frac{V_{j+1/2}}{n-1} \Delta p_c(j), \quad (2.17)$$

where the volume V during interval j is approximated with $V_{j+1/2}$ (the volume at the center of the interval), and $\Delta p_c(j)$ is found from (2.15). The heat-release trace is then found by summation. This method will be called the Rassweiler-Withrow heat release method. The calculated heat release approximates the released chemical energy from the fuel minus energy-consuming processes such as the heat transfer to the cylinder walls and crevice effects. If heat transfer and crevice effects

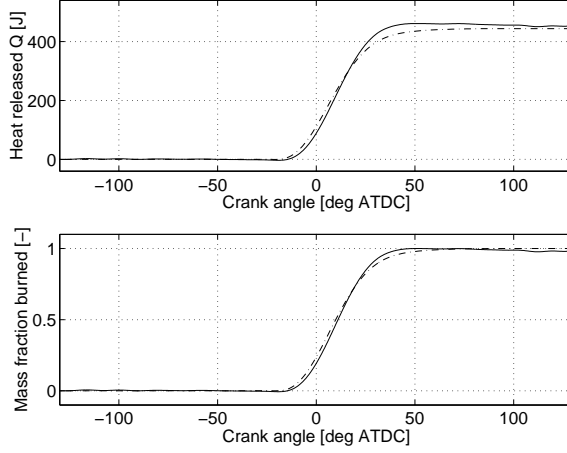


Figure 2.3: Calculated heat-release trace (upper) and mass fraction burned trace (lower), using the apparent heat release (solid) and Rassweiler-Withrow (dash-dotted) methods.

where non-existent, the heat release would correspond directly to the amount of energy added from the chemical reactions. The heat-release trace for the same data as in figure 2.2 is displayed in the upper plot of figure 2.3 as the dash-dotted line.

2.3 Apparent heat release model

The work by Krieger and Borman (1967) was derived from the first law of thermodynamics and called the computation of apparent heat release. It is also called the computation of net heat release. The method takes neither heat transfer nor crevice effects into account, thus dQ_{ht} is lumped into $dQ = dQ_{ch} - dQ_{ht}$ and $dm_{tot} = dm_i = 0$ in (2.8). Hence, the apparent heat release dQ can be expressed as:

$$dQ_{AHR} = \frac{1}{\gamma(T) - 1} V dp + \frac{\gamma(T)}{\gamma(T) - 1} p dV, \quad (2.18)$$

which is the same expression as the Rassweiler-Withrow method was based upon (2.12), but assuming that $\gamma(T) = n$. The mass fraction burned $x_{b,AHR}$ is computed by integrating (2.18) and then normalizing with the maximum value of the accumulated heat release Q_{AHR} , i.e.

$$x_{b,AHR}(\theta) = \frac{Q_{AHR}(\theta)}{\max Q_{AHR}} = \frac{\int \frac{dQ_{AHR}}{d\theta} d\theta}{\max Q_{AHR}}. \quad (2.19)$$

Method	θ_{10}	θ_{50}	θ_{85}	$\Delta\theta_b$
Rassweiler-Withrow	-6.4	9.8	26.9	33.3
Apparent heat release	-4.5	11.0	25.2	29.8

Table 2.1: Crank angle positions for 10 %, 50 % and 85 % mfb as well as the rapid burn angle $\Delta\theta_b = \theta_{85} - \theta_{10}$, all given in degrees ATDC for the mass fraction burned trace in figure 2.3.

The Rassweiler-Withrow method in (2.16) is a difference equation, and this causes a quantization effect compared to the ordinary differential equation given in (2.18). The net heat-release trace and mass fraction burned profile from the Krieger and Borman model are similar to those from the Rassweiler-Withrow method, the former being physically the more accurate one. One example is given in figure 2.3, where the upper plot shows the net heat-release traces and the lower plot shows the mass fraction burned traces, from the cylinder pressure in figure 2.2. For this particular case, the Rassweiler-Withrow method yields a slower burn rate compared to the apparent heat release method for the same data. This is reflected in the crank angle for 50 % mfb θ_{50} , which is 11.0 [deg ATDC] for the apparent heat release method and 9.8 [deg ATDC] for the Rassweiler-Withrow method. Table 2.1 summarizes the crank-angle positions for 10 %, 50 % and 85 % mfb as well as the rapid burn angle duration $\Delta\theta_b$, and shows that the Rassweiler-Withrow method yields a shorter burn duration for this particular case. The rapid burn angle duration is defined as $\Delta\theta_b = \theta_{85} - \theta_{10}$.

The shorter burn duration is also reflected in the heat release trace, and the difference is due to the assumptions on n and $V_{j+1/2}$ in the Rassweiler-Withrow method. The mass fraction burned profile is calculated assuming that the mass of burned mixture is proportional to the amount of released chemical energy.

Pressure simulation

An ordinary differential equation for the pressure can be simulated by solving (2.18) for the pressure differential dp :

$$dp = \frac{(\gamma(T) - 1) dQ - \gamma(T) p dV}{V}. \quad (2.20)$$

When performing a heat-release analysis the pressure is used as input and the heat release is given as output, and when the pressure trace is being simulated the heat-release trace is given as input. Therefore a cylinder pressure simulation based on (2.20), can be seen as the inverse of the heat release analysis (2.18). The only additional information that is needed for the computation is the initial value of the pressure.

2.4 Matekunas pressure ratio

The pressure ratio concept was developed by Matekunas (1983) and it is a computationally efficient method to determine an approximation of the mass fraction burned trace. The pressure ratio is defined as the ratio of the cylinder pressure from a fired cycle $p(\theta)$ and the corresponding motored cylinder pressure $p_0(\theta)$:

$$PR(\theta) = \frac{p(\theta)}{p_0(\theta)} - 1. \quad (2.21)$$

The pressure ratio (2.21) is then normalized by its maximum

$$PR_N(\theta) = \frac{PR(\theta)}{\max PR(\theta)}, \quad (2.22)$$

which produces traces that are similar to the mass fraction burned profiles. The difference between them has been investigated in Eriksson (1999), and for the operating points used, the difference in position for $PR_N(\theta) = 0.5$ was in the order of 1-2 degrees. This suggests $PR_N(\theta)$ can be used as the mass fraction burned trace $x_{b,MPR}$. The cylinder pressure in the upper plot of figure 2.4 yields the pressure ratio PR (2.21) given in the middle plot, and an approximation of the mass fraction burned in the lower plot.

2.5 Gatowski et al. model

A more complex model is to incorporate models of heat transfer, crevice effects and thermodynamic properties of the cylinder charge into the energy conservation equation (2.8). This was done in Gatowski et al. (1984), where a heat-release model was developed and applied to three different engine types, among those a spark-ignited engine.

Crevice effect model

Crevices are small, narrow volumes connected to the combustion chamber. During compression some of the charge flows into the crevices, and remain there until the expansion phase, when most of the charge returns to the combustion chamber and some charge stays in the crevices. Also, a small part of the charge in the cylinder blows by the top piston ring, before it either returns to the cylinder or ends up in the crankcase, a phenomena termed blow-by. Since the flame can not propagate into the crevices, the charge residing in the crevices is not combusted. The temperature in the crevices are assumed to be close to the cylinder wall temperature, due to that the crevices are narrow (Heywood,

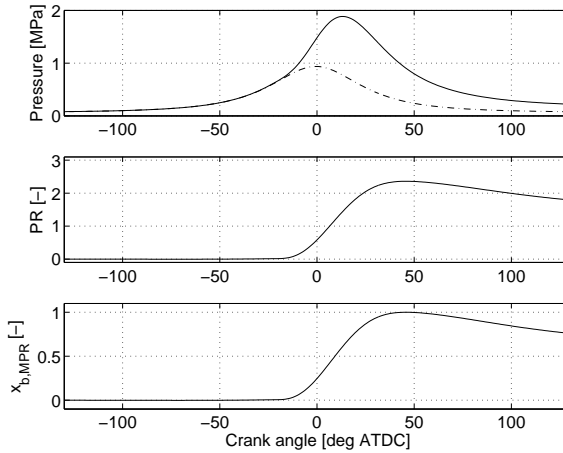


Figure 2.4: Top: Fired pressure trace (solid) and motored pressure trace (dash-dotted), same as in the upper plot of figure 2.2. Middle: Matekunas pressure ratio $PR(\theta)$ (2.21). Bottom: Computed mass fraction burned profile using (2.22).

1988, p.387). This has the result that during the closed phase a substantial amount of charge could be trapped in the crevices. According to Gatowski et al. (1984), the crevice volumes constitute as much as 1-2 percent of the clearance volume in size. It is also shown that due to the temperature difference in the cylinder and in the crevices, as much as 10 (mass) percent of the charge could then be trapped in crevices at peak pressure.

The model in Gatowski et al. (1984) assumes that all crevices can be modeled as a single aggregate constant volume V_{cr} , and that the charge in the crevice assumes the wall temperature T_w and has the same pressure as the combustion chamber. The ideal gas law thus gives the following expression for the mass in the crevice

$$m_{cr} = \frac{p V_{cr}}{R T_w} \implies dm_{cr} = \frac{V_{cr}}{R T_w} dp, \quad (2.23)$$

where it is assumed that T_w and R are constant.

Here, we will only consider spark-ignition engines with a premixed air-fuel charge during the closed part of the engine cycle. Blow-by is also neglected, hence the only mass flow occurring is the one in and out of the crevice region. Mass balance thus yields

$$dm_{tot} = dm_i = -dm_{cr}. \quad (2.24)$$

With the definition of enthalpy $h = RT + u$ and using (2.23)–(2.24),

then equation (2.8) can then be rewritten to:

$$\begin{aligned} \dot{d}Q_{ch} &= \frac{1}{\gamma-1}V dp + \frac{\gamma}{\gamma-1}p dV + \left(\frac{RT}{\gamma-1} + h' - u\right)\frac{V_{cr}}{RT_w}dp + \dot{d}Q_{ht} \\ &= \frac{1}{\gamma-1}V dp + \frac{\gamma}{\gamma-1}p dV + \left(\frac{T}{\gamma-1} + T' + \frac{u'-u}{R}\right)\frac{V_{cr}}{T_w}dp + \dot{d}Q_{ht}. \end{aligned} \quad (2.25)$$

To get a cylinder pressure model, equation (2.25) can be solved for the pressure differential yielding the following expression:

$$dp = \frac{\dot{d}Q_{ch} - \frac{\gamma}{\gamma-1}p dV - \dot{d}Q_{ht}}{\frac{1}{\gamma-1}V + \frac{V_{cr}}{T_w}\left(\frac{T}{\gamma-1} + T' + \frac{u'-u}{R}\right)}. \quad (2.26)$$

The enthalpy h' is evaluated at cylinder conditions when the crevice mass flow is out of the cylinder ($dm_{cr} > 0$), and at crevice conditions otherwise.

Heat transfer model

The heat transfer model relies upon Newton's law of cooling

$$\dot{Q}_{ht} = h_c A \Delta T = h_c A (T - T_w), \quad (2.27)$$

and Woschni (1967) found a correlation between the convection heat transfer coefficient h_c and some geometric and thermodynamic properties¹,

$$h_c = \frac{0.013B^{-0.2}p^{0.8}\left(C_1u_p + \frac{C_2(p-p_0)T_{ref}V_s}{P_{ref}V_{ref}}\right)^{0.8}}{T^{0.55}}. \quad (2.28)$$

Woschni's heat transfer correlation model will be further discussed in section 3.6. Note that when simulating heat transfer in the crank angle domain,

$$\frac{\dot{d}Q_{ht}}{d\theta} = \frac{\dot{d}Q_{ht}}{dt} \frac{dt}{d\theta} = \dot{Q}_{ht} \frac{60}{2\pi N} \quad (2.29)$$

should be used, where the engine speed N [rpm] is assumed constant in the last equality.

Model of thermodynamic properties

The ratio of specific heats $\gamma(T)$ is modeled as a linear function of temperature

$$\gamma_{lin}(T) = \gamma_{300} + b(T - 300). \quad (2.30)$$

In Gatowski et al. (1984) it is stated that this component is important, since it captures how the internal energy varies with temperature. This is an approximation of the thermodynamic properties

¹The value of the first coefficient differs from the one in (Woschni, 1967), since it is recalculated to fit the SI-unit system.

but it is further stated that this approximation is consistent with the other approximations made in the model. Using $\gamma(T) = \frac{c_p(T)}{c_v(T)}$ and $R(T) = c_p(T) - c_v(T)$, together with the linear model of $\gamma(T)$ in (2.30), gives the following expression for $c_v(T)$:

$$c_v(T) = \frac{R}{\gamma(T) - 1} = \frac{R}{\gamma_{300} + b(T - 300) - 1}. \quad (2.31)$$

The only thing remaining in (2.25) to obtain a full description of the model, is an expression for $u' - u$. Remembering that $c_v = (\frac{\partial u}{\partial T})_V$, $u' - u$ can be found by integrating c_v . This describes the sensible energy change for a mass that leaves the crevice and enters the cylinder. The integration is performed as:

$$\begin{aligned} u' - u &= \int_T^{T'} c_v dT \\ &= \frac{R}{b} \{ \ln(\gamma_{300} + b(T' - 300) - 1) - \ln(\gamma_{300} + b(T - 300) - 1) \} \\ &= \frac{R}{b} \ln \left(\frac{\gamma'_{in} - 1}{\gamma_{in} - 1} \right), \end{aligned} \quad (2.32)$$

where equation (2.31) is used.

Gross heat-release simulation

Inserting equations (2.23) to (2.32) into (2.8), yields the following expression for the released chemical energy:

$$\begin{aligned} dQ_{ch} = \\ \frac{1}{\gamma - 1} V dp + \frac{\gamma}{\gamma - 1} p dV + dQ_{ht} + (c_v T + RT' + \frac{R}{b} \ln \left(\frac{\gamma' - 1}{\gamma - 1} \right)) \frac{V_{cr}}{RT_w} dp, \end{aligned} \quad (2.33)$$

which is reformulated as

$$\boxed{\begin{aligned} dQ_{ch} = & \underbrace{\frac{1}{\gamma - 1} V dp + \frac{\gamma}{\gamma - 1} p dV}_{dQ_{net}} + dQ_{ht} + \\ & \underbrace{\left(\frac{1}{\gamma - 1} T + T' + \frac{1}{b} \ln \left(\frac{\gamma' - 1}{\gamma - 1} \right) \right) \frac{V_{cr}}{T_w}}_{dQ_{crevice}} dp. \end{aligned}} \quad (2.34)$$

This ordinary differential equation can easily be solved numerically for the heat-release trace, if a cylinder pressure trace is provided, together with an initial value for the heat release. Given the cylinder pressure in figure 2.2, the heat-release trace given in figure 2.5 is calculated. The solid line is the gross heat released, i.e. the chemical energy released

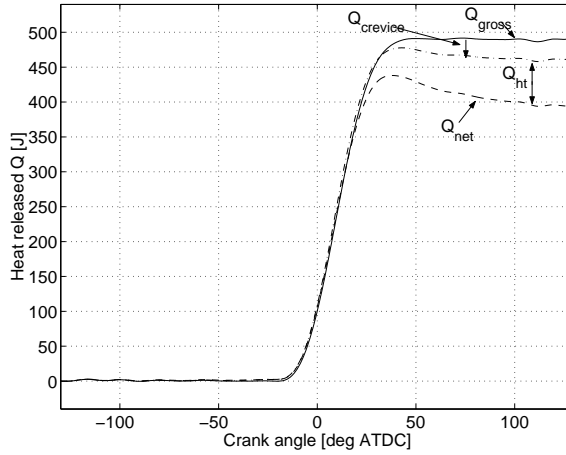


Figure 2.5: Heat-release trace from the Gatowski model given the cylinder pressure in figure 2.2.

during the engine cycle. The dash-dotted line shows the heat released if not considering the crevice effect, and the dashed line shows the net heat release, i.e. when neither heat transfer nor crevice effects are considered. For this particular case, the heat transfer is about 70 J and the crevice effect is about 30 J, i.e. approximately 14 and 6 percent of the total released energy respectively.

Cylinder pressure simulation

Reordering (2.34), gives an expression for the pressure differential as

$$dp = \frac{\dot{d}Q_{ch} - \frac{\gamma}{\gamma-1} p dV - \dot{d}Q_{ht}}{\frac{1}{\gamma-1} V + \frac{V_{cr}}{T_w} \left(\frac{T}{\gamma-1} + \frac{1}{b} \ln \left(\frac{\gamma'-1}{\gamma-1} \right) + T' \right)}. \quad (2.35)$$

This ordinary differential equation can easily be solved numerically for the cylinder pressure, if a heat-release trace $\dot{d}Q_{ch}$ is provided, together with an initial value for the cylinder pressure.

2.6 Comparison of heat release traces

The single-zone heat release models presented in the previous sections all yield different heat release traces for a given cylinder pressure trace. This is shown in figure 2.6, where the heat release traces for the Rassweiler-Withrow, apparent heat release and Gatowski models are

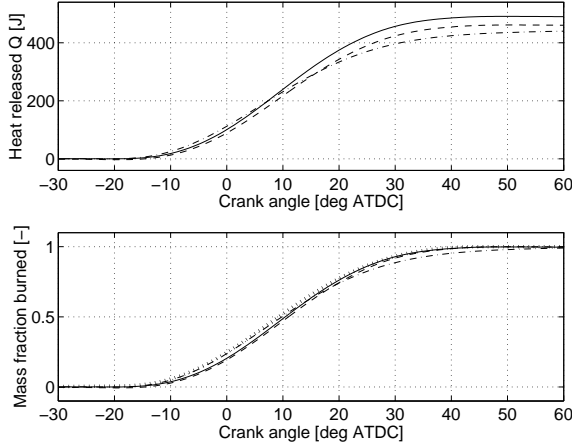


Figure 2.6: *Upper*: Heat-release traces from the three methods, Gatowski (solid), apparent heat release (dashed) and Rassweiler-Withrow (dash-dotted), given the cylinder pressure in figure 2.2. *Lower*: Mass fraction burned traces corresponding to the upper plot with the addition of the Matekunas pressure ratio (dotted).

displayed in the upper plot. As expected, the accumulated heat release is higher for the Gatowski model since it accounts for heat transfer and crevice effects. The mass fraction burned traces do not differ as much, as displayed in the lower plot of figure 2.6. For this operating point, the apparent heat release model produces a mass fraction burned trace more like the one found by the Gatowski model, as shown by comparing the burn angles given in table 2.2. Note that the heat release traces from the Rassweiler-Withrow, apparent heat release and Matekunas models are set constant when they have reached their maximum values in figure 2.6. If not, their behavior would be similar to the net heat release trace Q_{net} given in figure 2.5.

Method	θ_{10}	θ_{50}	θ_{85}	$\Delta\theta_b$
Rassweiler-Withrow	-6.4	9.8	26.9	33.3
Apparent heat release	-4.5	11.0	25.2	29.8
Matekunas	-6.9	9.2	24.0	30.9
Gatowski et.al.	-5.1	10.4	24.4	29.5

Table 2.2: Crank angle positions for 10 %, 50 % and 85 % mfb as well as the rapid burn angle $\Delta\theta_b = \theta_{85} - \theta_{10}$, all given in degrees ATDC for the mass fraction burned traces in the lower plot of figure 2.6.

2.7 Summary

A number of single-zone heat release models have been derived starting from the first law of thermodynamics. The four models described are then compared and their specific model assumptions are pointed out. The most elaborate one is the Gatowski et al. model, which includes heat transfer described by Woschni's heat transfer correlation and crevice effects. This model also assumes that the specific heat ratio for the cylinder charge can be described by a linear function in temperature. The other three models, the Rassweiler-Withrow model, the Matekunas pressure ratio and the apparent heat release model, are all more computationally efficient than the Gatowski et al. model, merely since they lack the modeling of heat transfer and crevice effect, as well as having a constant specific heat ratio for the first two cases. This computational efficiency of course comes to a cost of less descriptive models. The model components in the Gatowski et al. model will now be more thoroughly described in chapter 3.

HEAT-RELEASE MODEL COMPONENTS

Single-zone zero-dimensional heat-release models were introduced in the previous chapter, where their structure and interrelations were discussed. Now the attention is turned to the details of the various components given in chapter 2, and especially those for the Gatowski et al.-model are treated more fully here. Some of the model components have already been introduced in section 2.5, but all components will be more thoroughly explained and compared to other model components in sections 3.1–3.7. It is also described how to find initial values for all parameters. These values are used as initial values when using the single-zone models for parameter estimation. In chapters 5–8 they will also be used as nominal values for fixed parameters, i.e. parameters that are not estimated. The equations that form the complete Gatowski et al. single-zone heat release model are emphasized by boxes, and the model is summarized in section 3.8. In section 3.9 the cylinder pressure sensitivity to the initial values of the parameters is briefly investigated.

3.1 Pressure sensor model

The in-cylinder pressure is measured using a water-cooled quartz pressure transducer, a piezoelectric sensor that becomes electrically charged when there is a change in the forces acting upon it. Piezoelectric transducers react to pressure changes by producing a charge proportional to the pressure change. This charge is then integrated by the charge amplifier, that returns a voltage as output proportional to the pressure.

The charge amplifier has a slow drift due to charge leakage. It is however assumed that this drift is slow, and a static model of the pressure sensor can then be used:

$$\boxed{p_m(\theta) = K_p p(\theta) + \Delta p}, \quad (3.1)$$

where p_m is the measured cylinder pressure and p is the true cylinder pressure. The gain K_p is considered to be constant for the measurement setup, but the offset Δp changes during the cycle due to leakage in the charge amplifier and thermal shock of the sensor. Due to the assumption of a slow drift in the charge amplifier, the pressure offset Δp is considered to be constant for one cycle.

3.1.1 Parameter initialization – pressure offset Δp

The determination of the pressure offset is referred to as pegging the pressure signal, or as cylinder pressure referencing. The pressure offset can be estimated with various methods (Randolph, 1990; Brunt and Pond, 1997). It is generally recommended that pegging is performed once for every pressure cycle. One method is to find Δp in the least squares sense using a polytropic model for the cylinder pressure p .

Another method is to reference the measured cylinder pressure $p_m(\theta)$ to the intake manifold pressure p_{man} before inlet valve closing (IVC), for several samples of p_{man} . This method is often referred to as intake manifold pressure referencing (IMPR) (Brunt and Pond, 1997). Due to standing waves (tuning) in the intake runners at certain operating points, see figure 3.1, the referencing might prove to be insufficient. The referencing should be done at crank angles where the change in cylinder pressure is approximately flat for all operating points, i.e. where the intake manifold pressure p_{man} and the cylinder pressure p are the same or have a constant difference (Brunt and Pond, 1997). Figure 3.2 shows the cylinder pressure change for $\theta \in [-200, -160]$ [deg ATDC] for a number of operating points. Using the same approach as in Brunt and Pond (1997), the referencing should be done between -167 to -162 CAD.

If IMPR proves to be insufficient, Δp must be estimated from the measured cylinder pressure data during the compression phase to achieve a correct referencing. If so, referencing to p_{man} will however still serve as an initial value.

3.1.2 Parameter initialization – pressure gain K_p

The gain K_p can be determined in at least three different ways, summarized in Johansson (1995): The first is to determine the gain for each component in the measurement chain and multiply them to get K_p ;

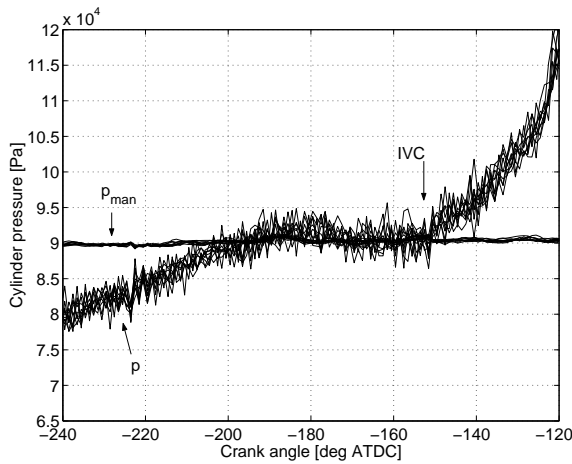


Figure 3.1: Speed dependent effects in the intake runners like ram and tuning effects, are clearly visible between -200 [deg ATDC] and IVC.

The second is to calibrate the total chain by applying a well defined pressure step and measure the result; The third way being to determine the total gain in conjunction with a thermodynamic model. Here the first method is used, and the gain K_p is determined by using tabulated values from the manufacturer.

3.1.3 Crank angle phasing

The pressure trace is sampled at certain events, such as every crank angle degree. Since the mounting can not be performed with infinite precision, an uncertainty in the exact crank angle position for the sampling pulses is inherent. Therefore when calculating the heat-release trace (2.34), or when simulating the cylinder pressure (2.35) to compare it with a measurement, the phasing of the pressure trace relative to the volume trace will most definitively affect the outcome. According to Amann (1985); Morishita and Kushiyama (1997); Staś (2000), this phasing need to be accurate within 0.1 CAD, in order to accurately calculate the work (imep) from a specific cylinder. According to Brunt and Emtage (1997) the phasing need to be within 0.2 CAD to find an imep accurate within 1 %, since typically a 1 CAD phase shift induce a 4 % imep error with gasoline engines and the relationship between imep error and crank angle error is linear (Brunt and Emtage, 1996).

In Andersson (2005), models for crank angle offset $\Delta\theta$ in a multi-cylinder engine are developed. The crank angle offset depends on the cylinder number and the phase of the cycle, i.e. $\Delta\theta$ differs during com-

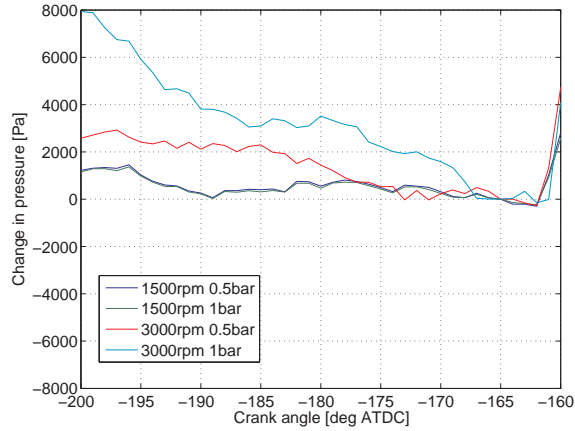


Figure 3.2: Pressure offset as function of CAD when referencing to intake manifold pressure. The pressure change is approximately flat for all operating points between -167 and -162 CAD.

pression, combustion and expansion. This is due to crank-shaft torsion and flexibility. Here we will study the cylinder closest to the crank angle encoder, so the torsion will be small. These effects are therefore not modeled here. Instead the crank shaft is considered to be rigid, and it is assumed that the sampled value at crank angle θ_i can be modeled as having a constant offset $\Delta\theta$ from the true crank angle $\theta_{i,\text{true}}$, the crank angle phasing is modeled as

$$\boxed{\theta_i + \Delta\theta = \theta_{i,\text{true}}}. \quad (3.2)$$

3.1.4 Parameter initialization – crank angle offset $\Delta\theta$

The determination of $\Delta\theta$ is often referred to as *TDC determination*. An initial value of $\Delta\theta$ is provided from a number of motored cycles, by referencing the peak pressure position for the measured cylinder pressure with the corresponding position for a simulated pressure trace, given the same operating conditions. The simulated pressure trace is computed using the Gatowski et al. model.

Other methods of finding the crank angle offset $\Delta\theta$

The easiest way to find $\Delta\theta$ is of course to consider only motored cycles, i.e. when there is no combustion. Then the cylinder pressure would have its maximum at TDC if it were not for heat transfer and crevice effects. Instead, the peak for the compression pressure occurs

before TDC. This difference is referred to as “thermodynamic loss angle” (Hohenberg, 1979). Attempts to avoid the problem connected with unknown heat transfer have been taken in Staś (1996); Morishita and Kushiyama (1997); Nilsson and Eriksson (2004), by using the polytropic relation to determine the position of TDC.

3.2 Cylinder volume and area models

The cylinder volume $V(\theta, x_{off})$ consists of a clearance volume $V_c(x_{off})$ and an instantaneous displacement volume $V_{id}(\theta, x_{off})$, as

$$\boxed{V(\theta, x_{off}) = V_c(x_{off}) + V_{id}(\theta, x_{off})}. \quad (3.3)$$

The instantaneous displaced volume V_{id} depends on the crank angle θ , cylinder bore B , crank radius a_r , connecting rod length l , pin-off x_{off} and is given by

$$\boxed{V_{id}(\theta, x_{off}) = \frac{\pi B^2}{4} (\sqrt{(l + a_r)^2 - x_{off}^2} - a_r \cos \theta - \sqrt{l^2 - (a_r \sin \theta - x_{off})^2})}, \quad (3.4)$$

for $x_{off} \in [-(l - a_r), (l - a_r)]$. The pin-off is defined as positive in the direction of the crank angle revolution. Note that for an engine with pin-off, the crank positions for BDC and TDC are affected. They are given by:

$$\theta_{TDC} = \arcsin \frac{x_{off}}{l + a_r}, \quad (3.5a)$$

$$\theta_{BDC} = \arcsin \left(\frac{x_{off}}{l - a_r} \right) + \pi, \quad (3.5b)$$

and are not symmetric, as in the case without pin-off. The impact of pin-off on the cylinder volume is investigated in (Klein, 2004, pp. 149). It is found, for the SVC engine with $x_{off} \in [-2.2, 4.7]$ mm, that the relative error in instantaneous cylinder volume can be as large as 3.4 %, when the pin-off is not considered. By interpreting the difference in crank angle position of TDC due to pin-off as a constant crank angle offset $\Delta\theta$, as in (3.2), the relative error in $V(\theta, x_{off})$ is reduced to less than 0.6 % in the worst case. Not accounting for pin-off therefore contributes to the problem of TDC determination. Thus if the engine’s pin-off is unknown, the discrepancy in computing the cylinder volume $V(\theta, 0)$ (3.3) can almost fully be captured by the crank angle offset model (3.2). However if the pin-off x_{off} is known, there is no reason for not including it in $V(\theta, x_{off})$ (3.3), since it increases the accuracy of $V(\theta, x_{off})$ at almost no additional computational cost.

When simulating either the heat release (2.34) or the cylinder pressure (2.35), it is necessary to know the differential of the volume function $\frac{dV(\theta, x_{off})}{d\theta}$ and it is given by

$$\boxed{\frac{dV(\theta, x_{off})}{d\theta} = \frac{\pi B^2 a_r}{4} \left(\sin \theta + \frac{(a_r \sin \theta - x_{off}) \cos \theta}{\sqrt{l^2 - (a_r \sin \theta - x_{off})^2}} \right)}. \quad (3.6)$$

When computing the heat transfer rate (3.28), the instantaneous combustion chamber surface area $A(\theta, x_{off})$ through which the heat transfer occurs is computed as

$$A(\theta, x_{off}) = A_{ch} + A_{pc} + A_{lat}(\theta, x_{off}), \quad (3.7)$$

where A_{ch} is the cylinder head surface area and A_{pc} is the piston crown surface area. Here it is assumed that these areas can be approximated by flat surfaces, $A_{pc} = A_{ch} = \frac{\pi B^2}{4}$. The lateral surface area $A_{lat}(\theta, x_{off})$ is approximated by the lateral surface of a cylinder. The instantaneous combustion chamber surface area can then be expressed as

$$\boxed{A(\theta, x_{off}) = \frac{\pi B^2}{2} + \pi B \left(\sqrt{(l + a_r)^2 - x_{off}^2} - a_r \cos \theta - \sqrt{l^2 - (a_r \sin \theta - x_{off})^2} \right)}. \quad (3.8)$$

The compression ratio r_c is defined as the ratio between the maximum ($V_d + V_c$) and minimum (V_c) cylinder volume:

$$r_c = \frac{V_d + V_c}{V_c} = 1 + \frac{V_d}{V_c}. \quad (3.9)$$

3.2.1 Parameter initialization – clearance volume V_c

The clearance volume V_c strongly influences the maximum cycle temperature and pressure through the compression ratio, and for heat release and pressure simulations it is therefore of great importance. Due to geometric uncertainties in manufacturing, a spread of the actual clearance volume from engine to engine and cylinder to cylinder is inherent (Amann, 1985). The compression ratio given from the manufacturer serves well as an initialization. It can also be initialized by using a polytropic relation, an initialization that works better the lower the real compression ratio is (Klein et al., 2003). This since the polytropic relation does not take heat transfer and crevice effects into account explicitly.

3.3 Temperature models

Two models for the in-cylinder temperature will be described, the first is the mean charge single-zone temperature model and it is the one

used in the Gatowski et al.-model. The second is a two-zone mean temperature model, used to compute the single-zone thermodynamic properties as mean values of the properties in a two-zone model, an approach that will be introduced in the next chapter in section 4.6.

3.3.1 Single-zone temperature model

The mean charge temperature T for the single-zone model is found from the state equation $pV = m_{tot}RT$, assuming the total mass of charge m_{tot} and the mass specific gas constant R to be constant. These assumptions are reasonable since the molecular weights of the reactants and the products are essentially the same (Gatowski et al., 1984). If all thermodynamic states $(p_{ref}, T_{ref}, V_{ref})$ are known/evaluated at a given reference condition ref , such as IVC, the mean charge temperature T is computed as

$$T(\theta) = \frac{T_{IVC}}{p_{IVC}V_{IVC}}p(\theta)V(\theta). \quad (3.10)$$

The cylinder volume at IVC is computed using the cylinder volume given in (3.3) for θ_{IVC} and is therefore considered to be known. The two other states at IVC (p_{IVC}, T_{IVC}) are considered unknown and have to be estimated.

3.3.2 Parameter initialization – cylinder pressure at IVC p_{IVC}

The parameter p_{IVC} is initialized by the measured cylinder pressure p_m in conjunction with the pressure sensor offset Δp and gain K_p , the crank angle position for IVC, and the crank angle offset $\Delta\theta$ by using equations (3.1) and (3.2). It needs to be pointed out that the position of IVC does not mean when the intake valve touches its seat, rather the position where intake mass flow has stopped. Therefore in most cases $p_{IVC} > p_{man}$. The parameter p_{IVC} is also used as an initial value for the ordinary differential equation in e.g. (2.35).

3.3.3 Parameter initialization – mean charge temperature at IVC T_{IVC}

The mean charge temperature at IVC differs from the gas temperature in the intake manifold T_{man} . The charge is heated due to both mixing with residual gases that are approximately at 1400 K (Heywood, 1988, p.178), and in-cylinder heat transfer from piston, valves and cylinder walls. On the other hand, fuel evaporation can cool the charge by as much as 25 K according to Stone (1999). Altogether these effects make T_{IVC} become larger than T_{man} . In Öberg and Eriksson (2006) three

models for computing the residual gas mass fraction $x_r = \frac{m_r}{m_{tot}}$ (Fox et al., 1993; Ponti et al., 2004; Mladek and Onder, 2000) are compared. The first model is based on a flow restriction model, and the other models are based on energy balance at a reference point e.g. IVC and require a cylinder pressure measurement. The last two methods also compute the residual gas temperature T_r and T_{IVC} . It is found that the model in Ponti et al. (2004) but with the exclusion of external EGR, is the best choice and it is therefore used here. It is described as follows; Compute T_{IVC} using the ideal gas law, the mass of the air-fuel charge m_{af} , and an estimate of x_r according to:

$$m_{tot} = \frac{m_{af}}{1 - x_r}, \quad (3.11)$$

where m_{tot} is the total charge mass, and

$$m_{af} = m_a \left(1 + \frac{1}{\lambda \left(\frac{A}{F} \right)_s} \right), \quad (3.12)$$

where λ and $\left(\frac{A}{F} \right)_s$ are the normalized and stoichiometric air-fuel ratios respectively, and m_a is calculated from the measured air mass flow. The specific gas constant and temperature at IVC are stated by

$$R_{IVC} = R_{b,r}(p_{IVC}, T_r) \cdot x_r + R_{u,af}(T_{af}) \cdot (1 - x_r), \quad (3.13)$$

$$T_{IVC} = \frac{p_{IVC} V_{IVC}}{R_{IVC} m_{tot}}. \quad (3.14)$$

Thermodynamic properties such as the specific gas constants R and specific heats c_v are evaluated using a chemical equilibrium program developed by Eriksson (2004), more thoroughly described in section 4.2.

The new residual gas mass fraction is computed using energy balance at IVC as

$$x_r = \frac{c_{vu,af}(T_{af}) \cdot (T_{IVC} - T_{af})}{c_{vb,r}(p_{man}, T_r) \cdot (T_r - T_{IVC}) + c_{vu,af}(T_{af}) \cdot (T_{IVC} - T_{af})}, \quad (3.15)$$

where the temperature for the air-fuel charge T_{af} is given by

$$T_{af} = T_{man} \left(\frac{p_{man}}{p_{IVC}} \right)^{\frac{1-\gamma_{af}}{\gamma_{af}}}, \quad (3.16)$$

assuming that the fresh charge experiences a polytropic process from manifold conditions to in-cylinder conditions. The residual gas temperature T_r is given by a correlation model developed in Mladek and Onder (2000) as

$$T_r = -(C_{1,T_r} (m_{tot} N))^{C_{2,T_r}} + C_{3,T_r}. \quad (3.17)$$

The parameters in (3.17) have to be tuned using simulations for each engine type, as done in Öberg and Eriksson (2006). In order to have a converging fix-point iteration scheme, x_r is updated according to

$$x_{r,used} = \frac{x_{r,new} + x_{r,old}}{2}, \quad (3.18)$$

where $x_{r,new}$ is given by (3.15) and $x_{r,old}$ is the estimate from the previous iteration.

The algorithm for computing x_r and T_{IVC} can then be summarized as:

Algorithm 3.1 – Residual gas mass fraction (Ponti et al., 2004)

Let x_r be the initial estimate of the residual gas mass fraction, and set $x_{r,old} = x_r$.

1. Compute the total mass m_{tot} (3.11).
 2. Compute the temperature at IVC, T_{IVC} (3.14).
 3. Compute the residual gas mass fraction, $x_{r,new}$ using (3.15).
 4. Update the estimate $x_{r,used}$ according to (3.18).
 5. Check if $x_{r,used}$ has converged, i.e. if $|\frac{x_{r,used} - x_{r,old}}{x_{r,used}}| < 1 \times 10^{-4}$, if not return to step 1 and set $x_{r,old} = x_{r,used}$.
 6. Return $x_r = x_{r,used}$ and T_{IVC} .
-

3.4 Crevice model

In an engine, gases flow in and out of the crevices connected to the combustion chamber as the cylinder pressure rises and falls. Crevices include those volumes between piston, rings and liner, any head gasket gap, spark plug threads and space around the pressure transducer. During compression some of the charge flows into the crevices, and remains there until the expansion phase, when most of the charge returns to the combustion chamber. The flame can not propagate into the crevices, and therefore some of the charge is not combusted. A small part of the cylinder charge blows by the piston rings and ends up in crank-case. Here this part is assumed to be zero and therefore not modeled.

When modeling the crevice effect, the temperature in the crevices are assumed to be close to the cylinder wall temperature, so during the closed phase a substantial amount of charge could be trapped in the crevices. Consider the ratio of total charge mass to the mass in the crevices:

$$\frac{m_{cr}}{m_{tot}} = \frac{V_{cr}}{V} \frac{T}{T_{cr}}. \quad (3.19)$$

According to Gatowski et al. (1984), the crevice volume V_{cr} can constitute as much as 1-2 percent of the clearance volume V_c in size. The temperature difference in the cylinder T and in the crevices T_{cr} approaches a factor 4-5 at the end of combustion. As a consequence as much as 10 (mass) percent of the charge could then be trapped in crevices at peak pressure.

The model developed and applied in Gatowski et al. (1984) assumes that all crevices can be modeled as a single aggregate constant volume V_{cr} , and that the charge in the crevice assumes the average wall temperature T_w and is at the same pressure as in the combustion chamber. The ideal gas law thus gives

$$pV_{cr} = m_{cr}RT_w \implies dm_{cr} = \frac{V_{cr}}{RT_w} dp, \quad (3.20)$$

where it is assumed that T_w and R are constant. Gatowski et al. (1984) points out that this model is not meant to account for each crevice, but rather to account for the overall crevice effect.

3.4.1 Parameter initialization – crevice volume V_{cr}

The single aggregate crevice volume V_{cr} is unknown and is therefore set to 1.5 percent of the clearance volume V_c , which is a reasonable value according to Gatowski et al. (1984). For an engine with varying clearance volume, such as the SVC engine, this would yield a crevice volume dependent of the compression ratio. To avoid this, V_{cr} is set to 1.5% V_c at $r_c = 11$, i.e. the clearance volume in the mid range of the compression ratio is used.

3.4.2 Parameter initialization – cylinder mean wall temperature T_w

The cylinder wall temperature T_w is not only used in the crevice model, but also in the heat transfer model described in section 3.6. It varies during the engine cycle due to heat transfer in the cylinder block, but the surface temperature fluctuations are locally relatively small (i.e. 5-10 K) suggesting that a constant surface temperature can be used (Anatone and Cipollone, 1996). Therefore an area-weighted mean value of

the temperatures of the exposed cylinder walls, the head and the piston crown for the closed part of the engine cycle is used. Here T_w is initialized to a constant value of 440 K (Brunt and Emtage, 1997; Eriksson, 1998), set only by it being a reasonable value. There exists other methods of estimating the cylinder wall temperature, see e.g. Arsie et al. (1999).

3.5 Combustion model

The combustion of fuel and air is a very complex process, and would require extensive modeling to be fully captured. The approach here is to use a parameterization of the burn rate of the combusted charge. The prevailing combustion model is the Vibe function (Vibe, 1970), which in some literature is spelled Wiebe function.

3.5.1 Vibe function

The Vibe function is often used as a parameterization of the mass fraction burned x_b , and it has the following form

$$x_b(\theta) = 1 - e^{-a\left(\frac{\theta - \theta_{ig}}{\Delta\theta_{cd}}\right)^{m+1}}, \quad (3.21)$$

and the burn rate is given by its differentiated form

$$\boxed{\frac{dx_b(\theta)}{d\theta} = \frac{a(m+1)}{\Delta\theta_{cd}} \left(\frac{\theta - \theta_{ig}}{\Delta\theta_{cd}}\right)^m e^{-a\left(\frac{\theta - \theta_{ig}}{\Delta\theta_{cd}}\right)^{m+1}}}, \quad (3.22)$$

where θ_{ig} is the start of the combustion, a and m are adjustable parameters, and $\Delta\theta_{cd}$ is the total combustion duration. The Vibe function is over-parameterized in a , m , and $\Delta\theta_{cd}$, since for example the sets $[a = 1, \Delta\theta_{cd} = 1, m = 1]$ and $[a = 4, \Delta\theta_{cd} = 2, m = 1]$ give identical function values. To parameterize the mass fraction burned (mfb) trace with physical parameters, two burn rate angles are often used, namely the flame-development angle $\Delta\theta_d$ which corresponds to the crank angle from 0 % mfb (ignition) to 10 % mfb, and the rapid burn angle $\Delta\theta_b$ (10-85 % mfb) (Heywood, 1988), illustrated in figure 3.3. The burn angle parameters have a direct relation to the parameters in the Vibe function, but due to the over-parameterization in a and $\Delta\theta_{cd}$, one of them must be specified before-hand to get a unique solution. If $\Delta\theta_{cd}$ is specified, the Vibe parameters become:

$$\boxed{m = \frac{\ln(\ln(1 - 0.1)) - \ln(\ln(1 - 0.85))}{\ln \Delta\theta_d - \ln(\Delta\theta_d + \Delta\theta_b)} - 1}, \quad (3.23a)$$

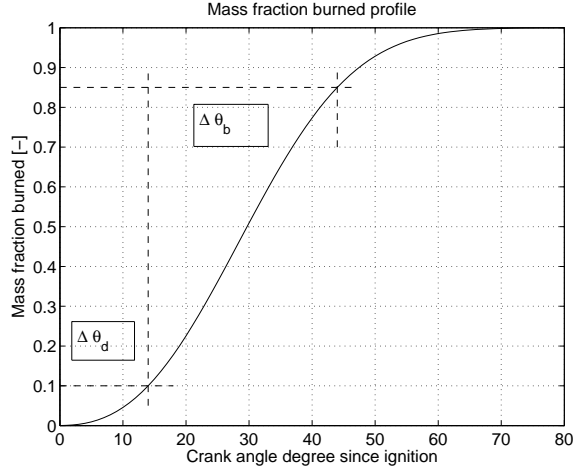


Figure 3.3: Mass fraction burned profile with the flame development angle $\Delta\theta_d$ and rapid burn angle $\Delta\theta_b$ marked.

$$a = -\left(\frac{\Delta\theta_{cd}}{\Delta\theta_d}\right)^{m+1} \ln(1 - 0.1), \quad (3.23b)$$

The differentiated Vibe function (3.22) is used to produce a mass fraction burned trace, i.e. a normalized heat-release trace. The absolute value of the heat-release rate $\frac{dQ_{ch}}{d\theta}$ is given by

$$\frac{dQ_{ch}}{d\theta} = Q_{in} \frac{dx_b}{d\theta}, \quad (3.24)$$

where Q_{in} represents the total energy released from combustion.

Summing up, the combustion process is described by (3.24) and parameterized by Q_{in} , θ_{ig} , $\Delta\theta_d$, and $\Delta\theta_b$.

3.5.2 Parameter initialization – energy released Q_{in}

The total energy released Q_{in} is influenced by a lot of parameters, such as residual gas fraction, combustion efficiency, mass of fuel, fuel heating value, but also the mass fraction burned rate due to the dependence of thermodynamic properties for the mixture of temperature and pressure. It is here modeled as

$$Q_{in} = m_f q_{HV} \eta_f, \quad (3.25)$$

where m_f is the fuel mass, q_{HV} the specific lower heating value of the fuel and η_f is the combustion efficiency. There at least two ways

of computing Q_{in} ; If the fuel mass m_f is measured, Q_{in} can be found from (3.25) by assuming a combustion efficiency. If m_f is not measured, another approach must be taken. One such approach is to rewrite m_f in (3.25) as

$$m_f = \frac{m_{af}}{1 + \lambda(\frac{A}{F})_s} = \frac{(1 - x_r)m_{tot}}{1 + \lambda(\frac{A}{F})_s}, \quad (3.26)$$

where the total charge mass m_{tot} is found using the ideal gas law at a reference point during the high-pressure phase, e.g. IVC, yielding $m_{tot} = \frac{p_{IVC} V_{IVC}}{R_{IVC} T_{IVC}}$. The fuel is assumed to be iso-octane, that has $R_u = 290 \frac{J}{kgK}$ (at 300 K), lower heating value $q_{HV} = 44.0 \frac{MJ}{kg}$, and stoichiometric air-fuel equivalence ratio $(\frac{A}{F})_s = 14.6$ (Heywood, 1988, p.915). The specific gas constant R_{IVC} is given by (3.13) and the residual gas fraction x_r by (3.15). So Q_{in} is initialized as

$$Q_{in} = m_f \eta_f q_{HV} = \frac{(1 - x_r)}{1 + \lambda(\frac{A}{F})_s} \frac{p_{IVC} V_{IVC}}{R_{IVC} T_{IVC}} \eta_f q_{HV}, \quad (3.27)$$

where the combustion efficiency η_f is assumed to be one.

To solve the ordinary differential equation in (2.34) an initial value for the accumulated heat released at IVC Q_{IVC} must be specified. It is set to zero.

3.5.3 Parameter initialization – angle-related parameters $\{\theta_{ig}, \Delta\theta_d, \Delta\theta_b\}$

The angle-related parameters $\{\theta_{ig}, \Delta\theta_d, \Delta\theta_b\}$ are initialized by the mass fraction burned trace found from the Rassweiler-Withrow method mentioned in section 2.2. Nominal values are in the intervals (Eriksson, 1999):

θ_{ig}	$\Delta\theta_d$	$\Delta\theta_b$
[-30, 0] [deg ATDC]	[15, 40] [deg]	[10, 50] [deg]

To get an unique solution for (3.23), the total combustion duration $\Delta\theta_{cd}$ is set to $\frac{100\pi}{180}$ rad.

3.6 Engine heat transfer

Typically 20-35 % of the fuel energy is passed on by heat transfer to the engine coolant, the upper limit is reached for low load conditions (Stone, 1999, p.429). Of the total heat transfer, about half comes from in-cylinder heat transfer and the rest from heat transfer in the exhaust port.

In-cylinder heat transfer

The in-cylinder heat transfer occurs by both convection and radiation, where convection constitutes the major part (Schmidt et al., 1993). In SI engines, up to approximately 20 %, but usually much less of the in-cylinder heat transfer is due to radiation, but this is in some instances included in the correlation for convective heat transfer (Woschni, 1967). For CI engines however, the heat transfer originating from radiation can constitute a more significant part (up to 40 % (Heywood, 1988, p.696)) and has to be accounted for explicitly (Annand, 1963). Since we are dealing with SI engines, only convective heat transfer is modeled, but keeping in mind that the radiative heat transfer is accounted for by the correlations.

The magnitude of the rate of energy transfer by convection \dot{Q}_{ht} , which occurs in a direction perpendicular to the fluid surface interface, is obtained by Newton's law of cooling

$$\boxed{\dot{Q}_{ht} = h_c A \Delta T = h_c A (T - T_w)}, \quad (3.28)$$

where A is the surface area of the body which is in contact with the fluid, ΔT is the appropriate temperature difference, and h_c is the convection heat transfer coefficient. The coefficient h_c varies both in time and space, and since it is a composite of both microscopic and macroscopic phenomena, many factors must be taken into consideration for a full description. A full description of h_c is needed if for example thermal stress on the cylinder head is to be investigated (Bergstedt, 2002). On the other hand, a position-averaged heat transfer coefficient will be sufficient for predicting the heat flow to the coolant, and this will be the approach taken here. There exists a number of models for h_c , for e.g. (Annand, 1963; Woschni, 1967; Hohenberg, 1979). Later works (Shayler et al., 1993; Hayes et al., 1993; Pivec et al., 1998; Wimmer et al., 2000) experimentally verified the Woschni correlation to be the better one for the closed part of the engine cycle.

Woschni's heat-transfer correlation

The form proposed by Woschni (1967) is:

$$h_c = C(pw)^{0.8} B^{-0.2} T^{-0.55}. \quad (3.29)$$

Woschni found that the exponent for T should be -0.53, but this is not consistent with the prerequisites in the derivation, see (Klein, 2004, pp. 37). Woschni states that the characteristic speed w depends on two terms. One is due to piston motion and is modeled as the mean piston speed $u_p = \frac{2aN}{60}$ [m/s], where a [m] is the crank radius and N [rpm] is the engine speed. The other term is due to swirl originating from the

combustion event, which is modeled as a function of the pressure rise due to combustion, i.e. $p-p_0$ where p_0 is the motored pressure. Woschni used the measured motored pressure, but later on Watson and Janota (1982) proposed to use the polytropic process model (2.11) instead:

$$p_0 = p_{ref} \left(\frac{V_{ref}}{V} \right)^n \quad (3.30)$$

where n is the polytropic exponent, and (p_{ref}, V_{ref}) are evaluated at any reference condition, such as IVC. The characteristic speed w can then be expressed as:

$$w = C_1 u_p + C_2 (T - T_0) = C_1 u_p + C_2 \frac{V T_{IVC}}{p_{IVC} V_{IVC}} (p - p_0), \quad (3.31)$$

where the first term originates from convection caused by piston motion and the second term from the combustion itself, where T_0 is the motored mean gas temperature. This results in the following expression for the heat transfer coefficient h_c ¹:

$$h_c = \frac{0.013 B^{-0.2} p^{0.8} \left(C_1 u_p + \frac{C_2 (p-p_0) T_{IVC} V}{p_{IVC} V_{IVC}} \right)^{0.8}}{T^{0.55}}, \quad (3.32)$$

where

p	cylinder pressure for fired cycle	[Pa]
p_0	cylinder pressure for motored cycle	[Pa]
T	mean gas temperature	[K]
u_p	mean piston speed	[m/s]
V	instantaneous cylinder volume	[m ³]
C_1	constant	[-]
C_2	constant	[m/(sK)]
$(p_{IVC}, V_{IVC}, T_{IVC})$	at reference condition IVC	

Simulation in crank angle domain

Note that $\dot{Q}_{ht} = \frac{dQ_{ht}}{dt}$, thus when simulating heat transfer in the crank angle domain,

$$\frac{dQ_{ht}}{d\theta} = \frac{dQ_{ht}}{dt} \frac{dt}{d\theta} = \dot{Q}_{ht} \frac{60}{2\pi N} \quad (3.33)$$

should be used where N [rpm] is the engine speed.

¹The numerical value of the first coefficient differs from the one in (Woschni, 1967), since it is calculated to fit the SI-unit system.

3.6.1 Parameter initialization – $\{C_1, C_2\}$

Woschni found experimentally that during the closed part of the engine cycle, the parameters $C_1 = 2.28$ and $C_2 = 3.24 \cdot 10^{-3}$ gave a good fit, and they therefore serve well as initial values. Woschni also pointed out that the parameters (C_1, C_2) are engine dependent, and are therefore likely to change for different engine geometries.

3.7 Thermodynamic properties

The accuracy with which the energy balance can be calculated for a combustion chamber depends in part on how accurately changes in the internal energy of the cylinder charge are represented. The most important thermodynamic property used in calculating the heat release rates for engines is the ratio of specific heats, $\gamma = \frac{c_p}{c_v}$ (Gatowski et al., 1984; Chun and Heywood, 1987; Guezennec and Hamama, 1999).

In the Gatowski et al.-model, the specific heats ratio $\gamma(T)$ is modeled as a linear function of temperature,

$$\boxed{\gamma_{lin}(T) = \gamma_{300} + b(T - 300)}. \quad (3.34)$$

Gatowski et al. (1984) states that this component is important, since it captures how the internal energy varies with temperature. This is an approximation of the thermodynamic properties but it is further stated that this approximation is consistent with the other approximations made in the model. It will be shown in chapter 4 that the linear model of γ in temperature T introduces a modeling error in cylinder pressure which is 15 times the cylinder pressure measurement noise in mean. A model of γ that introduces an error in the same order as the noise is also given in chapter 4.

3.7.1 Parameter initialization – γ_{300} and b

The initial values for the two parameters in the linear model of γ (3.34) are computed by using a chemical equilibrium program (Eriksson, 2004). First the specific heat ratio is computed for a specific fuel by assuming that the mixture is burned and at equilibrium at all instances. Then the two parameters γ_{300} and b are fitted in the least squares sense to the resulting γ . Nominal values are in the intervals; $\gamma_{300} \in [1.35, 1.41]$ and $b \in [-8 \cdot 10^{-5}, -12 \cdot 10^{-5}] K^{-1}$.

3.8 Summary of single-zone heat-release models

The model component equations, that are emphasized by boxes in chapter 2 and 3, for the Gatowski et al.-model are summarized here, together with the inputs, outputs and unknown parameters for the model.

Model inputs and outputs

Input	Description	Unit
λ	air-fuel ratio	[-]
N	engine speed	[rpm]
p_{exh}	exhaust manifold pressure	[Pa]
p_{man}	intake manifold pressure	[Pa]
T_{man}	intake manifold temperature	[K]
θ_{IVC}	crank angle degree for IVC	[deg ATDC]
θ_{EVO}	crank angle degree for EVO	[deg ATDC]
Output	Description	Unit
p	cylinder pressure	[Pa]
p_m	measured cylinder pressure	[Pa]
Q_{ch}	chemical energy released as heat	[J]

In heat release models a pressure trace is given as input and the heat release is the output, while in pressure models a heat release trace is the input and pressure is the output.

Model component equations

Heat release differential (2.25);

$$\mathrm{d}Q_{ch} = \frac{1}{\gamma-1}V dp + \frac{\gamma}{\gamma-1}p dV + \left(\frac{T}{\gamma-1} + T' + \frac{u'-u}{R}\right)\frac{V_{cr}}{T_w} dp + \mathrm{d}Q_{ht} \quad (3.35)$$

or cylinder pressure differential (2.26);

$$dp = \frac{\mathrm{d}Q_{ch} - \frac{\gamma}{\gamma-1}p dV - \mathrm{d}Q_{ht}}{\frac{1}{\gamma-1}V + \frac{V_{cr}}{T_w}\left(\frac{T}{\gamma-1} + T' + \frac{u'-u}{R}\right)} \quad (3.36)$$

Pressure sensor model (3.1);

$$p_m = K_p p + \Delta p \quad (3.37)$$

Crank angle phasing (3.2);

$$\theta_i + \Delta\theta = \theta_{i,\text{true}} \quad (3.38)$$

Cylinder volume $V(\theta, x_{off})$ (3.3), (3.4) and (3.6);

$$V(\theta, x_{off}) = V_c(x_{off}) + V_{id}(\theta, x_{off}) \quad (3.39a)$$

$$V_{id}(\theta, x_{off}) = \frac{\pi B^2}{4} (\sqrt{(l + a_r)^2 - x_{off}^2} - a_r \cos \theta - \sqrt{l^2 - (x_{off} + a_r \sin \theta)^2}) \quad (3.39b)$$

$$\frac{dV(\theta, x_{off})}{d\theta} = \frac{\pi B^2 a_r}{4} \left(\sin \theta + \frac{(x_{off} + a_r \sin \theta) \cos \theta}{\sqrt{l^2 - (x_{off} + a_r \sin \theta)^2}} \right) \quad (3.39c)$$

Temperature model (3.10);

$$T = \frac{T_{IVC}}{p_{IVC} V_{IVC}} p V \quad (3.40)$$

Crevice model (3.20);

$$dm_{cr} = \frac{V_{cr}}{R T_w} dp \quad (3.41)$$

Vibe combustion model (3.24), (3.22) and (3.23);

$$\frac{dQ_{ch}}{d\theta} = Q_{in} \frac{dx_b}{d\theta} \quad (3.42a)$$

$$\frac{dx_b(\theta)}{d\theta} = \frac{a(m+1)}{\Delta\theta_{cd}} \left(\frac{\theta - \theta_{ig}}{\Delta\theta_{cd}} \right)^m e^{-a \left(\frac{\theta - \theta_{ig}}{\Delta\theta_{cd}} \right)^{m+1}} \quad (3.42b)$$

$$m = \frac{\ln(\ln(1 - 0.1) - \ln(1 - 0.85))}{\ln \Delta\theta_d - \ln(\Delta\theta_d + \Delta\theta_b)} - 1 \quad (3.42c)$$

$$a = - \left(\frac{\Delta\theta_{cd}}{\Delta\theta_d} \right)^{m+1} \ln(1 - 0.1) \quad (3.42d)$$

Woschni's heat transfer correlation (3.33), (3.28), (3.32) and (3.8);

$$\frac{d\dot{Q}_{ht}}{d\theta} = \frac{d\dot{Q}_{ht}}{dt} \frac{dt}{d\theta} = \dot{Q}_{ht} \frac{60}{2\pi N} \quad (3.43a)$$

$$\dot{Q}_{ht} = h_c A \Delta T = h_c A (T - T_w) \quad (3.43b)$$

$$h_c = \frac{0.013 B^{-0.2} p^{0.8} \left(C_1 u_p + \frac{C_2 (p-p_0) T_{ref} V}{p_{ref} V_{ref}} \right)^{0.8}}{T^{0.55}} \quad (3.43c)$$

$$A(\theta, x_{off}) = \frac{\pi B^2}{2} + \pi B \left(\sqrt{(l + a_r)^2 - x_{off}^2} - a_r \cos \theta - \sqrt{l^2 - (x_{off} + a_r \sin \theta)^2} \right) \quad (3.43d)$$

To simulate the Gatowski et al.-model, equations (3.36)–(3.43) are used together with the linear specific heat ratio model (3.34);

$$\gamma_{lin}(T) = \gamma_{300} + b(T - 300) \quad (3.44)$$

and the corresponding crevice energy term (2.32);

$$u' - u = \frac{R}{b} \ln \left(\frac{\gamma' - 1}{\gamma - 1} \right) \quad (3.45)$$

Par.	Description	Value	Equation
γ_{300}	constant specific heat ratio [-]	1.3678	(3.34)
b	slope for specific heat ratio [K^{-1}]	$-8.13 \cdot 10^{-5}$	(3.34)
C_1	heat-transfer parameter [-]	2.28	(3.32)
C_2	heat-transfer parameter [$m/(s K)$]	$3.24 \cdot 10^{-3}$	(3.32)
$\Delta\theta$	crank angle phasing [deg ATDC]	0.4	(3.2)
Δp	bias in pressure measurements [kPa]	30	(3.1)
K_p	pressure measurement gain[-]	1	(3.1)
p_{IVC}	cylinder pressure at IVC [kPa]	100	(3.10), (2.26)
T_{IVC}	mean charge temperature at IVC [K]	340	(3.10)
T_w	mean wall temperature [K]	440	(3.20),(3.28)
V_c	clearance volume [cm^3]	62.9	(3.3)
V_{cr}	single aggregate crevice volume [% V_c]	1.5	(3.20)
θ_{ig}	ignition angle [deg ATDC]	-20	(3.22)
$\Delta\theta_d$	flame-development angle [deg ATDC]	15	(3.22)
$\Delta\theta_b$	rapid-burn angle [deg ATDC]	30	(3.22)
Q_{in}	released energy from combustion [J]	1500	(3.24)

Table 3.1: Nominal values for the parameters in the Gatowski et al. single-zone heat release model. For fired cycles, $T_w = 440$ K and $T_{IVC} = 340$ K, and for motored cycles, $T_w = 400$ K and $T_{IVC} = 310$ K.

Unknown parameters

The parameters used in the Gatowski et al. single-zone model and an example of nominal values is summarized in table 3.1.

3.9 Sensitivity in pressure to parameter initialization

The cylinder pressure is simulated for the nominal values in the table 3.2 using (3.36)–(3.45), and yields the cylinder pressure given in figure 3.4. The nominal values are the same as in table 3.1. To get an idea of how sensitive the cylinder pressure is to errors in the initialized parameters, a sensitivity analysis is performed by perturbing the parameters one at a time with the realistic perturbations given in table 3.2. In most cases the perturbation is set to 10 percent of their nominal value, but when the nominal value is small in comparison to the uncertainty in the parameter this approach would not give a fair comparison. The perturbation for these parameters are therefore set to reasonable values.

The perturbed simulated cylinder pressure is then compared to the nominal one, in terms of root mean square error (RMSE) and maximum absolute residual value (Max Res), where RMSE is the more important measure when considering least squares optimization. The residual is here defined as the difference between the nominal and perturbed

Par.	Nominal & perturbation value			RMSE [kPa]	Max Res [kPa]	S [-]
γ_{300}	1.3678	0.137	[-]	522.6	1407.3	5.25
$\Delta\theta_d$	15	5	[deg]	270.5	1029.2	0.58
θ_{ig}	-20	5	[deg ATDC]	237.9	860.3	0.73
V_c	62.9	6.29	[cm^3]	210.3	603.7	1.76
K_p	1	0.1	[-]	184.9	465.0	1.55
T_w	440	44	[K]	110.1	285.4	0.88
Q_{in}	1500	150	[J]	101.7	263.7	0.81
$\Delta\theta_b$	30	5	[deg]	101.6	397.4	0.45
p_{IVC}	100	10	[kPa]	95.7	217.9	0.77
T_{IVC}	340	44	[K]	63.7	176.7	0.36
V_{cr}	1.5	1.5	[% V_c]	36.3	122.3	0.03
b	$-8.13 \cdot 10^{-5}$	$-8.13 \cdot 10^{-6}$	[K^{-1}]	25.0	77.0	0.19
$\Delta\theta$	0.4	0.2	[deg]	10.3	31.4	0.02
Δp	30	10	[kPa]	10.0	10.0	0.02
C_2	$3.24 \cdot 10^{-3}$	$3.24 \cdot 10^{-4}$	[$m/(s K)$]	3.8	8.2	0.03
C_1	2.28	0.228	[-]	1.6	2.9	0.01

Table 3.2: Nominal and perturbation values, where the perturbations are performed by adding or subtracting the perturbation from the nominal value. The root mean square error (RMSE), maximal residual (Max Res) and sensitivity function S (3.46) are computed for the worst case for each parameter. The parameters are sorted in descending order of their RMSE.

cylinder pressures. The parameter sensitivity is also examined, and it is computed here as

$$S = \frac{\frac{RMSE(p)}{\bar{p}}}{\frac{|\Delta x|}{|x|}}, \quad (3.46)$$

where x is the nominal parameter value, Δx is the parameter perturbation and \bar{p} is the mean cylinder pressure. The results are summarized in table 3.2. When comparing the RMSE for every parameter, the constant γ_{300} in the linear specific heat ratio model, the burn related angles $\Delta\theta_d$ and θ_{ig} , and the clearance volume V_c show highest sensitivity in the mean and are therefore more in need of a proper initialization than the others. On the other hand, disturbances in the values of the two Woschni parameters C_1 and C_2 do not affect the resulting cylinder pressure significantly. Note that the model of the cylinder pressure is nonlinear, so the results found from this analysis is only valid locally, but it still gives an idea of which parameters are the most sensitive ones.

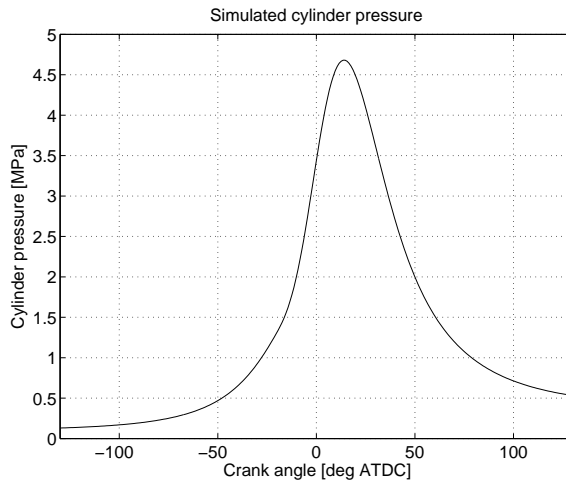


Figure 3.4: Simulated cylinder pressure using the nominal values in table 3.2.

A SPECIFIC HEAT RATIO MODEL FOR SINGLE-ZONE HEAT RELEASE MODELS

The accuracy with which the energy balance can be calculated for a combustion chamber depends in part on how accurately changes in the internal energy of the cylinder charge are represented. The most important thermodynamic property used when calculating the heat release rates in engines is the ratio of specific heats, $\gamma(T, p, \lambda) = \frac{c_p}{c_v}$ (Gatowski et al., 1984; Chun and Heywood, 1987; Guezennec and Hamama, 1999).

Based on the first law of thermodynamics, Gatowski et al. (1984) developed a single-zone heat release model that has been widely used, where the specific heat ratio is represented by a linear function in mean charge temperature T :

$$\gamma_{lin}(T) = \gamma_{300} + b(T - 300). \quad (4.1)$$

This allows a critical examination of the burning process by analysis of the heat release. In order to compute the heat release correctly, the parameters in the single-zone model need to be well tuned. These parameters, such as heat transfer coefficients, γ_{300} and b in the linear γ -model (4.1) and so on, can be tuned using well known methods. For instance, Eriksson (1998) uses standard prediction error methods (Ljung, 1999) to tune the parameters. This is done by minimizing the prediction error of the measured cylinder pressure, i.e. by minimizing the difference between the modeled and measured cylinder pressure. Applying standard parameter identification methods usually ends up in non-physical values of γ_{300} , as it becomes larger than 1.40, which is the value of γ_{300} for pure air. It has also been shown in table 3.2 that

γ_{300} is the most sensitive single-zone parameter. But more importantly, the linear approximation of γ (4.1) itself introduces a model error in the cylinder pressure which has a root mean square error of approximately 30 kPa, for low load engine operating points, and approximately 90 kPa in the mean for operating points covering the entire operating range. These errors are more than four times the error introduced by the measurement noise in the former case, and more than ten times in the latter case. These errors will affect the computed heat release and a better model of $\gamma(T, p, \lambda)$ is therefore sought. A correct model of $\gamma(T, p, \lambda)$ is also desirable in order to avoid badly tuned (biased) single-zone model parameters.

The objective is to investigate models of the specific heat ratio for the single-zone heat release model, and find a model accurate enough to only introduce a modeling error less than or in the order of the cylinder pressure measurement noise, while keeping the computational complexity at a minimum. Such a model would help us to compute a more accurate heat release trace.

This work relies upon the single-zone framework and the general single-zone heat release model given by (3.36)–(3.43) is used as a reference model. This is of course an approximation, but reasonable since single-zone models describe the cylinder pressure well. This has been verified experimentally e.g. in Gatowski et al. (1984).

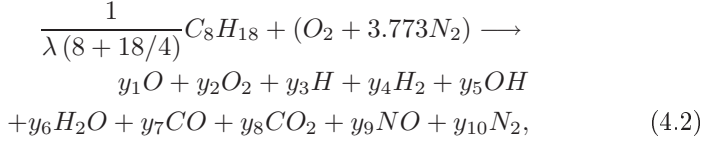
4.1 Outline

In the following section three existing γ -models are described. Then based on chemical equilibrium, a reference model for the specific heat ratio is described. Thereafter, the reference model is calculated for an unburned and a burned air-fuel mixture respectively, and compared to these existing models in the two following sections. With the knowledge of how to describe γ for the unburned and burned mixture respectively, the focus is turned to finding a γ -model during the combustion process, i.e. for a partially burned mixture. This is done in section 4.6, where a number of approximative models are proposed. These models are evaluated in terms of the normalized root mean square error related to the reference γ -model found from chemical equilibrium, as well as the influence the models have on the cylinder pressure, and also in terms of computational time.

4.2 Chemical equilibrium

According to Heywood (1988, p.86), it is a good approximation for performance estimates to consider the unburned gases as frozen and the

burned gases as in chemical equilibrium. Assuming that the unburned air-fuel mixture is frozen and that the burned mixture is at equilibrium at every instant, the specific heat ratio and other thermodynamic properties of various species can be calculated using the Matlab package CHEPP (Eriksson, 2004). The reference fuel used is iso-octane, C_8H_{18} , which reacts with air according to:



where the products given on the right hand side are chosen by the user and λ is the air-fuel ratio (AFR). The coefficients y_i are found by CHEPP and they reveal the mole fraction $\tilde{x}_i = \frac{y_i}{\sum_i y_i}$ of specie i that the mixture consists of at a given temperature, pressure and air-fuel ratio. From \tilde{x}_i , the mass fraction x_i is computed using the molar mass M_i as $x_i = \tilde{x}_i/M_i$.

The mixture is assumed to obey the Gibbs-Dalton law, which states that under the ideal-gas approximation, the properties of a gas in a mixture are not influenced by the presence of other gases, and each gas component in the mixture behaves as if it exists alone in the volume at the mixture temperature (Çengel and Boles, 2002, Ch 12). Therefore, the thermodynamic properties can be added together as e.g. in:

$$u(T, p, \lambda) = \sum_i x_i(T, p, \lambda) u_i(T), \quad (4.3)$$

where u_i is the internal energy from specie i and u is the total internal energy. The enthalpy $h(T, p, \lambda)$ is computed in the same manner. All thermodynamic properties depend on the air-fuel ratio λ , but for notational convenience this dependence is hereafter left out when there is no risk of confusion. The definition of the specific heat c_v is $c_v = \left(\frac{\partial u}{\partial T}\right)_V$, and by using (4.3) it is expressed as

$$c_v(T, p) = \sum_i x_i(T, p) c_{v,i}(T) + u_i(T) \frac{\partial x_i}{\partial T}(T, p), \quad (4.4)$$

where the individual species are ideal gases. The specific heat $c_p = \left(\frac{\partial h}{\partial T}\right)_p$ is calculated in the same manner, as

$$c_p(T, p) = \sum_i x_i(T, p) c_{p,i}(T) + h_i(T) \frac{\partial x_i}{\partial T}(T, p). \quad (4.5)$$

The specific heat ratio γ is defined as

$$\gamma(T, p) = \frac{c_p(T, p)}{c_v(T, p)}. \quad (4.6)$$

4.3 Existing models of γ

The computational time involved in repeated use of a full equilibrium program, such as CHEPP (Eriksson, 2004) or the NASA program (Gordon and McBride, 1971; Svehla and McBride, 1973), can be substantial, and therefore simpler models of the thermodynamic properties have been developed. Three such models will now be described.

4.3.1 Linear model in T

The specific heat ratio during the closed part of the cycle, i.e. when both intake and exhaust valves are closed, is most frequently modeled as either a constant, or as a linear function of temperature. The latter model is used in (Gatowski et al., 1984), where it is stated that the model approximation is in parity with the other approximations made for this family of single-zone heat-release models. The linear function in T can be written as:

$$\gamma_{lin}(T) = \gamma_{300} + b(T - 300). \quad (4.7)$$

Depending on which temperature region and what air-fuel ratio λ the model will be used for, the slope b and constant γ_{300} in (4.7) have to be adjusted. Concerning the temperature region, this shortcoming can be avoided by increasing the complexity of the model and use a second (or higher) order polynomial for $\gamma_{lin}(T)$. This has been done in for example Brunt et al. (1998). Such an extension reduces the need for having different values of γ_{300} and b for different temperature regions. Later on, $\gamma_{lin}(T)$ is calculated in a least squares sense for both burned and unburned mixtures.

4.3.2 Segmented linear model in T

According to Chun and Heywood (1987), the commonly made assumption that $\gamma(T)$ is constant or a linear function of mean temperature is not sufficiently accurate. Instead, they propose a segmentation of the closed part of the engine cycle into three segments; compression, combustion and post-combustion (expansion). Both the compression and post-combustion are modeled by linear functions of T , while the combustion event is modeled by a constant γ . They further state that with these assumptions, the one-zone analysis framework will provide accurate enough predictions. The model of γ can be written as:

$$\gamma_{seg}(T, x_b) = \begin{cases} \gamma_{300}^{comp} + b^{comp}(T - 300) & x_b < 0.01 \\ \gamma_{300}^{comb} & 0.01 \leq x_b \leq 0.99 \\ \gamma_{300}^{exp} + b^{exp}(T - 300) & x_b > 0.99 \end{cases} \quad (4.8)$$

where the mass fraction burned x_b is used to classify the three phases. The γ -model proposed by Chun and Heywood (1987) has discontinuities when switching between the phases compression, combustion and post-combustion.

4.3.3 Polynomial model in p and T

The third model is a polynomial model of the internal energy u developed in Krieger and Borman (1967) for combustion products of C_nH_{2n} . For lean and stoichiometric mixtures ($\lambda \geq 1$), a single set of equations was stated, whereas different sets were found for each $\lambda < 1$. The model of u for $\lambda \geq 1$ is given by:

$$u^{KB}(T, p, \lambda) = A(T) - \frac{B(T)}{\lambda} + u_{corr}(T, p, \lambda), \quad (4.9)$$

given in [kJ/(kg of original air)], where

$$A(T) = a_1T + a_2T^2 + \dots + a_5T^5 \quad (4.10a)$$

$$B(T) = b_0 + b_1T + \dots + b_4T^4. \quad (4.10b)$$

The gas constant was found to be:

$$R(T, p, \lambda) = 0.287 + \frac{0.020}{\lambda} + R_{corr}(T, p, \lambda), \quad (4.11)$$

given in [kJ/(kg of original air) K]. Krieger and Borman suggested that two correction terms u_{corr} and R_{corr} should account for dissociation, modeled as non-zero for $T > 1450$ K and given by:

$$u_{corr}(T, p, \lambda) = c_u \exp(D(\lambda) + E(T, \lambda) + F(T, p, \lambda)) \quad (4.12a)$$

$$D(\lambda) = d_0 + d_1\lambda^{-1} + d_3\lambda^{-3} \quad (4.12b)$$

$$E(T, \lambda) = \frac{e_0 + e_1\lambda^{-1} + e_3\lambda^{-3}}{T} \quad (4.12c)$$

$$F(T, p, \lambda) = (f_0 + f_1\lambda^{-1} + f_3\lambda^{-3} + \frac{f_4 + f_5\lambda^{-1}}{T}) \ln(f_6p) \quad (4.12d)$$

$$R_{corr}(T, p, \lambda) = c_r \exp\left(r_0 \ln \lambda + \frac{r_1 + r_2/T + r_3 \ln(f_6p)}{\lambda}\right), \quad (4.13)$$

where T is given in Kelvin (K) and p in bar. The values of the coefficients are given in table 4.1. For a fuel of composition C_nH_{2n} , the stoichiometric fuel-air ratio is 0.0676. Therefore, equations (4.9)-(4.11) should be divided by $(1+0.0676\lambda^{-1})$, to get the internal energy per unit mass of products. In general, Krieger and Borman (1967) found that

a_1 0.692	a_2 $39.17 \cdot 10^{-6}$	a_3 $52.9 \cdot 10^{-9}$	a_4 $-228.62 \cdot 10^{-13}$
a_5 $277.58 \cdot 10^{-17}$	b_0 3049.33	b_1 $-5.7 \cdot 10^{-2}$	b_2 $-9.5 \cdot 10^{-5}$
b_3 $21.53 \cdot 10^{-9}$	b_4 $-200.26 \cdot 10^{-14}$	c_u 2.32584	c_r $4.186 \cdot 10^{-3}$
d_0 10.41066	d_1 7.85125	d_3 -3.71257	e_0 $-15.001 \cdot 10^3$
e_1 $-15.838 \cdot 10^3$	e_3 $9.613 \cdot 10^3$	f_0 -0.10329	f_1 -0.38656
f_3 0.154226	f_4 -14.763	f_5 118.27	f_6 14.503
r_0 -0.2977	r_1 11.98	r_2 -25442	r_3 -0.4354

Table 4.1: Coefficient values for Krieger-Borman polynomial given in (4.10)-(4.13).

the error in u was less than 2.5 percent in the pressure and temperature range of interest, where the extreme end states were approximately $\{2300 \text{ K}, 0.07 \text{ MPa}\}$ and $\{3300 \text{ K}, 35 \text{ MPa}\}$, and less than 1 percent over most of the range. A model of γ is now given by its definition as

$$\gamma_{KB} = \frac{c_p}{c_v} = 1 + \frac{R}{c_v}, \quad (4.14)$$

where R is given by (4.11) and $c_v = \left(\frac{\partial u}{\partial T}\right)_V$ is found by differentiating (4.9) with respect to T .

4.4 Unburned mixture

Now the attention is turned to the unburned mixture. First of all, the specific heat ratio for an unburned frozen mixture of iso-octane is computed using CHEPP in the temperature region $T \in [300, 1000] \text{ K}$, which is valid for the entire closed part of a motored cycle. The specific heat ratio for $\lambda = 1$ is shown in figure 4.1 as a function of temperature, together with its linear approximation (4.7) in a least squares sense. The linear approximation γ_{lin}^u is fairly good for $\lambda = 1$. Actually, the specific heats c_p and c_v from which γ is formed, are fairly well described by linear functions of temperature. Table 4.2 summarizes the root mean square error (RMSE), normalized RMSE (NRMSE) and the coefficients of the respective linear function for γ , mass-specific heats c_v and c_p for temperature region $T \in [300, 1000] \text{ K}$ and $\lambda = 1$. The RMSE of γ_{lin}^u

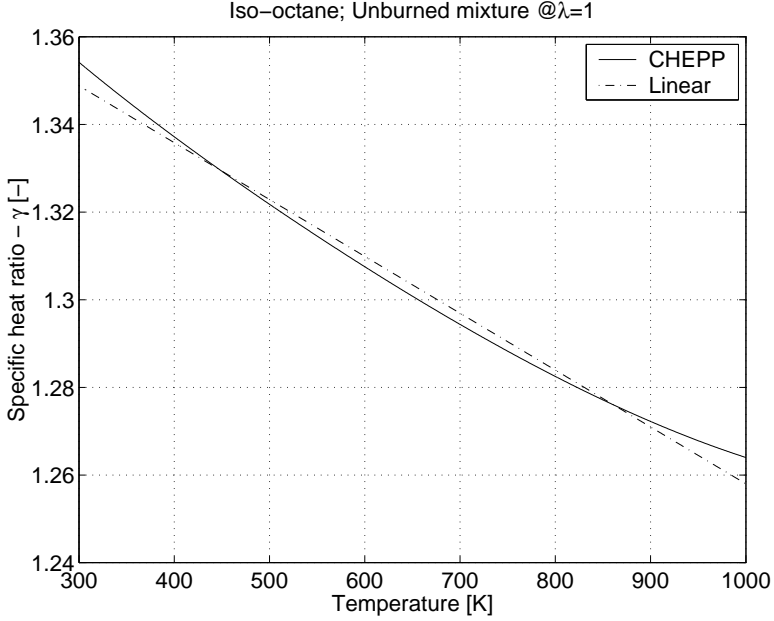


Figure 4.1: Specific heat ratio for unburned stoichiometric mixture using CHEPP and the corresponding linear function of temperature.

Property	Constant	Slope	NRMSE	RMSE
γ_{lin}^u [-]	1.3488	$-13.0 \cdot 10^{-5}$	0.19 %	0.0024
$c_{p,u}^{lin}$ [J/(kg K)]	1051.9	0.387	0.15 %	1.78
$c_{v,u}^{lin}$ [J/(kg K)]	777.0	0.387	0.20 %	1.78

Table 4.2: Coefficients, normalized RMSE and RMSE in linear approximations of γ , mass-specific c_v and c_p , for temperature region $T \in [300, 1000]$ K and $\lambda = 1$.

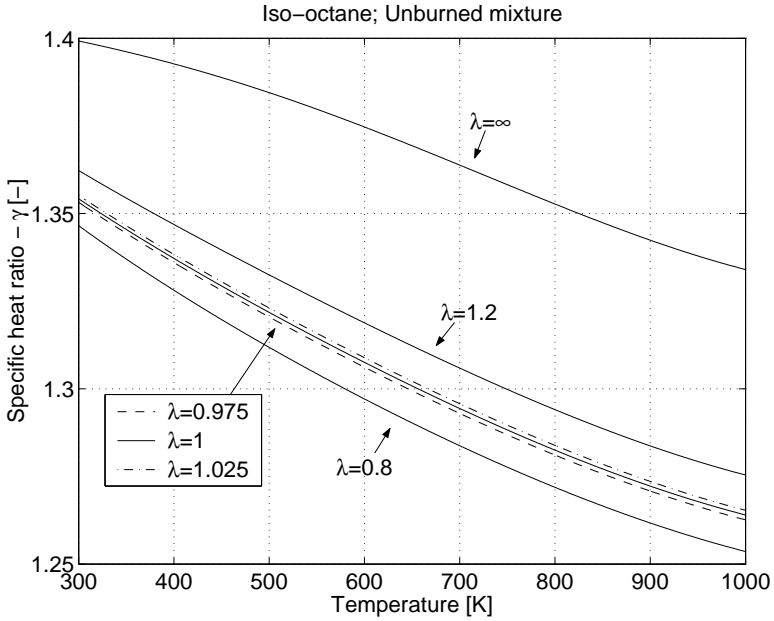


Figure 4.2: Specific heat ratio for unburned stoichiometric mixture using CHEPP for various air fuel ratios λ as functions of temperature. $\lambda = \infty$ corresponds to pure air.

is defined as:

$$RMSE = \sqrt{\frac{1}{M} \sum_{j=1}^M (\gamma(T_j) - \gamma_{lin}^u(T_j))^2}, \quad (4.15)$$

where M are the number of samples. The NRMSE is then found by normalizing the modeling error in each sample j according to:

$$NRMSE = \sqrt{\frac{1}{M} \sum_{j=1}^M \left(\frac{\gamma(T_j) - \gamma_{lin}^u(T_j)}{\gamma(T_j)} \right)^2}. \quad (4.16)$$

Besides temperature, the specific heat ratio also varies with AFR, as shown in figure 4.2 where λ is varied between 0.8 (rich) and 1.2 (lean). For comparison, $\gamma(T)$ is also shown for $\lambda = \infty$, i.e. pure air which corresponds to fuel cut-off.

The coefficients in γ_{lin}^u (4.7) vary with λ as shown in the two upper plots of figure 4.3. Both the constant γ_{300} and the slope b become smaller as the air-fuel ratio becomes richer. From the bottom plot

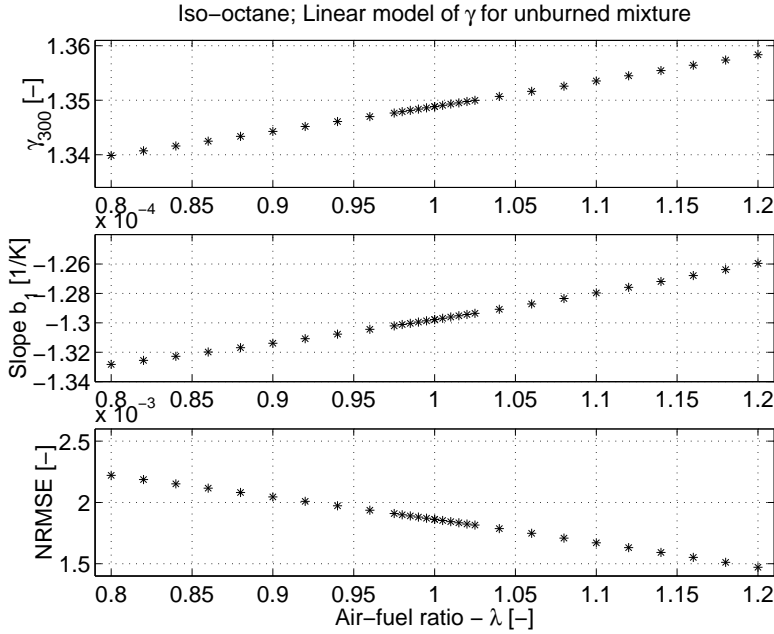


Figure 4.3: *Upper*: The constant value γ_{300} in (4.7) as a function of λ for unburned mixture at equilibrium. *Middle*: The value of the slope coefficient b in (4.7) as a function of AFR. *Bottom*: Normalized root mean square error (NRMSE) for $\gamma_{lin}^u(T)$.

of figure 4.3, which shows the NRMSE for different AFR:s, it can be concluded that the linear approximation $\gamma_{lin}^u(T)$ is better the leaner the mixture is, at least for $\lambda \in [0.8, 1.2]$.

4.4.1 Modeling λ -dependence with fixed slope, b

Since it is always desirable to have as simple models as possible, an important question is: –Would it inflict a major discrepancy to fix the slope coefficient b and let only γ_{300} vary with the air-fuel ratio? This is investigated by setting the slope b to the value for $\lambda = 1$, and finding the coefficient γ_{300} in a least squares sense. The slope is fixed at $\lambda = 1$, since for spark ignited engines this is the region where the engine should be operating most of the time, due to legislations. The results are shown in figure 4.4, where the coefficient γ_{300} becomes approximately the same as when letting the slope vary. The relative difference is less than 0.1 % for $\lambda \in [0.8, 1.2]$. For the NRMSE an increase for $\lambda \neq 1$ compared to when b is free is expected, but the increase is not very significant at all.

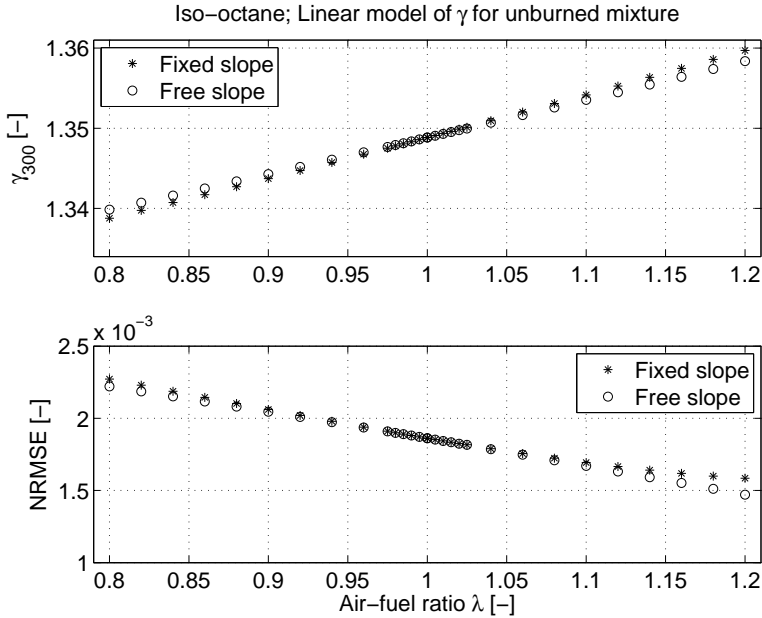


Figure 4.4: *Upper*: The constant value γ_{300} in (4.7) as a function of λ for unburned mixture at equilibrium with fixed and free slope b respectively. *Bottom*: NRMSE for $\gamma_{lin}^u(T)$ for fixed and free slope coefficient.

For $\lambda \in [0.8, 1.12]$ the relative difference in RMSE is less than 5 % and for $\lambda \in [0.94, 1.06]$ it is less than 1 %. This suggests that at least for $\lambda \in [0.94, 1.06]$, the linear approximation with fixed slope set at $\lambda = 1$, can be used as a model of $\gamma(T)$ with good accuracy for the unburned mixture. The parameter γ_{300} is then taking care of the λ -dependence with good accuracy.

4.5 Burned mixture

The specific heat ratio γ for a burned mixture of iso-octane is computed using CHEPP in temperature region $T \in [500, 3500]$ K and pressure region $p \in [0.25, 100]$ bar, which covers most of the closed part of a firing cycle. The mixture is assumed to be at equilibrium at every instant. The specific heat ratio depends strongly on mixture temperature T , but γ also on the air-fuel ratio λ and pressure p as shown in figure 4.5 and figure 4.6 respectively. For the same deviation from $\lambda = 1$, rich mixtures tend to deviate more from the stoichiometric mixture, than lean mixtures do. The pressure dependence in γ is only visible for

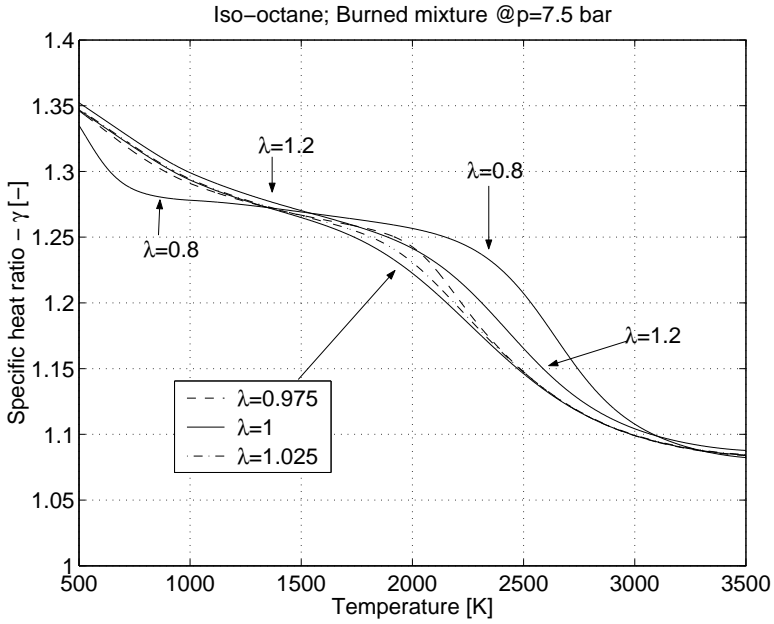


Figure 4.5: Specific heat ratio for burned mixture at various air-fuel ratios λ at 7.5 bar using CHEPP.

Region	$T \in$	γ_{300}	b
A	[500, 3500]	1.3695	$-9.6 \cdot 10^{-5}$
B	[500, 3000]	1.3726	$-9.9 \cdot 10^{-5}$
C	[500, 2700]	1.3678	$-9.4 \cdot 10^{-5}$
D	[500, 2500]	1.3623	$-8.8 \cdot 10^{-5}$
E	[1200, 3000]	1.4045	$-11.4 \cdot 10^{-5}$

Table 4.3: Coefficients in the linear approximation $\gamma_{lin}^b(T)$ found in (4.7) for $\lambda = 1$ and $p = 7.5$ bar.

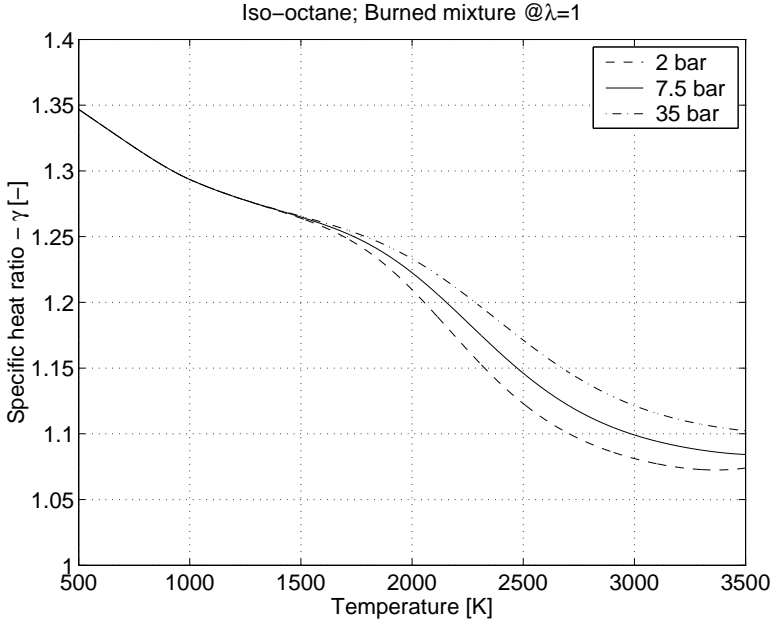


Figure 4.6: Specific heat ratio for burned stoichiometric mixture using CHEPP at various pressures.

$T > 1500$ K, and a higher pressure tends to retard the dissociation and yields a higher γ .

To model the specific heat ratio with a linear function $\gamma_{lin}^b(T)$ of temperature, and thereby neglecting the dependence of pressure, will of course introduce a modeling error. This modeling error depends on which temperature (and pressure) region the linear function is fitted to, since different regions will yield different coefficient values in (4.7). In figure 4.7 γ is computed at $\lambda = 1$ and $p = 7.5$ bar for $T \in [500, 3500]$ K, and as well as the corresponding linear function γ_{lin}^b (4.7) and the polynomial γ_{KB} (4.14) developed in Krieger and Borman (1967). In table 4.3, the coefficients in γ_{lin}^b are computed for five temperature regions. Table 4.4 displays the maximum relative error (MRE) and NRMSE for γ_{lin}^b and γ_{KB} . The maximum relative error for γ_{lin}^b is defined as

$$MRE = \max \left| \frac{\gamma(T_j, p) - \gamma_{lin}^b(T_j)}{\gamma(T_j, p)} \right|. \quad (4.17)$$

The linear approximation $\gamma_{lin}^b(T)$ does not capture the behavior of $\gamma(T)$ for $\lambda = 1$ very well, as shown in figure 4.7. The coefficients for the linear model $\gamma_{lin}^b(T)$ vary with the specific temperature region, as

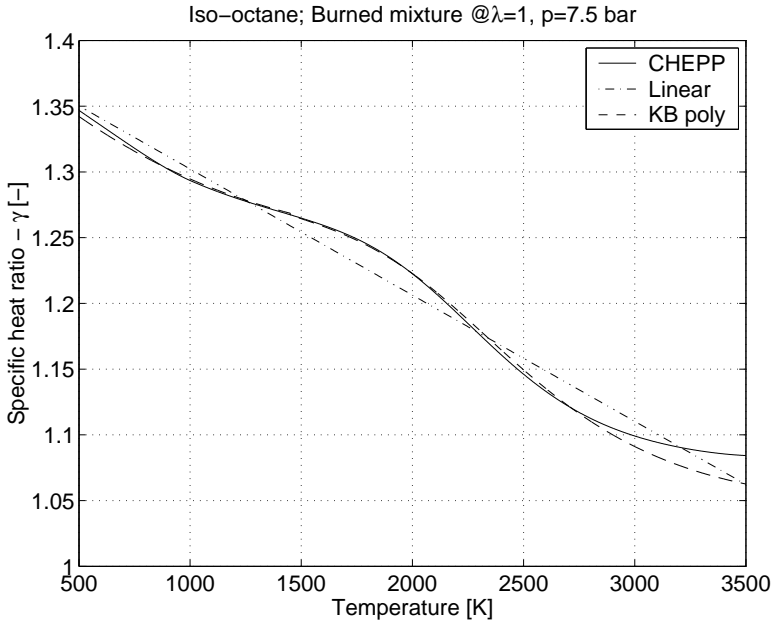


Figure 4.7: Specific heat ratio for burned stoichiometric mixture using CHEPP, the corresponding linear function γ_{lin}^b and Krieger-Borman polynomial γ_{KB} .

Region	$T \in$	γ_{lin}^b		γ_{KB}	
		MRE	NRMSE	MRE	NRMSE
A	[500, 3500]	2.0 %	0.97 %	2.0 %	0.56 %
B	[500, 3000]	1.6 %	0.95 %	0.7 %	0.20 %
C	[500, 2700]	1.9 %	0.90 %	0.3 %	0.17 %
D	[500, 2500]	2.4 %	0.74 %	0.3 %	0.17 %
E	[1200, 3000]	1.6 %	0.74 %	0.7 %	0.21 %

Table 4.4: Maximum relative error (MRE) and normalized root mean square error (NRMSE) for different temperature regions at $\lambda = 1$ and $p = 7.5$ bar.

Region	$\gamma_{KB}@\lambda = 0.975$		$\gamma_{KB}@\lambda = 1$		$\gamma_{KB}@\lambda = 1.025$	
	MRE	NRMSE	MRE	NRMSE	MRE	NRMSE
A	1.9 %	0.86 %	2.0 %	0.56 %	2.1 %	0.59 %
B	1.8 %	0.73 %	0.7 %	0.20 %	0.7 %	0.28 %

Table 4.5: Maximum relative error (MRE) and normalized root mean square error (NRMSE) for different temperature regions for $\gamma_{KB}(T, p, \lambda)$ at $p = 7.5$ bar and $\lambda = \{0.975, 1, 1.025\}$.

displayed for temperature regions A to E in table 4.3. A second order polynomial shows the same behavior as the linear case, but when the order of the polynomial is increased to three, the model captures the modes of $\gamma(T)$ quite well. By increasing the complexity of the model even more, an even better fit is found. This has been done in the Krieger-Borman polynomial, and for this example it captures the behavior of $\gamma(T)$ well for temperatures below 2800 K as seen in figure 4.7 and in the right-most (NRMSE) column in table 4.4, where the NRMSE value is much higher for temperature region A than for the other regions. As expected, the Krieger-Borman polynomial is better than the linear approximation in every chosen temperature region, since the NRMSE is smaller. Comparing the MRE:s for temperature region A, where the respective MRE are approximately the same, one could then conclude that the models describe γ equally well. However in figure 4.7 it was clearly visible that γ_{KB} is the better one, which is also the conclusion when comparing the respective NRMSE.

In table 4.5, the NRMSE and MRE for the Krieger-Borman polynomial $\gamma_{KB}(T, p, \lambda)$ for λ close to stoichiometric is displayed. For $\lambda \geq 1$ (lean), γ_{KB} fits the equilibrium γ better than for $\lambda < 1$, a tendency which is most evident when comparing the NRMSE for temperature region B. For temperature region A the difference for different λ is less striking, since the γ_{KB} does not fit γ as well for $T > 3000$ K. Therefore the Krieger-Borman polynomial is preferably only to be used on the lean side. On the rich side and close to stoichiometric (within 2.5 %), the Krieger-Borman polynomial does not introduce an error larger than the linear approximation given in table 4.4, and γ_{KB} should therefore be used in this operating range.

Summary for special case: Linear models

If a linear model of γ is preferred for computational reasons, the performance of the linear model could be enhanced by proper selection of temperature region. However, the MRE does not decrease for every reduction in interval, as seen when comparing MRE:s for regions D and

B in table 4.4. Thus, the temperature region should be chosen with care by using the NRMSE as evaluation criteria:

- When using the single-zone temperature T to describe the specific heat ratio of the burned mixture, temperature region B is preferable, since during the closed part $T \leq 3000$ K.
- When using the burned-zone temperature T_b in a two-zone model, temperature region E is recommended, since for most cases $T_b \in [1200, 3000]$. The temperature limits are found by evaluating a number of experimental cylinder pressure traces using (A.1) and (A.7). By choosing region E instead of region B, the NRMSE is reduced by 25%.

4.6 Partially burned mixture

The specific heat ratio γ as a function of mixture temperature T and air-fuel ratio λ for unburned and burned mixture of air and iso-octane has been investigated in the two previous sections. During the closed part of a motored engine cycle, the previous investigations would be enough since the models of the unburned mixture will be valid for the entire region. When considering firing cycles on the other hand, an assumption of either a purely unburned or a purely burned mixture approach is not valid for the entire combustion chamber during the closed part of the engine cycle.

To describe the specific heat ratio in the single-zone model for a partially burned mixture, the mass fraction burned trace x_b is used to interpolate the (mass-)specific heats of the unburned and burned zones to find the single-zone specific heats. The specific heat ratio is then found as the ratio between the interpolated specific heats.

4.6.1 Reference model

The single-zone specific heats are found from energy balance between the single-zone and the two-zone model, from which the single-zone specific heat ratio γ_{CE} can be stated:

$$c_p(T, p, x_b) = x_b c_{p,b}(T_b, p) + (1 - x_b) c_{p,u}(T_u) \quad (4.18a)$$

$$c_v(T, p, x_b) = x_b c_{v,b}(T_b, p) + (1 - x_b) c_{v,u}(T_u) \quad (4.18b)$$

$$\gamma_{CE}(T, p, x_b) = \frac{c_p(T, p, x_b)}{c_v(T, p, x_b)}, \quad (4.18c)$$

where the mass fraction burned x_b is used as an interpolation variable. The single-zone (T), burned zone (T_b) and unburned zone (T_u) temperatures are given by the two temperatures models (A.1) and (A.7)

described in appendix A.1. The first is the ordinary single-zone temperature model and the second is a two-zone mean temperature model presented in Andersson (2002). The mass specific heats in (4.18) are computed using CHEPP (Eriksson, 2004) and γ_{CE} then forms the reference model.

To compute γ_{CE} is computationally heavy. Even when the specific heats are computed before-hand at a number of operating points, the computational burden is still heavy due to the numerous table look-ups and interpolations required. Therefore, a computationally more efficient model which retains accuracy is sought for. A number of γ -models will therefore be described in the following subsection, where they are divided into three subgroups based upon their modeling assumptions. These γ -models are then compared to the reference model γ_{CE} (4.18), in terms of four evaluation criteria, specified in section 4.6.3.

How to find x_b ?

To compute the specific heat ratio γ_{CE} (4.18), a mass fraction burned trace x_b is needed. For simulated pressure data, the mass fraction burned is considered to be known, which is the case in this work. However, if one were to use experimental data to e.g. do heat release analysis, x_b can not be considered to be known. There are then two ways of determining the mass fraction burned; The first is to use a simple and computationally efficient method to get x_b from a given cylinder pressure trace. Such methods were described in chapter 2 and include the pressure ratio management by Matekunas (1983) described in section 2.4. If one does not settle for this, the second approach is to initialize x_b using a simple method from the first approach, and then iteratively refine the mass fraction burned trace x_b using the computed heat release.

4.6.2 Grouping of γ -models

Thirteen γ -models have been investigated and they are divided into three subgroups based upon their modeling assumptions; The first group contains models for *burned mixture* only. The second contains models based on *interpolation of the specific heat ratios* directly, and the third group, to which reference model (4.18) belongs, contains the models based on *interpolation of the specific heats*, from which the ratio is determined.

Group \mathcal{B} : Burned mixture

The first subgroup represents the in-cylinder mixture as a single zone of burned mixture with single-zone temperature T , computed by (A.1).

The first model, denoted \mathcal{B}_1 , is the linear approximation in (4.7):

$$\mathcal{B}_1 : \gamma_{\mathcal{B}_1}(T) = \gamma_{in}^b(T) = \gamma_{300} + b(T - 300), \quad (4.19)$$

where the coefficients can be determined in at least two ways; One way is to use the coefficients that are optimized for temperature region $T \in [500, 3000]$ (region B in table 4.3) for a burned mixture. This approach is used in (Gatowski et al., 1984), although the coefficients differ somewhat compared to the ones given in table 4.3. Another way is to optimize the coefficients from the reference model (4.18). This approach will be the one used here, since it yields the smallest modeling errors in both γ and cylinder pressure p . The approach has optimal conditions for the simulations, and will therefore give the best results possible for this model structure.

The second model, denoted \mathcal{B}_2 , is the Krieger-Borman polynomial described in (4.9)

$$\mathcal{B}_2 : u_{\mathcal{B}_2} = A(T) - \frac{B(T)}{\lambda} \longrightarrow \gamma_{\mathcal{B}_2}(T) = \gamma_{KB}(T), \quad (4.20)$$

without the correction term for dissociation. The Krieger-Borman polynomial is used in model \mathcal{B}_3 as well,

$$\begin{aligned} \mathcal{B}_3 : u_{\mathcal{B}_3} &= A(T) - \frac{B(T)}{\lambda} + u_{corr}(T, p, \lambda) \\ &\longrightarrow \gamma_{\mathcal{B}_3}(T, p) = \gamma_{KB}(T, p), \end{aligned} \quad (4.21)$$

with the correction term $u_{corr}(T, p, \lambda)$ for dissociation included. The fourth and simplest model uses a constant γ :

$$\mathcal{B}_4 : \gamma_{\mathcal{B}_4} = \text{constant}. \quad (4.22)$$

As for model \mathcal{B}_1 , the constant $\gamma_{\mathcal{B}_4}$ is determined from the reference model (4.18).

Group C: Interpolation of specific heat ratios

The second subgroup uses a two-zone model, i.e. a burned and an unburned zone, and calculates the specific heat ratio $\gamma_b(T_b)$ and $\gamma_u(T_u)$ for each zone respectively, where the temperatures are given by the two-zone mean temperature model (A.7). The mass fraction burned trace x_b is then used to find the single-zone γ by interpolating γ_b and γ_u .

Note that the relations for determining the thermodynamic properties, shown in (4.18), are not fulfilled for subgroup C during combustion. It is however fulfilled prior to combustion and after the combustion, i.e. when $x_b = 0$ or $x_b = 1$ and no interpolation is performed.

The first model, denoted \mathcal{C}_1 , interpolates linear approximations of γ for the unburned and burned mixture. The coefficients in the linear functions are optimized for temperature region $T \in [300, 1000]$ for the unburned mixture, and temperature region $T \in [1200, 3000]$ for the burned mixture. The resulting $\gamma_{\mathcal{C}_1}$ can therefore be written as:

$$\mathcal{C}_1 : \gamma_{\mathcal{C}_1}(T, x_b) = x_b \gamma_{lin}^b(T_b) + (1 - x_b) \gamma_{lin}^u(T_u), \quad (4.23)$$

where the coefficients for the linear functions are given in table 4.3 and table 4.2 respectively.

The second model was proposed in Stone (1999, p.423), here denoted \mathcal{C}_2 , and is based on interpolation of the internal energy u computed from the Krieger-Borman polynomial:

$$\mathcal{C}_2 : u_{\mathcal{C}_2} = A(T) - x_b \frac{B(T)}{\lambda} \longrightarrow \gamma_{\mathcal{C}_2}(T, x_b). \quad (4.24)$$

This model includes neither dissociation nor the internal energy of the unburned mixture.

An improvement of model \mathcal{C}_1 is expected when substituting the linear model for the burned mixture with the Krieger-Borman polynomial. This new model is denoted \mathcal{C}_3 and described by:

$$\mathcal{C}_3 : \gamma_{\mathcal{C}_3}(T, p, x_b) = x_b \gamma_{KB}(T_b, p) + (1 - x_b) \gamma_{lin}^u(T_u). \quad (4.25)$$

The fourth model interpolates $\gamma_u(T_u)$ and $\gamma_b(T_b, p)$ given by CHEPP:

$$\mathcal{C}_4 : \gamma_{\mathcal{C}_4}(T, p, x_b) = x_b \gamma_b(T_b, p) + (1 - x_b) \gamma_u(T_u), \quad (4.26)$$

and this model is denoted \mathcal{C}_4 . This model will reflect the modeling error introduced by interpolating the specific heat ratios directly instead of using the definition through the specific heats (4.18).

The segmented linear model (4.8) developed in Chun and Heywood (1987) is also investigated and here denoted by model \mathcal{C}_5 :

$$\mathcal{C}_5 : \gamma_{\mathcal{C}_5}(T, x_b) = \gamma_{seg}(T, x_b) = \begin{cases} \gamma_{300}^{comp} + b^{comp}(T - 300) & x_b < 0.01 \\ \gamma_{300}^{comb} & 0.01 \leq x_b \leq 0.99 \\ \gamma_{300}^{exp} + b^{exp}(T - 300) & x_b > 0.99. \end{cases} \quad (4.27)$$

Model \mathcal{C}_5 uses the single-zone temperature for each phase, and classifies into group \mathcal{C} due to that the switching used for x_b in (4.27) can be seen as a nearest neighbor interpolation. As for model \mathcal{B}_1 and \mathcal{B}_4 , the coefficients in (4.27) are determined from the reference model (4.18).

Group \mathcal{D} : Interpolation of specific heats

The last subgroup uses a two-zone model, i.e. a burned and an unburned zone, just as the second subgroup, and the specific heats are

interpolated to get the single-zone specific heats. The first model, denoted \mathcal{D}_1 , uses the Krieger-Borman polynomial for the burned zone to find $c_{p,b}(T_b, p)$ and $c_{v,b}(T_b, p)$, and the linear approximations of $c_{p,u}(T_u)$ and $c_{v,u}(T_u)$ given in table 4.2 for the unburned zone:

$$\mathcal{D}_1 : \gamma_{\mathcal{D}_1}(T, p, x_b) = \frac{x_b c_{p,b}^{KB}(T_b, p) + (1 - x_b) c_{p,u}^{lin}(T_u)}{x_b c_{v,b}^{KB}(T_b, p) + (1 - x_b) c_{v,u}^{lin}(T_u)}. \quad (4.28)$$

An extension of model \mathcal{D}_1 is to use the unburned specific heats $c_{p,u}(T_u)$ and $c_{v,u}(T_u)$ computed from CHEPP:

$$\mathcal{D}_2 : \gamma_{\mathcal{D}_2}(T, p, x_b) = \frac{x_b c_{p,b}^{KB}(T_b, p) + (1 - x_b) c_{p,u}(T_u)}{x_b c_{v,b}^{KB}(T_b, p) + (1 - x_b) c_{v,u}(T_u)}. \quad (4.29)$$

This model is denoted \mathcal{D}_2 and reflects the model error introduced by using the linear approximation of the unburned mixture specific heats, when comparing to \mathcal{D}_1 . When comparing it to \mathcal{D}_4 , it also shows the error induced by using the Krieger-Borman approximation.

Model \mathcal{D}_1 is also extended for the burned mixture, where the specific heats for the burned mixture $c_{p,b}(T_b, p)$ and $c_{v,b}(T_b, p)$ are computed using CHEPP. This model is denoted \mathcal{D}_3 :

$$\mathcal{D}_3 : \gamma_{\mathcal{D}_3}(T, p, x_b) = \frac{x_b c_{p,b}(T_b, p) + (1 - x_b) c_{p,u}^{lin}(T_u)}{x_b c_{v,b}(T_b, p) + (1 - x_b) c_{v,u}^{lin}(T_u)}, \quad (4.30)$$

and reflects the model error introduced by using the Krieger-Borman approximation of the specific heats, when comparing to \mathcal{D}_1 .

The reference model γ_{CE} (4.18) belongs to this group and is denoted \mathcal{D}_4 :

$$\mathcal{D}_4 : \gamma_{\mathcal{D}_4}(T, p, x_b) = \gamma_{CE}(T, p, x_b). \quad (4.31)$$

Modeling of crevice energy term

Note that the usage of a γ -model different from the linear model used in Gatowski et al. [1984], will also affect the amount of energy left or added to the system when a mass element enters or leaves the crevice volume. This energy term $u' - u$ is quantified by (2.32) for \mathcal{B}_1 . It has to be restated for every γ -model at hand except model \mathcal{B}_1 , and this is done in appendix A.4.

4.6.3 Evaluation criteria

The different γ -models given by (4.19)-(4.30) are evaluated in terms of four criteria. The criteria are:

1. Normalized root mean square error (NRMSE) in γ (4.16), which gives a measure of the mean error in γ .

2. Maximum relative error (MRE) for γ (4.17), which yields a measure of the maximum error in γ .
3. Root mean square error (RMSE) for the corresponding cylinder pressures, see (4.15) for the RMSE definition. This criterion gives a measure of the impact that a certain model error has on the cylinder pressure and will help to find a γ -model accurate enough for the single-zone model.
4. The computational time. It is measured as the time for one simulation of the cylinder pressure model during the closed part, given a burn rate trace and a specific γ -model.

The cylinder pressure model used for the simulations is the model developed in Gatowski et al. (1984), summarized in section 3.8. The parameters are given in appendix A.3 and the engine geometry is given in appendix A.2.

4.6.4 Evaluation covering one operating point

At first, only one operating point is considered. This operating point is given by the parameter values in table A.1, and corresponds to the cylinder pressure given in figure 4.8, i.e. a low engine load condition. The cylinder pressure given in figure 4.8 is used as an example that illustrates the effect that each model has on specific heat ratio γ and cylinder pressure. To investigate if the engine operating condition influences the choice of model, nine operating points covering most parts of the operating range of an engine are used to do the same evaluations. These operating points are given in table A.2 and their corresponding

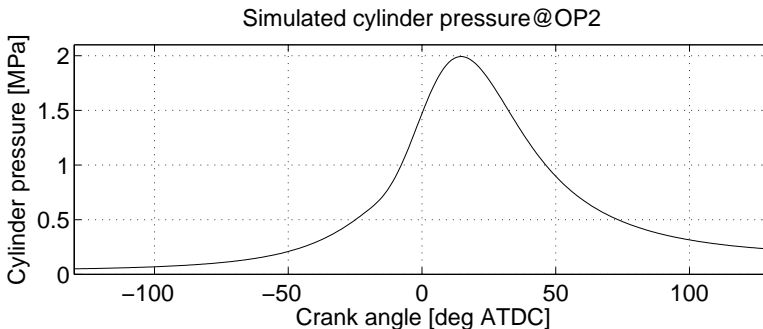


Figure 4.8: Simulated cylinder pressure using Gatowski et al.-model with nominal values in table A.1, and the linear γ -model \mathcal{B}_1 replaced by reference model \mathcal{D}_4 .

cylinder pressures are displayed in figure A.6, where operating point 2 corresponds to the cylinder pressure that is used in the first evaluation and shown in figure 4.8.

γ -domain

The γ -models in the three subgroups are compared to the reference model γ_{CE} (4.18). A summary of the results are given here while a complete picture is given in appendix A.8, see e.g. figures A.7 and A.8, where γ is plotted as a function of crank angle. The specific heat ratio for each model is also given in figure A.9 and figure A.10 as a function of single-zone temperature T . Table 4.6 summarizes the $MRE(\gamma)$ and $NRMSE(\gamma)$ for all models. Figure 4.9 compares the reference model \mathcal{D}_4 with the computed values of γ for a few of these models, namely \mathcal{B}_1 , \mathcal{B}_3 , \mathcal{C}_5 , \mathcal{C}_4 and \mathcal{D}_1 .

Of these models, model \mathcal{D}_1 (4.28) gives the best description of γ and captures the reference model well. This is confirmed by the $MRE(\gamma)$ and $NRMSE(\gamma)$ columns in table 4.6, where only model group \mathcal{D} yields errors lower than 1 % for both columns. The lower plot of figure 4.9 shows that model \mathcal{C}_4 deviates only during the combustion, which in this case occurs for $\theta \in [-15, 45]$ deg ATDC. This deviation is enough to yield a $NRMSE(\gamma)$ which is almost 0.6 %, approximately six times that of \mathcal{D}_1 .

Of the models previously proposed in literature, the linear model \mathcal{B}_1 (4.19) has the best performance, although it does not capture the reference model very well, as seen in the upper plot of figure 4.9. Model \mathcal{B}_3 (4.21) is only able to capture the reference model after the combustion, since model \mathcal{B}_3 is optimized for a burned mixture. Model \mathcal{C}_5 (4.27) has good behavior before and after the combustion. But during the combustion, the constant γ_{300}^{comb} does not capture γ_{CE} very well. Models \mathcal{B}_4 and \mathcal{C}_2 has even worse behavior, as shown in figure A.7.

To conclude, model group \mathcal{D} yields errors in γ which are less than 1 % for this operating point. Of these models, model \mathcal{D}_3 has the best performance compared to the reference model \mathcal{D}_4 .

Pressure domain

The impact each γ -model has on the corresponding cylinder pressure is shown in figure 4.10 for models \mathcal{B}_1 , \mathcal{B}_3 , \mathcal{C}_5 , \mathcal{C}_4 and \mathcal{D}_1 , and for all models in figures A.11 and A.12. The plots show the difference between the simulated cylinder pressure for reference model \mathcal{D}_4 and the γ -models, i.e. the error in the cylinder pressure that is induced by the modeling error in γ . Note that the scaling in the figures are different. The RMSE introduced in the cylinder pressure is given in table 4.6 for all models.

The RMSE of the measurement noise is approximately 6 kPa and

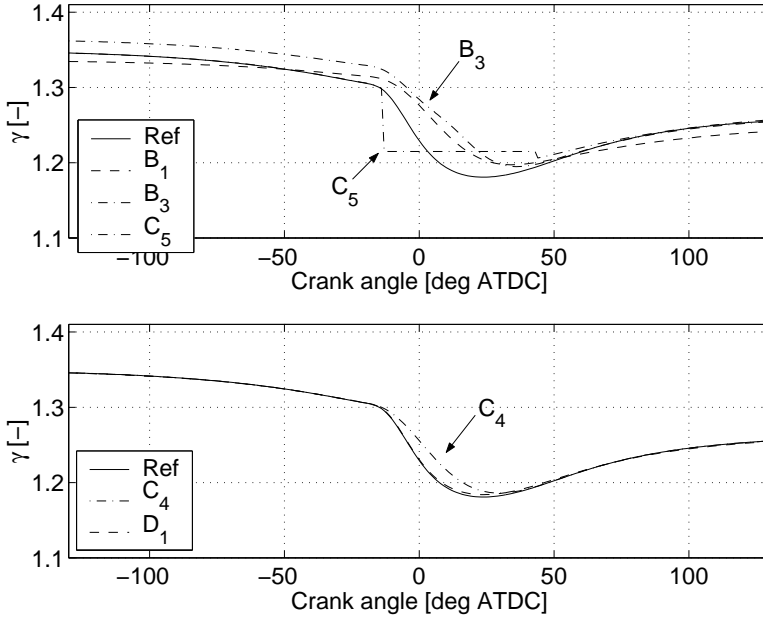


Figure 4.9: *Upper*: Specific heat ratios for models \mathcal{B}_1 , \mathcal{B}_3 and \mathcal{C}_5 as compared to the reference model \mathcal{D}_4 . *Lower*: Specific heat ratios for models \mathcal{C}_4 and \mathcal{D}_1 as compared to the reference model \mathcal{D}_4 .

Model	MRE: γ [%]	NRMSE: γ [%]	RMSE: p [kPa]	Time [s]
\mathcal{B}_1 (4.19)	4.7	1.3	52.3	3.8
\mathcal{B}_2 (4.20)	5.9	2.7	85.8	4.1
\mathcal{B}_3 (4.21)	5.2	1.8	76.0	4.2
\mathcal{B}_4 (4.22)	7.7	4.5	62.8	3.8
\mathcal{C}_1 (4.23)	2.3	0.69	39.8	4.7
\mathcal{C}_2 (4.24)	7.3	4.1	140.7	4.9
\mathcal{C}_3 (4.25)	2.4	0.65	25.4	5.1
\mathcal{C}_4 (4.26)	2.3	0.58	22.8	211.1
\mathcal{C}_5 (4.27)	8.4	1.5	82.9	4.0
\mathcal{D}_1 (4.28)	0.27	0.10	2.8	5.2
\mathcal{D}_2 (4.29)	0.26	0.09	2.6	12.3
\mathcal{D}_3 (4.30)	0.04	0.01	0.3	381.9
\mathcal{D}_4 (4.18)	0.0	0.0	0.0	384.2

Table 4.6: Evaluation of γ -models, on the single cycle shown in figure 4.8.

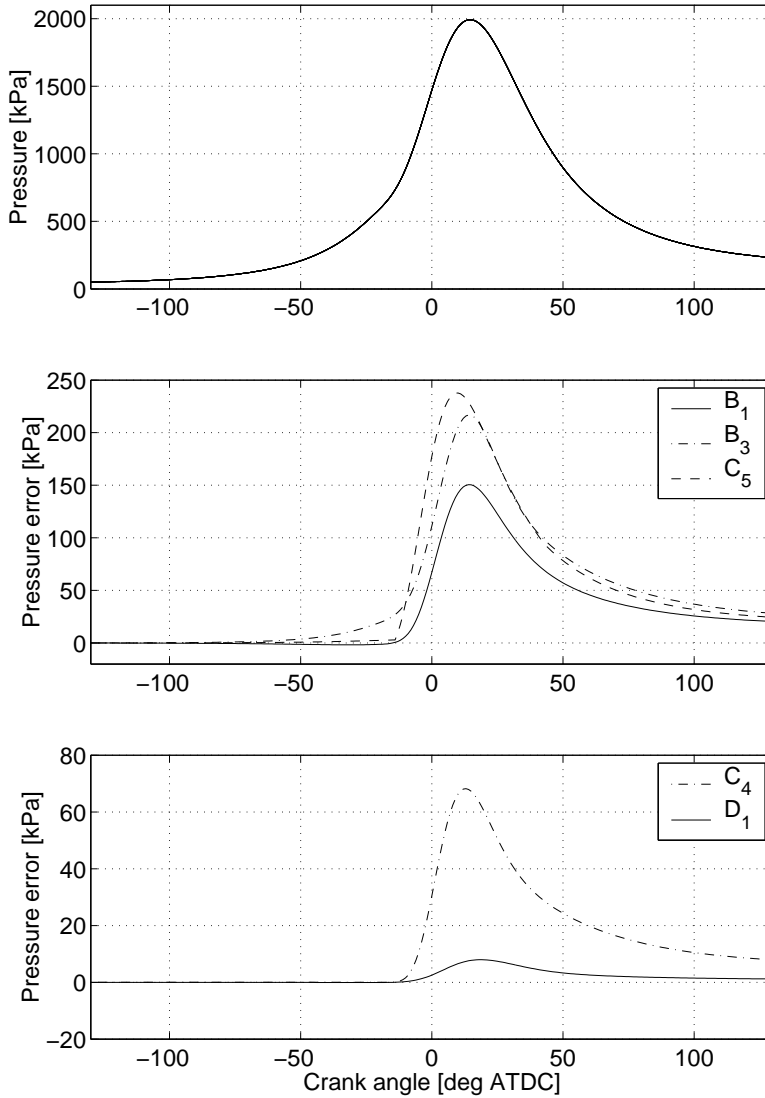


Figure 4.10: *Upper:* Reference cylinder pressure, the same as given in figure 4.8. *Middle:* Cylinder pressure error introduced by models B_1 , B_3 and C_5 . For convenience, the sign for C_5 is changed. *Lower:* Cylinder pressure error introduced by models C_4 and D_1 . Note that the scaling in the plots are different.

it is only model group \mathcal{D} that introduces a modeling error in the same order as the noise in terms of RMSE. Thus, the other γ -models will introduce a modeling error which is significantly larger than the measurement noise as seen in table 4.6, and thereby affect the accuracy of the parameter estimates. Within group \mathcal{D} , models \mathcal{D}_3 and \mathcal{D}_4 have the smallest RMSE(p), and therefore yield the highest accuracy. Model \mathcal{D}_1 does not introduce a significantly larger RMSE(p) than \mathcal{D}_2 , and therefore the most time efficient one should be used of these two. Altogether this suggests that any model in group \mathcal{D} could be used.

The previously proposed γ -models \mathcal{B}_1 , \mathcal{B}_2 , \mathcal{B}_3 , \mathcal{B}_4 and \mathcal{C}_5 , described in section 4.3, all introduce modeling errors which are at least seven times the measurement noise for this operating point. Clearly, a large error, so none of these models are recommended. Of these models, \mathcal{B}_1 induces the smallest RMSE(p) and should, if any, be the one used of the previously proposed models.

Computational time

The right-most column of table 4.6 shows the computational time. The time value given is the mean time for simulating the closed part of one engine cycle using Matlab 6.1 on a SunBlade 100, which has a 64-bit 500 MHz processor. The proposed model \mathcal{D}_1 is approximately 70 times faster than the reference model \mathcal{D}_4 , where the reference model uses look-up tables with precomputed values of the specific heats c_p and c_v . Introducing the model improvement in model \mathcal{D}_1 of the specific heat ratio to the Gatowski et al. single-zone heat release model is simple, and it does not increase the computational burden immensely compared to the original setting, i.e. \mathcal{B}_1 . The increase in computational effort is less than 40 % compared to the linear γ -model when simulating the Gatowski et al. single-zone heat release model.

4.6.5 Evaluation covering all operating points

The same analysis as above has been made for the simulated cylinder pressure from nine different operating points, where $p_{IVC} \in [0.25, 2]$ bar and $T_{IVC} \in [325, 372]$ K. The parameters for each cycle is given in table A.2 as well as the corresponding cylinder pressures in figure A.6. The operating range in p and T that these cycles cover is given in figure 4.11, where the upper plot shows the range covered for the unburned mixture, and the lower shows the range covered for single-zone (solid) and burned (dashed) mixture. According to (Heywood, 1988, p.109), the temperature region of interest for an SI engine is 400 to 900 K for the unburned mixture; for the burned mixture, the extreme end states are approximately $\{1200 \text{ K}, 0.2 \text{ MPa}\}$ and $\{2800 \text{ K}, 3.5 \text{ MPa}\}$. Of

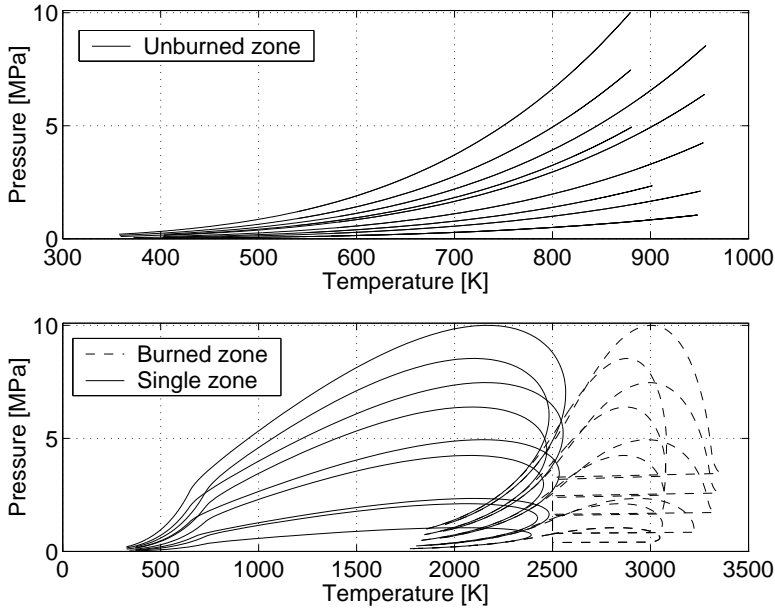


Figure 4.11: Operating range in p and T . *Upper*: Unburned zone. *Lower*: Single zone (solid) and burned zone (dashed).

course, not all points in the range are covered but the cycles at hand cover the extremes of the range of interest.

The results are summarized in terms of MRE for γ in table A.11, NRMSE for γ in table A.12 and RMSE for p in table A.13, where the mean values over the operating points for each model as well as the values for each cycle are given. The mean values for each model are also given here as a summary in table 4.7.

Ordering of models

When comparing the NRMSE for γ in table 4.7, the ordering of the γ -models, where the best one comes first, is:

$$\mathcal{D}_4 \prec \mathcal{D}_3 \prec \mathcal{D}_2 \prec \mathcal{D}_1 \prec \mathcal{C}_4 \prec \mathcal{C}_3 \prec \mathcal{C}_1 \prec \mathcal{B}_1 \prec \mathcal{C}_5 \prec \mathcal{B}_3 \prec \mathcal{B}_2 \prec \mathcal{C}_2 \prec \mathcal{B}_4. \quad (4.32)$$

Here $\mathcal{B}_2 \prec \mathcal{C}_2$ means that model \mathcal{B}_2 is better than \mathcal{C}_2 . Comparing RMSE for the cylinder pressure p , the ordering of the γ -models becomes:

$$\mathcal{D}_4 \prec \mathcal{D}_3 \prec \mathcal{D}_2 \prec \mathcal{D}_1 \prec \mathcal{C}_4 \prec \mathcal{C}_3 \prec \mathcal{C}_1 \prec \mathcal{B}_1 \prec \mathcal{B}_4 \prec \mathcal{B}_3 \prec \mathcal{B}_2 \prec \mathcal{C}_5 \prec \mathcal{C}_2. \quad (4.33)$$

Model	MRE: γ [%]	NRMSE: γ [%]	RMSE: p [kPa]
\mathcal{B}_1	3.4	1.2	84.9
\mathcal{B}_2	5.2	2.4	153.6
\mathcal{B}_3	4.5	1.7	137.3
\mathcal{B}_4	7.1	4.2	110.0
\mathcal{C}_1	1.9	0.77	56.6
\mathcal{C}_2	6.6	3.9	269.2
\mathcal{C}_3	1.9	0.53	42.4
\mathcal{C}_4	1.8	0.46	36.7
\mathcal{C}_5	8.3	1.6	191.9
\mathcal{D}_1	0.26	0.097	5.8
\mathcal{D}_2	0.25	0.092	5.1
\mathcal{D}_3	0.044	0.016	0.7

Table 4.7: Evaluation of γ -models, in terms of the mean values for all operating points in table A.2.

This ordering is not the same as in (4.32), but the only difference lies in models \mathcal{C}_5 and \mathcal{B}_4 that change their positions between the two orderings. Model \mathcal{C}_5 has poor performance in terms of $\text{RMSE}(p)$, compared to $\text{NRMSE}(\gamma)$. For model \mathcal{B}_4 , it is the other way around.

Model group \mathcal{D}

In terms of $\text{NRMSE}(\gamma)$ (4.32) and $\text{RMSE}(p)$ (4.33) model group \mathcal{D} behaves as expected, and obeys the rule: the higher the complexity is, the higher the accuracy becomes. According to the $\text{RMSE}(p)$ column in table 4.7, the models in \mathcal{D} all introduce an $\text{RMSE}(p)$ which is less than that found for the measurement noise. Comparing models \mathcal{D}_1 (4.28) and \mathcal{D}_2 (4.29), it is obvious that not much is gained in accuracy by using the unburned specific heats from CHEPP instead of the linear functions. The computational cost for \mathcal{D}_2 was more than two times the one for \mathcal{D}_1 , as shown in table 4.6. This suggests that the unburned specific heats are sufficiently well described by the linear approximation. Model \mathcal{D}_3 (4.30) utilizes the burned specific heat from CHEPP, and this is an improvement compared to model \mathcal{D}_1 which uses the Krieger-Borman polynomial for $c_{p,b}$ and $c_{v,b}$. This improvement reduces the $\text{RMSE}(p)$ with a factor 7, but the cost in computational time is high, approximately a factor 70 according to table 4.6. The comparison also shows that if we want to reduce the impact on the cylinder pressure, the effort should be to increase the accuracy of the Krieger-Borman polynomial for the burned mixture. In figures A.4 and A.5, the specific

heats for CHEPP and the Krieger-Borman polynomial are given, and this verifies that the polynomial has poorer performance for higher temperatures. A new polynomial for the burned mixture, valid for a smaller but more relevant region for SI engines could increase the accuracy for high temperatures. A perfect model of the burned mixture yields the results given by \mathcal{D}_3 , which then poses the lower limit for the accuracy. The $\text{RMSE}(p)$ in table 4.7 for \mathcal{D}_1 is however considered to be small. Therefore finding a better a model for the burned mixture is not pursued here, and model \mathcal{D}_1 is recommended as a good compromise between computational accuracy and efficiency.

Model group \mathcal{C}

In model group \mathcal{C} , model \mathcal{C}_5 has good performance when considering the NRMSE in γ (4.32), but not as good in $\text{RMSE}(p)$ (4.33). This illustrates the importance of transforming the modeling error in the γ -domain to the cylinder pressure domain. One objective was to get a model that gives a good description of the cylinder pressure. This motivates why $\text{RMSE}(p)$ is the more important model performance measure of the two. Model \mathcal{C}_2 (Stone, 1999, p.423) has really bad performance and would be the last choice here. The rest of the models in group \mathcal{C} obey the same rule as group \mathcal{D} , i.e. $\mathcal{C}_4 \prec \mathcal{C}_3 \prec \mathcal{C}_1$.

When the best model in group \mathcal{C} , i.e. \mathcal{C}_4 , is compared to all models in group \mathcal{D} , and especially the reference model \mathcal{D}_4 , it is concluded that the specific heats should be interpolated, and not the specific heat ratios. This conclusion can be drawn since the only difference between \mathcal{C}_4 and \mathcal{D}_4 is how the interpolation is performed. Model \mathcal{C}_4 interpolates the specific heat ratios found from CHEPP directly, and model \mathcal{D}_4 interpolates the specific heats from CHEPP and then form the specific heat ratio. Therefore, group \mathcal{D} has better performance than group \mathcal{C} . Since \mathcal{D}_1 has higher accuracy and approximately the same computational time as all models in group \mathcal{C} , there is no point in using any of the models in group \mathcal{C} .

Model group \mathcal{B}

As expected, the models in group \mathcal{B} has the worst performance of them all, if excluding models \mathcal{C}_2 and \mathcal{C}_5 . It is interesting to note that the linear model γ_{lin}^b (\mathcal{B}_1) performs best in the group, although it introduces a modeling error in p which is at least ten times the measurement noise in the mean. It has better performance than γ_{KB} (\mathcal{B}_3) in the pressure domain, although this is not the case in the γ -domain. This again points out the necessity of evaluating the impact of the γ -model on to the cylinder pressure. Therefore, if the assumption is that the cylinder contents should be treated as a burned mixture during the entire closed

part of the engine cycle, \mathcal{B}_1 is the model to use.

Summary

To conclude, the models are ordered by their performance and with computational efficiency in ascending order:

$$\mathcal{D}_4 \prec \mathcal{D}_1 \prec \mathcal{B}_1 \prec \mathcal{B}_4 \quad (4.34)$$

Most of the models are excluded from this list, either due to their low accuracy, high computational time, or because another model with approximately the same computational time has higher accuracy. Of the models given in (4.34), \mathcal{D}_1 is recommended as a compromise between computational time and accuracy. Compared to the original setting in Gatowski et al. (1984), the computational burden increases with 40 % and the modeling error is more than ten times smaller in the mean. This also stresses that the γ -model is an important part of the heat release model, since it has a large impact on the cylinder pressure. The focus is now turned to how the γ -models will affect the heat release parameters.

4.6.6 Influence of γ -models on heat release parameters

The next question is: –What impact does each of the proposed γ -models have on the heat release parameters? This is investigated by using the cylinder pressure for operating point 2, given in figure 4.8, and estimating the three heat release parameters $\Delta\theta_d$, $\Delta\theta_b$ and Q_{in} in the Vibe function, introduced in section 3.5. The cylinder pressure is simulated using reference model \mathcal{D}_4 in conjunction with the Gatowski et al. cylinder pressure model, and this forms the cylinder pressure measurement signal to which measurement noise is added.

The heat release trace is then estimated given the measurement from reference model \mathcal{D}_4 . The heat release trace is parameterized by the Vibe function, which has the heat release parameters $\Delta\theta_d$, $\Delta\theta_b$ and Q_{in} where it is assumed that θ_{ig} is known a priori. The estimation is performed by minimizing the prediction error, i.e. by minimizing the difference between the measured cylinder pressure and the modeled cylinder pressure. The Levenberg-Marquardt method described in appendix C.1 is used as optimization algorithm. The heat release parameters are then estimated for each of the γ -models using the Gatowski et al.-model, where the γ -model is replaced in an obvious manner in the equations. In the estimations, only the three heat release parameters are estimated. The other parameters are set to their true values given in table A.1. The results are summarized in table 4.8, which displays

Model	$\Delta\theta_d$ [%]		$\Delta\theta_b$ [%]		Q_{in} [%]		RMSE(p) [kPa]	Time [min]
	RME	RCI	RME	RCI	RME	RCI		
\mathcal{B}_1	5.1	1.7	0.29	3.1	-9.2	1.4	9.8	3.5
\mathcal{B}_2	3.1	1.7	0.63	2.9	-7.3	1.3	9.1	3.8
\mathcal{B}_3	3.4	1.7	-0.2	2.9	-7.2	1.3	9.1	3.9
\mathcal{B}_4	6.8	1.7	-0.11	3.2	-6.2	1.4	10.1	3.5
\mathcal{C}_1	0.074	1.4	1.1	2.4	-2.9	1.1	6.5	4.4
\mathcal{C}_2	9.6	2.1	-1	3.9	-14	1.7	16.0	4.6
\mathcal{C}_3	0.19	1.4	0.75	2.4	-2.5	1.2	6.5	4.8
\mathcal{C}_4	0.14	1.5	0.64	2.4	-2	1.2	6.7	200
\mathcal{C}_5	-8	1.5	-2.5	2.3	27	0.92	6.6	3.7
\mathcal{D}_1	0.21	1.5	-0.062	2.4	-0.67	1.3	6.7	4.9
\mathcal{D}_2	0.2	1.5	-0.08	2.4	-0.61	1.3	6.7	11
\mathcal{D}_3	0.22	1.5	-0.13	2.4	-0.48	1.3	6.7	360
\mathcal{D}_4	0.21	1.5	-0.13	2.4	-0.42	1.3	6.7	360

Table 4.8: Relative mean estimation error (RME) and mean relative 95 % confidence interval (RCI) given in percent, for heat release parameters using various γ -models at operating point 2. The nominal values for the heat release parameters are: $\Delta\theta_d = 20$ deg, $\Delta\theta_b = 40$ deg and $Q_{in} = 760$ J. The computational time and cylinder pressure RMSE are also given.

the relative mean estimation error RME (D.4) and the mean relative 95 % confidence interval RCI (D.5) in $\Delta\theta_d$, $\Delta\theta_b$ and Q_{in} respectively for each γ -model. The computational time and RMSE(p) are also given.

Discussion

The RMSE of the applied measurement noise is approximately 6.7 kPa, which is also the RMSE found when using most γ -models. For every γ -model used, the rapid burn angle θ_b is most accurately estimated of the three parameters, and nearly all of them are accurate within 1%. On the other hand, only model group \mathcal{D} is accurate within 1 % for all three parameters, and this suggests that any of the \mathcal{D} -models can be used, preferably model \mathcal{D}_1 due to its lower computational time. Model \mathcal{C}_5 has the highest deviation in the estimates of them all.

4.6.7 Influence of air-fuel ratio λ

An investigation is performed here to see how the proposed model \mathcal{D}_1 behaves for different air-fuel ratios λ . The NRMSE($\gamma, \lambda|\mathcal{D}_1$) and RMSE($p, \lambda|\mathcal{D}_1$) are computed for model \mathcal{D}_1 (4.28) compared to reference model \mathcal{D}_4 for the air-fuel ratio region $\lambda \in [0.975, 1.025]$, at operating point 2. It is assumed that the λ -controller of the SI engine

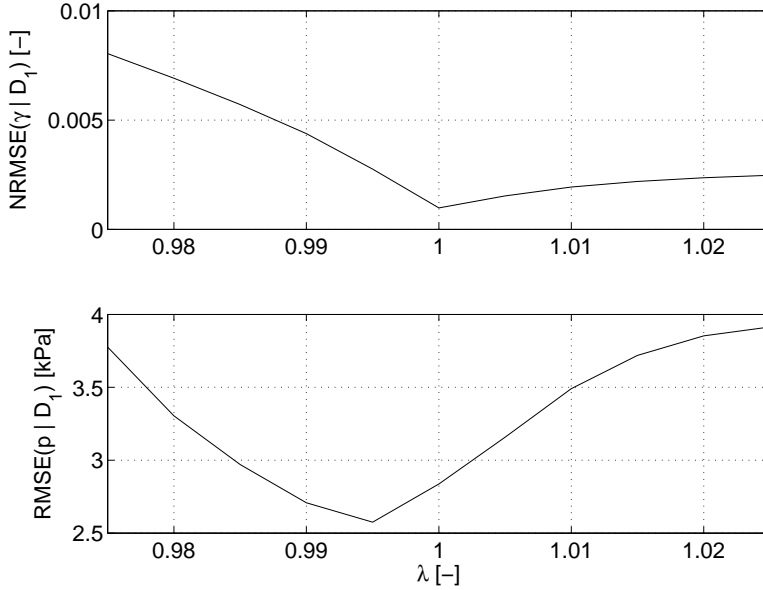


Figure 4.12: *Upper:* $\text{NRMSE}(\gamma, \lambda | \mathcal{D}_1)$ for $\lambda \in [0.975, 1.025]$ at OP 2. *Lower:* $\text{RMSE}(p, \lambda | \mathcal{D}_1)$ for $\lambda \in [0.975, 1.025]$ at OP 2.

has good performance, and therefore keeps the variations in λ small. The results are displayed in figure 4.12, where the upper plot shows the $\text{NRMSE}(\gamma, \lambda | \mathcal{D}_1)$, and the lower plot shows the $\text{RMSE}(p, \lambda | \mathcal{D}_1)$. Lean and stoichiometric mixtures have the lowest errors in the γ domain, which is expected since the Krieger-Borman polynomial for the burned mixture is estimated for lean mixtures. The error in pressure domain is approximately symmetric around $\lambda = 0.995$, and the magnitude is still less than the measurement noise. This assures that for a few percent deviation in λ from stoichiometric conditions, the introduced error is still small and acceptable.

Fuel composition

A small, and by no means exhaustive sensitivity analysis is made for fuels such as methane and two commercial fuels in appendix A.6. This in order to see if the results are valid for other fuels than iso-octane. The hydrocarbon ratio for the fuel $C_a H_b$ is given by $y = b/a$. It is found that if $y \in [1.69, 2.25]$, the $\text{RMSE}(p)$ introduced at OP 2 when using \mathcal{D}_1 is increased with less than 20 % compared to iso-octane, which is acceptable.

4.6.8 Influence of residual gas

The influence of the residual gas on the specific heat ratio has so far been neglected. Introducing the residual gas mass fraction x_r , the single-zone specific heat ratio γ_{CE} in (4.18) is reformulated as:

$$c_p(T, p, x_b, x_r) = x_b c_{p,b}(T_b, p) + (1 - x_b) ((1 - x_r) c_{p,u}(T_u) + x_r c_{p,b}(T_u, p)) \quad (4.35a)$$

$$c_v(T, p, x_b, x_r) = x_b c_{v,b}(T_b, p) + (1 - x_b) ((1 - x_r) c_{v,u}(T_u) + x_r c_{v,b}(T_u, p)) \quad (4.35b)$$

$$\gamma_{CE}(T, p, x_b, x_r) = \frac{c_p(T, p, x_b, x_r)}{c_v(T, p, x_b, x_r)}. \quad (4.35c)$$

The model assumptions are:

- the residual gas is homogeneously distributed throughout the combustion chamber.
- the residual gas is described by a burned mixture at the appropriate temperature and pressure.
- a residual gas mass element in the unburned zone assumes the unburned zone temperature T_u .
- when a residual gas mass element crosses the flame front, it enters the burned zone and assumes the burned zone temperature T_b . The pressure is assumed to be homogeneous throughout all zones.

In figure 4.13, the specific heat ratio γ_{CE} is computed according to (4.35) for residual gas fractions $x_r = [0, 0.05, 0.1, 0.15, 0.20]$ given the cylinder pressure in figure 4.8. It shows that the larger the residual gas fraction, the larger the γ .

The difference in γ for $x_r = [0.05, 0.1, 0.15, 0.20]$ compared to $x_r = 0$ is shown in figure 4.14. The difference is largest during compression and combustion. After the combustion, the mass specific heats for the single zone will coincide with the ones for the burned zone in accordance with the model assumptions, and there is thus no difference in γ .

Modeling of x_r -dependence

A simple model of the influence of x_r on γ is to model the influence as a linear function of x_r during the closed part, i.e.

$$\gamma(T, p, x_b, x_r) = \gamma_{CE}(T, p, x_b) + b_{x_r} x_r = \gamma_{CE}(T, p, x_b) + \gamma_{bias}(x_r), \quad (4.36)$$

where $\gamma_{CE}(T, p, x_b)$ is given by (4.18). Since x_r is constant during a cycle, the term $b_{x_r} x_r$ can be considered as a constant bias $\gamma_{bias}(x_r)$

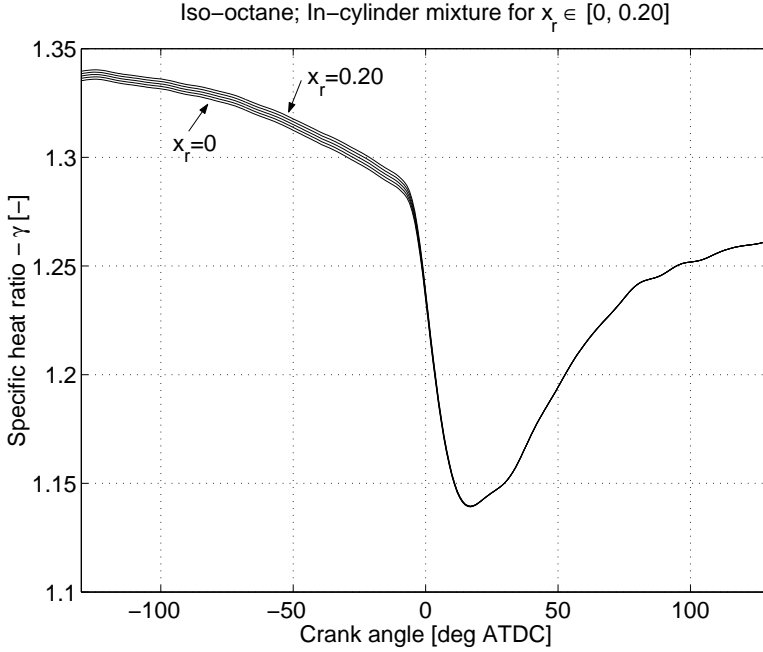


Figure 4.13: Specific heat ratio γ_{CE} (4.35) for residual gas fraction $x_r = [0, 0.05, 0.1, 0.15, 0.20]$.

that changes from cycle to cycle. A better model is gained if the mass fraction burned x_b is used, as described in

$$\gamma(T, p, x_b, x_r) = \gamma_{CE}(T, p, x_b) + (1 - x_b)b_{x_r}x_r = \gamma_{CE}(T, p, x_b) + (1 - x_b)\gamma_{bias}(x_r), \quad (4.37)$$

which relies on the fact that $\gamma(T, p, x_b, x_r)$ coincides with γ_{CE} for every x_r when the mixture is fully burned.

A more appealing and more physically correct model is to extend model \mathcal{D}_1 in (4.28) with the Krieger-Borman polynomial for the residual gas fraction, in the same manner as in (4.35). Thus (4.28) is rewritten as

$$c_p(T, p, x_b, x_r) = x_b c_{p,b}^{KB}(T_b, p) + (1 - x_b) \left((1 - x_r)c_{p,u}^{lin}(T_u) + x_r c_{p,b}^{KB}(T_u, p) \right) \quad (4.38a)$$

$$c_v(T, p, x_b, x_r) = x_b c_{v,b}^{KB}(T_b, p) + (1 - x_b) \left((1 - x_r)c_{v,u}^{lin}(T_u) + x_r c_{v,b}^{KB}(T_u, p) \right) \quad (4.38b)$$

$$\gamma_{\mathcal{D}_{1x_r}}(T, p, x_b, x_r) = \frac{c_p(T, p, x_b, x_r)}{c_v(T, p, x_b, x_r)} \quad (4.38c)$$

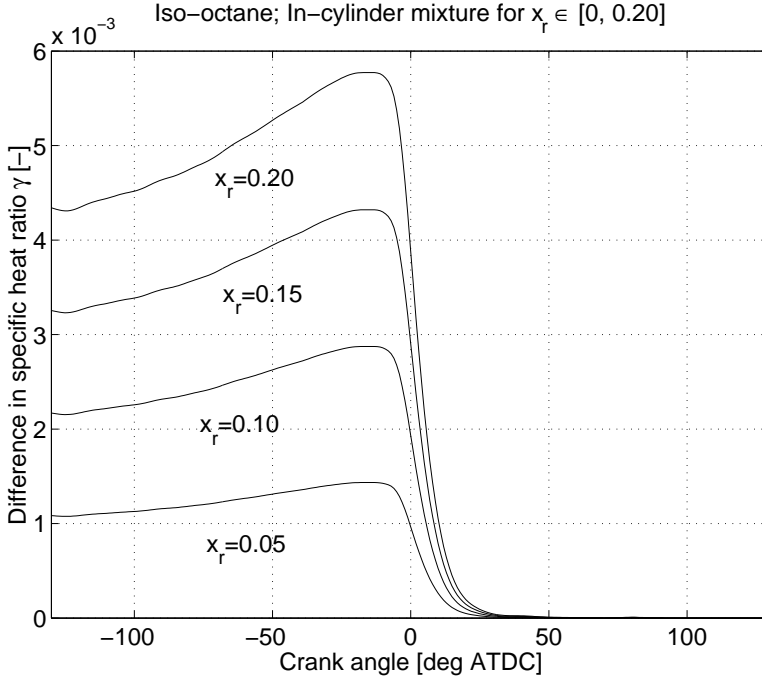


Figure 4.14: Difference in specific heat ratio γ_{CE} (4.35) for residual gas fraction $x_r = [0.05, 0.1, 0.15, 0.20]$ compared to $x_r = 0$.

to form the specific heat ratio $\gamma_{\mathcal{D}_{1x_r}}$ for a partially burned mixture with residual gas mass fraction x_r . In the same spirit as for (4.36) and (4.37) but with model \mathcal{D}_1 as a base, the following models are formed:

$$\gamma(T, p, x_b, x_r) = \gamma_{\mathcal{D}_1}(T, p, x_b) + b_{x_r} x_r = \gamma_{\mathcal{D}_1}(T, p, x_b) + \gamma_{bias}(x_r), \quad (4.39)$$

$$\gamma(T, p, x_b, x_r) = \gamma_{\mathcal{D}_1}(T, p, x_b) + (1 - x_b) b_{x_r} x_r = \gamma_{\mathcal{D}_1}(T, p, x_b) + (1 - x_b) \gamma_{bias}(x_r). \quad (4.40)$$

Evaluation

The specific heat ratio for the six models (4.36)–(4.40) and (4.18), i.e. no x_r -modeling, are all compared to the reference model (4.35) for a given x_r . At the operating point in figure 4.14, the NRMSE in γ and the corresponding value of $\gamma_{bias}(x_r)$ for models (4.36), (4.37), (4.39) and (4.40) are given for the x_r :s at hand in table 4.9. The NRMSE for all six models are also included.

Model (4.37) has the best performance and decreases the NRMSE

Model	NRMSE(γ) [%]				
	$x_r = 0$	$x_r = 0.05$	$x_r = 0.10$	$x_r = 0.15$	$x_r = 0.20$
No model	0	$7.1 \cdot 10^{-2}$	$1.4 \cdot 10^{-1}$	$2.1 \cdot 10^{-1}$	$2.8 \cdot 10^{-1}$
(4.36)	0	$4.8 \cdot 10^{-2}$	$9.7 \cdot 10^{-2}$	$1.5 \cdot 10^{-1}$	$1.9 \cdot 10^{-1}$
(4.37)	0	$8.2 \cdot 10^{-3}$	$1.7 \cdot 10^{-2}$	$2.5 \cdot 10^{-2}$	$3.4 \cdot 10^{-2}$
(4.38)	$9.8 \cdot 10^{-2}$	$9.9 \cdot 10^{-2}$	$1.0 \cdot 10^{-1}$	$1.0 \cdot 10^{-1}$	$1.1 \cdot 10^{-1}$
(4.39)	$9.8 \cdot 10^{-2}$	$1.1 \cdot 10^{-1}$	$1.4 \cdot 10^{-1}$	$1.8 \cdot 10^{-1}$	$2.2 \cdot 10^{-1}$
(4.40)	$9.8 \cdot 10^{-2}$	$9.5 \cdot 10^{-2}$	$9.2 \cdot 10^{-2}$	$9.1 \cdot 10^{-2}$	$9.0 \cdot 10^{-2}$
Model	γ_{bias}				
	$x_r = 0$	$x_r = 0.05$	$x_r = 0.10$	$x_r = 0.15$	$x_r = 0.20$
(4.36)	0	$6.5 \cdot 10^{-4}$	$1.3 \cdot 10^{-3}$	$2.0 \cdot 10^{-3}$	$2.6 \cdot 10^{-3}$
(4.37)	0	$1.2 \cdot 10^{-3}$	$2.5 \cdot 10^{-3}$	$3.7 \cdot 10^{-3}$	$5.0 \cdot 10^{-3}$
(4.39)	$-6.3 \cdot 10^{-5}$	$5.9 \cdot 10^{-4}$	$1.2 \cdot 10^{-3}$	$1.9 \cdot 10^{-3}$	$2.5 \cdot 10^{-3}$
(4.40)	$9.6 \cdot 10^{-5}$	$1.3 \cdot 10^{-3}$	$2.6 \cdot 10^{-3}$	$3.8 \cdot 10^{-3}$	$5.0 \cdot 10^{-3}$

Table 4.9: Normalized root mean square error (NRMSE) and γ_{bias} for $x_r = [0, 0.05, 0.10, 0.15, 0.20]$ using approximative models (4.36)-(4.40). Model (4.18) corresponds to no x_r -modeling.

with approximately a factor 8, compared to model (4.18). Note that the NRMSE in table 4.9 are relatively small compared e.g. to the NRMSE given in table 4.6. When comparing models that are based on \mathcal{D}_1 the NRMSE(γ) is in the same order as in the case of no x_r , at least for models (4.38) and (4.40). The values for $\gamma_{bias}(x_r)$ depend almost linearly upon x_r , and it therefore seems promising to model $\gamma_{bias}(x_r)$ as a linear function of x_r . Especially since model (4.40) gives a smaller NRMSE than model (4.38). However, the slope b_{x_r} in $\gamma_{bias}(x_r) = b_{x_r}x_r$ will change for operating conditions other than the one given here. The model used therefore needs to be robust to changing operating conditions, a feature the Krieger-Borman polynomial has. Model (4.38) only adds an NRMSE(γ) of 1.2 % for $x_r = 0.20$ compared to $x_r = 0$, as shown in table 4.9. Therefore model (4.38) which uses the Krieger-Borman polynomial is recommended, although it did not have the best performance of the x_r -models at this operating point.

4.6.9 Summary for partially burned mixture

The results can be summarized as:

- The modeling error must be compared both in terms of how they describe γ and the cylinder pressure.
- Comparing models \mathcal{C}_4 and \mathcal{D}_4 , it is obvious that interpolating the specific heat ratios directly instead of the specific heats causes a large pressure error. Interpolation of specific heat ratios does not fulfill the energy equation.

- The γ -models $\mathcal{B}_1, \mathcal{B}_2, \mathcal{B}_3, \mathcal{B}_4, \mathcal{C}_2$ and \mathcal{C}_5 proposed in earlier works, introduce a pressure modeling error which is at least four times the measurement noise, and at least ten times the measurement noise in the mean in our investigation. Out of these models, model \mathcal{B}_1 is the best compromise of computational time and model accuracy.
- If only single-zone temperatures are allowed, model \mathcal{B}_1 is the best one.
- The computation times are of the same order for all models except $\mathcal{D}_3, \mathcal{D}_4$ and \mathcal{C}_4 .
- The models in group \mathcal{D} are required to get a cylinder pressure RMSE that is of the same order as the measurement noise.
- As a compromise between accuracy and computational time, model \mathcal{D}_1 is recommended. Compared to the original setting in Gatowski et al. (1984), the computational burden increases with 40 % and the cylinder pressure modeling error is 15 times smaller in mean.
- For a residual gas mass fraction x_r up to 20 %, model \mathcal{D}_1 can be extended with specific heats for the residual gas (4.38). These specific heats are modeled by the Krieger-Borman polynomial. This model extension adds a $\text{NRMSE}(\gamma)$ which is less than 1.2 % to the previous modeling error for $x_r = 0.20$.
- Only model group \mathcal{D} produces prediction error estimates of the heat release parameters, that are accurate within 1 % for all three parameters, and this suggests that any of the \mathcal{D} -models can be used, preferably model \mathcal{D}_1 due to its lower computational time.

4.7 Summary and conclusions

Based on assumptions of frozen mixture for the unburned mixture and chemical equilibrium for the burned mixture (Krieger and Borman, 1967), the specific heat ratio is calculated, using a full equilibrium program (Eriksson, 2004), for an unburned and a burned air-fuel mixture, and compared to several previously proposed models of γ . It is shown that the specific heat ratio and the specific heats for the unburned mixture is captured to within 0.25 % by a linear function in mean charge temperature T for $\lambda \in [0.8, 1.2]$. Furthermore the burned mixture are captured to within 1 % by the higher-order polynomial in cylinder pressure p and temperature T developed in Krieger and Borman (1967) for the major operating range of a spark ignited (SI) engine. If a linear model is preferred for computational reasons for the burned mixture,

then the temperature region should be chosen with care which can reduce the modeling error in γ by 25 %.

With the knowledge of how to describe γ for the unburned and burned mixture respectively, the focus is turned to finding a γ -model during the combustion process, i.e. for a partially burned mixture. This is done by interpolating the specific heats for the unburned and burned mixture using the mass fraction burned x_b . The objective was to find a model of γ , which results in a cylinder pressure error that is lower than or in the order of the measurement noise. It is found that interpolating the linear specific heats for the unburned mixture and the higher-order polynomial specific heats for the burned mixture, and then forming the specific heat ratio

$$\gamma(T, p, x_b) = \frac{c_p(T, p, x_b)}{c_v(T, p, x_b)} = \frac{x_b c_{p,b}^{KB} + (1 - x_b) c_{p,u}^{lin}}{x_b c_{v,b}^{KB} + (1 - x_b) c_{v,u}^{lin}} \quad (4.41)$$

results in a small enough modeling error in γ . This modeling error results in a cylinder pressure error that is lower than 6 kPa in mean, which is in the same order as the cylinder pressure measurement noise. If the residual gas mass fraction x_r is known, it should be incorporated into (4.41) which then extends to (4.38).

It was also shown that it is important to evaluate the model error in γ to see what impact it has on the cylinder pressure, since a small error in γ can yield a large cylinder pressure error. This also stresses that the γ -model is an important part of the heat release model.

Applying the proposed model improvement \mathcal{D}_1 (4.41) of the specific heat ratio to the Gatowski et al. (1984) single-zone heat release model is simple, and it does not increase the computational burden immensely. Compared to the original setting, the computational burden increases with 40 % and the modeling error introduced in the cylinder pressure is reduced by a factor 15 in mean.

Part II

Compression Ratio Estimation

COMPRESSION RATIO ESTIMATION – WITH FOCUS ON MOTORED CYCLES

The ability to vary the compression ratio opens up new possibilities but if the compression ratio gets stuck at too high ratios, the risk of engine destruction by heavy knock increases rapidly. On the other hand if the compression ratio gets stuck at too low ratios, this results in low efficiency, and therefore an unnecessary high fuel consumption. It is therefore vital to monitor and diagnose the continuously changing compression ratio.

Determination of the compression ratio is in itself an issue of high importance (Amann, 1985; Lancaster et al., 1975) since it influences the analysis and control of the combustion process. Due to geometrical uncertainties, a spread in compression ratio among the different cylinders is inherent (Amann, 1985), and since it is impossible to measure the compression ratio directly it is necessary to estimate it. Here four compression ratio estimation methods are developed and their properties with respect to 1) accuracy, 2) convergence speed, and 3) over all convergence, are investigated. The approach is to use measured cylinder pressure traces combined with a cylinder pressure model, to estimate the compression ratio. A desirable property of the estimator is that it should be able to cope with the unknown offset introduced by the charge amplifier, changing thermodynamic conditions, and possibly also the unknown phasing of the pressure trace in relation to the crank angle revolution.

Two models for the cylinder pressure with different complexity levels are used; a polytropic model and a single-zone zero-dimensional

heat release model. Three different optimization algorithms that minimize the prediction error are utilized to estimate the parameters in the cylinder pressure models. These are:

1. *Linear subproblem method.* The non-linear problem is formulated as two linear least-squares problems, that are solved alternately.
2. *Variable projection method.* It has two steps where the first step determines only the parameters that appear linearly in the model through the linear least-squares method. In the second step a line search is performed for the other parameters in the direction of the negative gradient. This method is a separable least-squares method.
3. *Levenberg-Marquardt method.* This is a well known Gauss-Newton method with regularization. Numerical approximations of the gradient and the Hessian are used.

Based on these models and optimization algorithms, four different compression ratio estimation methods are formulated. The methods are applicable to both motored and fired cycles.

5.1 Outline

The two cylinder pressure models that will be used are given in section 5.2. They have been derived in chapter 2 and are summarized here for convenience. Based on these two models and the three optimization algorithms described above, four methods for compression ratio estimation are introduced in section 5.3. Thereafter, the performance of the four methods is evaluated for simulated cylinder pressure traces in terms of bias, variance and computational time in section 5.4. The simulation study is an important and necessary step for a fair evaluation, due to that the true value of the compression ratio for an engine is unknown. The simulation evaluation includes a sensitivity analysis. In section 5.5 the focus is turned to an evaluation of the methods performance on experimental data. Data was collected from the SAAB Variable Compression (SVC) engine shown in figure 5.1. By tilting the mono-head, the compression ratio can be continuously varied between 8.13 and 14.67. The geometric data for the SVC engine is given in appendix B.3. A discussion on compression ratio diagnosis is given. The conclusions and recommendations of the chapter are summarized in section 5.6.

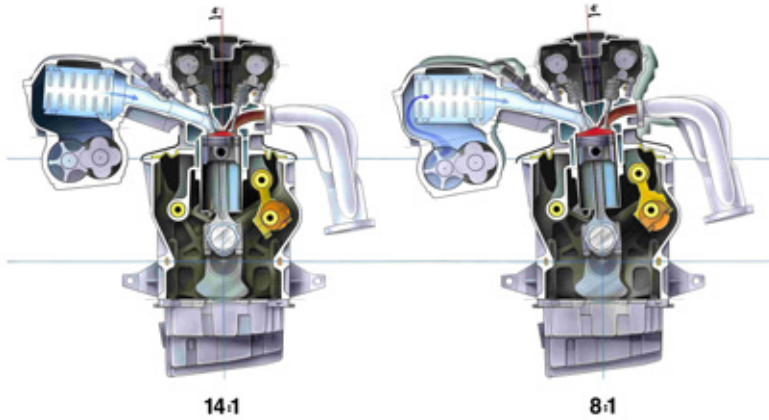


Figure 5.1: Schematic of engine with variable compression. With courtesy of SAAB Automobile AB.

5.2 Cylinder pressure modeling

Two models are used to describe the cylinder pressure trace and they are referred to as the polytropic model and the standard model.

5.2.1 Polytropic model

A simple and efficient model is the polytropic model, presented earlier in section 2.2,

$$p(\theta)V(\theta)^n = C, \quad (5.1)$$

where $p(\theta)$ is the cylinder pressure as function of crank angle θ , $V(\theta)$ is the volume, n is the polytropic exponent and C is a cycle-to-cycle dependent constant. Sometimes the volume is written as the following sum,

$$V(\theta) = V_{id}(\theta) + V_c, \quad (5.2)$$

where $V_{id}(\theta)$ is the instantaneous volume displaced by the piston (3.4) and V_c is the clearance volume. The compression ratio r_c is related to these volumes through

$$r_c = \frac{\max[V_{id}(\theta)] + V_c}{V_c}, \quad (5.3)$$

where $\min[V_{id}(\theta)] = 0$. The polytropic model (5.1) describes the compression and expansion phases of the engine cycle well, but not the

combustion phase (Heywood, 1988). Therefore, for cycles with combustion only data between inlet valve closing (IVC) and start of combustion (SOC) will be used, while for motored cycles all data acquired during the closed part of the cycle, i.e. between IVC and exhaust valve opening (EVO), is utilized.

5.2.2 Standard model

Gatowski et al. (1984) develops, tests and applies this model for heat release analysis. This model is from hereon named the standard model. It is based on the first law of thermodynamics and maintains simplicity while still including the well known effects of heat transfer and crevice flows. It has become widely used (Heywood, 1988) and is described in section 2.5. The pressure is described by the following differential equation,

$$\frac{dp}{d\theta} = \frac{\frac{dQ_{ch}}{d\theta} - \frac{\gamma}{\gamma-1} p \frac{dV}{d\theta} - \frac{dQ_{ht}}{d\theta}}{\frac{1}{\gamma-1} V + \frac{V_{cr}}{T_w} \left(\frac{T}{\gamma-1} + T' + \frac{1}{6} \ln \left(\frac{\gamma'-1}{\gamma-1} \right) \right)}, \quad (5.4)$$

see Gatowski et al. (1984) for the derivation and section 3.8 for details on model components and parameters. This corresponds to model \mathcal{B}_1 in chapter 4. Equation (5.4) is an ordinary differential equation that can easily be solved numerically, given an initial value for the cylinder pressure. The heat release $\frac{dQ_{ch}}{d\theta}$ is zero for motored cycles and for cycles with combustion it is modeled using the Vibe function x_b (Vibe, 1970) in its differentiated form (5.5b)

$$x_b(\theta) = 1 - e^{-a \left(\frac{\theta - \theta_{ig}}{\Delta\theta_{cd}} \right)^{m+1}}, \quad (5.5a)$$

$$\frac{dx_b(\theta)}{d\theta} = \frac{a(m+1)}{\Delta\theta_{cd}} \left(\frac{\theta - \theta_{ig}}{\Delta\theta_{cd}} \right)^m e^{-a \left(\frac{\theta - \theta_{ig}}{\Delta\theta_{cd}} \right)^{m+1}}, \quad (5.5b)$$

where x_b is the mass fraction burned, θ_{ig} is the start of combustion, $\Delta\theta_{cd}$ is the total combustion duration, and a and m are adjustable parameters. The heat release is modeled as

$$\frac{dQ_{ch}}{d\theta} = Q_{in} \frac{dx_b(\theta)}{d\theta}, \quad (5.6)$$

where Q_{in} is the total amount of heat released. The standard model (5.4)–(5.6) is valid between IVC and EVO.

5.2.3 Cylinder pressure referencing

Piezoelectric pressure transducers are used for measuring the in-cylinder pressure, which will cause a drift in the pressure trace, i.e. the absolute

level is unknown and it is slowly varying. This issue was introduced and discussed in section 3.1. The modeling assumption was that the pressure offset is considered to be constant during one engine cycle. The pressure offset is estimated using intake manifold pressure referencing as described in section 3.1, i.e. by referencing the measured cylinder pressure $p_m(\theta)$ to the intake manifold pressure p_{man} just before inlet valve closing (IVC), for several samples of p_{man} . Due to standing waves in the intake runners and flow losses over the valves at certain operating points, the referencing might prove to be insufficient. This is investigated by including a parameter for cylinder pressure offset in estimation methods 3 and 4, described in the next section.

5.3 Estimation methods

Four methods are developed and investigated for compression ratio estimation. These methods are described below and their relations are summarized at the end of this section. All four methods are formulated as least-squares problems in a set of unknown parameters x as

$$\min_x \|\varepsilon(x)\|_2^2, \quad (5.7)$$

where a residual $\varepsilon(x)$ is formed as the difference between a model and measurement. The differences between the methods lie in how the residuals are formed, and in the iterative methods used for solving the resulting problem (5.7).

The termination criterion for all methods are the same; If the relative improvement in the residual $\|\varepsilon(x)\|_2$ is less than 1×10^{-6} in one iteration, the method terminates. This numerical value is chosen to ensure convergence for all initial values.

5.3.1 Method 1 – Sublinear approach

The first method uses the polytropic model (5.1)

$$p(\theta) (V_{id}(\theta) + V_c)^n = C \quad (5.8)$$

to estimate the polytropic exponent n , the compression ratio r_c and the constant C . The method alternates between two problems, one to determine the polytropic exponent n , and the other to determine the clearance volume V_c (i.e. $r_c = (\max[V_{id}(\theta)] + V_c) / V_c$).

Applying logarithms on (5.8) yields the residual

$$\varepsilon_{1a}(C_1, n) = \ln p(\theta) - (C_1 - n \ln(V_{id}(\theta) + V_c)) \quad (5.9)$$

which is linear in the parameters $C_1 = \ln C$ and n , if V_c is fixed. Another residual, that can be derived from (5.8), is

$$\varepsilon_{1b}(C_2, V_c) = V_{id}(\theta) - (C_2 p(\theta)^{-1/n} - V_c) \quad (5.10)$$

which is linear in the parameters $C_2 = C^{1/n}$ and V_c , if n is fixed. The basic idea is to use the two residuals, ε_{1a} and ε_{1b} , alternately to estimate the parameters n , V_c and C by solving two linear least-squares problems. Using a Taylor expansion, see appendix B.1, the following approximate relation between the residuals is obtained

$$\varepsilon_{1a}(\theta, x) \approx \frac{n}{V_{id}(\theta) + V_c} \varepsilon_{1b}(\theta, x). \quad (5.11)$$

The relation (5.11) must be taken into account and the residual ε_{1a} is therefore multiplied by the weight $w(\theta) = V_{id}(\theta) + V_c$, to obtain comparable norms in the least-squares problem. To use this weight is of crucial importance and without it the algorithm diverges (Klein, 2004, pp.85). Convergence of the method can however not be proved. If the residuals were equal, i.e. $\varepsilon_{1a} = \varepsilon_{1b}$, the problem would be bilinear and the convergence linear (Björck, 1996).

Each iteration for estimating the three parameters $x = [V_c \ C \ n]$ in the algorithm consists of three steps.

Algorithm 5.1 – Sublinear approach

Initialize the parameters $x = [V_c \ C \ n]$.

1. Solve the weighted linear least-squares problem

$$\min_{n, C_1} \|w \varepsilon_{1a}\|_2^2$$

with V_c from the previous iteration and $C_1 = \ln C$.

2. Solve the linear least-squares problem

$$\min_{V_c, C_2} \|\varepsilon_{1b}\|_2^2$$

with n from step 1 and $c_2 = C^{1/n}$.

3. Check the termination criterion, if not fulfilled return to step 1.
-

5.3.2 Method 2 – Variable projection

The second method also uses the polytropic model (5.1), together with a variable projection algorithm. A nonlinear least-squares problem (5.7) is *separable* if the parameter vector can be partitioned $x = (y \ z)$ such that

$$\min_y \|\varepsilon(y, z)\|_2^2 \quad (5.12)$$

is easy to solve. If $\varepsilon(y, z)$ is linear in y , $\varepsilon(y, z)$ can be rewritten as

$$\varepsilon(y, z) = F(z)y - g(z). \quad (5.13)$$

For a given z , this is minimized by

$$y(z) = [F^T(z)F(z)]^{-1}F^T(z)g(z) = F^\dagger(z)g(z), \quad (5.14)$$

i.e. by using linear least-squares, where $F^\dagger(z)$ is the pseudo-inverse of $F(z)$. The original problem $\min_x \|\varepsilon(x)\|_2^2$ can then be rewritten as

$$\min_z \|\varepsilon(y, z)\|_2^2 = \min_z \|g(z) - F(z)y(z)\|_2^2 \quad (5.15)$$

and

$$\varepsilon(y, z) = g(z) - F(z)y(z) = g(z) - F(z)F^\dagger(z)g(z) = (I - P_{F(z)})g(z), \quad (5.16)$$

where $P_{F(z)}$ is the orthogonal *projection* onto the range of $F(z)$, thus the name variable projection method.

Rewriting the polytropic model (5.1) as

$$\varepsilon_2(C_1, n, V_c) = \ln p(\theta) - (C_1 - n \ln(V_{id}(\theta) + V_c)) \quad (5.17)$$

results in an equation that is linear in the parameters $C_1 = \ln C$ and n , and nonlinear in V_c . It is thus expressed on the form given in (5.13). The residual (5.10) is not suitable, since the parameters are coupled for this formulation, see appendix B.2. With this method the three parameters $x = [V_c \ \ln C \ n]$ are estimated. A computationally efficient algorithm, based on Björck (1996, p.352), is summarized in appendix B.2.

5.3.3 Method 3 – Levenberg-Marquardt and polytropic model

The third method uses the polytropic model (5.1), as methods 1 and 2 did, with a pressure sensor model (3.1) added according to

$$p_m(\theta) = K_p p(\theta) + \Delta p = p(\theta) + \Delta p \quad (5.18)$$

in order to make the pressure referencing better. The measured cylinder pressure is given by $p_m(\theta)$, and the additive pressure bias Δp is considered to be constant during one cycle. The measurement chain is considered to be well calibrated, and therefore the measurement gain K_p is set equal to 1. Furthermore, errors in the crank angle phasing $\Delta\theta$ between the volume and pressure are also included in the polytropic model, which then can be written as the following residual:

$$\varepsilon_3(V_c, n, C, \Delta p, \Delta\theta) = p_m(\theta) - \Delta p - C(V_{id}(\theta + \Delta\theta) + V_c)^{-n}. \quad (5.19)$$

A Levenberg–Marquardt method (Gill et al., 1981) is used to solve this nonlinear least-squares problem, that has five unknown parameters: V_c , n , C , Δp , $\Delta\theta$.

5.3.4 Method 4 – Levenberg-Marquardt and standard model

The fourth method uses the single-zone model (5.4) from Gatowski et al. (1984) which, in contrast to the other methods, also includes heat transfer and crevice effects. The model is given in section 3.8 and the parameters used are summarized in appendix B.4. Due to the complexity of this model, the sublinear approach and variable projection approach are not applicable, and therefore only the Levenberg–Marquardt method is used. The increased complexity also causes identifiability problems for some of the parameters, since there exist many dependencies between them. This is the case for the crevice volume V_{cr} and the clearance volume V_c , in which estimating the two parameters at the same time results in coupled and biased estimates. Therefore one of them is set constant, in this case the crevice volume (Klein, 2004, p. 94). The estimation problem is however still hard, as will be shown in chapter 6, and therefore the number of parameters to estimate are reduced to five for motored cycles, and eight for fired cycles. The remaining parameters are fixed to their initial values. The number of parameters to estimate are determined by comparing the bias and variance in the parameter values using simulations for different settings of parameters. For motored cycles the estimated parameters are: T_{ivc} , γ_{300} , Δp , $\Delta\theta$, and of course V_c . For fired cycles the parameters $\Delta\theta_d$, $\Delta\theta_b$, and Q_{in} are also included.

5.3.5 Summary of methods

Table 5.1 shows the relations between the methods. For fired cycles, methods 1, 2 and 3 use cylinder pressure data between IVC and SOC only, in contrast to method 4 which uses data from the entire closed part of the engine cycle. For motored cycles, all data during the closed part of the cycle is utilized by all methods. It is also noteworthy that if the clearance volume V_c is considered to be known, then methods 1 and 2 can be reformulated such that Δp is estimated instead of V_c . In such a case all methods can be used to estimate an additive pressure bias, see Klein (2004, p. 143) for more details.

Algorithm	Polytropic model	Standard model
Sublinear	Method 1	
Variable projection	Method 2	
Levenberg-Marquardt	Method 3	Method 4

Table 5.1: Relation between methods.

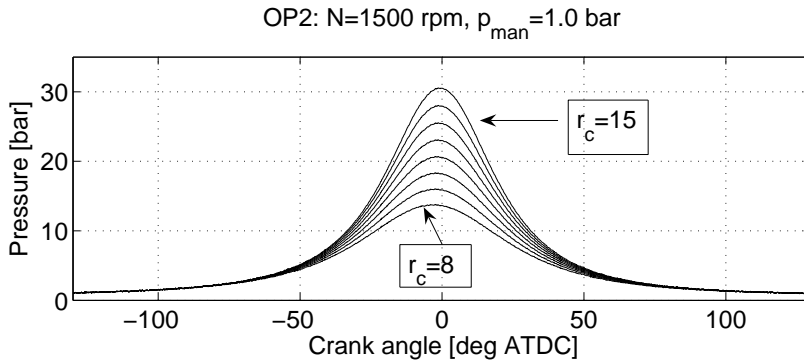


Figure 5.2: Simulated cylinder pressure at OP2 with the compression ratio set to integer values from 8 to 15.

5.4 Simulation results

A fundamental problem is that the exact value of the compression ratio in an engine is unknown, which makes the evaluation of the compression ratio estimation methods difficult. To overcome this obstacle simulated pressure traces, with well known compression ratios, are used. The methods are first evaluated on data from motored cycles in one operating point with respect to the estimation bias, variance and the residual. Then they are evaluated on all cycles in the generated data set and a sensitivity analysis is performed. Finally the methods are evaluated on fired cycles.

5.4.1 Simulated engine data

Cylinder pressure traces were generated by simulating the standard model (5.4) with representative single-zone parameters, given in appendix B.4. Three operating points were selected with engine speed $N = 1500$ rpm and intake manifold pressures $p_{man} \in \{0.5, 1.0, 1.8\}$ bar, which define operating points OP1, OP2 and OP3 respectively. Pressure traces were generated for both motored and fired cycles at each operating point for integer compression ratios between 8 and 15, which covers the compression ratio operating range of the prototype SI engine. To each trace ten realizations of Gaussian noise with zero mean and standard deviation 0.038 bar were added, forming altogether 240 motored and 240 fired cycles. This noise level was chosen since it has the same RMSE as the residual for method 4 in the experimental evaluation, and thus reflects the application to experimental data. The data was sampled with a resolution of 1 crank-angle degree (CAD).

In figure 5.2, one motored cycle is shown for each integer compression ratio r_c at operating point 2 (OP2).

5.4.2 Results and evaluation for motored cycles at OP2

The performance of the estimation methods is first evaluated for OP2. This operating point has an intake manifold pressure in the midrange of the engine, and a relatively low engine speed for which the effects of heat transfer and crevices are significant. OP2 is therefore chosen as a representable operating point. For the simulated pressure, the parameters in the models are estimated using all methods, for each individual cycle.

Estimation results

For the variable compression ratio engine, the difference in r_c between two consecutive cycles can be as large as 5 %. Since the estimation is performed on each cycle, the methods should be able to deal with initial values that are 5 % off, in order to cope with compression ratio transients. For the simulated data, the initial parameter values for the estimations are therefore set to a ± 5 % perturbation of the true parameter values. The termination criterion, described in section 5.3, is chosen in order to assure that the methods have converged, i.e. yield the same estimate for every initial parameter set.

Figure 5.3 shows a summary of the estimates for all cycles at OP2. In the figure the true compression ratios are the integer values 8 to 15 and for convenience, the results for methods 1 to 4 are separated for each true value. The estimate should be as close as possible to the corresponding dotted horizontal line.

Table 5.2 summarizes the results in terms of relative mean error (RME) and mean 95 % relative confidence interval (RCI) in r_c , as well as the mean computational time and mean number of iterations in completing the estimate for one cycle. The measures RME and RCI are given for the lower ($r_c = 8$) and upper ($r_c = 15$) limits of the compression ratio, and as a mean for all compression ratios. The relative mean error RME is defined by

$$RME = \frac{\frac{1}{M} \sum_{j=1}^M r_c^j - r_c^*}{r_c^*}, \quad (5.20)$$

where r_c^j , $j = 1, \dots, M$ is the estimate of r_c corresponding to cycle j and r_c^* is the true compression ratio. The mean 95 % relative confidence

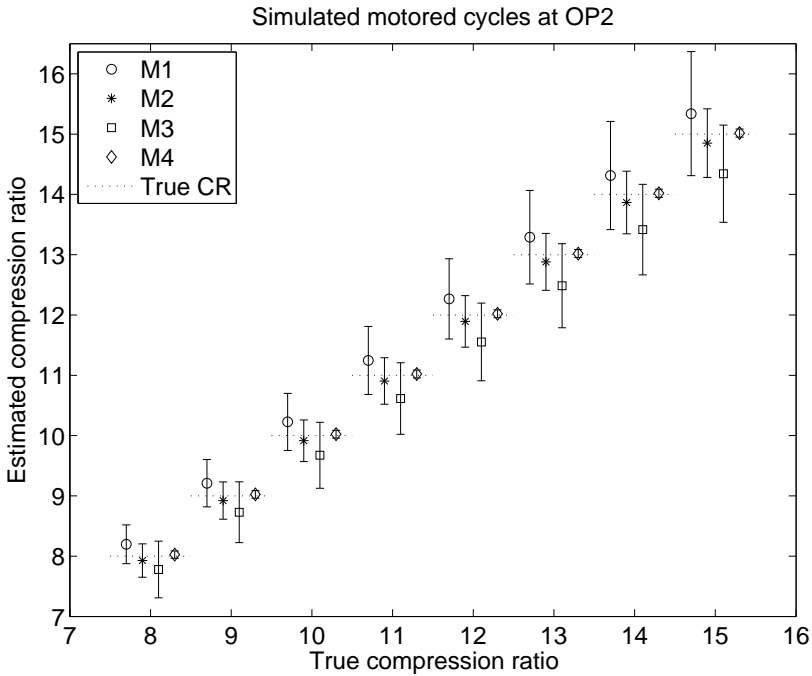


Figure 5.3: Mean value and 95 % confidence interval of the estimated compression ratio for motored cycles using the four methods, compared to the true compression ratio. The estimate should be as close as possible to the corresponding dotted horizontal line.

interval RCI is computed as

$$RCI = \frac{1}{M} \sum_{j=1}^M \frac{1.96\sigma_j}{r_c^*}, \quad (5.21)$$

where σ_j is computed using (C.18) and (C.20) in appendix C.1. The mean computational time and mean number of iterations in table 5.2 are given for the worst case of the initial parameter sets. The calculations were made using Matlab 6.1 on a SunBlade 100, which has a 64-bit 500 Mhz processor.

Analysis of estimation results

Figure 5.3 shows that the estimates from methods 1, 2 and 3 become poorer the higher the compression ratio is. It stresses that heat transfer and crevice effects, which are not considered explicitly in the polytropic

model (5.1), must be taken into account when a better estimate is desired for higher compression ratios. Method 4 has the correct model structure and therefore yields a better estimate with much lower bias and variance for all compression ratios.

These results are further confirmed by the relative mean errors in table 5.2, where method 4 is the most accurate but also the most time-consuming method. Method 4 is at the time being not suitable for on-line implementation, unless a batching technique is used, e.g. where one cycle is collected and then processed until finished. Of the other three methods, method 2 performs best concerning estimation accuracy and is outstanding regarding convergence speed. Method 1 has the potential of low computational time since it solves linear least-squares problems only, however the rate of convergence is low which makes it unsuitable for practical use.

Residual analysis

The residuals corresponding to the cylinder pressures in figure 5.2 are displayed for all four methods in figure 5.4 for $r_c = 8$ and in figure 5.5 for $r_c = 15$, together with their respective root mean square error (RMSE).

There is a systematic deviation for methods 1 and 2 that becomes more pronounced when r_c increases, as seen by comparing figures 5.4 and 5.5. The same systematic deviation occurs for method 3, although it is smaller. The residuals for method 4 are white noise, which is expected since method 4 has the correct model structure. The systematic deviation for methods 1-3 is due to the polytropic model (5.1), which does not explicitly account for heat transfer and crevice effects. The systematic deviation for method 3 would be of the same order as for methods 1 and 2, if it were not for the two extra parameters $\Delta\theta$ and Δp in (5.19). These two parameters compensate for the lack of heat transfer and crevice effect with the penalty of parameter biases. The most pronounced change is the shifted crank angle phasing $\Delta\theta$, which results in a peak pressure position which is closer to top dead center (TDC). However this model flexibility does not improve the compression ratio estimate for method 3, which according to table 5.2 has a bias of -3.6 % in mean.

5.4.3 Results and evaluation for motored cycles at all OP

The results for all motored operating points are given in table 5.3, where the relative mean estimation errors and 95 % confidence intervals are computed as a mean for all compression ratios. For all operating points, the estimate from method 2 is within 1.5 % and within 0.5 % from method 4. The confidence intervals are smallest for method 4,

Method vs. True	$r_c = 8$		$r_c = 15$		all r_c				
	RME [%]	RCI [%]	RME [%]	RCI [%]	RME [%]	RCI [%]	std [-]	Time [ms]	Iter [-]
1	2.6	4.1	2.3	6.9	2.4	5.4	0.093	63	26.1
2	-0.9	3.5	-1.0	3.8	-0.9	3.6	0.072	3	3.0
3	-2.8	5.9	-4.4	5.4	-3.6	5.5	0.19	86	5.0
4	0.35	0.87	0.12	0.49	0.21	0.65	0.0013	2.6×10^5	14.0

Table 5.2: Relative mean error and mean 95 % relative confidence interval (RCI) in the estimated r_c for $r_c = 8$, $r_c = 15$ and as a mean for all compression ratios for *simulated data* from OP2. The standard deviation, as well as the mean computational time and mean number of iterations in completing the estimation for one engine cycle are also given.

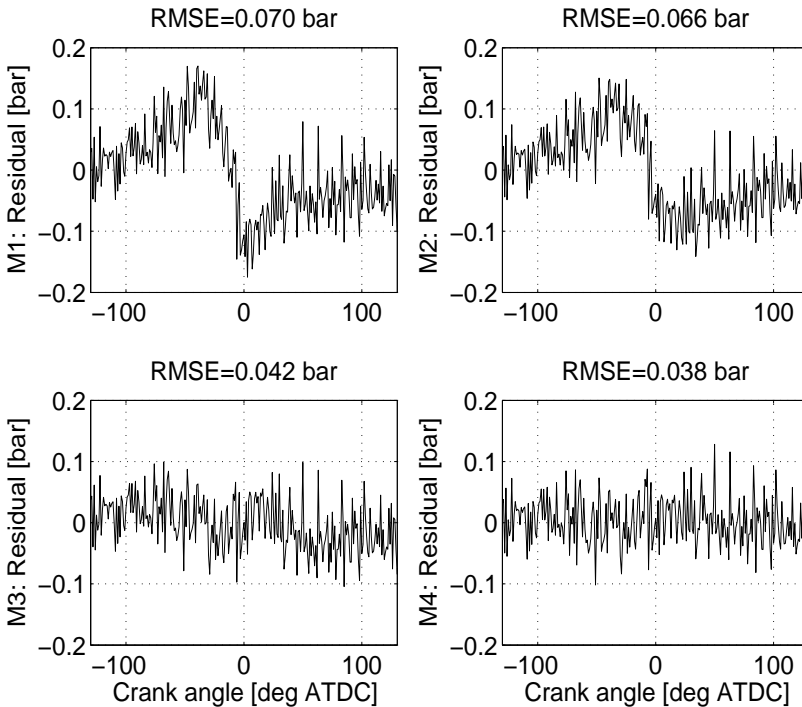


Figure 5.4: Difference between estimated and simulated cylinder pressure for all methods, given the motored cycle at $r_c = 8$ in figure 5.2. The RMSE for the added measurement noise is 0.038 bar.

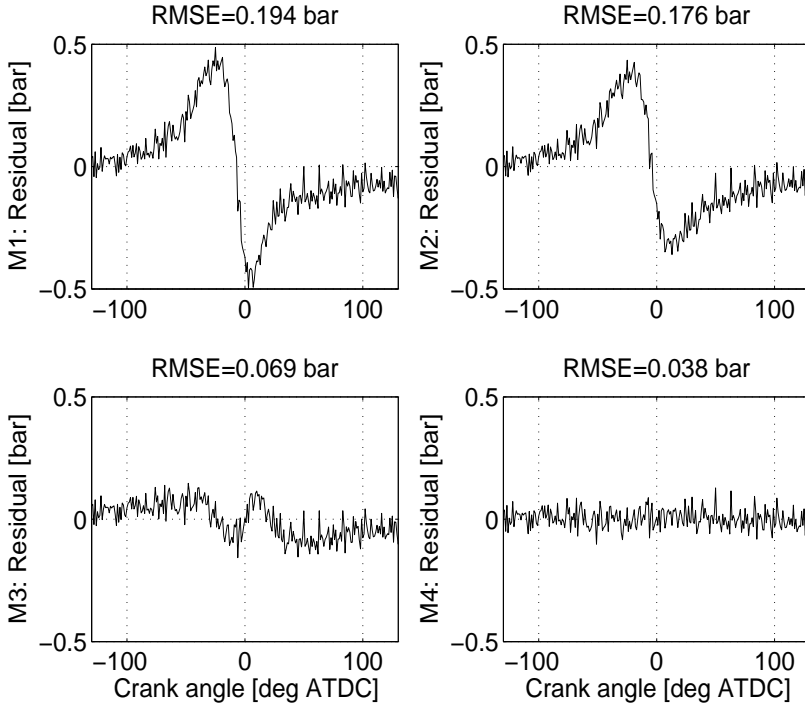


Figure 5.5: Difference between estimated and simulated cylinder pressure for all methods, given the motored cycle at $r_c = 15$ in figure 5.2. The RMSE for the added measurement noise is 0.038 bar.

followed by method 2. The observations made for OP2 with respect to bias and variance are confirmed by the results for all operating points.

A trend among the estimates is that a higher intake manifold pressure p_{man} reduces the confidence interval. A higher pressure improves the signal to noise ratio, while the effects of heat transfer and crevice flows remain the same.

The choice of residual is important. This is illustrated by the fact that the estimates and confidence intervals for methods 1 and 2 differ, for which the only difference is the formulation of the residual. Furthermore, methods 1 and 2 use a logarithmic residual of the pressure, that weighs the low pressure parts between IVC and EVO relatively higher than method 3 does. For method 3, the samples corresponding to the highest pressure are the most important ones. This however coincides with the highest mean charge temperature, and thus the highest heat transfer losses. This is where the polytropic pressure model used in methods 1-3 has its largest model error, since heat transfer is not

	OP1		OP2		OP3	
N	1500 rpm		1500 rpm		1500 rpm	
p_{man}	0.5 bar		1.0 bar		1.8 bar	
Method	RME [%]	RCI [%]	RME [%]	RCI [%]	RME [%]	RCI [%]
1	3.6	8.5	2.4	5.4	0.45	4.3
2	-0.35	5.7	-0.9	3.6	-1.4	2.7
3	-3.8	7.1	-3.6	5.5	-3.6	4.7
4	0.37	1.2	0.21	0.65	0.094	0.37

Table 5.3: Relative mean error (RME) and mean 95 % relative confidence interval (RCI) in estimated r_c , for simulated motored cylinder pressures from three operating points defined by engine speed N and intake manifold pressure p_{man} . The estimate improves with increased pressure.

Parameter	Nominal value	Deviations				
Δp [kPa]	0	-5	-2	2	5	
$\Delta \theta$ [deg]	0	-0.25	-0.1	0.1	0.25	
C_1 [-]	2.28	0	1.14	3.42	4.56	
V_{cr} [% V_c]	1.5	0	0.75	2.25	3.0	

Table 5.4: Nominal values for the parameters and the deviations used in the sensitivity analysis.

included explicitly. This explains why both methods 1 and 2 yield a more accurate estimate than method 3.

5.4.4 Sensitivity analysis at OP2

The next question asked is: – How sensitive are the methods to changes in heat transfer, crevice volume, an inaccurate TDC determination or a badly referenced cylinder pressure? A sensitivity analysis is therefore performed and model parameter values are altered according to table 5.4. The estimates for all four methods are summarized in figure 5.6, where the relative mean error in r_c is given as a function of parameter deviation for each of the four parameters.

According to figure 5.6, methods 3 and 4 are insensitive to an additive pressure bias Δp , since their respective models include a pressure bias. Methods 1 and 2 which do not model a pressure bias, are approximately equally sensitive. This is due to that an additive pressure bias affects all pressure samples equally. A parameter deviation of $|\Delta p| \leq 2$ kPa assures that the estimates from methods 1 and 2 are within the accuracy of method 3, at least for OP2.

Methods 3 and 4 are also insensitive to a crank angle offset $\Delta \theta$, for

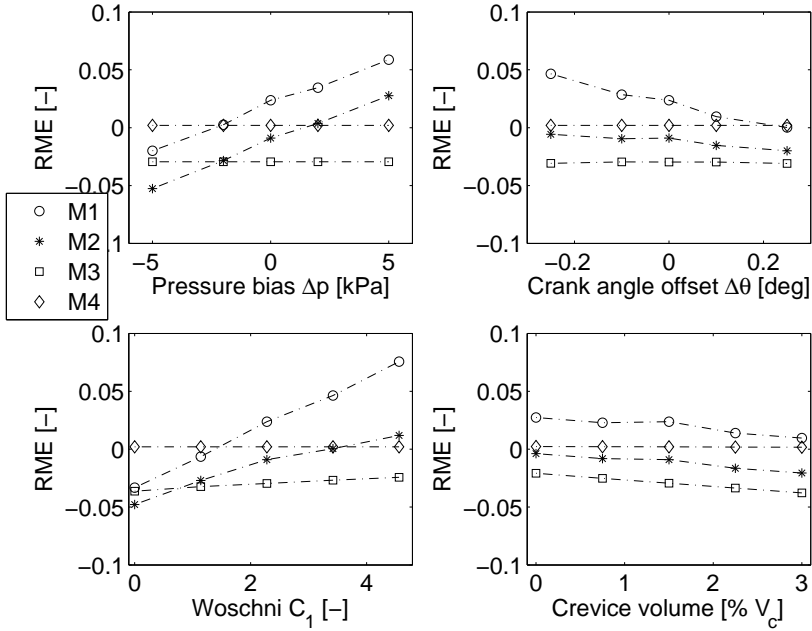


Figure 5.6: Relative mean error for parameter deviations in Δp , $\Delta\theta$, normalized C_1 and V_{cr} for methods 1-4 at OP2. Nominal parameter values are given in table 5.4, and correspond to the third value on the x-axis.

the same reasons as for the pressure bias Δp . Comparing methods 1 and 2, method 1 is far more sensitive to $\Delta\theta$ than method 2. This is explained by the following: A crank angle offset affects the pressure in the vicinity of TDC the most, due to the higher pressure. It is therefore logical that method 2 which uses a logarithmic residual of p , is less sensitive than method 1. For a parameter deviation of $|\Delta\theta| \leq 0.2$ deg, method 2 yields more accurate estimates of r_c than method 3 does. Today's calibration systems have a possibility to determine the crank angle offset with an accuracy of 0.1 degree. This suggests that the crank angle offset $\Delta\theta$ can be left out when using method 2.

Methods 1, 2 and 3 are all affected, while method 4 is unaffected by changes in heat transfer C_1 . The heat transfer affects the pressure in the vicinity of TDC the most, due to the higher in-cylinder temperature. Therefore method 1 is more sensitive to heat transfer than method 2 for the same reasons as for the crank angle offset $\Delta\theta$.

All methods are sensitive to deviations in crevice volume V_{cr} , although method 4 is not as sensitive as the other methods. It is however important to set V_{cr} constant, to avoid an even larger bias in clearance

volume V_c . For motored cycles the clearance volume and the crevice volume are modeled in almost the same way, due to the relatively low in-cylinder temperatures. It is therefore natural that a larger crevice volume causes a larger estimate of the clearance volume, and thereby a smaller compression ratio. This is the case in figure 5.6, and it has been seen earlier for motored and fired cycles in Klein (2004, p. 94).

To conclude, the more robust methods 3 and 4 are able to cope with the parameter deviations imposed upon them, due to their high model flexibility. Of the other two methods, method 2 has the best performance although it is equally sensitive to a pressure bias as method 1 is.

5.4.5 Results and evaluation for fired cycles at OP2

Figure 5.7 displays the results for simulated cycles with combustion, in terms of mean value and 95 % confidence interval at each integer compression ratio from 8 to 15.

The estimates for methods 1-3 are poor, and the relative mean error for all r_c is in the order of 10 %. These methods all suffer from the fact that the pressure corresponding to TDC is not included, since they only use the data between IVC and SOC. This also yields larger confidence intervals compared to motored cycles, reflecting a more uncertain estimate. Method 4 on the other hand uses all data between IVC and EVO, and yields an estimate accurate within 0.4 % for OP2. Due to the poor performance of methods 1-3, an experimental evaluation on fired data is not pursued. Out of the four proposed methods, method 4 is required to estimate the compression ratio from a fired cycle.

The conclusions from this investigation of how the methods perform on simulated data is summarized in section 5.6.

5.5 Experimental results

The attention is now turned to the issue of evaluating the methods on experimental engine data. As mentioned before, the true value of the compression ratio is unknown. Therefore it is important too see if the effects and trends from the simulation evaluation are also present when the methods are applied to experimental data. The performance of the methods is discussed using one specific operating point, and is then followed by an evaluation including all operating points.

5.5.1 Experimental engine data

Data is collected during stationary operation at engine speeds $N \in \{1500, 3000\}$ rpm, intake manifold pressures $p_{man} \in \{0.5, 1.0\}$ bar alto-

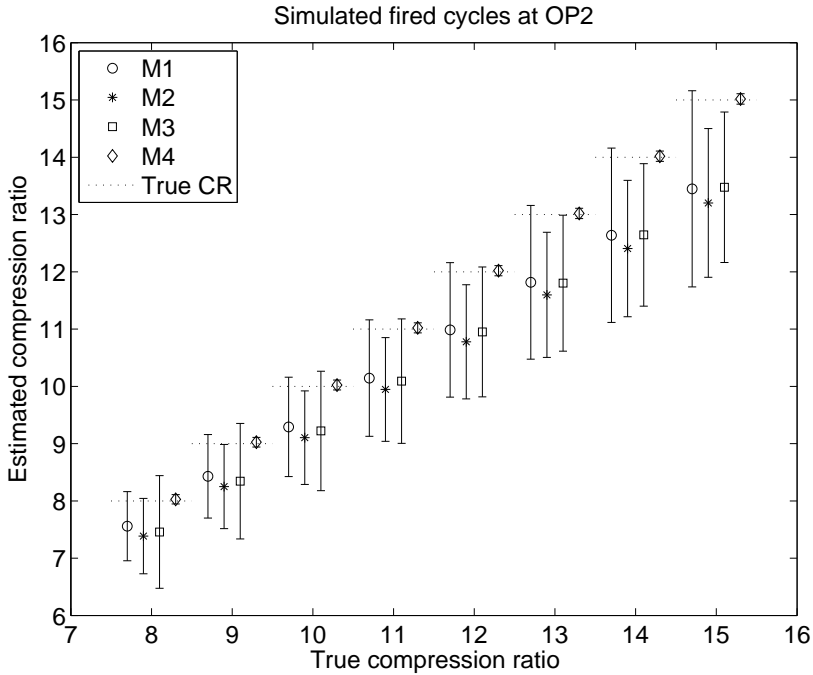


Figure 5.7: Mean value and 95 % confidence interval of the estimated compression ratio for fired cycles using the four methods, compared to the true compression ratio.

gether forming four different operating points, defined in the upper part of table 5.6. The measurements are performed for actuated compression ratio values from the lower limit 8.13 to the upper limit 14.66, through integer values 9 to 14 in between. With actuated compression ratio it is meant the value commanded from the electronic control unit (ECU). These values were determined from engine production drawings and implemented in the ECU, but can be affected by production tolerances or non-ideal sensors (Amann, 1985), as well as mechanical and thermal deformation during engine operation (Lancaster et al., 1975).

For each operating point and compression ratio, 250 consecutive motored cycles with the fuel injection shut-off were sampled with a crank-angle resolution of 1 degree, using a Kiestler 6052 cylinder pressure sensor. Figure 5.8 displays one measured cycle for each r_c at operating point 2 (OP2). For a given r_c the mono-head of the engine is tilted, see figure 5.1, which causes the position for TDC to be advanced from 0 CAD (Klein et al., 2003). The lower the compression ratio is,

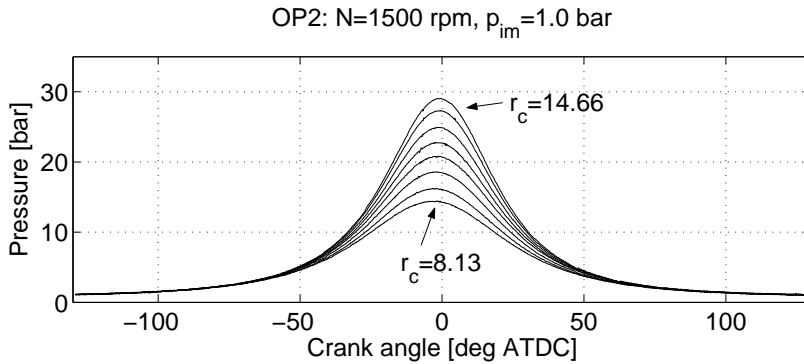


Figure 5.8: Experimentally measured cylinder pressures at OP2. The actuated compression ratios are 8.13, integer values 9 to 14, and 14.66.

the more advanced the position for TDC becomes. This explains why the peak pressure position for $r_c = 8.13$ in figure 5.8 is advanced compared to $r_c = 14.66$, and not the other way around which would be the case if only heat transfer and crevice effects were present.

5.5.2 Results and evaluation for OP2

The performance of the estimation methods is first evaluated for operating point OP2, defined in table 5.6. This operating point has an intake manifold pressure in the midrange of the engine, and a relatively low engine speed for which the effects of heat transfer and crevices are significant. OP2 is therefore chosen as a representative operating point.

Estimation results

The estimation results are presented in the same manner as for the simulated data. Figure 5.9 displays the mean estimate and the mean 95 % confidence interval for 250 consecutive cycles at OP2, where the estimate has been computed for each individual cycle. Table 5.5 shows mean computational time and mean number of iterations, as well as the relative mean error and mean 95 % relative confidence interval. Two examples of residuals are given in figures 5.10 and 5.11.

Analysis of estimation results

Figure 5.9 shows that method 3 underestimates and methods 1, 2 and 4 overestimate the compression ratio. The spread of the estimates between the methods is more pronounced than for the simulated data,

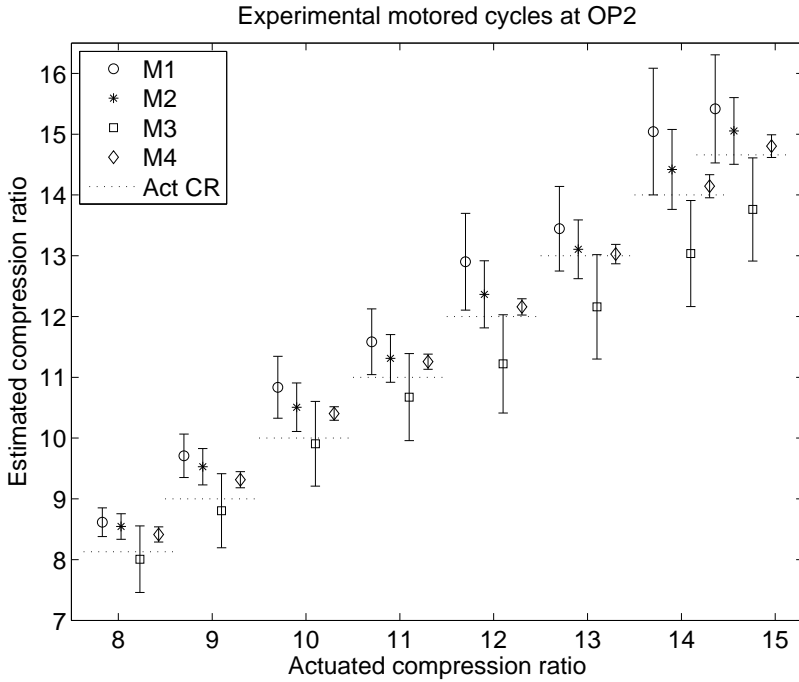


Figure 5.9: Mean value and 95 % confidence interval of the estimated compression ratio for motored cycles using the four methods, compared to the actuated compression ratio. The estimate should be as close as possible to the dotted horizontal line.

compare figures 5.9 and 5.3. This spread increases as the compression ratio becomes higher, a trend also found for the confidence intervals of the estimates. The interrelation among methods 1-3 are however the same, where method 1 always yields the largest estimates, and method 3 the smallest. The trends and effects in the simulation evaluation are also present in the experimental investigation, which gives a first indication that the conclusions drawn from the simulation study are valid.

All methods have approximately the same confidence intervals for the experimental and simulated data, compare tables 5.5 and 5.2. Again method 4 yields the smallest confidence intervals followed by method 2. The difference is most significant for method 4, which had the correct model structure in the simulation case while here it is an approximation of the real engine. This is also seen in the residual, figure 5.11, as a systematic deviation around TDC. This model error thus adds to

Method vs. Act.	$r_c = 8.13$		$r_c = 14.66$		all r_c				
	RME [%]	RCI [%]	RME [%]	RCI [%]	RME [%]	RCI [%]	std [-]	Time [ms]	Iter [-]
1	6.0	2.9	5.2	6.1	6.4	5.3	0.11	89	30.2
2	5.1	2.6	2.7	3.7	3.6	3.8	0.083	5	3.7
3	-1.5	6.7	-6.1	5.8	-4.2	6.5	0.066	128	5.7
4	3.6	1.6	1.0	1.3	2.2	1.3	0.051	6.6×10^5	14.0

Table 5.5: Relative mean error (RME) and mean 95 % relative confidence interval (RCI) of the estimated r_c for extreme values $r_c = 8.13$ and $r_c = 14.66$, and as a mean for all compression ratios for *experimental data* from OP2. They are computed relative to the actuated compression ratio. The standard deviation, mean computational time and mean number of iterations in completing the estimation for one engine cycle are also given.

the variance of the estimate. It also changes the interrelation between methods 1-3 and method 4, e.g. method 4 always gives a smaller estimate on experimental data than method 2, while the converse occurs on the simulated data.

The mean computational time and number of iterations are higher for the experimental data, as shown in table 5.5. As for the simulations, method 2 is the most computationally efficient method of them all.

Residual analysis

The residuals corresponding to the cylinder pressures in figure 5.8 are displayed for all four methods in figure 5.10 for $r_c = 8.13$ and in figure 5.11 for $r_c = 14.66$, together with their respective root mean square error (RMSE).

As for the simulations, there is a systematic deviation for methods 1, 2 and 3. This deviation increases with r_c . The residuals for method 4 have a comparatively small deviation near TDC. This small deviation illustrates that the model structure is acceptable but not perfect, since it is not able to fully capture the measurement data. This is most evident for the higher compression ratio, $r_c = 14.66$, in figure 5.11. The relative mean error for $r_c = 14.66$ is however small, less than 0.8 %, and method 4 can therefore be considered to capture the data well. The residuals from the experimental data have a higher RMSE compared to the simulations, but they are still of the same order. The differences between the methods are due to different formulations of the residuals and model simplifications. These properties give rise to the systematic deviations that are visible in both simulated and experimental data.

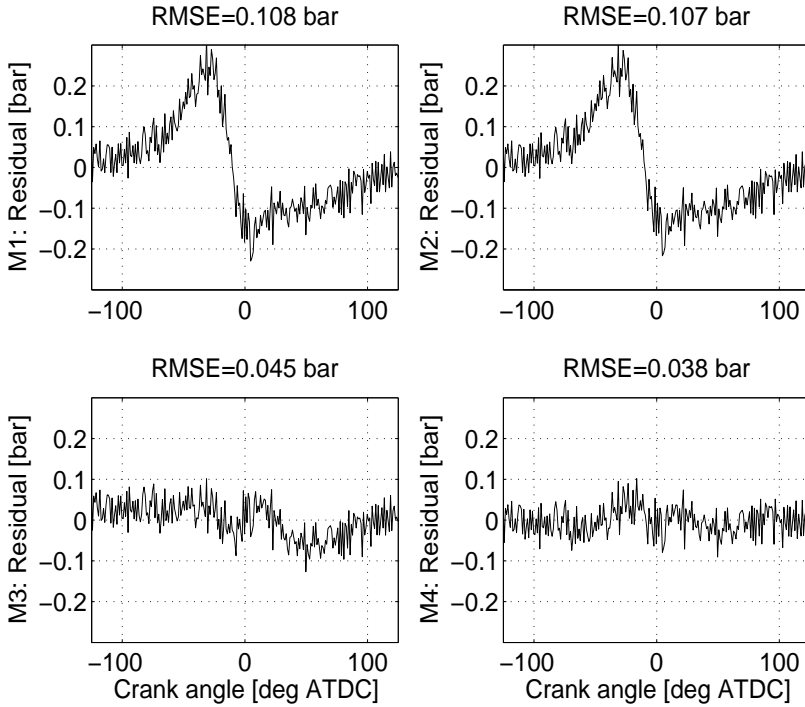


Figure 5.10: Difference between estimated and experimental cylinder pressure for all methods, given the motored cycle in figure 5.8 at $r_c = 8.13$.

5.5.3 Results and evaluation for all OP

The trends shown for OP2 are also present in the full data set, displayed in table 5.6. This table shows that as the intake manifold pressure p_{man} increases, the variance for all methods decreases. A high p_{man} is therefore desirable. However, the influence of the engine speed has no clear trend as two of the methods yield higher variance and the other two lower variance, as the engine speed is increased. For all operating points, method 4 yields the smallest confidence intervals followed by method 2. Therefore the conclusions made in the simulation evaluation with respect to models, residual formulation, methods, heat transfer and crevice effects are the same for the experimental evaluation.

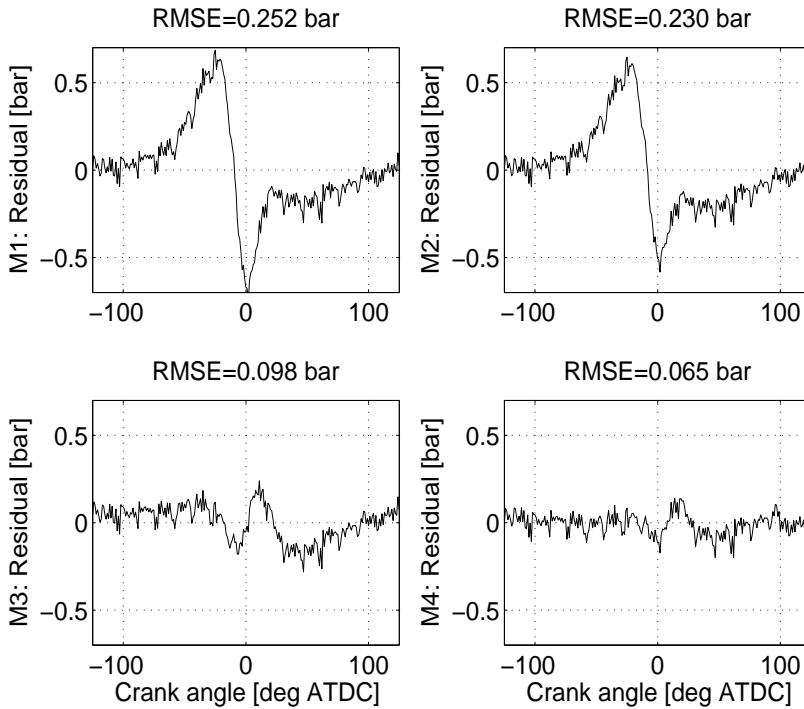


Figure 5.11: Difference between estimated and experimental cylinder pressure for all methods, given the motored cycle in figure 5.8 at $r_c = 14.66$.

	OP1		OP2		OP3		OP4	
N	1500 rpm		1500 rpm		3000 rpm		3000 rpm	
p_{man}	0.5 bar		1.0 bar		0.5 bar		1.0 bar	
Method	RME	RCI	RME	RCI	RME	RCI	RME	RCI
vs. Act.	[%]	[%]	[%]	[%]	[%]	[%]	[%]	[%]
1	10	6.2	6.4	5.3	8	7.5	3.6	5.9
2	6	4.6	3.6	3.8	1.3	5.2	-0.083	4
3	-2.3	8.2	-4.2	6.5	-3.9	7.3	-6.2	5.9
4	2.8	2.0	2.2	1.3	2.9	1.6	2.4	1.2

Table 5.6: Relative mean error (RME) and mean 95 % relative confidence interval (RCI) in estimated r_c , for four different operating points defined by engine speed N and intake manifold pressure p_{man} .

Discussion on compression ratio diagnosis

One application that the proposed methods were developed for was compression ratio diagnosis. The applicability of the methods will be illustrated by a short example. Consider the issue of diagnosing the compression ratio. A possible fault mode is that the compression ratio gets stuck at a too high level, e.g. at $r_c = 12$. A diagnostic test is then used to detect and alarm when r_c gets stuck. This is realized by a hypothesis test, where the null hypothesis is formulated as $H^0 : r_c$ not stuck. This is illustrated by the following example which uses the diagnosis framework presented in Nyberg (1999) and Nyberg (2001):

Example 5.1 – Detecting r_c stuck at 12

Consider the task of detecting when the compression ratio gets stuck. Only two fault modes are considered

$$\begin{aligned} \mathbf{NF} : & r_c^{est} \in [0.9r_c^{act}, 1.1r_c^{act}] \\ \mathbf{F} : & r_c^{est} \notin [0.9r_c^{act}, 1.1r_c^{act}], \end{aligned} \quad (5.22)$$

i.e. an estimated r_c^{est} within 10 percent of the actuated r_c^{act} is considered as no fault (**NF**). The hypothesis test is then formulated as

$$\begin{aligned} H^0 : & \mathbf{NF} \\ H^1 : & \mathbf{F}. \end{aligned} \quad (5.23)$$

The test quantity T is based on comparing the actuated r_c^{act} and estimated r_c^{est} , according to

$$T = |r_c^{act} - r_c^{est}|. \quad (5.24)$$

Then if the controller e.g. actuates $r_c^{act} = 9$ and r_c is really stuck at 12, the test should alarm with a certain level of confidence. This is formalized by the power function $\beta(r_c^{est})$ here defined by

$$\beta(r_c^{est}) = P(\text{reject } H^0 | r_c^{est}) = P(T \geq J | r_c^{est}), \quad (5.25)$$

where J is a threshold designed by the user. The significance level of the test is defined by

$$\alpha = \max \beta(r_c^{est} | r_c^{est} \in \mathbf{NF}), \quad (5.26)$$

which corresponds to the worst case of the false alarm probability. To be able to make the assumption that H^1 is true if H^0 is rejected, the threshold J must be set to obtain a sufficiently low false alarm probability.

Based on the estimates and confidence intervals for method 2 using the experimental results at OP2 in table 5.5, the power function β is

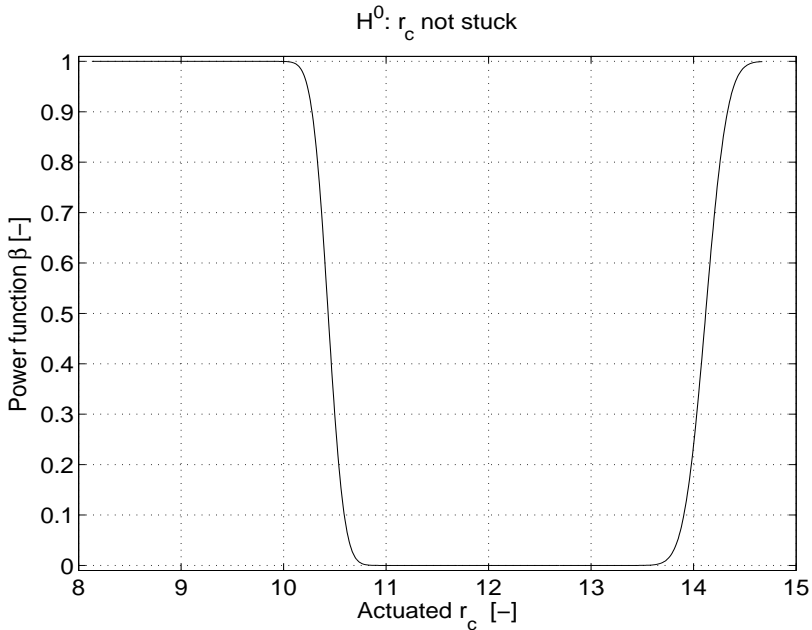


Figure 5.12: Power function β at OP2 for experimental data when r_c is stuck at 12.

computed and displayed in figure 5.12. In the computations it is assumed that the true r_c is stuck at 12 and that linear interpolation can be used to find the estimates and confidence intervals at compression ratios where no actual measurements have been performed. When designing a diagnosis system, there is generally a compromise between a low false alarm probability (FAP) and a low missed detection probability (MDP), given by (D.6) and (D.7).

The (adaptive) threshold is chosen as $J = 0.15 r_c^{act}$, and figure 5.12 shows that this results in a significance level of less than 0.2 %, which is assumed sufficiently low. In this case the false alarm probability comes to the cost of a low missed detection probability for r_c^{est} close to but not within the **NF** fault mode, $r_c^{est} \in [10.8, 13.2]$. This is illustrated by the region $r_c^{est} \in [10.5, 10.8[$ where $MDP = 1 - \beta \geq 0.5$, i.e. the error will not be detected in more than 50 % of the cases. But when $r_c^{est} \leq 10$ the missed detection probability goes to zero, indicating that we will always detect if r_c gets stuck if a proper excitation of the actuated compression ratio is made.

Example 5.1 illustrates the principle of how a diagnosis system can be designed and analyzed using method 2 at operating point OP2. This can be generalized to a diagnosis system for all operating points, and it is only a matter of design to find an appropriate threshold for all methods. The diagnostic performance in terms of false alarm probability, missed detection probability and computational time are of course expected to become best for method 2.

Therefore during driving, all methods are able to detect if the compression ratio is stuck at a too high or at a too low level, given an appropriate number of cycles and an appropriate excitation of r_c . This is sufficient both for safety reasons, where the compression ratio can be too high and engine knock is the consequence, and for fuel economic reasons, where a too low compression ratio will lead to higher fuel consumption.

5.6 Conclusions

Four methods for compression ratio estimation based on cylinder pressure traces have been developed and evaluated for both simulated and experimental cycles.

Conclusions from the simulation results

The first three methods rely upon the assumption of a polytropic compression and expansion. It is shown that this is sufficient to get a rough estimate of the compression ratio r_c for motored cycles, especially for a low r_c and by letting the polytropic exponent become small. For a high r_c it is important to take the heat transfer into account, and then only method 4 is accurate to within 0.5 % for all operating points. Method 4 is however slow and not suitable for on-line implementation. Method 2 on the other hand is substantially faster and still yields estimates that are within 1.5 %. The formulation of the residual is also important, since it influences the estimated r_c . For fired cycles, methods 1-3 yield poor estimates and therefore only method 4 is recommended.

A sensitivity analysis, with respect to crank angle phasing, cylinder pressure bias, crevice volume, and heat transfer, shows that the third and fourth method are more robust. They therefore deal with these parameter deviations better than methods 1 and 2. Of the latter two, method 2 has the best performance for all parameter deviations except for an additive pressure bias.

Conclusions from the experimental results

All methods yield approximately the same confidence intervals for the simulated and experimental data. The confidence intervals resulting

from method 4 are smallest of all methods, but it suffers from a high computational time. Method 2 yields smaller confidence intervals than methods 1 and 3, and is outstanding regarding convergence speed. The effects and trends shown in the simulation evaluation are also present in the experimental data. Therefore the conclusions made in the simulation evaluation with respect to models, residuals, methods, heat transfer and crevice effects are the same for the experimental evaluation. For diagnostic purposes, all methods are able to detect if the compression ratio is stuck at a too high or too low level.

Concluding recommendations

The accuracy of the compression ratio estimate is higher for motored cycles with high initial pressures. Thus if it is possible to choose the initial pressure, it should be as high as possible. Using motored cycles assures that all pressure information available is utilized and the high initial pressure improves the signal-to-noise ratio, while the effects of heat transfer and crevice flows remain the same.

Two methods are recommended; If estimation accuracy has the highest priority, and time is available, method 4 should be used. Method 4 yields the smallest confidence intervals of all investigated methods for both simulated and experimental data. In the simulation case where the true value of the compression ratio is known, method 4 gave estimates with smallest bias. If computational time is the most important property, method 2 is recommended. It is the most computationally efficient of all investigated methods, and yields the smallest confidence intervals out of methods 1-3.

Part III

Prior Knowledge based Heat Release Analysis

USING PRIOR KNOWLEDGE FOR SINGLE-ZONE HEAT RELEASE ANALYSIS

Internal combustion engines operate by converting the chemical energy in the air-fuel mixture into useful work by raising the cylinder pressure through combustion. The cylinder pressure data itself is therefore a reflection of the combustion process, heat transfer, volume change etc. and thus gives important insight into the control and tuning of the engine. To accurately model and extract information from the cylinder pressure is important for the interpretation and validity of the result. Due to the short time scale of the process, a sequence of measurements from an engine gives huge amounts of data. These large sets of data have to be analyzed efficiently, systematically, and with high accuracy. The objective here is therefore to develop a tool for efficient, systematic and accurate off-line heat release analysis of cylinder pressure data.

Problem outline

The focus is on a single-zone heat release model (Gatowski et al., 1984) that describes the cylinder pressure accurately and has a low computational complexity. A low computational complexity is an important feature when analyzing large data sets. However, this model includes at most 16 unknown parameters, as shown in section 3.8, among which there are couplings causing identifiability problems. This is due to that the estimation problem is on the verge of being over-parameterized. An example is the clearance volume and the crevice volume, which are hard to identify simultaneously. This is often solved by setting one of these parameters to a constant fixed value. The correct value of the constant

parameter is however unknown, and is therefore most likely set with an error. This error causes a bias in the other parameter estimates.

Problem solution

Two methods for parameter estimation are developed and compared. Method 1 is called *SVD-based parameter reduction* and is summarized as:

1. Estimate the parameter values and variances using a constrained local optimizer.
2. Find the most uncertain parameter, i.e. the one that has the highest variance by using singular value decomposition (SVD) of the estimated hessian, for the given measured cylinder pressure.
3. Set the uncertain parameter from step 2 constant using prior knowledge of the parameter and return to step 1.

The uncertain parameters are set constant one-by-one in step 3, which reduces the variance for the remaining (efficient) parameters when no modeling error is induced. A recommended number of efficient parameters is then found by minimizing the Akaike final prediction error criterion (Ljung, 1999). Step 3 is motivated by the following; The most uncertain parameters generally drift off from their nominal values. This nominal parameter deviation will cause a bias even in the most certain parameters. This motivates why the most certain parameter is not set constant. However, if the most uncertain parameters are set fixed to their nominal values, it is believed that this will reduce the bias in the efficient parameters.

The second method uses *prior knowledge* of all the parameters explicitly in the optimization. The parameters x are estimated by minimizing the criterion function:

$$W_N = \frac{1}{N} \sum_{i=1}^N (p(\theta_i) - \hat{p}(\theta_i, x))^2 + (x - x^\#)^T \delta (x - x^\#) \quad (6.1)$$

w.r.t. x , i.e. by minimizing the standard prediction error $\varepsilon(\theta_i, x) = p(\theta_i) - \hat{p}(\theta_i, x)$ using a regularization technique. Method 2 is therefore named *regularization using prior knowledge*. The first term in (6.1) minimizes the difference between the modeled $\hat{p}(\theta, x)$ and measured $p(\theta)$ cylinder pressure, while the second term pulls the parameters x towards $x^\#$, i.e. towards the nominal values obtained from prior knowledge. The matrix δ and vector $x^\#$ account for prior knowledge of the parameters, where δ influences how strong the pulling force should be. This can be interpreted as that all parameters are assigned a prior

probability density function (pdf), with a nominal mean value $x^\#$. If the pdf is Gaussian, minimizing W_N produces the maximum a posteriori estimate. For example, our prior knowledge of an additive pressure offset (after pegging with the intake manifold pressure) could be that the parameter is Gaussian distributed with a nominal mean value of 0 kPa, and a standard deviation of 2.5 kPa. It is however only the inter-group relation among the parameters, and not the absolute value of the standard deviation that is important as will be shown later. The nominal vector $x^\#$ is found from appropriate initial values and the size of the matrix δ is tuned using simulations to give a balanced compromise between the prior knowledge and the measured cylinder pressure.

A fundamental problem is that the true values of the parameters are unknown in a real engine, which makes the evaluation of the two methods on experimental data difficult. This is mainly due to two reasons: First of all, the chosen model structure is bound to be incorrect since not every physical process influencing the measured cylinder pressure is modeled, which will cause inexact parameter values. Secondly the criterion function can be small for a given data set, although the parameter estimates are, due to physical reasons, bad. It is therefore not sufficient to minimize the criterion function on validation data to evaluate the two proposed methods. To overcome these obstacles simulated pressure traces, with well-known parameter values and a well-known model structure, are used. In the simulations noise of the same order as for the experimental data is added to the measurement signal. The methods are evaluated on simulated data from motored and fired cycles with respect to estimation bias, variance and residual analysis using both false and correct prior knowledge. The results are also validated on experimental data from an SI engine.

6.1 Outline

The outline of this chapter and the two following chapters is presented here. One cylinder pressure is described in section 6.2. It has been derived in chapters 2 and is summarized here for convenience. Then the problem associated with this parameter estimation application is illustrated in section 6.3 by two simple approaches, which are based purely on either data fitting or parameter prior knowledge, and they are both unsuccessful. Therefore two methods, referred to earlier in this chapter as method 1 and 2, that incorporate parameter prior knowledge in the estimation problem are proposed in section 6.4. These two methods are then evaluated using simulated and experimental data in chapter 7 for motored cycles, and in chapter 8 for fired cycles. The compiled conclusions from both evaluations are given in section 9.3. A method of how to express the prior knowledge is also presented in general terms in section 6.4, and in chapters 7 and 8 for the specific cases.

6.2 Cylinder pressure modeling

One single-zone models is used to describe the cylinder pressure trace and it is referred to as the standard model. Gatowski et al. (1984) develops, tests and applies a single-zone model for heat release analysis. See section 2.5 for the derivation and section 3.8 for details on the parameters and model components. The model is based on the first law of thermodynamics and maintain simplicity while still including the well known effects of heat transfer and crevice flows.

6.2.1 Standard model

The most important thermodynamic property when calculating the heat release rates in engines is the ratio of specific heats, $\gamma(T, p, \lambda) = \frac{c_p}{c_v}$ (Gatowski et al., 1984; Chun and Heywood, 1987; Guezennec and Hamama, 1999). In the standard model γ is represented by a linear function in mean charge temperature T

$$\gamma_{lin}(T) = \gamma_{300} + b(T - 300), \quad (6.2)$$

i.e. model \mathcal{B}_1 in chapter 4. The standard cylinder pressure model is simulated by using (3.36)–(3.45).

6.2.2 Cylinder pressure parameters

The parameters used in the standard model and how to find its nominal values was given in chapter 3. In the standard model, two parameters (γ_{300} and b) are estimated for γ .

6.3 Problem illustration

To illustrate the difficulties associated with parameter estimation given a cylinder pressure trace, two simple but different approaches are used. The first approach estimates all parameters in the standard cylinder pressure model simultaneously by applying a Levenberg-Marquardt method with constraints on the parameters, which is a local optimizer described in appendix C.1. The constraints are physically motivated and are set widely, in order to only influence whenever the parameter values become physically invalid. Two examples of applied constraints are a positive cylinder pressure at IVC, p_{IVC} , and a mean charge temperature at IVC, T_{IVC} , larger than 270 K. Without these constraints the approach yields e.g. a T_{IVC} -estimate that typically is approximately 200 K, i.e. a physically invalid value. The second approach tunes the parameters manually one at a time until a satisfactory pressure trace is found, an approach sometimes referred to as “heat release playing”.

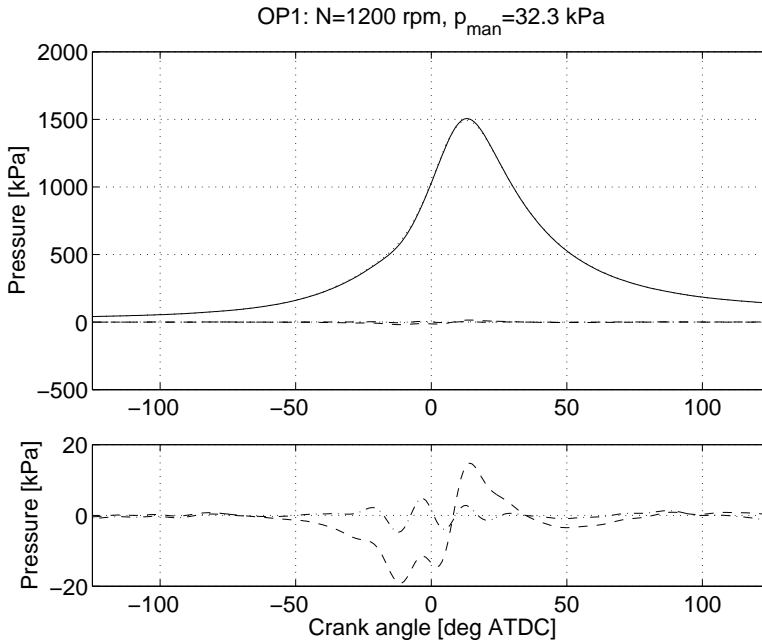


Figure 6.1: Filtered experimental firing cycle and the modeled cylinder pressure for the two simple approaches. The residual for approach 1 (dash-dotted) and approach 2 (dashed) are also given in both the upper and lower plot. The RMSE:s are 1.3 and 5.8 kPa respectively.

This approach requires a lot of patience combined with prior knowledge of nominal values as well as expert knowledge of what influence each parameter has on the cylinder pressure, and also cross-couplings in between the parameters.

The results for both approaches are given in figure 6.1, where the modeled and measured cylinder pressure traces are displayed, and in table 6.1 where the parameter estimates are given. In fairness of the second approach, it should be pointed out that less than an hour was spent on tuning the parameters, thus the result could of course be better. It however illustrates how time-consuming this approach can be.

As shown in figure 6.1 approach 1 has a good residual fit, but according to table 6.1 the parameter estimates are bad. The small residual in figure 6.1 also illustrates that the model structure is flexible enough to describe the cylinder pressure, but that the parameters are hard to identify. The bad parameter estimates are exemplified by the temperature at IVC, T_{IVC} , which is as low as 270 K and also the lower bound

Par.	Description	Approach 1	Approach 2	Nominal
γ_{300}	constant specific heat ratio [-]	1.285	1.335	1.335
b	slope for specific heat ratio [K^{-1}]	$-2.11 \cdot 10^{-5}$	$-7.42 \cdot 10^{-5}$	$-7.42 \cdot 10^{-5}$
C_1	heat-transfer parameter [-]	2.44	4.56	2.28
C_2	heat-transfer parameter [-]	$3.14 \cdot 10^{-3}$	$3.24 \cdot 10^{-3}$	$3.24 \cdot 10^{-3}$
$\Delta\theta$	crank angle phasing [deg ATDC]	0.048	0.043	0.047
Δp	bias in pressure measurements [Pa]	-1.34	-1.37	-1.37
K_p	pressure measurement gain[-]	0.908	1	1
p_{IVC}	cylinder pressure at IVC [kPa]	45.7	41.0	41.3
T_{IVC}	mean charge temperature at IVC [K]	270.0	400.0	388.8
T_w	mean wall temperature [K]	563	475	440
V_c	clearance volume [cm^3]	61.1	58.8	58.8
V_{cr}	single aggregate crevice volume [cm^3]	0.61	0.71	0.58
θ_{ig}	ignition angle [deg ATDC]	-31.4	-32.6	-32.6
$\Delta\theta_d$	flame-development angle [deg ATDC]	24.6	26.6	26.6
$\Delta\theta_b$	rapid-burn angle [deg ATDC]	20.1	20.1	20.1
Q_{in}	released energy from combustion [J]	352	350	350

Table 6.1: Nominal values and estimates for the two simple approaches.

chosen for this parameter, clearly a too low value. This is compensated for by having a higher mean cylinder wall temperature, T_w , and a smaller γ_{300} . Without the constraints the estimation would render an even smaller T_{IVC} . Typically all temperatures drift off to non-physical values, independent of initial value, when estimating all parameters at the same time. This is of course unwanted and yields parameter estimates that are inaccurate and not physically valid. The same behavior arise for estimation problems that are either rank-deficient or ill-posed. As an illustration, the behavior for a simple linear example of a rank-deficient problem is given in appendix C.2.

For the second approach it is the other way around compared to the first approach. The second approach gives reasonable parameter values, see table 6.1, but the residual fit is worse than for the first approach as shown in the lower part of figure 6.1. This approach can therefore be said to give physically valid parameter estimates, but not in a time efficient way. In addition the user's presumption also plays a role in the estimation and could result in a bias. The residual error is however small compared to the measured cylinder pressure, as shown in the upper part of the figure. However none of these approaches comply very well with all our demands on the estimation procedure; efficient, systematic and accurate. To enhance the performance of these two approaches, their advantages are combined by using the systematic minimization of the residual from the first approach and the parameter guess approach based on expert and prior knowledge from the second. The idea for doing so is to use prior knowledge or information about the parameters and use it in a central way to enhance the estimation procedure.

6.4 Estimation methods

Two methods that use prior knowledge of the parameters are presented. They both estimate the parameters x by minimizing the difference between the measured $p(\theta_i)$ and modeled cylinder pressure $\hat{p}(\theta_i, x)$, i.e. by minimizing the prediction error $\varepsilon(\theta_i, x) = p(\theta_i) - \hat{p}(\theta_i, x)$. As shown in figure 6.1 the data is well described by a direct simulation of the standard model in section 6.2.1. It is therefore reasonable to use direct simulation as a predictor, which corresponds to an output-error model assumption.

The first method uses the prior knowledge indirectly by reducing the number of parameters to estimate. This is done by setting those that are hardest to estimate to fixed values, given by the prior knowledge. Method 1 is referred to as *SVD-based parameter reduction*. The second method includes the prior knowledge directly into the optimization problem. This is achieved by including a parameter deviation penalty

term in the criterion function, that will help to *regularize* and thereby control and attract the estimates to the vicinity of the priorly given nominal values. This method is therefore called *regularization using prior knowledge*.

6.4.1 Method 1 – SVD-based parameter reduction

The first method starts by estimating all parameters \hat{x} by minimizing

$$V_N = \frac{1}{N} \sum_{i=1}^N (p(\theta_i) - \hat{p}(\theta_i, x))^2 \quad (6.3)$$

w.r.t. x . This is done by using a Gauss-Newton method called the Levenberg-Marquardt procedure, see appendix C.1 for details. The number of parameters to estimate are then reduced one by one by setting them fixed, starting with the most uncertain parameter. This is motivated by the following; The most uncertain parameters generally drift off from their nominal values. This nominal parameter deviation will cause a bias even in the most certain parameters, as illustrated for γ_{300} in table 6.1 for approach 1 where all parameters were estimated simultaneously. Altogether, this motivates why the most certain parameter is not set constant. However, if the most uncertain parameters are set fixed to their nominal values, it is believed that this will reduce the bias in the efficient parameters.

Method 1 finds these uncertain (spurious) parameters by studying the SVD of the estimated hessian, which reflects how much a certain parameter affects the loss function V_N . When the most spurious parameter is found, it is set constant and the estimation starts over again with one parameter less to estimate. This systematic procedure of reducing the number of parameters was presented in (Eriksson, 1998) for motored cycles. A recommended number of parameters was then found by using the condition number of the hessian. Here all parameter estimates \hat{x} for any given number of parameters are compared, and the estimate minimizing the Akaike final prediction error (FPE) is the best parameter estimate, \hat{x}^* .

Efficient and spurious parameters

Method 1 aims at handling the difficulties associated with the first simple approach in section 6.3 that were due to an over-parameterization of the problem. The over-parameterization causes the jacobian ψ to become ill-conditioned or rank deficient. A rank deficient jacobian can occur if one or more columns of ψ are parallel or almost parallel. Here “almost” means in the order of the working precision of the computer.

This case reflects sets or combinations of parameters that do not influence the criterion function that much. According to (Sjöberg et al.,

1995; Lindskog, 1996), the parameters can be divided into two sets: *spurious* and *efficient* parameter sets, where the former corresponds to parameters with small influence on the criterion function value. Due to this small influence on the criterion function, it is reasonable to treat those parameters as constants that are not estimated. This parameter classification can be made in quite a number of ways, as shown in Example 6.1.

Example 6.1 – Spurious and efficient parameters

Consider the static model with two parameters

$$y = (x_1 + x_2). \quad (6.4)$$

If x_2 is set constant and thereby considered as spurious, then x_1 is considered to be efficient. The other way around works equally well, and does not affect the flexibility of the model structure.

Eigenvector of hessian H_N – finding the spurious parameters

Locally, the estimated hessian $H_N(\hat{x})$ gives insight into how sensitive $V_N(\hat{x})$ is to a certain parameter or combination of parameters. To be able to estimate a certain parameter, that parameter has to have a clear effect on the output predictions (Ljung, 1999, p.453). This is reflected in the hessian, which has large values for efficient parameters. Therefore, it is of interest to find the group of parameters that corresponds to the smallest effect, i.e. the spurious parameters, and set these parameters to appropriate constant values. This is reasonable since the spurious parameters are the hardest to estimate with the given model $\mathcal{M}(x)$ and the observed data Z^N . The observed data is defined as $Z^N = [y(\theta_1), u(\theta_1), y(\theta_2), u(\theta_2), \dots, y(\theta_N), u(\theta_N)]$, given the inputs $u(\theta)$ and outputs $y(\theta)$.

The spurious parameters are classified by finding the smallest singular value of $H_N(\hat{x}, Z^N)$, and from the corresponding eigenvector the group of parameters can be picked out. An algorithm for this is given by algorithm 6.1. The algorithm assumes that the parameters that influence this eigenvector of the hessian $H_N(\hat{x}, Z^N)$ are the same for the estimate \hat{x} , as for the true solution x^t . The use of the algorithm is illustrated in example 6.2.

Algorithm 6.1 can include an optional preferred ordering of the parameters, that is used in step 7. The ordering tells us which parameter is best known a priori, and which parameter we therefore prefer to set fixed first. This preferably applies to parameters that are similar in their physical properties, such as two temperatures, which then can be grouped together and have a relative ordering. This ordering should be

based on prior knowledge of the parameters, and could be the result of a pre-estimation of the parameters, knowledge of the measurement situation and sensor properties, or by expert knowledge. For example, the cylinder wall temperature T_w and the mean charge temperature at IVC, T_{IVC} , can be ordered as $B_1 = [T_w \ T_{IVC}]$ if it is believed that T_w is better known than T_{IVC} . This means that if the two temperatures end up in the same group of parameters in the eigenvector from the hessian and as long as T_{IVC} is not totally dominating, T_w will be set constant prior to T_{IVC} .

A special case for the preferred ordering groups, is when only one (large) group B_1 containing all parameters is used. This case is supported by the algorithm, but not recommended since it could result in that one spurious parameter is exchanged for another although there is no physical coupling in between them. As mentioned earlier, it is preferable if the parameters in the same ordering group are similar in their physical properties or coupled in the chosen model structure. This speaks in favor of using multiple ordering groups. An example of this are the parameters C_1 , T_w and T_{IVC} which are coupled by the heat transfer model (3.43b) and the temperature model (3.40).

It is assumed in the algorithm that a parameter only occurs in one ordering group B_i . In the algorithm there are two ad-hoc decision rules, in step 4 and step 6 respectively. These are motivated after the algorithm.

Algorithm 6.1 – Determining the spurious parameter using a preferred ordering

Let \hat{x}^{eff} be estimated parameters from the local optimizer used for $d^\#$ efficient parameters and x^{sp} are the spurious parameters.

1. Compute the estimated hessian $H_N(\hat{x}, Z^N)$ (C.8), where $\hat{x} = (\hat{x}^{eff} \ x^{sp})^T$.
2. Compute the singular values $\varsigma_1 \geq \dots \geq \varsigma_{d^\#} \geq 0$ and the corresponding eigenvectors $v_1, \dots, v_{d^\#}$, by using singular value decomposition (SVD).
3. The eigenvector $v_{d^\#}$ which corresponds to the smallest singular value $\varsigma_{d^\#}$, is chosen. Then the element in $v_{d^\#}$ that has the largest absolute value is named e_k and is picked out. This element corresponds to the most spurious parameter according to the data.
4. If the element e_k is dominating, the preferred ordering is overridden. This is realized as if the absolute value of the element e_k is

- greater than 0.9, go to step 8.
- 5.If no preferred ordering exists, go to step 8.
- 6.Form a group A of elements from the eigenvector $v_{d\#}$ corresponding to $\varsigma_{d\#}$, by using the following strategy: Find the elements in $v_{d\#}$ that have absolute values greater than $\sqrt{0.1}$. Sort these elements in a descending order of their size in group A .
- 7.Find the ordering group B_i to which e_k belongs. The element in B_i that has the highest ordering in B_i and at the same time belongs to group A , is the new e_k .
- 8.Return the parameter x_k that corresponds to element e_k .
-

Steps 1–3 in algorithm 6.1 are similar to the approach in principal component analysis, but here a parameter is set fixed rather than a direction of the eigenvector.

If one parameter dominates the eigenvector $v_{d\#}$ substantially (according to the data), then this parameter is labeled spurious no matter what the preferred ordering, i.e. prior knowledge, says. This assures that the dominating parameter is not exchanged. This approach is implemented in step 4 such that a parameter is classified as dominating if its absolute value is greater than 0.9, which corresponds to more than 81 percent of the total vector length of $v_{d\#}$.

In step 6 another ad-hoc decision rule is used. It is based upon the assumption that if a parameter x_k is to be exchanged for another x_j , they both have to have an influence on the eigenvector $v_{d\#}$. In step 6 a parameter is classified as influencing if its absolute value is greater than $\sqrt{0.1}$, i.e. if it constitutes more than 10 percent of the total length of eigenvector $v_{d\#}$. This assures that a parameter is not exchanged for one that only constitutes a small part of $v_{d\#}$.

The numerical values in steps 4 and 6 are ad-hoc choices, and can therefore be adjusted according to the specific requirements of the user.

Example 6.2 – Determining the spurious parameter using algorithm 6.1

Consider an estimation problem where there are five unknown parameters x_1, \dots, x_5 . The parameters are ordered relative to each other into ordering groups B_i . For this example they are given by $B_1 = [x_1, x_2]$ and $B_2 = [x_3, x_4, x_5]$. Algorithm 6.1 is used to find the most spurious parameter in three different cases, all having different Hessians. Following the algorithm, first the estimated Hessian is computed (step 1),

and from this the singular values are found (step 2). The eigenvector that corresponds to the smallest singular value is v_5 (step 3). Three different cases are now illustrated by using different v_5 vectors.

a) The elements e_k in Group A_a are found by

$$v_5 = \begin{bmatrix} 0 \\ 1 \\ 0 \\ 0 \\ 0 \end{bmatrix} \Rightarrow A_a = \{e_2\}$$

using steps 3–4. The absolute value of this element is greater than 0.9, and therefore x_2 is returned by the algorithm using step 8.

b) The elements e_k in Group A_b are found by

$$v_5 = \begin{bmatrix} 0 \\ 0.7 \\ -0.7 \\ 0.14 \\ 0 \end{bmatrix} \Rightarrow A_b = \{e_2, e_3\}$$

using steps 3–6. In step 7 no re-ordering of the elements occurs since the elements e_2 and e_3 belong to different ordering groups B_i , and therefore x_2 is returned in step 8.

c) The elements e_k in Group A_c are found by

$$v_5 = \begin{bmatrix} -0.4 \\ 0.65 \\ 0.5 \\ 0.2 \\ -0.2 \end{bmatrix} \Rightarrow A_c = \{e_2, e_3, e_1\}$$

using steps 3–6. In step 7 it is found that the largest element e_2 belongs to B_1 as well as e_1 . The ordering tells us that e_1 should be picked out before e_2 , and thus x_1 is returned in step 8.

Note that without the preferred ordering B_i , all three cases would return parameter x_2 .

Loss function V_N – finding the number of efficient parameters

The value of the estimated loss function $V_N(\hat{x}, Z^N)$ serves not only as a measure of the model fit to the measured output, but also as a test quantity for over-parameterization. By increasing the number

of parameters, and thereby the flexibility of a model, more and more features in the measured output data can be explained by the model, and thereby decreasing the value of the loss function. It is therefore reasonable that the loss function is a monotonically decreasing function of the number of model parameters. But by adding more and eventually unnecessary parameters, the parameters adjust themselves to features in the particular noise realization, and will in fact decrease the loss function even more. This is known as *over-fit* (Ljung, 1999, p.501), and is unwanted since the noise realization is bound to change.

To be able to compare model structures with different numbers of efficient parameters in a fair way, the Akaike's Final Prediction Error (FPE) Criterion (Akaike, 1969) is used. In the derivation of the Akaike FPE it is assumed that the true system can be described by our model $\mathcal{M}(x)$, and that the parameters are identifiable such that the hessian is invertible. The expectation value of the loss function V_N is then found to be (Ljung, 1999, pp.503):

$$EV_N(\hat{x}) \approx V_N(\hat{x}, Z^N) + \lambda_0 \frac{2d}{N}, \quad (6.5)$$

where λ_0 is the noise variance (compare (C.18b)), N is the number of samples and d is the number of parameters for model $\mathcal{M}(x)$. The more parameters the model structure uses, the smaller the first term will be. Each new parameter contributes with a variance penalty of $2\lambda_0/N$, which is reflected by the second term. Any parameter that improves the fit of V_N with less than $2\lambda_0/N$ will thus be harmful, and introduce an over-fit. Such a parameter is termed *spurious*.

From equation (6.5) and an estimate of λ_0 (C.18b), the Akaike FPE $V_N^{FPE}(\hat{x}, d)$ is stated as (Ljung, 1999, pp.503)

$$EV_N(\hat{x}) \approx \frac{1 + \frac{d}{N}}{1 - \frac{d}{N}} V_N(\hat{x}, Z^N) =: V_N^{FPE}(\hat{x}, d). \quad (6.6)$$

The equation shows how the loss function $V_N(\hat{x})$ should be modified to give a fair measure of the number of model parameters.

Algorithm – Method 1

We are now ready to formulate the algorithm.

Algorithm 6.2 – SVD-based parameter reduction

Let x^{init} be the initial values for the parameters $x \in \mathbf{R}^{d \times 1}$. The parameter vector is partitioned as $x = [x^{eff} x^{sp}]^T$, where $x^{eff} \in \mathbf{R}^{d^{\#} \times 1}$ are the efficient parameters and $x^{sp} \in \mathbf{R}^{(d-d^{\#}) \times 1}$ are the spurious parameters. The maximum and minimum number of efficient parameters are given by $d_{max}^{\#}$ and $d_{min}^{\#}$ respectively, related by $1 \leq d_{min}^{\#} \leq d_{max}^{\#} \leq d$.

1. Initialization: Set the best parameter estimate $\hat{x}^* = x^{init}$ and the number of efficient parameters $d^\# = d_{max}^\#$.
2. Use the Levenberg-Marquardt procedure (C.11) to estimate the efficient parameters \hat{x}^{eff} in $\hat{x} = [\hat{x}^{eff} x^{sp}]^T$. The vector x^{init} is used as initial values for x^{eff} and fixed values for x^{sp} .
3. If there are more than $d_{min}^\#$ efficient parameters left, i.e. $d^\# > d_{min}^\#$, compute the most spurious parameter x_{new}^{sp} out of x^{eff} using Algorithm 6.1. Then move x_{new}^{sp} from x^{eff} to x^{sp} and reduce the number of efficient parameters by one, i.e. $d^\# = d^\# - 1$. Return to step 2.
4. Compute the Akaike FPE $V_N^{FPE}(\hat{x}^{eff}, d^\#)$ from (6.6) for all $d^\#$. Find the number of efficient parameters d^* that minimizes $V_N^{FPE}(\hat{x}^{eff}, d^\#)$. The best estimate is then given by

$$\hat{x}^* = \hat{x}^{eff}(d^*).$$

5. Return the best parameter estimate \hat{x}^* .

The algorithm can be made more computationally efficient, either by reducing the maximum number of efficient parameters $d_{max}^\#$ in step 1, i.e. by making more parameters spurious from the start, or by increasing the minimum number of efficient parameters $d_{min}^\#$ for the criteria in step 4. Both these simplifications of course rely upon some kind of prior knowledge. Another improvement in computation time can be achieved if several parameters are made spurious at the same time in step 4. A test for this is to consider only parameters for which the ratio ζ_1^2/ζ_i^2 is larger than the machine precision. If $d_{max}^\# < d$, i.e. the maximum number of efficient parameters are less than the number of parameters, the initial partitioning of the parameter vector x into efficient and spurious parameters has to be done by the user. For the sake of completeness, the number of efficient parameters in chapters 7 and 8 are set to $d_{min}^\# = 1$ and $d_{max}^\# = d$.

6.4.2 Method 2 – Regularization using prior knowledge

The second method uses prior knowledge of the parameters explicitly in the optimization. The drive for this is to regularize the solution of the estimation problem, and this is done by including a parameter penalty term in the loss function.

Regularization through prior knowledge of the parameters

As mentioned earlier, a regularization technique can be used to avoid an ill-conditioned jacobian ψ and thereby avoiding a singular or almost singular hessian H_N . In the Levenberg-Marquardt procedure, this was done by adding $\nu > 0$ to (C.10) and thereby a positive definite H_N is guaranteed. A regularizing effect is also imposed by adding a penalty term to the criterion function $V_N(x, Z^N)$ (C.2) resulting in

$$\begin{aligned} W_N(x, x^\#, Z^N, \delta) &= \frac{1}{N} \sum_{i=1}^N \frac{1}{2} \varepsilon^2(\theta_i, x) + (x - x^\#)^T \delta (x - x^\#) \\ &= V_N(x, Z^N) + \delta_x V_N^\delta(x, x^\#, \delta). \end{aligned} \tag{6.7}$$

It differs from the basic criterion V_N by also penalizing the squared distance between x and $x^\#$, where $x^\#$ are the nominal parameter values. It is divided into two terms, where V_N corresponds to the residual error introduced by the measurement and V_N^δ corresponds to the nominal parameter deviation. The scalar term δ_x is named regularization factor and will be returned to later. The main reason for using this criterion is: If the model parameterization contains many parameters, it may not be possible to estimate several of them accurately. There are then advantages in pulling the parameters towards a fixed point $x^\#$ (Ljung, 1999, pp.221). This definitively applies to an ill-posed problem. The penalty term V_N^δ in (6.7) will effect the parameters with the smallest influence on V_N , i.e. the spurious ones, the most. This forces the spurious parameters to the vicinity of $x^\#$. The regularization matrix δ can be seen as a tuning knob for the number of efficient parameters. A large δ simply means that the number of efficient parameters $d^\#$ becomes smaller and that more parameters are locked to the vicinity of $x^\#$. It can also be seen as the weighted compromise between residual error ε and nominal parameter deviation $\varepsilon_x^\# = x - x^\#$. A large δ thus corresponds to a large confidence in the nominal parameter values.

The impact of the prior on the final estimate will now be illustrated in the following example.

Example 6.3 – Impact of prior $x^\#$ and δ on final estimate x

Again, consider the static model

$$y = (x_1 + x_2), \tag{6.8}$$

which formed the base for example 6.1. Here, $x_1 = x_2 = 1$ are the true values of the parameters, the nominal values are given by $x_1^\#$ and $x_2^\#$ respectively, the measurement is y and the regularization matrix δ is given by $\delta = \text{diag}(\delta_1, \delta_2)$. The residual ε is then formed as

$$\varepsilon(x) = y - \hat{y}(x) = y - (x_1 + x_2). \tag{6.9}$$

The criterion function $W_N(x, x^\#, Z^N, \delta)$ (6.7) is thereby given as

$$W_N(x, x^\#, Z^N, \delta) = (y - x_1 - x_2)^2 + (x - x^\#)^T \delta (x - x^\#). \quad (6.10)$$

It is minimized analytically by differentiating W_N partially w.r.t. each parameter and setting the partial derivative to zero, resulting in the following set of equations

$$(1 + 2\delta_1)x_1 + x_2 = y + 2\delta_1 x_1^\#, \quad (6.11a)$$

$$x_1 + (1 + 2\delta_2)x_2 = y + 2\delta_2 x_2^\#. \quad (6.11b)$$

There are two solutions of (6.11), one for $\delta = 0$ and the other for $\delta \neq 0$. For the $\delta = 0$ case, which corresponds to no prior knowledge of the parameters, the solution is given by

$$x_1 + x_2 = y, \quad (6.12)$$

i.e. a parameterized solution which has an infinite number of solutions. For $\delta \neq 0$, the solution is given by

$$x_1 = \delta_2 \frac{y - (x_1^\# + x_2^\#)}{\delta_1 + \delta_2 + \delta_1 \delta_2} + x_1^\#, \quad (6.13a)$$

$$x_2 = \delta_1 \frac{y - (x_1^\# + x_2^\#)}{\delta_1 + \delta_2 + \delta_1 \delta_2} + x_2^\#. \quad (6.13b)$$

In the special case when the measurement y is fully captured by the model (6.12) and the prior parameter values $x_i^\#$, i.e. if $y = x_1^\# + x_2^\#$, then the estimates x_i are given by the nominal values $x_i^\#$. However, when the prior does not exactly match the measurement, i.e. when $y \neq x_1^\# + x_2^\#$, the estimates x_i are biased from their nominal values. Equation 6.13 illustrates that δ can be seen as a tuning knob; the larger the components δ_i are, the more the estimates x_i are drawn to the nominal values $x_i^\#$. In the case when $\delta_1 \gg \delta_2$, x_1 is more attracted to $x_1^\#$ than x_2 is to $x_2^\#$.

Minimizing the criterion function W_N

The regularizing effect imposed by the penalty term in W_N (6.7) requires that the optimization search method is reformulated. The expressions for the gradient and the hessian of W_N (6.7) are therefore given here. For comparison, references to the derivation of a local optimizer without regularization (appendix C.1) are given. The gradient $V_N(x, Z^N)'$ (C.4) and the hessian approximation H_N (C.8) for such an optimizer have to be rewritten when the parameter penalty term in (6.7) is included. It is here assumed that there are no cross-couplings

between the parameter prior knowledge, i.e. the regularization matrix δ is assumed to be diagonal. The gradient is then written as

$$\begin{aligned} W'_N(x, x^\#, Z^N, \delta) &= \frac{1}{N} \sum_{t=1}^N \psi(t, x) \varepsilon(t, x) + 2\delta(x - x^\#) \\ &= V'_N(x, Z^N) + 2\delta(x - x^\#), \end{aligned} \quad (6.14)$$

where as before the jacobian vector $\psi(t, x) = \frac{d}{dx} \varepsilon(t, x)$ is given by (C.5). The hessian $W''_N(x, Z^N, \delta)$ is then computed as

$$\begin{aligned} W''_N(x, Z^N, \delta) &= V''_N(x, Z^N) + 2\delta \\ &\approx H_N(x, Z^N) + 2\delta = H_N^\delta(x, Z^N, \delta), \end{aligned} \quad (6.15)$$

and its approximation is given by $H_N^\delta(x, Z^N, \delta) = H_N(x, Z^N) + 2\delta$. The estimate \hat{x} is found numerically by updating the estimate of the minimizing point \hat{x}^i iteratively as

$$\begin{aligned} \hat{x}^{i+1}(x^\#, Z^N, \delta) &= \hat{x}^i(x^\#, Z^N, \delta) - \mu_N^i [H_N^{\delta, i}(\hat{x}^i, Z^N, \delta)]^{-1} W'_N(\hat{x}^i, x^\#, Z^N, \delta) \\ &= \hat{x}^i(x^\#, Z^N, \delta) + d^i(\hat{x}^i, x^\#, Z^N, \delta), \end{aligned} \quad (6.16)$$

where i is the i th iterate, in which d^i is the search direction and $H_N^{\delta, i}$ is the approximate hessian in (6.15).

Prior distribution of parameters

Both $x^\#$ and δ in (6.7) can represent prior knowledge of the parameters. If a gaussian probability distribution can be assigned as a prior probability density function (pdf) to the parameters x with mean $x^\#$ and covariance matrix $\frac{1}{2N\delta}$, the maximum a posteriori estimation is made when the noise is gaussian distributed with zero mean (Ljung, 1999, pp.221). However, since no restrictions are made considering the scaling of the two terms V_N and V_N^δ , they can differ quite substantially in size and can therefore be hard to compare in a fair way. This is solved by introducing a regularization factor δ_x in the regularization matrix δ according to

$$\delta = \delta_x \text{diag}(\delta_i), \quad i = 1, \dots, d, \quad (6.17)$$

where δ_i are called regularization elements. The factor δ_x is then used as a tuning knob to find a good compromise between residual error ε and nominal parameter deviation $\varepsilon_x^\#$. In (6.17) no cross-terms in the covariance matrix are considered. The methodology could however be extended to cover the case of non-zero cross-terms, with slight modifications of the expressions in (6.14), (6.15) and (6.17) by exchanging the diagonal matrix δ for a symmetric positive semi-definite matrix δ .

The diagonal elements δ_i in δ are given by

$$\delta_i = \frac{1}{2N\sigma_i^2}, \quad (6.18)$$

where σ_i is the standard deviation for parameter x_i and it is assumed that there are no cross-terms in the covariance matrix. From hereon the nominal value $x^\#$ and the regularization elements δ_i are referred to as the prior knowledge, and the tuning parameter δ_x is referred to as the regularization parameter.

How to determine the regularization parameter δ_x ?

The best way to determine δ_x would be to find the δ_x that minimizes the size of the true parameter error, $\varepsilon_x^t = x - x^t$. However the true parameter values x^t are only available in simulations, and this approach is therefore not applicable for experimental data. It can however be used for evaluation of simulated data.

A systematic method for finding δ_x that gives a good compromise between the measures V_N and V_N^δ is therefore sought. In order to find an unequivocal δ_x , it is important that V_N and V_N^δ are monotonic. The two measures V_N and V_N^δ are directly related to ε and $\varepsilon_x^\#$ according to

$$RMSE(\varepsilon) = \sqrt{\frac{1}{2} V_N} \quad (6.19a)$$

$$RMSE(L^\delta \varepsilon_x^\#) = \sqrt{\frac{1}{d} V_N^\delta} \quad (6.19b)$$

where $L^\delta = \text{diag}(\delta_i)^{1/2}$ and d is the number of parameters. The two measures in (6.19) are also monotonic whenever V_N and V_N^δ are.

Figure 6.2 shows an example of the dependence between $RMSE(\varepsilon)$ and $RMSE(L^\delta \varepsilon_x^\#)$. For large values of δ_x , the regularized estimates x^δ are pulled towards the nominal values $x^\#$, i.e. a small $RMSE(L^\delta \varepsilon_x^\#)$. The matrix L^δ serves as a weighting function and determines how strong the pulling force is for the individual parameters. The form on which the prior is given is therefore important for the shape of the resulting curve. The notation x^δ is used for the estimate $\hat{x}(\delta)$ from hereon. For small values of δ_x , the pulling force is small and the estimates are no longer suppressed by the prior and therefore free to adjust to the measurement data. This results in an $RMSE(\varepsilon)$ that is approximately the same as the noise level. These two cases are the extremes concerning confidence in the prior knowledge and measurement data respectively.

For moderate δ_x in between the two extremes, there is a sharp transition where the residual error ε falls while the nominal parameter deviation $x^\#$ remains basically constant. Due to that the upper

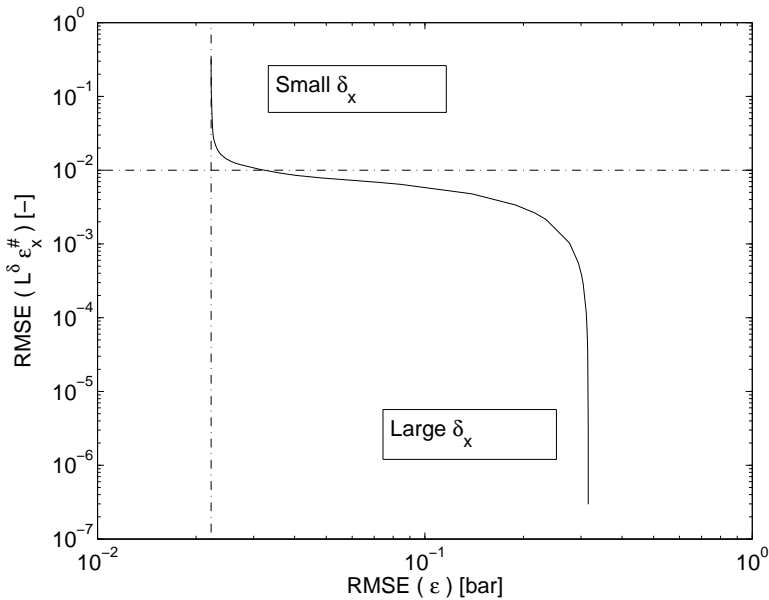


Figure 6.2: Example of a L-curve. The dashed-dotted lines correspond to the noise level and parameter deviation $x^t - x^\#$ used in the simulation.

part of the graph resembles the letter “L”, the curve is called an *L-curve* (Hansen and O’Leary, 1993). The noise level and the parameter deviation $x^\# - x^t$ are known in simulations, and are therefore included in figure 6.2 as dashed lines. The cross-over point of these two lines is close to the corner of the L. It is therefore natural to expect that the corresponding δ_x is a good compromise between data fitting and penalizing the parameter deviation (Engl et al., 1996).

Note that the L-curve is computed in a set of discrete points that can be connected by e.g. a cubic spline. Typically there is a wide range of δ_x :s corresponding to the points on the L-curve near its corner. Therefore, the location of the corner should be found by some numerical optimization routine, and not by visual inspection (Hansen and O’Leary, 1993; Engl et al., 1996), especially if one wants to automate the search procedure.

Routines for determining δ_x

Three optimization routines for determining δ_x are presented here:

1. Millers a priori choice rule for δ_x (Miller, 1970). Consider computing an estimate \hat{x} for which

$$RMSE(\varepsilon(\hat{x}, x^\#, \delta, Z^N)) \leq m_\varepsilon, \quad (6.20a)$$

$$RMSE(L^\delta \varepsilon_x^\#(\hat{x}, x^\#, \delta, Z^N)) \leq m_\delta. \quad (6.20b)$$

Then Miller showed that

$$\delta_x = \frac{m_\delta}{m_\varepsilon} \quad (6.21)$$

yields a regularized estimate x^δ such that $RMSE(\varepsilon(x^\delta, x^\#, \delta, Z^N)) \leq \sqrt{2}m_\varepsilon$ and $RMSE(L^\delta \varepsilon_x^\#(x^\delta, x^\#, \delta, Z^N)) \leq \sqrt{2}m_\delta$. The result is valid for linear systems. Then if m_ε and m_δ are good estimates of $RMSE(\eta)$ and $RMSE(L^\delta \varepsilon_x^\#)$ respectively, the regularization parameter δ_x from (6.21) yields a solution close to the L-curve's corner (Hansen, 1998).

2. Morozovs discrepancy principle (Morozov, 1984). The regularization parameter δ_x is the solution to the problem

$$RMSE(\varepsilon(x, x^\#, \delta, Z^N)) = a_\varepsilon RMSE(\eta), \quad (6.22)$$

where η is the noise level and $a_\varepsilon \geq 1$ is a constant chosen by the user. Typically this routine overestimates δ_x (Hansen, 1994), and therefore gives a solution which is regularized to hard.

3. Maximum curvature of Hansen's L-curve (Hansen and O'Leary, 1993). The curvature τ is defined as

$$\tau(\delta_x) = \frac{\psi_\varepsilon''(\delta_x)\psi_\delta'(\delta_x) - \psi_\varepsilon'(\delta_x)\psi_\delta''(\delta_x)}{(\psi_\varepsilon'(\delta_x)^2 + \psi_\delta'(\delta_x)^2)^{3/2}}, \quad (6.23a)$$

$$\psi_\varepsilon(\delta_x) = \log\|\varepsilon(x, x^\#, \delta, Z^N)\|_2, \quad (6.23b)$$

$$\psi_\delta(\delta_x) = \log\|L^\delta \varepsilon_x^\#(x, x^\#, \delta, Z^N)\|_2. \quad (6.23c)$$

The L-curve is approximated by a 2D spline curve given the set of discrete points for which it is computed, and from which δ_x corresponding to the point of maximum curvature τ is determined.

The first two routines require knowledge of the noise level η , while the third does not. The latter is thus categorized as error-free in Engl et al. (1996).

If the noise level is changed and an approximative value for the new δ_x is sought for routines 1 and 2, the following example gives an approximation if the new noise level is known.

Example 6.4 – Impact of measurement noise on regularization parameter δ_x

The objective is to keep the ratio between the residual loss function V_N and the prior loss function V_N^δ constant. Assume that measurement noise is white and described by $\varepsilon_1(t)$ and that this results in the residual loss function $V_N(\varepsilon_1)$ and the prior (or nominal parameter) loss function $V_N^\delta(\varepsilon_1)$. Now assume a second noise realization such that it can be described by $\varepsilon_2(t) = a\varepsilon_1(t)$, i.e. the first one is multiplied by a factor a . This means that the standard deviation σ is increased by a factor a and yields a residual loss function $V_N(\varepsilon_2)$

$$V_N(\varepsilon_2) = \frac{1}{N} \sum_{i=1}^N (a\varepsilon_1^i)^2 = a^2 V_N(\varepsilon_1). \quad (6.24)$$

Keeping the ratio between $V_N(\varepsilon_2)$ and $V_N^\delta(\varepsilon_2)$ constant results in

$$\frac{V_N(\varepsilon_1)}{V_N^\delta(\varepsilon_1)} = \frac{V_N(\varepsilon_2)}{V_N^\delta(\varepsilon_2)} = \frac{a^2 V_N(\varepsilon_1)}{V_N^\delta(\varepsilon_2)} \Rightarrow V_N^\delta(\varepsilon_2) = a^2 V_N^\delta(\varepsilon_1) \quad (6.25)$$

which is realized by setting the prior factor $\delta_x(\varepsilon_2) = a^2 \delta_x(\varepsilon_1)$. Thus if the standard deviation of the measurement noise is increased by a factor a , the prior factor δ_x should be increased by a^2 as a first approximation. This is natural since the regularization parameter δ_x is related to the variance through (6.17)–(6.18).

Special case: Equal δ_i

In the special case when all elements δ_i are equal, the matrix $L^\delta = \text{diag}(\delta_i)^{1/2}$ is given by the identity matrix times a constant. This assures that $\text{RMSE}(\varepsilon_x^\#)$ is monotonic whenever V_N^δ is, and thus the measure $\text{RMSE}(\varepsilon_x^\#)$ can be used in the L-curve plots instead of $\text{RMSE}(L^\delta \varepsilon_x^\#)$. The advantage is that $\text{RMSE}(\varepsilon_x^\#)$ corresponds directly to the nominal parameter deviation. This will be used in chapters 7 and 8 whenever all δ_i :s are equal.

Algorithms – Method 2

Algorithms for three versions of method 2 are now given. They differ in how they find the regularization parameter δ_x based on the three optimization routines described earlier, and are labeled M2:1, M2:2 and M2:3 respectively. In all cases when the criterion function W_N (6.7) is minimized, the initial values x^{init} are given by the nominal values $x^\#$.

Algorithm 6.3 – Millers a priori choice rule (M2:1)

1. Assign a prior $x_i^\#$ and δ_i to each of the parameters $x \in \mathbf{R}^{d \times 1}$.
The regularization matrix is then formed as $\delta = \delta_x \text{diag}(\delta_i)$.
 2. Compute boundaries m_ε and m_δ in (6.20), that give δ_x from (6.21).
 3. Minimize W_N (6.7) w.r.t. x using δ_x from step 2.
 4. Return the estimate $x^{\delta,*}$.
-

Algorithm 6.4 requires an investigation for finding the search region for δ_x in which the corner is always included. This region is denoted Δ_x , and it only needs to be computed once for each application.

Algorithm 6.4 – Morozovs discrepancy principle (M2:2)

1. Assign a prior $x_i^\#$ and δ_i to each of the parameters $x \in \mathbf{R}^{d \times 1}$.
The regularization matrix is then formed as $\delta = \delta_x \text{diag}(\delta_i)$.
 2. Assign the parameter a_ε (6.22) a numerical value slightly larger than 1.
 3. Compute the RMSE(η) by minimizing the criterion function W_N (6.7) with $\delta_x = 0$.
 4. Minimize the criterion function W_N (6.7) for the discrete points $\delta_x \in \Delta_x$, equally spaced in a logarithmic scale.
 5. Find the δ_x for which (6.22) is fulfilled, by using a cubic spline interpolation.
 6. Minimize W_N (6.7) w.r.t. x using δ_x from step 5.
 7. Return the estimate $x^{\delta,*}$.
-

A quicker version of algorithm 6.4 is to reuse an estimation of the noise level made earlier in step 3. Another alternative to make the algorithm faster is to start with the lowest value of δ_x in step 4 and compute for as long as $RMSE(\varepsilon(\delta_x)) \leq a_\varepsilon RMSE(\eta)$. A third alternative is to use nearest neighbor interpolation in step 5, in which step 6 becomes obsolete. This is an option worth to consider if relatively many discrete points are used in Δ_x . This will be further investigated in chapters 7 and 8.

Algorithm 6.5 also requires an investigation for finding the search region Δ_x for δ_x in which the corner is always included.

Algorithm 6.5 – Hansen’s L-curve (M2:3)

1. Assign a prior $x_i^\#$ and δ_i to each of the parameters $x \in \mathbf{R}^{d \times 1}$. The regularization matrix is then formed as $\delta = \delta_x \text{diag}(\delta_i)$.
2. Minimize the criterion function W_N (6.7) for the discrete points $\delta_x \in \Delta_x$, equally spaced in a logarithmic scale.
3. Find the δ_x for which (6.22) is fulfilled, by using a cubic spline interpolation.
4. Minimize W_N (6.7) w.r.t. x using δ_x from step 3.
5. Return the estimate $x^{\delta,*}$.

An alternative is to use nearest neighbor interpolation in step 3, in which step 4 becomes obsolete. This is an option worth to consider if relatively many discrete points are used in Δ_x . This will be further investigated in chapters 7 and 8.

Note that in step 1 for all versions of method 2, the parameters $x \in \mathbf{R}^{d \times 1}$ could be assigned a Gaussian distributed prior, as $x_i \in N(x_i^\#, \sigma_i)$. The matrix δ is then formed as $\delta = \delta_x \text{diag}(\delta_i)$, where δ_i is given by (6.18). As mentioned earlier, this results in the maximum a posteriori estimate.

6.4.3 How to determine the prior knowledge?

The prior knowledge is used for more reasons than to give the best parameter estimates. It should primarily be used to reflect the insight and knowledge the user has of the system at hand, and to give physically reasonable parameter values.

Nominal parameter values $x^\#$

The nominal prior parameter values $x^\#$ can be determined in at least three alternative ways:

1. By using the parameter initialization methods described in chapter 3 for every parameter x_i .
2. By using expert prior knowledge of what the numerical value of $x^\#$ should be.
3. A combination of alternative 1 and 2.

Depending on the validity of the prior for parameter x_i , it has to be updated at certain events. For the cylinder pressure models described in section 6.2 this can be exemplified by the following; Consider the two parameters: pressure sensor offset Δp and clearance volume V_c . The former is assumed to be constant during one engine cycle according to section 3.1, and therefore has to be updated for every engine cycle. On the other hand, in section 3.2 the latter parameter is assumed to be engine dependent. It therefore only needs to be updated once a different engine is used.

Regularization elements δ_i

The element δ_i in the regularization matrix δ reflects the uncertainty of the nominal parameter value x_i and is related to the standard deviation σ_i of the prior pdf, as pointed out earlier. As for $x^\#$ there are three corresponding alternatives to determine δ_i . If the first alternative is used, the standard deviation of $x_i^\#$ is computed directly from the parameter initializations given in chapter 3. This value does however not reflect how uncertain the model approximation is when computing $x_i^\#$. If the nominal value $x^\#$ is unsure, δ_i should be chosen small to give a large parameter flexibility and a small penalty on the criterion function W_N (6.7). On the other hand when $x_j^\#$ is determined with a high confidence, this should be reflected in large value of δ_j (compared to δ_i). This corresponds to penalizing $|x_j - x_j^\#|$ harder in W_N (6.7), and thereby exercising a strong pulling force on x_j towards $x_j^\#$. The parameter uncertainty is generally different for the individual parameters in the case of cylinder pressure modeling. In this case it is therefore more suitable to base δ_i upon the second alternative, i.e. expert knowledge of the uncertainty.

Also, from (6.17) it can be concluded that it is only the relative intergroup size of δ_i that is relevant, since the regularization parameter δ_x compensates for contingent scalings. It is therefore not vital for the performance of method 2 that the best value in a ε_x^t -sense for δ_i is used, as long as the relative size to the other parameters stands. This also

speaks in favor for the second alternative. It also suggests that other probability density functions can be assigned to the parameters, as long as they are of the same kind.

Note that only the nominal value, and not the uncertainty of $x_i^\#$ that is related to δ_i , is used in method 1. The prior values $x^\#$ and δ are determined for each specific application, and this issue is therefore returned to in chapters 7 and 8.

6.4.4 Summarizing comparison of methods 1 and 2

Both methods use prior knowledge of the parameters in the estimation problem, but they differ in how they use it. Method 1 only uses the nominal value $x^\#$ indirectly when setting the spurious parameters fixed, while method 2 is more flexible and uses both the nominal value $x^\#$ and the parameter uncertainty δ directly in the criterion function to regularize the solution. If the prior knowledge in method 2 is Gaussian distributed, the estimation method yields the maximum a posteriori estimate (Ljung, 1999, pp.221).

RESULTS AND EVALUATION FOR MOTORED CYCLES

Method 1 and method 2 described in section 6.4 will now be evaluated for motored cylinder pressure data. The evaluation covers both simulated and experimental data. As mentioned earlier in chapter 6 this is due to that the true value of the parameters are unknown in the experimental data. The experimental data is collected on a turbo-charged 2.0L SAAB engine, whose engine geometry is given in appendix C.4.

In this and the following chapter, it is worth noting that all numerical calculations have been made for normalized values of the parameters, while the individual parameter values that are given in tables are not normalized if not explicitly stated. The purpose of the normalization is to yield parameters that are in the order of 1, and the normalization is described in appendix C.1.

7.1 Simulation results – motored cycles

First the simulated engine data will be described, followed by a discussion on the parameter prior knowledge used. The focus is then turned to evaluating the performance of method 1, followed by method 2.

7.1.1 Simulated engine data

Cylinder pressure traces were generated by simulating the standard model from section 6.2.1 with representative single-zone parameters, given in appendix C.5. Eight operating points were selected with

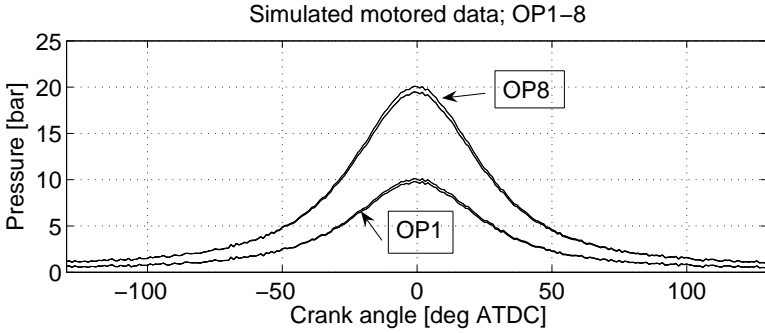


Figure 7.1: Simulated cylinder pressures for the different operating points OP1–8.

engine speeds $N \in \{1500, 3000\}$ rpm, mean charge temperatures at IVC $T_{IVC} \in \{310, 370\}$ K and cylinder pressures at IVC $p_{IVC} \in \{50, 100\}$ kPa, where table C.3 defines the individual operating points. For each operating point a cylinder pressure trace was simulated and ten realizations of Gaussian noise with zero mean and standard deviation 3.8 kPa were added, forming altogether 80 motored cycles. The chosen noise level is the same as the one used in chapter 5, and thus reflects the level seen in experimental data. The data was sampled with a resolution of 1 crank-angle degree (CAD). In figure 7.1, one motored cycle is shown for each operating point. The cylinder pressures corresponding to OP1 and OP8 differ the most, and will therefore be the two extremes in the investigation.

7.1.2 Parameter prior knowledge

The simulations are evaluated using simulated pressure traces with known parameter values and a known model structure. To resemble the experimental situation, both a false and a correct prior knowledge of the nominal parameter values $x^\#$ will be used. For method 1, a preferred ordering of the parameters can be assigned and this will be done later in section 7.1.3. For method 2, the regularization elements δ_i needs to be assigned. In the simulations a gaussian distributed prior $x \in N(x^\#, \sigma)$ is assumed, where δ_i are given by (6.18), i.e. as

$$\delta_i = \frac{1}{2N\sigma_i^2}. \quad (7.1)$$

When (7.1) was stated it was assumed that there are no cross-terms in the covariance matrix.

Two different setups of nominal parameters $x^\#$ will be used, and for each of these setups two cases of regularization elements δ_i will be investigated for method 2.

Two cases (of δ_i)

In the first case, the standard deviation σ_i for each parameter x_i is chosen as $\sigma_i = 0.01 x_i^t$. This choice is made for two reasons; As mentioned earlier the absolute value of δ_i is not interesting in itself, rather it is the relative size of δ_i compared to δ_j that is. This was due to the regularization parameter δ_x . By choosing the same δ_i for all parameters, this allows for a direct measure of the nominal and true parameter deviations, $\varepsilon_x^\#$ and ε_x^t respectively, in the plots of an L-curve. Secondly, since each parameter is assigned the same parameter uncertainty, this results in a parameter guiding of the estimates towards the nominal values but it does not give any joint ordering of the parameters. This case can therefore be seen as the first and simplest approach. It will from hereon also be referred to as $\delta_i = c$, where c is a constant.

In the second case the regularization elements are determined by our prior knowledge of the parameter uncertainty, and it illustrates the application of the methods to an experimental situation. It can be seen as the more advanced case of the two, and typically yields regularization elements that are not the same. This case is referred to as $\delta_i \neq c$. For this particular application the standard deviation σ_i for each parameter are given in table 7.1. These values are not verified experimentally, they are merely chosen since they are physically reasonable. To illustrate the principle of how the uncertainties are set, consider that the nominal value for the crevice volume V_{cr} is 1 cm^3 which is approximately 1.5 percent of the clearance volume V_c . According to section 3.4 a reasonable region for V_{cr} is $[1, 2] \% V_c$. Now if the standard deviation for V_{cr} is chosen as $\sigma_i = 0.15 \text{ cm}^3$, this corresponds to that 95 percent of the values belongs to that region. The two parameters Δp and $\Delta \theta$ are set to their expected uncertainty, and results in relative mean errors (RME) that are 50 %.

Two setups (of $x^\#$)

The first setup uses an equal relative parameter deviation. These nominal parameter deviations from the true parameter values, i.e. $\varepsilon_x^{\#-t} = x^\# - x^t$, are chosen to be $\{0, 1, 2.5, 5\} \% x^t$. This will from hereon be referred to as the false prior (FP) at the specified level. This setup is chosen in order to investigate what influence the prior knowledge has on the individual parameters.

The second setup is based upon a relative parameter deviation directly related to the relative uncertainty for each parameter. This is

x_i	V_c	C_1	T_{IVC}	p_{IVC}	γ_{300}	b
Unit	[cm^3]	[-]	[K]	[kPa]	[-]	[K^{-1}]
σ_i	0.5	0.114	10	2.5	0.005	$1 \cdot 10^{-5}$
RME [%]	0.9	5.0	2.7	5.0	0.4	10.0
x_i	T_w	V_{cr}	Δp	$\Delta\theta$	K_p	
Unit	[K]	[cm^3]	[kPa]	[deg]	[-]	
σ_i	10	0.15	2.5	0.05	0.005	
RME [%]	2.5	15.0	50.0	50.0	0.5	

Table 7.1: Assigned standard deviation σ_i of the model parameters x_i used for second case of δ_i :s. The relative mean error (RME) corresponding to one standard deviation from the true value (for OP1) is also given.

implemented as a nominal parameter deviation from the true values of one standard deviation of the prior knowledge, i.e. $x_i^\# = (1 + \sigma_i)x^t$, where the individual standard deviations σ_i are given in table 7.1.

7.1.3 Method 1– Results and evaluation

First method 1 is evaluated for setup 1 using no preferred ordering of the parameters, i.e. the algorithms rely fully upon the measured data and include no prior knowledge of the parameters. Secondly, a preferred ordering is introduced and it is investigated how this effects the estimation problem.

The evaluation starts by determining in which order the parameters are set fixed. Then the minimizing number of efficient parameters using Akaike's FPE is given, followed by a recommendation of how many parameters to estimate. After that an investigation of the estimation accuracy is performed, followed by a residual analysis.

Evaluation without a preferred ordering – setup 1

First of all, the order in which the parameters are set fixed for setup 1 when using algorithm 6.2 without a preferred ordering is investigated. This corresponds to keeping track of the spurious parameters x_{new}^{sp} in step 3. In this case all parameters need to be included, and therefore the maximum and minimum number of efficient parameters are given by $d_{max}^\# = d$ and $d_{min}^\# = 1$, where $d = 11$ is the number of parameters.

The resulting parameter order *without* a preferred ordering is given by

$$\underline{b} \prec p_{IVC} \prec \underline{V}_{cr} \prec T_{IVC} \prec \underline{\Delta\theta} \prec \Delta p \prec C_1 \prec T_w \prec \underline{V}_c \prec K_p \prec \underline{\gamma}_{300}, \quad (7.2)$$

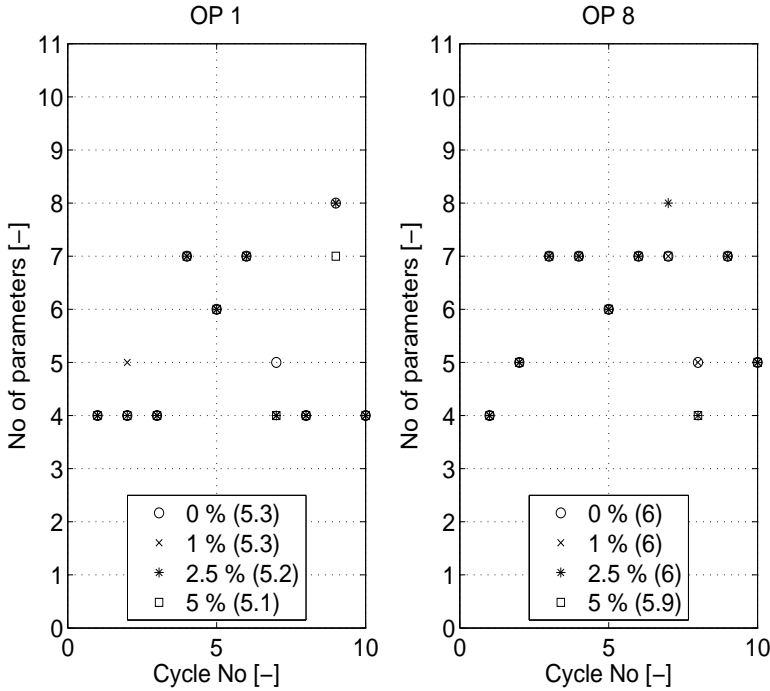


Figure 7.2: Minimizing number of parameters d^* for method 1, when using no preferred ordering.

which reflects a typical average case. Here $b \prec p_{IVC}$ means that b is set fixed prior to p_{IVC} . The underlined parameters are invariant in position to the investigated noise realizations, false prior levels and different operating conditions. The other parameters however differ in a few number of cases and out of the three variations, mostly from different noise realizations. The differences in order appear almost without exception as permutations of two groups, namely $[C_1, T_{IVC}, T_w]$ and $[K_p, p_{IVC}]$. This means that p_{IVC} is sometimes replaced by K_p and that T_{IVC} is at some instances replaced by either C_1 or T_w . It is also worth to mention that γ_{300} is the most efficient parameter of them all, according to (7.2).

The minimizing number of parameters using algorithm 6.2 are given in figure 7.2 for OP1 and OP8, which are the two extremes in the simulation-based investigation. Ten different noise realizations corresponding to ten engine cycles have been used, as well as four different cases of false prior. The corresponding results for all eight operating points are given in table 7.2, but now as a mean value for the ten cycles.

FP [%]	Operating point (OP)							
	1	2	3	4	5	6	7	8
0	5.3	5.4	6.1	6.1	5.5	5.3	6.1	6.0
1	5.3	4.9	6.1	6.1	5.2	4.9	6.1	6.0
2.5	5.2	4.9	6.1	6.1	5.2	4.9	6.1	6.0
5	5.1	5.0	6.2	6.0	5.1	5.2	6.1	5.9
$d^* \in$	[4, 8]	[4, 8]	[4, 8]	[4, 8]	[4, 8]	[4, 8]	[4, 7]	[4, 8]

Table 7.2: Minimizing number of parameters d^* for method 1, without a preferred ordering. Four false prior levels are used and the range of d^* is given for each operating point.

Table 7.2 shows that the average numbers of $d^\#$ are between 4.9 and 6.1, but figure 7.2 and table 7.2 indicate that $d^\# \in [4, 8]$. The variation in $d^\#$ depending on the level of false prior FP is comparatively small, but the variation is larger depending on the operating point. This makes it hard to determine how many efficient parameters in (7.2) to use.

Estimation accuracy

Tables 7.3 and 7.4 show the parameter estimates for the entire range of $d^\#$, i.e. from 11 to 1 parameter, for one engine cycle. For this specific cycle (OP1, cycle1), the Akaike FPE is minimized by four parameters, i.e. $d^* = 4$. The false prior level used is 0 % in table 7.3 and 5 % in table 7.4 respectively. The parameters are set fixed using algorithm 6.1, i.e. in accordance with (7.2), and this corresponds to the emphasized values in two tables. For instance when p_{IVC} is set fixed at 50.0 kPa for $d^\# = 9$, this is indicated in the tables by emphasizing the nominal value. The parameter values for p_{IVC} are then fixed for $d^\# \in [1, 8]$ as well, but to increase the readability these values are left out.

Table 7.4 shows that the parameter estimates are clearly biased when a false prior is present. As expected the individual parameter estimates depend upon the number of efficient parameters $d^\#$, as well as the false prior level. The estimates of course also depend upon what parameters that are classified as efficient. In order to have a $\bar{\varepsilon}_x^t \leq 1$ %, a maximum of three parameters in combination with a false prior level of 0 % is required, see table 7.3. For $FP = 5$ % (table 7.4), the same limit on $d^\#$ is found if the true parameter deviation should be less or equal to the false prior level, i.e. $\bar{\varepsilon}_x^t \leq 5$ %. This means that for $d^\# \geq 4$, the parameter estimates deviate more from x^t than $x^\#$ does.

However, by considering the individual estimates it is notable that the C_1 -estimate has the largest normalized bias in general. Until C_1 is fixed the other parameters, especially K_p , T_{IVC} , γ_{300} and to some

$d^\#$	V_c [cm^3]	C_1 [-]	T_{IVC} [K]	p_{IVC} [kPa]	γ_{300} [-]	b [K^{-1}]	T_w [K]	V_{cr} [cm^3]	Δp [kPa]	$\Delta\theta$ [deg]	K_p [-]	$\bar{\varepsilon}_x^t$ [%]	$\bar{\varepsilon}_x^\#$ [%]
11	57.1	1.91	402	51.7	1.38	-0.00012	420	1	3.2	0.11	0.99	8.7	8.7
10	57.4	1.88	404	51.8	1.38	-0.0001	418	1	3.0	0.10	0.99	6.6	6.6
9	57.4	1.87	404	50.0	1.38		418	1	3.0	0.10	1.03	6.7	6.7
8	57.4	1.87	404		1.38		418	1	3.0	0.10	1.03	6.7	6.7
7	57.5	1.96	370		1.37		381		3.0	0.10	1.03	5.1	5.1
6	57.5	1.96			1.37		382		3.0	0.10	1.03	5.0	5.0
5	58.6	1.70			1.40		378		5.0		1.00	7.8	7.8
4	58.5	2.28			1.40		446				0.99	3.5	3.5
3	58.1				1.39		400				1.01	0.5	0.5
2	58.8				1.40						1.00	0.1	0.1
1					1.40						1.00	0.0	0.0
$x^\#$	58.8	2.28	370	50.0	1.40	-0.0001	400	1	5.0	0.10	1.00	5.0	0.0
x^t	58.8	2.28	370	50.0	1.40	-0.0001	400	1	5.0	0.10	1.00	0.0	5.0

Table 7.3: Parameter estimates at OP1 for $d^\# \in [1, 11]$ parameters when using no preferred ordering and a false prior level of 0%. The true and nominal parameter deviations $\bar{\varepsilon}_x^t$ and $\bar{\varepsilon}_x^\#$ are given as RMSE:s of their relative values, i.e. $\bar{\varepsilon}_x^t = RMSE(\varepsilon_x^t)$ and $\bar{\varepsilon}_x^\# = RMSE(\varepsilon_x^\#)$.

$d^\#$	V_c [cm^3]	C_1 [-]	T_{IVC} [K]	p_{IVC} [kPa]	γ_{300} [-]	b [K^{-1}]	T_w [K]	V_{cr} [cm^3]	Δp [kPa]	$\Delta\theta$ [deg]	K_p [-]	$\bar{\varepsilon}_x^t$ [%]	$\bar{\varepsilon}_x^\#$ [%]
11	57.1	1.91	402	51.7	1.38	-0.00012	420	1	3.2	0.11	0.99	8.7	9.1
10	57.3	1.89	405	51.8	1.38	-0.000105	420	1	3.1	0.10	0.99	6.8	8.1
9	57.3	1.89	406	52.5	1.38		421	1	3.1	0.10	0.98	6.9	8.2
8	57.3	1.89	406		1.38		421	1.1	3.1	0.10	0.98	7.0	8.1
7	57.4	1.96	389		1.38		405		3.1	0.10	0.98	5.7	7.3
6	57.4	1.90			1.38		400		3.1	0.11	0.98	6.3	7.9
5	58.5	1.63			1.40		394		5.3		0.95	9.3	11.0
4	58.5	1.78			1.40		420				0.95	7.6	9.0
3	57.8	2.39			1.39						0.96	3.9	3.8
2	61.7				1.45						0.93	4.6	3.5
1					1.37						1.05	4.3	2.0
$x^\#$	61.7	2.39	389	52.5	1.47	-0.000105	420	1.1	5.3	0.11	1.05	5.0	0.0
x^t	58.8	2.28	370	50.0	1.40	-0.0001	400	1	5.0	0.10	1.00	0.0	5.0

Table 7.4: Parameter estimates at OP1 for $d^\# \in [1, 11]$ parameters when using no preferred ordering and a false prior level of 5%. The true and nominal parameter deviations $\bar{\varepsilon}_x^t$ and $\bar{\varepsilon}_x^\#$ are given as RMSE:s of their relative values, i.e. $\bar{\varepsilon}_x^t = RMSE(\varepsilon_x^t)$ and $\bar{\varepsilon}_x^\# = RMSE(\varepsilon_x^\#)$.

extent T_w , compensate for the bad C_1 -estimates. This results in biased estimates for these parameters as well. When C_1 is fixed, the pressure gain K_p still has a considerable bias, especially in the presence of a large false prior. It is however believed that K_p is known more accurately a priori through calibration, compared to the other parameters. Therefore if a preferred parameter ordering is to be used, it is recommended that K_p and C_1 are set fixed at an early stage.

As mentioned earlier, the bias in the individual parameters depend upon $d^\#$ and FP . This is exemplified by the two parameters V_c and γ_{300} , which have their smallest biases for five parameters for both cases of the false prior level, according to tables 7.3 and 7.4. These two parameters have already been shown to be important in the sensitivity analysis in table 3.2. This illustrates that if $\bar{\varepsilon}_x^t$ or individual parameters are monitored to find the best $d^\#$, this can result in different numbers of recommended parameters, depending on the specific application. For the specific application considered in chapter 5, where the focus was on estimating V_c , it is appropriate to settle for five efficient parameters in method 4.

To summarize, method 1 does not yield a unequivocal number of efficient parameters, as it fluctuates in between four and eight. Using a mean value of $d^\#$ is not optimal either since it does not correspond to the best parameter estimates, especially in the presence of a false prior. This is however not unexpected, since the minimization of V_N (6.3) is only based upon the residuals, and is therefore not influenced directly by the parameter estimates.

Residual analysis

In figure 7.3 the residuals for two cases of false prior offset at OP1 are shown. The upper plots show the residual corresponding to minimization of the Akaike criterion, in these cases $d^* = 4$. The middle plots display the difference between the modeled pressure for 4 and 1 parameter, while the lower plots show the difference for 4 and 11 parameters.

The data is well described by both 11 pars and 4 pars, for both 0 and 5 % false prior offset. However for less than four parameters the residual becomes larger, reflecting that too few parameters are used to describe the data. This effect is more pronounced for $FP = 5\%$, as the difference between the modeled pressure for $d^\# = 4$ and $d^\# = 1$ becomes larger.

The parameter values for $d^\# = 4$ and $d^\# = 11$ are however not the same, see table 7.4, and this reflects that it is not sufficient to have a small residual error for an accurate parameter estimate.

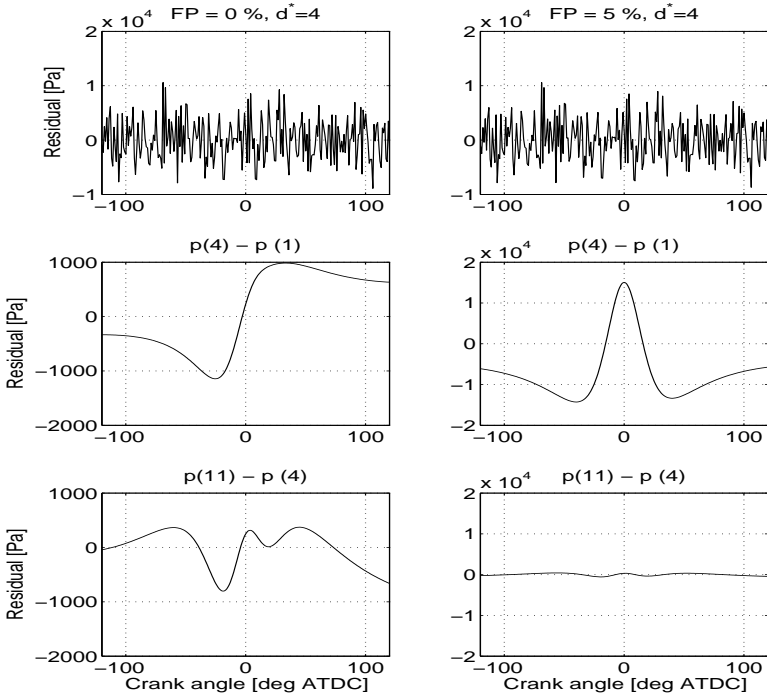


Figure 7.3: *Upper*: The residual for four parameters when the false prior is 0 and 5 %. *Middle*: Difference between the cylinder pressure for four parameters and one parameter. *Lower*: Difference between the cylinder pressure for eleven and four parameters. The scales are different for 0 and 5 %.

Evaluation with a preferred ordering – setup 1

To include parameter prior knowledge and to gain a more unequivocal order in which the parameters are set spurious, the aforementioned permutations of the parameters are used in our case when a preferred ordering is used. The preferred ordering is given by the following ordering groups: $B_1 = [b, T_w, C_1, T_{IVC}]$, $B_2 = [K_p, p_{IVC}, \Delta\theta, \Delta p]$, $B_3 = [V_{cr}, V_c]$ and $B_4 = [\gamma_{300}]$. The order of the parameters in each group B_i is set according to what is believed to be known a priori of the parameters. For instance, for group B_1 the slope coefficient b for γ , is well known from the chemical equilibrium program used in chapter 4 and is therefore set first in the group. The order given here should by no means be interpreted as the best one, rather as a fully-qualified suggestion.

This results in the following parameter order *with* a preferred or-

dering used

$$\underline{b} \prec K_p \prec \underline{V}_{cr} \prec T_{IVC} \prec \underline{\Delta\theta} \prec \Delta p \prec T_w \prec C_1 \prec \underline{V}_c \prec p_{IVC} \prec \underline{\gamma_{300}}. \quad (7.3)$$

The difference in orders between (7.2) and (7.3) occurs for two locations; Firstly for K_p and p_{IVC} , and secondly for C_1 and T_w . The permutations however still exist, but are reduced in their number of occurrences and would extinguish if the ad-hoc decision rules corresponding to step 4 and step 6 in algorithm 6.1 were set to 1 and 0 respectively. The parameter T_{IVC} is set fixed prior to T_w and C_1 although its relative order in B_1 , which also is an effect of the ad-hoc decision rules in algorithm 6.1.

The minimizing number of parameters d^* at OP1 and OP8 are given in figure 7.4, and the mean value of d^* is given in table 7.5 for all operating points and false prior levels. The individual parameter estimates for one engine cycle are given in tables 7.6 and 7.7 for FP = 0 % and 5 % respectively.

Compared to the case with no preferred ordering, the spread of d^* is smaller, especially for OP8 as shown in figure 7.4. This is also reflected in table 7.5, where the mean values are more focused. However, as tables 7.6 and 7.7 both indicate, the estimates are not significantly improved compared to tables 7.3 and 7.4.

Due to the unsuccessful results of method 1 for setup 1, the evaluation for setup 2 is left out.

Summary of method 1

To summarize, using method 1 to estimate the parameters in the presence of a false prior has not been successful. Minimizing the Akaike FPE criterion gives a recommended number of parameters between 4 and 8, but this number fluctuates with both operating point and noise realization. If we instead just consider the true parameter deviation, a maximum of three parameters can be used in order to yield $\bar{\varepsilon}_x^t \leq 1\%$ in the case of no false prior. In the case of a false prior it gets even worse. Method 1 is therefore in itself not recommended to use for estimation, and is therefore not investigated further for the simulation part of the chapter.

It can however be used for a specific application, like compression ratio estimation in chapter 5. In this case only the V_c -estimate is monitored when deciding upon the efficient number of parameters to use, and this results in that five parameters are used.

Method 1 has also given valuable insight in which parameters that are most efficient. For instance it has been shown that γ_{300} is the most efficient parameter, given the structure of the standard model in section 3.8.

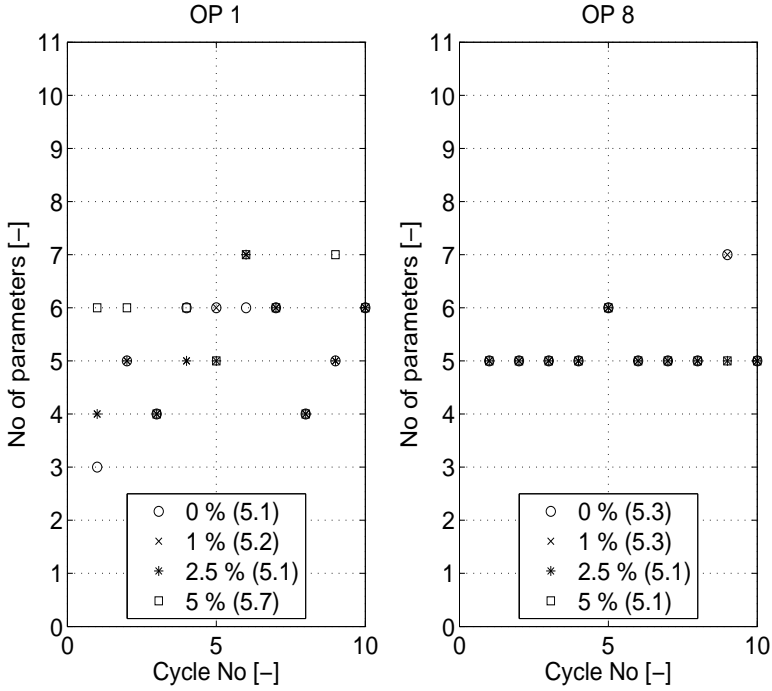


Figure 7.4: Minimizing number of parameters d^* for method 1, when using a preferred ordering.

FP [%]	Operating point (OP)							
	1	2	3	4	5	6	7	8
0	5.1	5.6	5.5	5.3	5.5	5.6	5.3	5.3
1	5.2	5.6	5.3	5.3	5.5	5.5	5.3	5.3
2.5	5.1	5.6	5.3	5.3	5.5	5.5	5.1	5.1
5	5.7	5.5	5.1	5.1	5.5	5.5	5.1	5.1
$d^* \in$	[3, 7]	[4, 7]	[5, 8]	[5, 7]	[4, 6]	[4, 7]	[5, 7]	[5, 7]

Table 7.5: Minimizing number of parameters d^* for method 1, when using a preferred ordering. Four false prior levels are used and the range of d^* is given for each operating point.

$d^\#$	V_c [cm^3]	C_1 [-]	T_{IVC} [K]	p_{IVC} [kPa]	γ_{300} [-]	b [K^{-1}]	T_w [K]	V_{cr} [cm^3]	Δp [kPa]	$\Delta\theta$ [deg]	K_p [-]	$\bar{\varepsilon}_x^t$ [%]	$\bar{\varepsilon}_x^\#$ [%]
11	57.1	1.91	402	51.7	1.38	-0.00012	420	1	3.2	0.11	0.99	8.7	8.7
10	57.4	1.88	404	51.8	1.38	-0.0001	418	1	3.0	0.10	0.99	6.6	6.6
9	57.4	1.88	404	51.5	1.38		418	1	3.0	0.10	1.00	6.6	6.6
8	57.4	1.88	404	51.5	1.38		418	1	3.0	0.10		6.6	6.6
7	57.5	2.28	352	51.6	1.37		379		2.9	0.08		3.4	3.4
6	57.5		368	51.6	1.37		400		2.9	0.08		2.6	2.6
5	58.6		349	50.0	1.39				4.7	0.07		1.9	1.9
4	58.6		340		1.39				4.5	0.10		2.5	2.5
3	58.4		346		1.39				5.0			2.0	2.0
2	58.6		370		1.40							0.1	0.1
1	58.8				1.40							0.0	0.0
$x^\#$	58.8	2.28	370	50.0	1.40	-0.0001	400	1	5.0	0.10	1.00	5.0	0.0
x^t	58.8	2.28	370	50.0	1.40	-0.0001	400	1	5.0	0.10	1.00	0.0	5.0

Table 7.6: Parameter estimates at OPI for $d^\# \in [1, 11]$ parameters when using a preferred ordering and a false prior level of 0%. The true and nominal parameter deviations $\bar{\varepsilon}_x^t$ and $\bar{\varepsilon}_x^\#$ are given as RMSE:s of their relative values, i.e. $\bar{\varepsilon}_x^t = RMSE(\varepsilon_x^t)$ and $\bar{\varepsilon}_x^\# = RMSE(\varepsilon_x^\#)$.

$d^\#$	V_c [cm^3]	C_1 [-]	T_{IVC} [K]	p_{IVC} [kPa]	γ_{300} [-]	b [K^{-1}]	T_w [K]	V_{cr} [cm^3]	Δp [kPa]	$\Delta\theta$ [deg]	K_p [-]	$\bar{\varepsilon}_x^t$ [%]	$\bar{\varepsilon}_x^\#$ [%]
11	57.1	1.91	402	51.7	1.38	-0.00012	420	1	3.2	0.11	0.99	8.7	9.1
10	57.3	1.89	405	51.8	1.38	-0.000105	420	1	3.1	0.10	0.99	6.8	8.1
9	57.3	1.86	405	49.0	1.38		420	1	3.1	0.10	1.05	7.1	8.5
8	57.3	1.86	405	49.0	1.38		420	1.1	3.1	0.10		7.3	8.3
7	57.5	2.39	334	49.2	1.37		364		2.8	0.08		5.6	7.6
6	57.3		376	49.1	1.37		420		2.9	0.07		4.2	4.6
5	54.9		420	52.5	1.33		420		-1.2	0.10		8.7	8.4
4	54.9		420		1.33				-1.2	0.11		8.7	8.4
3	52.6		565		1.33				5.3			16.7	15.4
2	51.7		389		1.28							6.0	6.5
1	61.7				1.37							4.3	2.0
$x^\#$	61.7	2.39	389	52.5	1.47	-0.000105	420	1.1	5.3	0.11	1.05	5.0	0.0
x^t	58.8	2.28	370	50.0	1.40	-0.0001	400	1	5.0	0.10	1.00	0.0	5.0

Table 7.7: Parameter estimates at OPI for $d^\# \in [1, 11]$ parameters when using a preferred ordering and a false prior level of 5%. The true and nominal parameter deviations $\bar{\varepsilon}_x^t$ and $\bar{\varepsilon}_x^\#$ are given as RMSE:s of their relative values, i.e. $\bar{\varepsilon}_x^t = RMSE(\varepsilon_x^t)$ and $\bar{\varepsilon}_x^\# = RMSE(\varepsilon_x^\#)$.

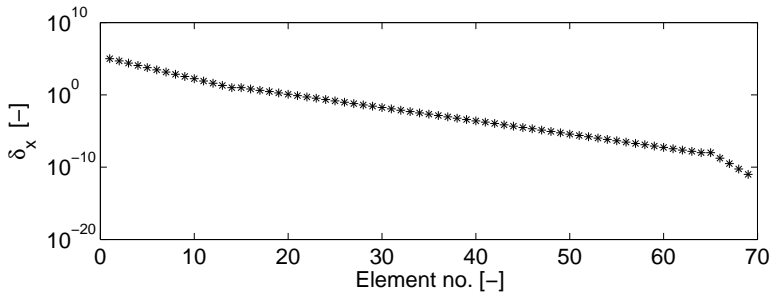


Figure 7.5: Values of the regularization parameter δ_x used in the investigations.

7.1.4 Method 2– Results and evaluation

First some important implementation details are given. Then the three versions of method 2 are evaluated using the two setups described in section 7.1.2.

Implementation details

First the interesting search region for the regularization parameter δ_x is discussed, followed by a motivation for the implementation choices that can be made for each specific version of method 2.

The search region Δ_x for the regularization parameter δ_x is chosen as $\delta_x \in [10^{-11}, 10^5]$, which is found by testing to assure that the L-shape corresponding to figure 6.2 occurs for all examined cases. The region is then divided into three intervals, where δ_x is equally spaced in a logarithmic scale for each interval. The middle interval is where the corner of the L-curve is expected to appear, and this interval is therefore more densely sampled. The limits of the intervals are 10^5 , 10^1 , 10^{-8} and 10^{-11} , and the number of samples are 14, 50 and 5 respectively. The regularization parameter is plotted in figure 7.5. These numerical values are all based upon that the residual ε is computed in bars, and should therefore be altered if a different unit is used.

Millers a priori choice rule, see algorithm 6.3, will from hereon be referred to as M2:1. It requires that the constants m_ε and m_δ from (6.20) are set. The drive for setting these values is twofold; First of all the regularization parameter δ_x from (6.21) must be assured to be on the horizontal plateau of the L-curve (see figure 6.2), preferably as close to the leftmost corner as possible. Secondly, the same equations for m_ε and m_δ should be used for all operating points and setups. The constant m_ε is therefore chosen as $m_\varepsilon = 1.01RMSE(\eta)$, and corre-

sponds to a data fitting which is 1 % above the estimated noise level. The other constant is chosen as a nominal parameter deviation of 1 %, which is then weighted with the uncertainty matrix L^δ . This results in $m_\delta = RMSE(0.01 L^\delta)$, and assures that both requirements are fulfilled for all the investigated cases.

The second version M2:2 is called Morozovs discrepancy principle (algorithm 6.4), where the constant a_ε needs to assigned. Due to the same reasons as for M2:1, it is chosen as

$$\ln(a_\varepsilon) = 0.05 \ln(RMSE(\varepsilon(x^\#))) + 0.95 \ln(RMSE(\eta)), \quad (7.4)$$

where $RMSE(\varepsilon(x^\#))$ is the RMSE of the residual for the nominal parameter values $x^\#$. Including $RMSE(\varepsilon(x^\#))$, which corresponds to $\delta_x \rightarrow \infty$, assures the flexibility to different false prior levels.

Algorithm 6.5 is the third version and is named Hansen's L-curve or M2:3. It uses a 2D cubic spline function of order four (Hansen, 1994) to find the position of maximum curvature. Apart from that, no choices are required.

An example of an L-curve is given in figure 7.6 for one engine cycle at OP1 and FP = 5 %. It also shows the true parameter deviation $\bar{\varepsilon}_x^t$ and the false prior level, as well as the results for the three versions of method 2 and the optimal choice of δ_x . The optimal choice of δ_x is determined as the one minimizing $\bar{\varepsilon}_x^t = RMSE(\varepsilon_x^t)$, for the δ_x :s used in the computation. It is hereon referred to as δ_x^* .

Evaluation for setup 1

Method 2 is now evaluated for setup 1, where the nominal values are given by $x^\# = (1 + \text{FP})x^t$ for $\text{FP} \in \{0, 1, 2.5, 5\}$ % and the assigned standard deviation $\sigma = 0.01x^t$ is equal for all parameters, which yields equal regularization elements δ_i , i.e. case 1 of δ_i ($\delta_i = c$). In section 6.4.2 it was shown that in the special case of equal δ_i :s, $\bar{\varepsilon}_x^\# = RMSE(\varepsilon_x^\#)$ could be used in the L-curve plots.

Figure 7.6 shows that as δ_x is decreased, $\bar{\varepsilon}_x^t$ becomes smaller until it reaches its optimal value. This means that the estimate is a compromise between the data and the prior knowledge, and it lies in between the true value and the nominal (false) value, which is good. The figure also illustrates that all three versions of method 2 find positions close to the corner of the "L", at least visually.

Evaluation for OP1 and OP8: The focus will now be on evaluating the performance of method 2 for the two extreme operating points OP1 and OP8. Figure 7.7 displays the optimal δ_x^* at ten consecutive cycles, for which only the noise realization differs. The false prior level is indicated by the figure legend, and the corresponding mean value for δ_x^* are given within the parentheses. The values for FP = 0 % are left out since they all correspond to the highest value of δ_x .

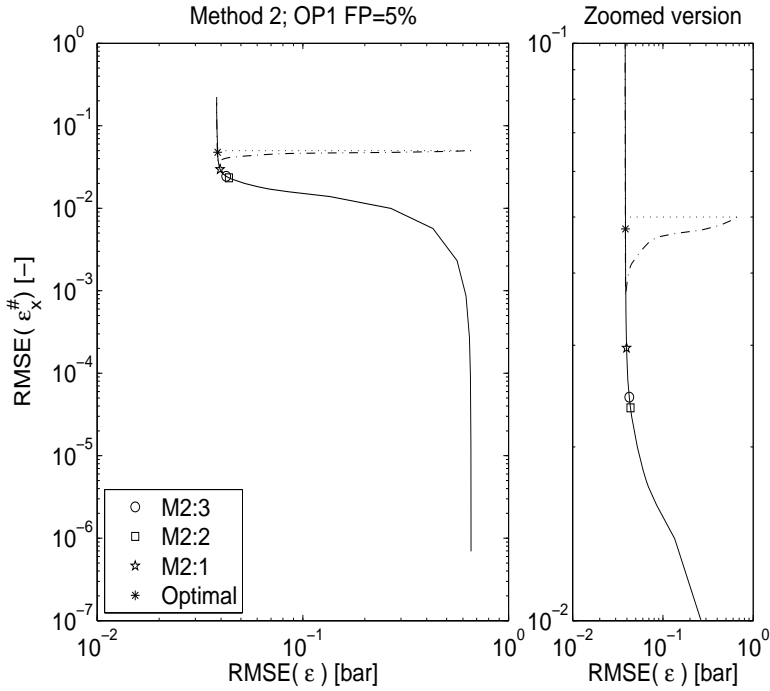


Figure 7.6: L-curve (solid line) for one engine cycle at OP1 with FP=5 % (dotted line) for setup 1. The results for the three versions of method 2 and the optimal choice of regularization parameter are indicated by the legend. The mean true parameter deviation $\bar{\varepsilon}_x^t$ (dash-dotted line) is also given.

The figure shows that there is a difference in optimal δ_x^* depending both on the false prior level and the operating point. There is also a smaller difference depending on the cycle number, which is most pronounced for OP1 at FP = 5 %. A general trend for δ_x^* at a given operating point, is that δ_x^* decreases with FP. This is expected since a lower δ_x is required when $\bar{\varepsilon}_x^\#$ is larger, for the two terms V_N and $\delta_x V_N^\delta$ in W_N (6.7) to become well balanced. It does however not say anything about the estimation accuracy.

The estimation accuracy is investigated in figure 7.8, where the true parameter deviations corresponding to the optimal δ_x :s in figure 7.7 are given. Again, the false prior level is indicated by the figure legend and the corresponding mean value for $\bar{\varepsilon}_x^t$ are given in percent within the parentheses.

Figure 7.8 illustrates that the resulting $\bar{\varepsilon}_x^t$ is less than the specified

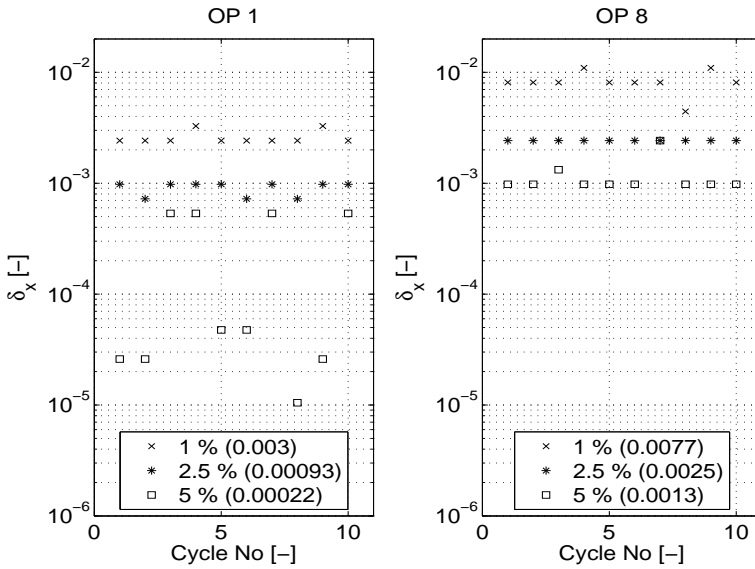


Figure 7.7: Value of optimal regularization parameter δ_x^* in method 2 for ten cycles when minimizing ε_x^t for setup 1.

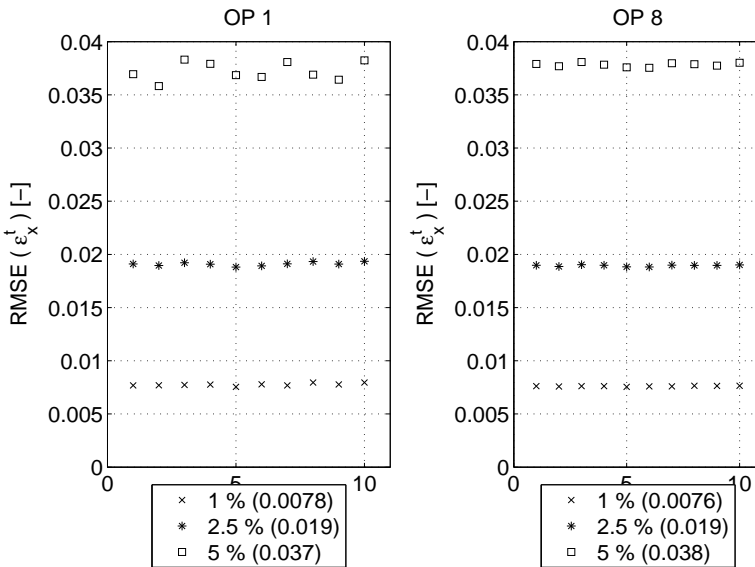


Figure 7.8: Mean true parameter deviation $\bar{\varepsilon}_x^t = RMSE(\varepsilon_x^t)$ corresponding to figure 7.7 for setup 1.

OP	False prior (FP) [%]			
	0	1	2.5	5
1	$1 \cdot 10^5$	0.0030	0.00093	0.00022
2	$1 \cdot 10^5$	0.0024	0.00072	$2.6 \cdot 10^{-5}$
3	$1 \cdot 10^5$	0.0011	0.0044	0.0024
4	$1 \cdot 10^5$	0.0011	0.0024	0.00098
5	$1 \cdot 10^5$	0.0024	0.00098	$1.0 \cdot 10^{-5}$
6	$1 \cdot 10^5$	0.0024	0.00072	0.00022
7	$1 \cdot 10^5$	0.0011	0.0044	0.0024
8	$1 \cdot 10^5$	0.0077	0.0025	0.0013

Table 7.8: Value of optimal regularization parameter δ_x^* , for operating points OP1 to OP8 for setup 1. For FP = 0 %, δ_x^* is the highest value used in the computation.

FP [%]	Operating point (OP)							
	1	2	3	4	5	6	7	8
0	10^{-7}	10^{-7}	10^{-7}	10^{-7}	10^{-7}	10^{-7}	10^{-7}	10^{-7}
1	0.78	0.76	0.77	0.76	0.77	0.76	0.77	0.76
2.5	1.9	1.9	1.9	1.9	1.9	1.9	1.9	1.9
5	3.7	3.7	3.8	3.8	3.8	3.8	3.8	3.8

Table 7.9: Mean true parameter deviation $\bar{\varepsilon}_x^t$ [%] corresponding to optimal δ_x^* in table 7.8, for setup 1 and operating points OP1 to OP8.

false prior level FP. This renders an estimate in between the true and nominal value, i.e. a compromise between data and prior knowledge, although the estimate is more biased towards the nominal value. The figure also shows that for a given FP, the true parameter deviation $\bar{\varepsilon}_x^t$ is fairly constant from cycle-to-cycle. In the worst case (OP1, FP = 5 %), the difference between the estimates are within 0.2 %. This suggests that it is not vital to find exactly the optimal δ_x^* , to get good estimates.

Evaluation for all OP:s: The focus is now turned to evaluating method 2 for all operating points. The optimal δ_x^* is given in table 7.8 for all operating points and false prior levels used in setup 1. The corresponding true parameter deviations $\bar{\varepsilon}_x^t$ are summarized in table 7.9. The numerical values in tables 7.8 and 7.9 are given as mean values for ten cycles.

Table 7.8 shows that the optimal δ_x^* differs for the FP level and operating point used, and the effect is most pronounced for changes in the FP level. This is in accordance with what was pointed out earlier. Table 7.9 shows that the true parameter deviation $\bar{\varepsilon}_x^t$ is less than the false prior level used for FP > 0 %. The table also illustrates that even

OP	δ_x^*	δ_x (M2:1)	δ_x (M2:2)	δ_x (M2:3)	$mv(\delta_x^*)$
1	3.7	3.8	4.1	4.0	3.9
2	3.7	3.8	4.1	4.0	3.9
3	3.8	3.9	3.9	3.9	3.8
4	3.8	3.8	3.9	3.9	3.8
5	3.8	3.8	4.1	4.0	3.9
6	3.8	3.8	4.1	4.0	3.9
7	3.8	3.9	3.9	3.9	3.8
8	3.8	3.9	3.9	3.8	3.8
Max Diff	0	0.092	0.35	0.31	0.21
Mean Diff	0	0.040	0.19	0.15	0.094
Time [s]	2579	32	1333	2579	57

Table 7.10: True parameter deviation $\bar{\varepsilon}_x^t$ for the optimal δ_x^* in table 7.8, the three versions of method 2 and as mean value for the optimal δ_x^* corresponding to table 7.8. The numerical values are given in percent and are evaluated for $FP = 5\%$ for setup 1. The mean computational time for completing the estimation for one engine cycle is also given.

though the optimal δ_x^* varies depending on the operating point at a given FP level, this has almost no effect on the estimation accuracy. It therefore seems probable that the estimation accuracy is relatively insensitive to variations in δ_x .

This is further investigated by computing the mean value of the optimal δ_x^* in table 7.8, discarding $FP = 0\%$. This value is from hereon denoted $mv(\delta_x^*)$, and is used together with the three versions of method 2 to compute the true parameter deviation in table 7.10. The $\bar{\varepsilon}_x^t$ -values in table 7.10 are computed as a mean value of ten cycles for all operating points at $FP = 5\%$. The maximum and mean difference are computed relative to δ_x^* . All of these values are given in percent. The mean computational time is also given, where the following assumptions have been made; For δ_x^* and algorithm M2:3 all δ_x in the search region Δ_x are used, and are therefore included in the computational time. Algorithm M2:2 starts by estimating the noise level η , and then increases the $\delta_x \in \Delta_x$ until the criterion (6.22) is fulfilled, see steps 4 and 5 in algorithm 6.4. Thus the computational time for this algorithm can differ quite extensively from cycle to cycle, depending on when a δ_x resulting in $RMSE(\varepsilon(\delta_x)) > a_\varepsilon RMSE(\eta)$ is found. For algorithm M2:1 and $mv(\delta_x^*)$ the computational time is based on one value of δ_x , i.e. it is assumed that these values are found priorly.

Table 7.10 shows that the estimation accuracy in terms of $\bar{\varepsilon}_x^t$ is not as good for the approximative methods as for the optimal one, since the true parameter deviation $\bar{\varepsilon}_x^t$ increases for all four approximations of

δ_x . However the mean difference is small, especially for M2:1 and the mean-value based $mv(\delta_x^*)$ as the table indicates. The latter is however not an option when considering experimental data, since then δ_x^* is not available, and is therefore not included in the tables from hereon. An alternative is to use the mean value for $\delta_x(M2 : 3)$, which is available. The performance of M2:3 itself is however not better than that of M2:1, according to the mean difference in table 7.10. It is therefore expected that using the mean value of $\delta_x(M2 : 3)$ instead does not result in better results than for M2:1.

There is a disadvantage of M2:1 compared to M2:3 when changing operating conditions, in that it might require some ad-hoc tuning of one of the parameters m_ε and m_δ to assure good performance. This has however not been required in the simulations. However if it would be required, one should instead consider using M2:3 which is flexible to changing operating conditions and is the second best choice with respect to estimation accuracy, given that the required computational time is available. The third choice would be M2:2, but like M2:1 it might require some ad-hoc tuning, in this case for the parameter a_ε .

The two algorithms M2:2 and M2:3 both tend to give too high values of δ_x compared to δ_x^* , as illustrated in figure 7.6. This results in estimates closer to the nominal values, i.e. estimates that are over-smoothed by the regularization. For M2:2, this is due to the restrictive choice made when determining the ad-hoc constant a_ε in M2:2. This effect has already been pointed out for M2:2 by Hansen (1994).

Concerning computational time, algorithm M2:1 and $mv(\delta_x^*)$ are the fastest and they differ merely due to that they use a different number of iterations to minimize the loss function W_N . Compared to M2:3, M2:1 is approximately 80 times faster according to table 7.10.

Estimation accuracy for x_i : Now the attention is turned to the estimation accuracy for the individual parameters x_i . Tables 7.11 and 7.12 show the individual parameter estimates and the corresponding mean true and nominal parameter deviations $\bar{\varepsilon}_x^t$ and $\bar{\varepsilon}_x^\#$ at OP1 and OP8 respectively for FP = 5 %. These parameter values are computed as mean values for ten consecutive cycles. The tables also entail the relative mean estimation error (RME) in percent, as well as numerical values for the true and (emphasized) nominal values.

Both tables show that the estimates for C_1 , T_{IVC} , T_w , Δp , $\Delta\theta$, and especially for V_{cr} and b , are regularized to the vicinity of their respective nominal value $x_i^\#$, indicated by an RME close to 5 %. These seven parameters corresponds fairly well with the order in which the parameters are set spurious for method 1 when no preferred ordering is used, compare (7.2). The difference is p_{IVC} , otherwise it corresponds to the seven most spurious parameters. The estimates for the other parameters, i.e. V_c , p_{IVC} , γ_{300} and K_p ends up close to their true val-

δ_x :	V_c [cm^3]	C_1 [-]	T_{IVC} [K]	p_{IVC} [kPa]	γ_{300} [-]	b [K^{-1}]	T_w [K]	V_{cr} [cm^3]	Δp [kPa]	$\Delta\theta$ [deg]	K_p [-]	$\bar{\varepsilon}_x^t$ [%]	$\varepsilon_x^\#$ [%]
δ_x^*	58.4	2.28	366	50.2	1.397	-0.000106	436	1.05	5.1	0.10	0.990	3.7	4.4
RME	-0.6	-0.1	-1.1	0.4	-0.2	6.0	8.9	5.0	1.3	2.9	-1.0	3.7	4.4
$\delta_x(M2:1)$	58.8	2.37	382	50.0	1.403	-0.000105	425	1.05	5.2	0.10	0.998	3.8	3.1
RME	-0.0	4.0	3.3	0.1	0.2	5.0	6.2	5.0	4.6	4.7	-0.2	3.8	3.1
$\delta_x(M2:2)$	60.6	2.39	389	50.1	1.421	-0.000105	419	1.05	5.2	0.10	1.002	4.1	2.4
RME	3.1	4.9	5.1	0.2	1.5	5.0	4.9	5.0	4.8	5.0	0.2	4.1	2.4
$\delta_x(M2:3)$	60.3	2.39	388	50.0	1.420	-0.000105	420	1.05	5.2	0.10	1.000	4.0	2.5
RME	2.6	4.8	5.0	0.1	1.4	5.0	5.0	5.0	4.8	4.9	0.0	4.0	2.5
$x^\#$	61.7	2.39	389	52.5	1.470	-0.000105	420	1.05	5.3	0.11	1.050	5.0	0.0
RME($x^\#$)	5.0	5.0	5.0	5.0	5.0	5.0	5.0	5.0	5.0	5.0	5.0	5.0	0.0
x^t	58.8	2.28	370	50.0	1.400	-0.0001	400	1	5.0	0.10	1.000	0.0	5.0

Table 7.11: Parameter estimates and corresponding relative mean estimation error (RME) for OP1 at FP = 5 %, using method 2 and setup 1.

δ_x :	V_c [cm^3]	C_1 [-]	T_{IVC} [K]	p_{IVC} [kPa]	γ_{300} [-]	b [K^{-1}]	T_w [K]	V_{cr} [cm^3]	Δp [kPa]	$\Delta\theta$ [deg]	K_p [-]	$\bar{\varepsilon}_x^t$ [%]	$\bar{\varepsilon}_x^\#$ [%]
δ_x^*	58.8	2.38	320	100.0	1.403	-0.000105	425	1.05	5.2	0.10	0.998	3.8	3.1
RME	0.0	4.2	3.2	0.0	0.2	5.0	6.3	5.0	4.8	4.6	-0.2	3.8	3.1
$\delta_x(M2:1)$	58.5	2.35	313	100.1	1.398	-0.000105	432	1.05	5.2	0.10	0.996	3.9	3.6
RME	-0.5	3.2	0.9	0.1	-0.1	5.1	8.1	5.0	4.6	4.0	-0.4	3.9	3.6
$\delta_x(M2:2)$	59.2	2.38	323	100.0	1.408	-0.000105	423	1.05	5.2	0.10	0.998	3.9	2.9
RME	0.7	4.5	4.1	-0.0	0.6	4.9	5.6	5.0	4.9	4.8	-0.2	3.9	2.9
$\delta_x(M2:3)$	58.8	2.38	320	100.0	1.403	-0.000105	425	1.05	5.2	0.10	0.998	3.8	3.1
RME	0.0	4.2	3.2	0.0	0.2	5.0	6.3	5.0	4.8	4.6	-0.2	3.8	3.1
$x^\#$	61.7	2.39	326	105.0	1.470	-0.000105	420	1.05	5.3	0.11	1.050	5.0	0.0
RME($x^\#$)	5.0	5.0	5.0	5.0	5.0	5.0	5.0	5.0	5.0	5.0	5.0	5.0	0.0
x^t	58.8	2.28	310	100.0	1.400	-0.0001	400	1	5.0	0.10	1.000	0.0	5.0

Table 7.12: Parameter estimates and corresponding relative mean estimation error (RME) for OP8 at FP = 5 %, using method 2 and setup 1.

ues especially for OP8. This is due to the higher p_{IVC} , which results in a higher cylinder pressure and therefore a better excitation of the parameters and a better signal-to-noise ratio. For both cases the estimates for p_{IVC} has the overall smallest RME ($< 0.4\%$) closely followed by K_p , while the accuracy for V_c and γ_{300} are within 3.1% and 1.5% respectively for all versions. The estimates of the two latter parameters are significantly better for OP8 compared to OP1.

The estimation accuracy also depend upon the routine used to determine the regularization parameter δ_x . From table 7.10 it was found that routine M2:1 gave the smallest overall mean error, followed by M2:3 and M2:2. When considering the individual estimates of the four parameters, the same relative ordering is found if both operating points are considered. In the case for M2:1, the accuracy for the four parameters is high; The estimates are within 0.5% . The other estimates end up as a compromise in between the true value and the (false) nominal value, except for T_w . In the case of the two parameters V_{cr} and b , these two estimates coincides with the nominal values.

In the presence of a false prior of 5% , the estimates for method 2 are equally or more accurate compared to method 1 for all number of efficient parameters, as shown by comparing the $\bar{\varepsilon}_x^t$ -columns in tables 7.4 and 7.11. This illustrates that method 2 is more robust to a false prior than method 1 and this results in better estimates.

Evaluation for setup 2

Method 2 is now evaluated for setup 2, where the nominal values are given by $x_i^\# = (1 + \sigma_i)x_i^t$, for which the standard deviations are given in table 7.1. The assigned regularization elements are given for two cases; The first case is $\delta_i = \frac{1}{2N} \frac{1}{(0.01x_i^t)^2}$, i.e. all elements are equal, and in the second case $\delta_i = \frac{1}{2N\sigma_i^2}$. Therefore some of the plots and tables based on the second case from now on use the *weighted* versions of the nominal parameter deviation $RMSE(L^\delta \varepsilon_x^\#)$ and so on. The two cases are abbreviated as $\delta_i = c$ and $\delta_i \neq c$ respectively, where c is a constant.

The L-curves based on one engine cycle for each case at OP1 are given in figures 7.9 and 7.10 respectively. For completeness, the corresponding L-curves at OP8 are given in figures C.5 and C.6 in appendix C.7. The individual parameter estimates are given in tables 7.14–7.17, and corresponds to the form used in table 7.11. Tables 7.14 and 7.15 represent case 1 ($\delta_i = c$), while the corresponding tables for case 2 ($\delta_i \neq c$) are given in tables 7.16 and 7.17. Note that the optimal regularization parameter δ_x^* now is determined as the one minimizing the weighted true parameter deviation, i.e. $RMSE(L^\delta \varepsilon_x^t)$. The nominal and true parameter deviations $\bar{\varepsilon}_x^t$ and $\bar{\varepsilon}_x^\#$ for both cases at OP1 and OP8 are then summarized in table 7.13.

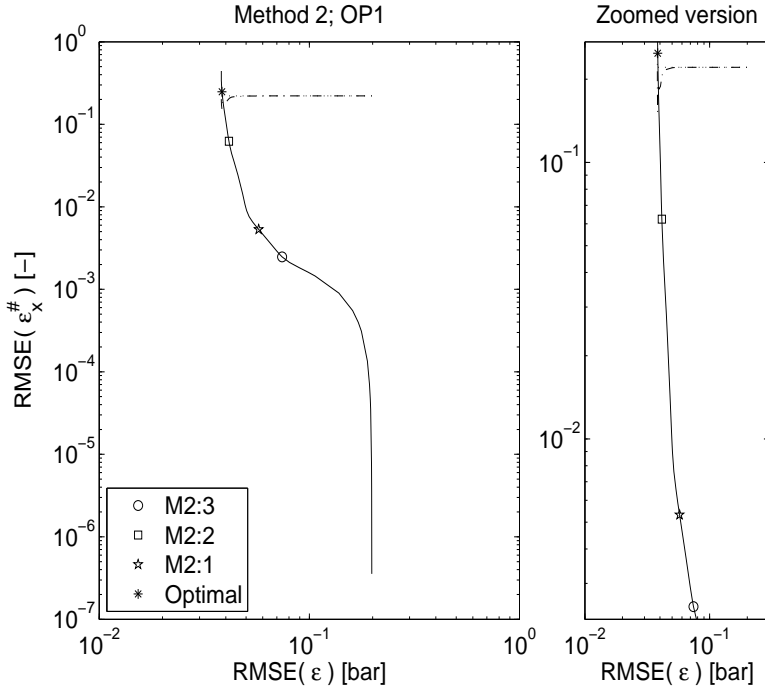


Figure 7.9: L-curve (solid line) for one engine cycle at OP1 with false prior $RMSE(\varepsilon_x^{\#-t})$ (dotted line), when using setup 2 and case 1 of the δ_i ($\delta_i = c$). The results for the three versions of method 2 and the optimal choice of regularization parameter are indicated by the legend. The true parameter deviation $RMSE(\varepsilon_x^t)$ (dash-dotted line) is also given.

$\delta_x:$	$\delta_i = c$				$\delta_i \neq c$			
	OP1		OP8		OP1		OP8	
	$\bar{\varepsilon}_x^t$ [%]	$\bar{\varepsilon}_x^{\#}$ [%]	$\bar{\varepsilon}_x^t$ [%]	$\bar{\varepsilon}_x^{\#}$ [%]	$\bar{\varepsilon}_x^t$ [%]	$\bar{\varepsilon}_x^{\#}$ [%]	$\bar{\varepsilon}_x^t$ [%]	$\bar{\varepsilon}_x^{\#}$ [%]
δ_x^*	14.1	22.8	14.9	18.2	6.1	20.3	6.5	20.1
$\delta_x(M2 : 1)$	22.1	1.4	22.1	0.7	6.2	20.7	6.6	20.9
$\delta_x(M2 : 2)$	20.6	5.8	20.5	5.7	10.5	27.6	10.7	27.3
$\delta_x(M2 : 3)$	22.1	0.9	22.1	0.3	9.4	18.9	9.4	18.4
$x^{\#}$	22.1	0.0	22.1	0.0	22.1	0.0	22.1	0.0
x^t	0.0	22.1	0.0	22.1	0.0	22.1	0.0	22.1

Table 7.13: Mean true and nominal parameter deviation for method 2 using two cases of δ_i at OP1 and OP8 for setup 2.

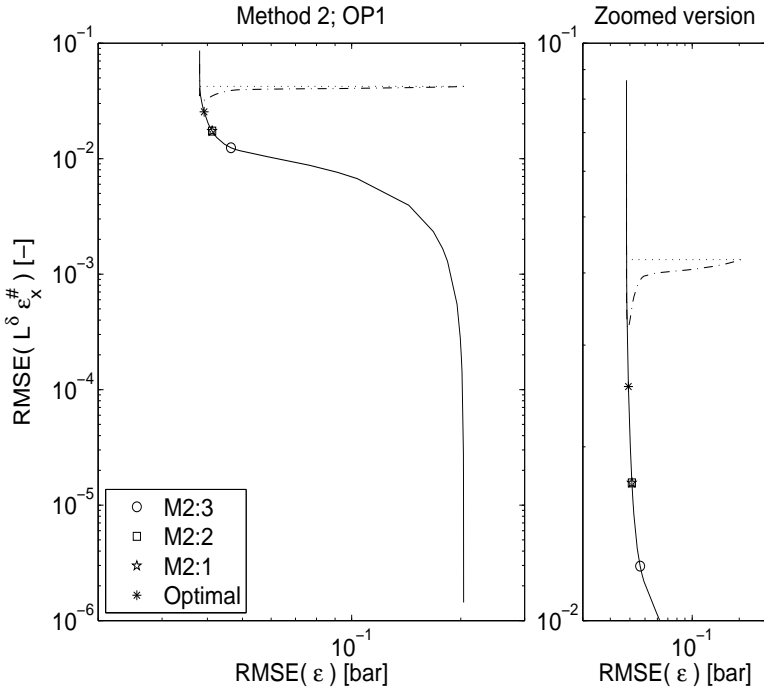


Figure 7.10: L-curve (solid line) for one engine cycle at OP1 with weighted false prior $RMSE(L^\delta \varepsilon_x^{\#-t})$ (dotted line), when using setup 2 and case 2 of the δ_i ($\delta_i \neq c$). The results for the three versions of method 2 and the optimal choice of regularization parameter are indicated by the legend. The weighted true parameter deviation $RMSE(L^\delta \varepsilon_x^t)$ (dash-dotted line) is also given.

Evaluation for individual estimates x_i : When considering the four parameters V_c , p_{IVC} , γ_{300} and K_p , the estimates are again better for the second case as shown in tables 7.14–7.17. It is also notable that the estimates for the case of $\delta_i \neq c$ do not necessarily end up in between the true and nominal value, see for instance the negative RME:s for p_{IVC} and $\Delta\theta$ in table 7.16. This reflects a more flexible solution, than the one for the case of $\delta_i = c$.

Evaluation for all OP:s. Table 7.13 shows that the mean true parameter deviation is smaller when $\delta_i \neq c$ than for $\delta_i = c$, for all three versions of method 2 and for the optimal choice of δ_x . It is also worth to mention that the mean nominal parameter deviation $\bar{\varepsilon}_x^\#$ is relatively small for $\delta_i = c$ and significantly higher for $\delta_i \neq c$. This together with the smaller $\bar{\varepsilon}_x^t$ reflects that the second case is more robust to a false

prior, which of course is preferable.

Now the focus is turned to finding which version of method 2 that performs the best. In the case of $\delta_i = c$ both M2:1 and M2:3 are restrictive and yield estimates close to the nominal values. This is, as pointed out previously, reflected by a relatively low value of $\bar{\varepsilon}_x^\#$ in table 7.13. M2:2 actually performs better than these two, but the difference is small and the estimation bias is still significant as reflected by the $\bar{\varepsilon}_x^t$ -columns.

In the case of $\delta_i \neq c$, all three versions render weighted parameter deviations $RMSE(L^\delta \varepsilon_x^t)$ and $RMSE(L^\delta \varepsilon_x^\#)$ that are virtually the same, see tables 7.16 and 7.17. The only difference is in $RMSE(L^\delta \varepsilon_x^\#)$ for M2:2, which is due to the relatively large error in $\Delta\theta$. However when considering $\bar{\varepsilon}_x^t$ for all investigated operating points, it is lowest for M2:1 and fairly close to the optimal, followed by M2:3 at most instances as shown in table 7.13. If computational time is crucial and therefore needs to be taken into account, M2:1 is outstanding as shown earlier in table 7.13 and would therefore unequivocally be the first choice.

7.1.5 Summary for simulation results

Method 1 resulted in parameter estimates that are significantly biased in the presence of a false prior, since the bias is larger than the false prior level used. It is therefore in itself not recommended to use for estimation of all parameters in the given formulation. For a specific application such as for example compression ratio estimation it can however serve as a guideline of how many parameters to use.

Method 2 outperforms method 1 since it is more robust to a false prior level and yields more accurate parameter estimates. The drive for method 2 was to regularize the solution such that the parameters that are hard to determine are pulled towards their nominal values, while the efficient parameters are free to fit the data. This has shown to be the case in the simulations. Method 2 is systematic and accurate, and therefore fulfills two of the requirements for the estimation tool.

The user can chose between two cases of the parameter uncertainty, namely $\delta_i = c$ and $\delta_i \neq c$. The former is directly applicable once nominal values of the parameters are determined and yields good estimates. However, they can be too restricted by the nominal values, as seen in setup 2. Instead it is recommended to use the second case. It requires more effort to decide upon the uncertainty for each parameter, but pays off in better estimates that are more robust to a false nominal parameter value.

Method 2 is given in three versions, and the version M2:1 followed by M2:3 give the most accurate results for changing operating conditions, false prior levels and noise realizations. M2:1 is also computationally efficient and outstanding compared to the other versions. It

δ_x :	V_c [cm^3]	C_1 [-]	T_{IVC} [K]	p_{IVC} [kPa]	γ_{300} [-]	b [K^{-1}]	T_w [K]	V_{cr} [cm^3]	Δp [kPa]	$\Delta\theta$ [deg]	K_p [-]	$\bar{\varepsilon}_x^t$ [%]	$\bar{\varepsilon}_x^\#$ [%]
δ_x^*	58.8	1.48	380	52.0	1.411	-0.000118	382	1.1	6.1	0.09	0.950	14.1	22.8
RME	-0.0	-35.2	2.8	4.0	0.8	17.6	-4.5	9.7	21.2	-5.5	-5.0	14.1	22.8
$\delta_x(M2:1)$	58.7	2.39	379	50.5	1.404	-0.00011	410	1.15	7.5	0.15	0.989	22.1	1.4
RME	-0.1	4.9	2.5	0.9	0.3	10.0	2.6	15.0	49.9	49.9	-1.1	22.1	1.4
$\delta_x(M2:2)$	59.2	2.16	338	50.5	1.410	-0.000112	436	1.15	7.4	0.14	0.964	20.6	5.8
RME	0.8	-5.3	-8.7	0.9	0.7	11.8	9.0	15.0	47.4	43.2	-3.6	20.6	5.8
$\delta_x(M2:3)$	59.3	2.39	380	51.0	1.398	-0.00011	410	1.15	7.5	0.15	1.001	22.1	0.9
RME	0.9	5.0	2.7	2.1	-0.2	10.0	2.5	15.0	50.0	50.0	0.1	22.1	0.9
$x^\#$	59.3	2.39	380	52.5	1.405	-0.00011	410	1.15	7.5	0.15	1.005	22.1	0.0
RME($x^\#$)	0.9	5.0	2.7	5.0	0.4	10.0	2.5	15.0	50.0	50.0	0.5	22.1	0.0
x^t	58.8	2.28	370	50.0	1.400	-0.0001	400	1	5.0	0.10	1.000	0.0	22.1

Table 7.14: Parameter estimates and corresponding relative mean estimation error (RME) for OP1 when $\delta_i = c$, using method 2 and setup 2.

δ_x :	V_c [cm^3]	C_1 [-]	T_{IVC} [K]	p_{IVC} [kPa]	γ_{300} [-]	b [K^{-1}]	T_w [K]	V_{cr} [cm^3]	Δp [kPa]	$\Delta\theta$ [deg]	K_p [-]	$\bar{\varepsilon}_x^t$ [%]	$\bar{\varepsilon}_x^\#$ [%]
δ_x^*	59.1	1.56	296	103.6	1.409	-0.000115	404	1.12	6.5	0.11	0.949	14.9	18.2
RME	0.6	-31.7	-4.6	3.6	0.7	15.3	1.0	12.4	30.2	8.0	-5.1	14.9	18.2
$\delta_x(M2:1)$	58.7	2.39	319	100.9	1.404	-0.00011	411	1.15	7.5	0.15	0.989	22.1	0.7
RME	-0.1	4.9	3.0	0.9	0.3	10.0	2.6	15.0	49.9	49.9	-1.1	22.1	0.7
$\delta_x(M2:2)$	59.2	2.18	283	100.8	1.410	-0.000111	438	1.15	7.4	0.14	0.964	20.5	5.7
RME	0.8	-4.3	-8.8	0.8	0.7	11.4	9.4	15.0	47.4	42.9	-3.6	20.5	5.7
$\delta_x(M2:3)$	59.3	2.39	320	102.0	1.397	-0.00011	410	1.15	7.5	0.15	1.000	22.1	0.3
RME	0.9	5.0	3.3	2.0	-0.2	10.0	2.5	15.0	50.0	50.0	0.0	22.1	0.3
$x^\#$	59.3	2.39	320	102.5	1.405	-0.00011	410	1.15	7.5	0.15	1.005	22.1	0.0
RME($x^\#$)	0.9	5.0	3.2	2.5	0.4	10.0	2.5	15.0	50.0	50.0	0.5	22.1	0.0
x^t	58.8	2.28	310	100.0	1.400	-0.0001	400	1	5.0	0.10	1.000	0.0	22.1

Table 7.15: Parameter estimates and corresponding relative mean estimation error (RME) for OP8 when $\delta_i = c$, using method 2 and setup 2.

δ_x :	V_c [cm^3]	C_1 [-]	T_{IVC} [K]	p_{IVC} [kPa]	γ_{300} [-]	b [K^{-1}]	T_w [K]	V_{cr} [cm^3]	Δp [kPa]	$\Delta\theta$ [deg]	K_p [-]	$L^{\delta\epsilon_x}$ [%]	$L^{\delta\epsilon_x^t}$ [%]
δ_x^*	59.0	2.37	377	49.9	1.405	-0.000108	411	1.15	5.5	0.10	1.004	3.1	3.3
RME	0.4	3.8	2.0	-0.3	0.4	8.5	2.8	15.0	9.0	-3.1	0.4	3.1	3.3
$\delta_x(M2:1)$	59.0	2.36	377	49.8	1.405	-0.000108	411	1.15	5.4	0.10	1.004	3.1	3.3
RME	0.4	3.7	2.0	-0.3	0.4	8.5	2.8	15.0	8.8	-4.5	0.4	3.1	3.3
$\delta_x(M2:2)$	59.0	2.35	376	49.8	1.405	-0.000108	412	1.15	5.3	0.07	1.004	3.1	3.8
RME	0.3	3.1	1.6	-0.5	0.4	8.4	3.0	15.0	5.3	-29.6	0.4	3.1	3.8
$\delta_x(M2:3)$	59.1	2.36	377	50.0	1.405	-0.000109	412	1.15	6.2	0.09	1.004	3.3	3.1
RME	0.6	3.7	1.9	-0.1	0.3	9.4	3.0	15.0	24.2	-7.0	0.4	3.3	3.1
$x^\#$	59.3	2.39	380	52.5	1.405	-0.00011	410	1.15	7.5	0.15	1.005	4.8	0.0
RME($x^\#$)	0.9	5.0	2.7	5.0	0.4	10.0	2.5	15.0	50.0	50.0	0.5	4.8	0.0
x^t	58.8	2.28	370	50.0	1.400	-0.0001	400	1	5.0	0.10	1.000	0.0	4.8

Table 7.16: Parameter estimates and corresponding relative mean estimation error (RME) for OP1 when $\delta_i \neq c$, using method 2 and setup 2.

δ_x :	V_c [cm ³]	C_1 [-]	T_{IVC} [K]	p_{IVC} [kPa]	γ_{300} [-]	b [K ⁻¹]	T_w [K]	V_{cr} [cm ³]	Δp [kPa]	$\Delta\theta$ [deg]	K_p [-]	$L^{\delta}\epsilon_x^t$ [%]	$L^{\delta}\epsilon_x^{\#}$ [%]
δ_x^*	59.0	2.37	317	99.6	1.405	-0.000109	411	1.15	5.5	0.10	1.004	3.2	2.4
RME	0.5	3.9	2.3	-0.4	0.4	8.8	2.8	15.0	10.6	-3.8	0.4	3.2	2.4
$\delta_x(M2:1)$	59.0	2.37	317	99.6	1.405	-0.000109	411	1.15	5.5	0.09	1.004	3.2	2.5
RME	0.5	3.9	2.2	-0.4	0.4	8.8	2.9	15.0	10.2	-6.7	0.4	3.2	2.5
$\delta_x(M2:2)$	59.0	2.36	315	99.4	1.405	-0.000109	412	1.15	5.4	0.07	1.004	3.2	3.0
RME	0.4	3.4	1.8	-0.6	0.4	8.7	3.1	15.0	7.3	-29.6	0.4	3.2	3.0
$\delta_x(M2:3)$	59.1	2.37	317	99.9	1.404	-0.000109	412	1.15	6.2	0.09	1.004	3.3	2.2
RME	0.6	4.0	2.3	-0.1	0.3	9.5	2.9	15.0	24.3	-5.4	0.4	3.3	2.2
$x^{\#}$	59.3	2.39	320	102.5	1.405	-0.00011	410	1.15	7.5	0.15	1.005	4.2	0.0
RME($x^{\#}$)	0.9	5.0	3.2	2.5	0.4	10.0	2.5	15.0	50.0	50.0	0.5	4.2	0.0
x^t	58.8	2.28	310	100.0	1.400	-0.0001	400	1	5.0	0.10	1.000	0.0	4.2

Table 7.17: Parameter estimates and corresponding relative mean estimation error (RME) for OP8 when $\delta_i \neq c$, using method 2 and setup 2.

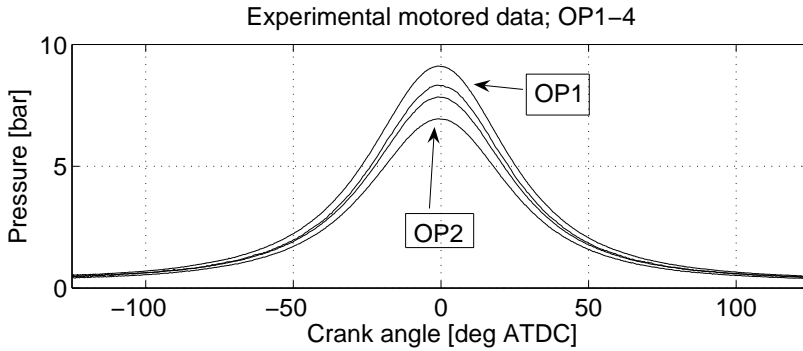


Figure 7.11: Experimentally measured motored cylinder pressures at operating conditions OP1–4.

can therefore be stated that the third requirement is also fulfilled. For the simulated motored cycles, M2:1 is therefore recommended as the best choice.

7.2 Experimental results – motored cycles

The attention is now turned to the issue of evaluating the methods on experimental engine data. As mentioned before, the true model structure and parameter values are unknown. Therefore it is important too see if the effects and trends from the simulation-based evaluation are also present when the methods are applied to experimental data. First the experimental engine data will be described, followed by a discussion on the parameter prior knowledge used. The focus is then turned to evaluating the performance of method 1, followed by method 2.

7.2.1 Experimental engine data

Data is collected during stationary operation at engine speeds $N \in [2000, 5000]$ rpm, intake manifold pressures $p_{man} \in [32, 43]$ kPa altogether forming four different operating points. These operating points are defined in the upper part of table 7.18.

For each operating point 101 consecutive motored cycles with the fuel injection shut-off were sampled for two cylinders with a crank-angle resolution of 1 degree, using an AVL GU21D cylinder pressure sensor. Figure 7.11 displays one measured cycle for each operating point.

7.2.2 Parameter prior knowledge

The parameter prior knowledge used in the experimental evaluation is based on different strategies to set the nominal parameter values $x^\#$ and the regularization elements δ_i .

Nominal parameter values $x^\#$

The nominal parameter values $x^\#$ are set based on a combination of the parameter initial methods described in chapter 3 and expert prior knowledge of what the numerical value of $x^\#$ should be. The values for $x^\#$ for each operating point are given as the emphasized values in table 7.19. Of these parameters it is only the nominal value for Δp that is updated for each cycle, while the others are updated for each operating condition.

Regularization elements δ_i

Two cases of regularization parameter elements are used in method 2 and they correspond to the two cases used in the simulation-based evaluation done previously. The first case, again denoted $\delta_i = c$, sets the standard deviation σ_i for each parameter as $\sigma_i = 0.01\bar{x}_i^\#$, where $\bar{x}_i^\#$ is the mean value of $x_i^\#$ for one operating point. It is used to assure that σ_i does not fluctuate in size from cycle-to-cycle. In the simulation-based evaluation x^t was used instead of $\bar{x}^\#$.

The second case ($\delta_i \neq c$) is based on expert knowledge of the uncertainty for each parameter and it is therefore subjectively chosen by the user. The standard deviation used here in the experimental evaluation coincides with the one used for the simulation-based evaluation in table 7.1.

The first case is updated for each operating point, while this is not required for the second case.

7.2.3 Method 1– Results and evaluation

Method 1 is evaluated only without a preferred ordering, since no gain was found in the simulation-based evaluation by using one. The parameter order for all four operating points is given by

$$C_1 \prec K_p \prec \underline{\Delta\theta} \prec T_{IVC} \prec \underline{V_{cr}} \prec \Delta p \prec b \prec T_w \prec \underline{V_c} \prec \underline{p_{IVC}} \prec \underline{\gamma_{300}}, \quad (7.5)$$

which reflects the average case. This parameter order differs somewhat from the corresponding order found in simulations (7.2), but γ_{300} is still the most efficient parameter. The underlined parameters in (7.5) are invariant in position for the investigated operating conditions cycle-to-cycle variations. The other parameters differ in order as permutations

	OP1	OP2	OP3	OP4
N [rpm]	2000	3000	4000	5000
p_{man} [kPa]	43	32	35	37
$\text{mean}(d^*)$	9.5	10.3	10.4	10.4
$d^* \in$	[9, 10]	[9, 11]	[9, 11]	[9, 11]

Table 7.18: Mean number and region of d^* for 101 experimental cycles at OP1–4.

of the three groups $[T_{IVC}, T_w]$, $[\Delta p, b]$ and $[K_p, C_1]$. These groups are not exactly the same as the ones for the simulation-based evaluation.

The minimizing number of parameters d^* using algorithm 6.2 are given in table 7.18 as a mean over the 101 cycles at all four operating points. The range of d^* for each operating point is also given. The table shows that the mean values of d^* are larger and the variation is smaller in the experimental case, compared to the simulations given in table 7.2.

The mean value, standard deviation, and relative mean error for the individual estimates are given in table 7.19. The relative mean error is computed relative to the nominal parameter value at each cycle and is given in percent. All parameters give reasonable values except for C_1 , T_{IVC} , and T_w that yield unreasonably large parameter values. In accordance with the simulation-based evaluation in section 7.1.3, method 1 is not recommended to use for parameter estimation in the given formulation. The attention is therefore turned to method 2.

7.2.4 Method 2– Results and evaluation

The same implementation settings, as for the simulation-based evaluation in section 7.1.4, are used and are therefore not repeated here.

Results for case 1 ($\delta_i = c$) and case 2 ($\delta_i \neq c$)

The results are first described for case 1. An example of an L-curve is given in figure 7.12. A fourth version, M2:3+, is also included in the figure. The algorithm is motivated and fully described in appendix C.3. This version is an extension of M2:3, and uses a smaller search region Δ_x of δ_x as compared to the original form. Version M2:3+ uses the regularization parameter δ_x from M2:1 as a mid-value of the search region Δ_x , for a Δ_x given by 25 samples of δ_x from figure 7.5. The usage of M2:3+ is only needed for experimental cycles and is due to problems occurring when searching for the maximum curvature of the L-curve. For simulated cycles this problem has not occurred, and therefore results in the same value of δ_x for M2:3 and M2:3+.

	V_c [cm^3]	C_1 [-]	T_{IVC} [K]	p_{IVC} [kPa]	γ_{300} [-]	b [K^{-1}]	T_w [K]	V_{cr} [cm^3]	Δp [kPa]	$\Delta\theta$ [deg]	K_p [-]	$\varepsilon_x^\#$ [%]
OP1	mean	5.03	588	54.7	1.369	$-4.39 \cdot 10^{-6}$	690	1.12	-0.3	0.32	1.000	92.5
	σ_{est}	2.98	220	0.4	0.007	$5.82 \cdot 10^{-6}$	230	0.755	0.5	0.13	0.000	92.5
	RME	120.5	87.1	-4.1	1.5	-96.6	64.4	89.8	-88.3	-31.7	0.0	92.5
	$x^\#$	2.28	314	56.4	1.400	$-9.3 \cdot 10^5$	400	0.882	-1.4	0.47	1.000	0.0
OP2	mean	5.94	474	37.4	1.422	$-1.11 \cdot 10^{-5}$	621	1.2	1.7	0.14	1.043	99.8
	σ_{est}	2.07	187	1.8	0.011	$1.48 \cdot 10^{-5}$	209	0.524	0.6	0.08	0.049	99.8
	RME	160.5	50.8	-34.4	5.4	-91.5	47.9	103.9	-177.2	-70.1	4.3	99.8
	$x^\#$	2.28	314	42.5	1.400	$-9.3 \cdot 10^{-5}$	400	0.882	-1.6	0.47	1.000	0.0
OP3	mean	6.34	403	41.3	1.429	$-1.1 \cdot 10^{-5}$	526	0.448	3.4	0.13	1.041	108.4
	σ_{est}	1.71	170	2.2	0.010	$1.63 \cdot 10^{-5}$	186	0.352	0.8	0.06	0.058	108.4
	RME	178.1	28.3	-27.5	5.9	-91.5	25.3	-23.7	-257.1	-71.7	4.1	108.4
	$x^\#$	2.28	314	47.3	1.400	$-9.3 \cdot 10^{-5}$	400	0.882	-0.6	0.47	1.000	0.0
OP4	mean	5.04	454	43.8	1.431	$-5.03 \cdot 10^{-5}$	562	0.859	2.2	0.11	1.020	88.1
	σ_{est}	1.63	184	1.7	0.019	$4.39 \cdot 10^{-5}$	200	0.318	0.9	0.05	0.032	88.1
	RME	120.8	44.5	-23.2	6.1	-61.3	33.9	46.1	-199.0	-77.3	2.0	88.1
	$x^\#$	2.28	314	48.4	1.400	$-9.3 \cdot 10^{-5}$	400	0.882	-1.2	0.47	1.000	0.0

Table 7.19: Mean value, standard deviation σ_{est} , relative mean error (RME) and nominal parameter deviation $\varepsilon_x^\#$ of the estimate for method 1, evaluated at d^* for 101 experimental cycles at OPI–4.

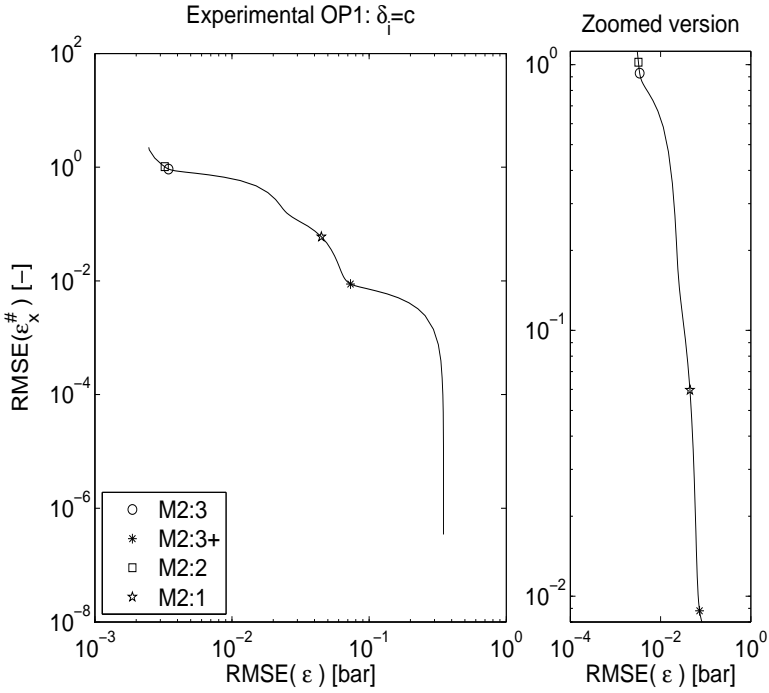


Figure 7.12: L-curve (solid line) for one engine cycle at OP1, when using case 1 of the δ_i ($\delta_i = c$). The results for the four versions of method 2 are indicated by the legend.

		OP1	OP2	OP3	OP4
N [rpm]		2000	3000	4000	5000
p_{man} [kPa]		43	32	35	37
$\delta_x(M2:1)$	mean	$3.8 \cdot 10^{-5}$	$4.1 \cdot 10^{-5}$	$6.5 \cdot 10^{-5}$	$4.2 \cdot 10^{-5}$
	σ_{est}	$6.3 \cdot 10^{-5}$	$3.9 \cdot 10^{-5}$	$1.5 \cdot 10^{-6}$	$4.8 \cdot 10^{-5}$
$\delta_x(M2:2)$	mean	$2.3 \cdot 10^{-8}$	$7.5 \cdot 10^{-8}$	$9.6 \cdot 10^{-8}$	$6.3 \cdot 10^{-8}$
	σ_{est}	$1.9 \cdot 10^{-8}$	$8.1 \cdot 10^{-8}$	$6.6 \cdot 10^{-8}$	$4.3 \cdot 10^{-8}$
$\delta_x(M2:3)$	mean	$4.2 \cdot 10^{-8}$	$3.9 \cdot 10^{-8}$	$0.4 \cdot 10^{-8}$	$2.1 \cdot 10^{-8}$
	σ_{est}	$1.5 \cdot 10^{-8}$	$3.4 \cdot 10^{-8}$	$0.8 \cdot 10^{-8}$	$4.1 \cdot 10^{-8}$
$\delta_x(M2:3+)$	mean	$5.1 \cdot 10^{-5}$	$9.2 \cdot 10^{-5}$	$9.0 \cdot 10^{-5}$	$3.4 \cdot 10^{-5}$
	σ_{est}	$1.6 \cdot 10^{-5}$	$4.3 \cdot 10^{-6}$	$5.8 \cdot 10^{-5}$	$3.4 \cdot 10^{-5}$

Table 7.20: Mean value and standard deviation (σ_{est}) of δ_x for the four versions of method 2 using case 1, evaluated for 101 experimental cycles at OP1-4.

Table 7.20 summarizes the mean value and standard deviation of the computed regularization parameter δ_x for 101 experimental cycles. This is done for all four operating points and for each of the four versions of method 2. The corresponding individual parameter estimates are given as mean values for 101 cycles at each operating point in table 7.21, as well as the corresponding (emphasized) nominal values $x^\#$ and the nominal parameter deviation $\bar{\varepsilon}_x^\#$. More detailed results for OP1 are given in table C.6, where also the standard deviation and the relative mean error with respect to the nominal parameters $x^\#$ are given.

The corresponding figures and tables for case 2 are given in figure 7.13, table 7.22, table 7.23 that now also include the weighted nominal parameter deviation $RMSE(L^\delta \varepsilon_x^\#)$, and table C.7 respectively.

Evaluation for case 1 ($\delta_i = c$)

Case 1 is considered first. Figure 7.12 illustrates that the L-curve does not have as sharp transition as in the corresponding simulated case given in figure 7.9. The difference is believed to be due to that the model structure is not correct. Figure 7.12 also shows that the four versions yield different regularization parameters δ_x . The two versions M2:2 and M2:3 render approximately the same δ_x , which is confirmed in table 7.20 for all operating points. M2:1 and M2:3+ result in higher δ_x :s in the mean, and therefore relies more on the prior knowledge compared to M2:2 and M2:3.

For all four operating points table 7.20 shows that the regularization parameter for the four versions are ordered in size according to

$$\delta_x(M2 : 3+) > \delta_x(M2 : 1) > \delta_x(M2 : 2) > \delta_x(M2 : 3), \quad (7.6)$$

with two exceptions. For OP1 it is the other way around for M2:2 and M2:3, and the same goes for M2:1 and M2:3+ at OP4. As expected the difference between $\delta_x(M2 : 1)$ and $\delta_x(M2 : 3+)$ is smaller than between $\delta_x(M2 : 1)$ and $\delta_x(M2 : 3)$. Unlike M2:1, M2:3+ is assured to find a convex corner of the L-curve. For the investigated operating points, M2:3+ gives a higher value of δ_x , than for M2:1, M2:2 and M2:3. For M2:3 this corresponds to the high value of the left-most curvature found in figure C.4. Table 7.20 also shows that the mean value of δ_x depends upon operating condition, and that for a given version of method 2 δ_x is in the same order of magnitude for all four operating points.

The different δ_x :s result in different nominal parameter deviations and individual estimates, as shown in table 7.21 for OP1-4. In general M2:2 and M2:3 yield similar parameter estimates, especially for OP1. This is due to that δ_x is approximately the same. These estimates are however unreasonably large, see e.g. T_{IVC} , T_w and K_p , while b is unreasonably small. All parameters except V_c and γ_{300} deviate significantly

δ_x :	V_c [cm^3]	C_1 [-]	T_{IVC} [K]	p_{IVC} [kPa]	γ_{300} [-]	b [K^{-1}]	T_w [K]	V_{cr} [cm^3]	Δp [kPa]	$\Delta\theta$ [deg]	K_p [-]	$\varepsilon_x^\#$ [%]
OP1 δ_x :	$\delta_x(M2:1)$	2.70	358	53.8	1.396	$-8.8 \cdot 10^{-5}$	370	0.883	1.1	0.45	0.998	5.8
	$\delta_x(M2:2)$	6.27	550	34.1	1.370	$-3.0 \cdot 10^{-7}$	712	0.64	-0.4	0.15	1.596	103.9
	$\delta_x(M2:3)$	6.54	567	32.8	1.371	$-2.1 \cdot 10^{-7}$	741	0.597	-0.3	0.11	1.658	73.5
	$\delta_x(M2:3+)$ $x^\#$	2.70	357	53.8	1.393	$-8.7 \cdot 10^{-5}$	373	0.882	1.3	0.47	0.999	0.8
		2.28	314	56.4	1.400	$-9.3 \cdot 10^{-5}$	400	0.882	-1.4	0.47	1.000	0.0
OP2 δ_x :	$\delta_x(M2:1)$	2.67	347	39.6	1.420	$-7.9 \cdot 10^{-5}$	374	0.882	1.4	0.39	0.999	3.4
	$\delta_x(M2:2)$	5.64	502	27.4	1.402	$-1.4 \cdot 10^{-6}$	663	0.909	0.4	0.08	1.460	82.3
	$\delta_x(M2:3)$	5.77	501	27.0	1.412	$-8.4 \cdot 10^{-7}$	677	0.73	1.0	0.06	1.457	97.6
	$\delta_x(M2:3+)$ $x^\#$	2.61	347	39.8	1.414	$-8.1 \cdot 10^{-5}$	372	0.882	1.2	0.47	1.000	0.6
		2.28	314	42.5	1.400	$-9.3 \cdot 10^{-5}$	400	0.882	-1.6	0.47	1.000	0.0
OP3 δ_x :	$\delta_x(M2:1)$	2.60	344	43.8	1.420	$-7.6 \cdot 10^{-5}$	374	0.882	2.9	0.37	0.998	2.4
	$\delta_x(M2:2)$	5.96	523	29.1	1.392	$-3.4 \cdot 10^{-7}$	696	0.782	1.1	0.07	1.534	83.3
	$\delta_x(M2:3)$	5.81	500	29.8	1.418	$-8.1 \cdot 10^{-7}$	687	0.382	2.7	0.06	1.449	137.1
	$\delta_x(M2:3+)$ $x^\#$	2.58	345	43.9	1.418	$-7.6 \cdot 10^{-5}$	373	0.882	2.8	0.47	1.000	2.6
		2.28	314	47.3	1.400	$-9.3 \cdot 10^{-5}$	400	0.882	-0.6	0.47	1.000	0.0
OP4 δ_x :	$\delta_x(M2:1)$	2.61	350	45.3	1.422	$-7.3 \cdot 10^{-5}$	367	0.882	1.7	0.25	0.999	3.3
	$\delta_x(M2:2)$	4.67	448	36.3	1.406	$-1.3 \cdot 10^{-5}$	551	1.03	0.6	0.06	1.272	65.5
	$\delta_x(M2:3)$	4.82	456	36.1	1.426	$-2.9 \cdot 10^{-5}$	578	0.787	1.6	0.03	1.253	87.0
	$\delta_x(M2:3+)$ $x^\#$	2.62	352	45.3	1.420	$-7.2 \cdot 10^{-5}$	363	0.884	1.7	0.47	1.001	11.4
		2.28	314	48.4	1.400	$-9.3 \cdot 10^{-5}$	400	0.882	-1.2	0.47	1.000	0.0

Table 7.21: Mean value of the estimate for the four versions of method 2 using case 1, evaluated for 101 experimental cycles at OP1-4. The nominal values $x^\#$ are also included.

from their respective nominal value. This is reflected in the relatively large nominal parameter deviation $\bar{\varepsilon}_x^\#$, and is due to a small δ_x .

The individual estimates for M2:1 and M2:3+ are all reasonable, which is expected since they end up close to their nominal values. The estimates are in general closer to $x^\#$ for all parameters (except for V_c and γ_{300}), than for M2:2 and M2:3. Out of M2:1 and M2:3+, the latter has a smaller nominal parameter deviation $\bar{\varepsilon}_x^\#$ for all operating points except OP4. This corresponds to the ordering given in (7.6). The maximum deviation occurs for the parameters C_1 , T_{IVC} and T_w for both versions.

To summarize the evaluation for $\delta_i = c$, using M2:1 or M2:3+ yield estimates that deviate less than 6 and 11 percent from the nominal values in the mean.

Evaluation for case 2 ($\delta_i \neq c$)

Now the second case will be evaluated. Figure 7.13 displays that the four versions yield approximately the same δ_x , which is confirmed by table 7.22 for OP1-4. In general, the mean values and standard deviations of the regularization parameter for the three versions M2:1, M2:3 and M2:3+ are basically the same for all operating points, as shown in table 7.22. The reason that M2:3 and M2:3+ do not coincide is that the former finds a corner at a smaller δ_x in some instances. The second version (M2:2) yields a δ_x that has a lower mean value than the other three, which reflects a higher confidence in the data.

Concerning the individual parameter estimates in table 7.23, all four versions render estimates that are reasonable. An exception is the Woschni heat transfer coefficient C_1 , which can be considered to be too large for M2:2. A trend for all versions is that the estimated p_{IVC} is smaller than the nominal p_{IVC} , which is partly compensated by Δp and T_{IVC} that are larger than their nominal values.

As for the simulation-based evaluation the parameters V_{cr} , K_p , and b are attracted to the vicinity of their nominal values, while others like V_c and γ_{300} are adjusted to the data. Out of the four versions, M2:3+ closely followed by M2:1 yields the smallest weighted nominal parameter deviations for all OP:s, as indicated by table 7.23.

Compared to case 1, the estimates for M2:2 and M2:3 are much closer to their nominal values, which is reflected by the $\bar{\varepsilon}_x^\#$ -columns in tables 7.21 and 7.23. For M2:1 and M2:3+ it is the other way around. This is mostly due to the Δp -estimate, which yields a large normalized nominal deviation and therefore contributes very much to $\bar{\varepsilon}_x^\#$.

To summarize the evaluation for $\delta_i \neq c$, using M2:1 or M2:3+ yield weighted nominal parameter deviations that are less than 15 percent in both cases.

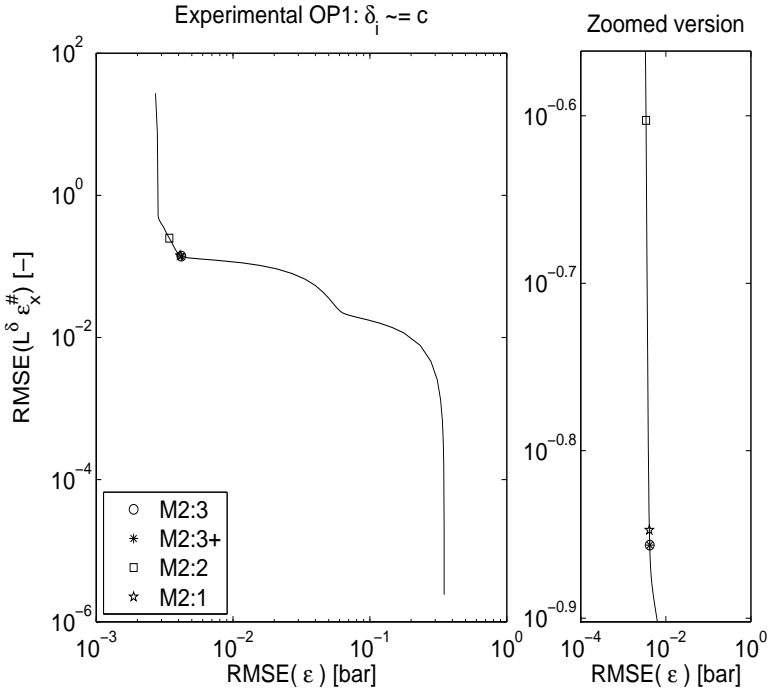


Figure 7.13: L-curve (solid line) for one engine cycle at OP1, when using case 2 of the δ_i ($\delta_i \neq c$). The results for the four versions of method 2 are indicated by the legend.

		OP1	OP2	OP3	OP4
N [rpm]		2000	3000	4000	5000
p_{man} [kPa]		43	32	35	37
$\delta_x(M2:1)$	mean	$3.3 \cdot 10^{-5}$	$3.5 \cdot 10^{-5}$	$5.5 \cdot 10^{-5}$	$3.6 \cdot 10^{-5}$
	σ_{est}	$1.1 \cdot 10^{-5}$	$9.6 \cdot 10^{-6}$	$2.6 \cdot 10^{-5}$	$1.3 \cdot 10^{-5}$
$\delta_x(M2:2)$	mean	$7.8 \cdot 10^{-6}$	$4.4 \cdot 10^{-6}$	$3.0 \cdot 10^{-5}$	$2.1 \cdot 10^{-5}$
	σ_{est}	$3.7 \cdot 10^{-5}$	$2.7 \cdot 10^{-5}$	$1.0 \cdot 10^{-4}$	$8.1 \cdot 10^{-5}$
$\delta_x(M2:3)$	mean	$2.8 \cdot 10^{-5}$	$5.9 \cdot 10^{-5}$	$5.6 \cdot 10^{-5}$	$3.2 \cdot 10^{-5}$
	σ_{est}	$2.0 \cdot 10^{-5}$	$5.1 \cdot 10^{-5}$	$2.7 \cdot 10^{-5}$	$2.1 \cdot 10^{-5}$
$\delta_x(M2:3+)$	mean	$3.4 \cdot 10^{-5}$	$6.3 \cdot 10^{-5}$	$6.6 \cdot 10^{-5}$	$3.5 \cdot 10^{-5}$
	σ_{est}	$2.1 \cdot 10^{-5}$	$2.1 \cdot 10^{-5}$	$2.6 \cdot 10^{-5}$	$2.0 \cdot 10^{-5}$

Table 7.22: Mean value and standard deviation (σ_{est}) of δ_x for the four versions of method 2 using case 2, evaluated for 101 experimental cycles at OP1–4.

δ_x :	V_c [cm^3]	C_1 [-]	T_{IVC} [K]	p_{IVC} [kPa]	γ_{300} [-]	b [K^{-1}]	T_w [K]	V_{cr} [cm^3]	Δp [kPa]	$\Delta\theta$ [deg]	K_p [-]	$L^\delta \varepsilon_x^\#$ [%]	$\varepsilon_x^\#$ [%]
OP1	$\delta_x(M2:1)$	2.73	359	53.7	1.394	$-8.7 \cdot 10^{-5}$	372	0.882	1.4	0.49	1.000	14.7	34.4
	$\delta_x(M2:2)$	3.54	368	53.8	1.389	$-8.8 \cdot 10^{-5}$	406	0.882	1.0	0.46	1.002	21.0	36.7
	$\delta_x(M2:3)$	2.72	359	53.7	1.394	$-8.7 \cdot 10^{-5}$	371	0.882	1.4	0.49	1.000	15.8	35.4
	$\delta_x(M2:3+)$	2.72	359	53.7	1.394	$-8.7 \cdot 10^{-5}$	371	0.882	1.4	0.49	1.000	14.7	34.5
	$x^\#$	2.28	314	56.4	1.400	$-9.3 \cdot 10^{-5}$	400	0.882	-1.4	0.47	1.000	0.0	0.0
OP2	$\delta_x(M2:1)$	2.68	348	39.5	1.420	$-7.9 \cdot 10^{-5}$	374	0.882	1.6	0.41	1.000	13.1	31.6
	$\delta_x(M2:2)$	3.87	353	38.7	1.432	$-7.8 \cdot 10^{-5}$	426	0.882	2.1	0.33	1.003	23.3	38.3
	$\delta_x(M2:3)$	2.63	349	39.7	1.416	$-8 \cdot 10^{-5}$	371	0.882	1.4	0.42	1.000	13.1	31.1
	$\delta_x(M2:3+)$	2.63	349	39.7	1.416	$-8 \cdot 10^{-5}$	371	0.882	1.3	0.42	1.000	12.7	30.9
	$x^\#$	2.28	314	42.5	1.400	$-9.3 \cdot 10^{-5}$	400	0.882	-1.6	0.47	1.000	0.0	0.0
OP3	$\delta_x(M2:1)$	2.61	345	43.7	1.420	$-7.5 \cdot 10^{-5}$	373	0.882	3.0	0.39	1.000	12.7	33.0
	$\delta_x(M2:2)$	3.04	346	43.4	1.424	$-7.7 \cdot 10^{-5}$	392	0.882	3.2	0.36	1.001	16.0	35.1
	$\delta_x(M2:3)$	2.60	345	43.8	1.420	$-7.5 \cdot 10^{-5}$	373	0.882	3.0	0.39	1.000	12.9	33.0
	$\delta_x(M2:3+)$	2.60	345	43.8	1.419	$-7.5 \cdot 10^{-5}$	372	0.882	3.0	0.39	1.000	12.6	32.6
	$x^\#$	2.28	314	47.3	1.400	$-9.3 \cdot 10^{-5}$	400	0.882	-0.6	0.47	1.000	0.0	0.0
OP4	$\delta_x(M2:1)$	2.63	351	45.2	1.422	$-7.2 \cdot 10^{-5}$	367	0.882	1.9	0.26	1.000	12.0	25.3
	$\delta_x(M2:2)$	3.07	352	45.0	1.425	$-7.7 \cdot 10^{-5}$	387	0.882	2.0	0.24	1.001	15.7	28.2
	$\delta_x(M2:3)$	2.62	351	45.2	1.422	$-7.2 \cdot 10^{-5}$	366	0.882	1.8	0.26	1.000	12.3	25.5
	$\delta_x(M2:3+)$	2.62	351	45.2	1.422	$-7.2 \cdot 10^{-5}$	367	0.882	1.8	0.26	1.000	12.0	25.2
	$x^\#$	2.28	314	48.4	1.400	$-9.3 \cdot 10^{-5}$	400	0.882	-1.2	0.47	1.000	0.0	0.0

Table 7.23: Mean value of the estimate for the four versions of method 2 using case 2, evaluated for 101 experimental cycles at OP1-4. The nominal values $x^\#$ are also included.

Summary of method 2

In the simulations the gain in choosing case 2 instead of case 1 was not distinct. However in the experimental situation the gain in using case 2 is stronger, especially for M2:2 and M2:3 since all estimates are physically reasonable. It has also been shown that M2:1 and M2:3+ give more reasonable estimates, compared to M2:2 and M2:3. Version M2:3+ is more flexible to changes in operating condition than M2:1, since it finds a convex corner of the L-curve. For motored cycles, this flexibility has not been shown to be necessary for the examined operating points. To conclude, the argumentation speaks in favor of using version M2:1 and case 2 of δ_i for motored cycles.

7.3 Summary of results for motored cycles

Both the simulation and experimental studies showed that method 1 did not render accurate estimates. It was even hard to decide upon the number of efficient parameters to use. However, method 1 allows for the parameters to be ordered in how efficient they are for the given estimation problem and data. It was also shown that γ_{300} is the most efficient parameter.

Method 2 outperforms method 1 since it is more robust to a false prior level and yields more accurate parameter estimates, according to the simulation-based evaluation. In the experimental situation method 2 was found to give reasonable estimates for all parameters. The drive for method 2 was to regularize the solution such that the parameters that are hard to determine are pulled towards their nominal values, while the efficient parameters are free to fit the data. This has shown to be the case in the simulations.

The user can chose between two cases of the parameter uncertainty, namely $\delta_i = c$ and $\delta_i \neq c$. The former is directly applicable once nominal values of the parameters are determined and yields good estimates, almost as good as for the second case when considering only the simulations. However, when also considering the experimental evaluation the gain in using the second case is stronger. Thus it is recommended to use the second case. It requires more effort to decide upon the uncertainty for each parameter, but pays off in better estimates that are more robust to a false nominal parameter value.

Method 2 was originally given in three variants, and variant M2:1 gives the most accurate results for changes in operating condition, false prior levels and noise realizations for simulated cylinder pressure data. In the experimental evaluation a fourth variant, M2:3+, was included to cope with unreasonably high curvature for low δ_x that can occur for experimental data. It was found that the two variants M2:1 and M2:3+

both yield reasonable estimates, and that the flexibility of M2:3+ for a change in operating condition was not necessary. Since M2:1 is also computationally efficient and outstanding compared to the other variants, usage of M2:1 together with $\delta_i \neq c$ is therefore recommended as the best choice for motored cycles.

RESULTS AND EVALUATION FOR FIRED CYCLES

Method 1 and method 2 described in section 6.4 will now be evaluated for fired cylinder pressure data. These methods were evaluated for motored cycles in chapter 7 and the evaluation in this chapter follows the same structure. The evaluation covers both simulated and experimental data.

It is worth noting that all numerical calculations have been made for normalized values of the parameters, while the individual parameter values that are given in tables are not normalized if not explicitly stated. The purpose of the normalization is to yield parameters that are in the order of 1, and the normalization is described in appendix C.1.

8.1 Simulation results – fired cycles

First the simulated engine data will be described, followed by a discussion on the parameter prior knowledge used. The focus is then turned to evaluating the performance of method 1, followed by method 2.

8.1.1 Simulated engine data

Cylinder pressure traces were generated by simulating the standard model from section 6.2.1 with representative single-zone parameters, given in appendix C.6. Six operating points were selected with engine speeds $N \in \{1500, 3000\}$ rpm, mean charge temperatures at IVC $T_{IVC} \in \{370, 414\}$ K, cylinder pressures at IVC $p_{IVC} \in \{50, 100\}$ kPa

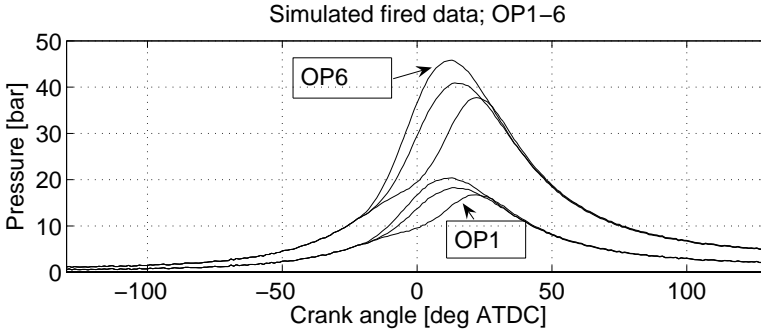


Figure 8.1: Simulated cylinder pressures for the different operating points OP1–6.

x_i	V_c	C_1	T_{IVC}	p_{IVC}	γ_{300}	b	T_w	V_{cr}
Unit	[cm^3]	[-]	[K]	[kPa]	[-]	[K^{-1}]	[K]	[cm^3]
σ_i	0.5	0.114	10	2.5	0.005	$1 \cdot 10^{-5}$	10	0.15
RME [%]	0.9	5.0	2.4	5.0	0.4	14.3	2.1	15.0
x_i	Δp	$\Delta\theta$	K_p	C_2	Q_{in}	θ_{ig}	$\Delta\theta_d$	$\Delta\theta_b$
Unit	[kPa]	[deg]	[-]	[$m/(s K)$]	[J]	[deg]	[deg]	[deg]
σ_i	2.5	0.05	0.005	$1.62 \cdot 10^{-4}$	25	1	2	2
RME [%]	50.0	50.0	0.5	5.0	5.0	6.7	10.0	10.0

Table 8.1: Assigned standard deviation σ_i of the model parameters x_i used for the second case of δ_i :s. The relative mean error (RME) corresponding to one standard deviation from the value (for OP1) is also given.

and different heat release traces, where table C.5 defines the individual operating points. For each operating point a cylinder pressure trace was simulated and ten realizations of Gaussian noise with zero mean and standard deviation 3.8 kPa were added, forming altogether 60 fired cycles. The chosen noise level is the same as the one used in chapter 5 (and chapter 7), and thus reflects the level seen in experimental data. The data was sampled with a resolution of 1 crank-angle degree (CAD). In figure 8.1, one fired cycle is shown for each operating point. The cylinder pressures corresponding to OP1 and OP6 differ the most, and will therefore be the two extremes in the investigation.

8.1.2 Parameter prior knowledge

The setting of parameter prior knowledge for fired cycles is based on the same principles as for motored cycles, see section 7.1.2, and most

details are therefore not repeated here. The standard model for fired cycles entails 16 parameters, i.e. five more than for the motored cycle. This has consequences for the second case of δ_i , i.e. $\delta_i \neq c$, where the expected parameter uncertainty for the five extra parameters must be assigned. For this particular application the standard deviation σ_i for each parameter are given in table 8.1.

8.1.3 Method 1– Results and evaluation

First of all, the order in which the parameters are set fixed when using algorithm 6.2 without a preferred ordering is investigated. This corresponds to keeping track of the spurious parameters x_{new}^{sp} in step 3. In this case all parameters need to be included, and therefore the maximum and minimum number of efficient parameters are given by $d_{max}^\# = d$ and $d_{min}^\# = 1$, where $d = 16$ is the number of parameters.

The resulting parameter order *without* a preferred ordering is given by

$$C_2 \prec C_1 \prec K_p \prec T_w \prec \Delta\theta \prec \Delta p \prec V_{cr} \prec T_{IVC} \\ \prec b \prec \theta_{ig} \prec V_c \prec p_{IVC} \prec \Delta\theta_b \prec Q_{in} \prec \Delta\theta_d \prec \underline{\gamma_{300}}, \quad (8.1)$$

which reflects a typical case. As before, the underlined parameter is invariant in position to the investigated noise realizations, false prior levels and different operating conditions. The other parameters differ in position, and compared to the simulated motored case the permutation groups are larger and as well as the variation in position. At many instances the difference in order occurs as permutations of the three groups $[b, C_1, C_2, T_{IVC}, p_{IVC}, T_w]$, $[K_p, p_{IVC}, Q_{in}]$ and $[\theta_{ig}, \Delta\theta_d]$, but this is not the case as frequently as in the motored case. The first group is expected since these parameters are coupled to temperature through Woschni's heat transfer correlation (3.43) and the linear model of γ (3.44), and corresponds well to the motored case described in (7.2) except for b which is now included. All parameters in the second group have a multiplicative effect on the cylinder pressure, although Q_{in} has no effect on the compression phase prior to ignition. Comparing the parameter order for motored (7.2) and fired (8.1) cycles, the order is changed for most positions. However γ_{300} is again the most efficient parameter, given the structure of the standard model.

The minimizing number of parameters using algorithm 6.2 are given in figure 8.2 for OP1 and OP6, that are the two extremes in the simulation-based investigation. Ten different noise realizations corresponding to ten engine cycles have been used, as well as four different cases of false prior. The corresponding results for all six operating points are given in table 8.2, but now as a mean value for the ten cycles.

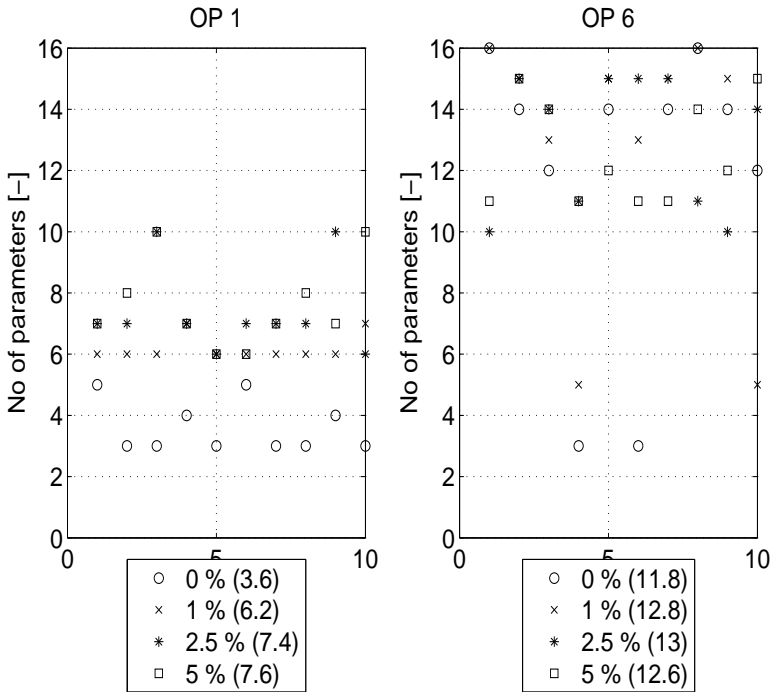


Figure 8.2: Minimizing number of parameters d^* for method 1, when using no preferred ordering.

Table 8.2 shows that the number of efficient parameters $d^\#$ range from 3 to 16, which is also illustrated in figure 8.2. The table also illustrates that for a high load, i.e. OP2, OP4 and OP6, the number of efficient parameters $d^\#$ increases. Compared to the motored cycles the variation in $d^\#$ depending on the level of false prior FP is larger, but again the variation is larger depending on the operating point. The large range of $d^\#$ makes it hard to use the Akaike FPE to determine how many of the parameters in (8.1) that are efficient.

Estimation accuracy

Table 8.3 shows the parameter estimates for the entire range of $d^\#$, i.e. from 16 to 1 parameter, for one engine cycle in the presence of a false prior level of 5%. For this specific cycle (OP1, cycle1), the Akaike FPE is minimized by seven parameters, i.e. $d^* = 7$. The results for a false prior level of 0% is given in appendix C.7, see table C.8.

Table 8.3 shows that the parameter estimates are biased when a

FP [%]	Operating point (OP)					
	1	2	3	4	5	6
0	3.6	10.2	4.2	12.6	3.8	11.8
1	6.2	15.8	5.6	11.0	5.6	12.8
2.5	7.4	15.6	5.4	13.4	5.6	13.0
5	7.6	14.0	6.0	12.2	6.4	12.6
$d^* \in$	[3, 10]	[3, 16]	[3, 8]	[4, 16]	[3, 9]	[3, 16]

Table 8.2: Minimizing number of parameters d^* for method 1, without a preferred ordering. Four false prior levels are used and the range of d^* is given for each operating point.

false prior is present, which was also found for motored cycles in table 7.4. As expected the individual parameter estimates depend upon the number of efficient parameters $d^\#$, the false prior level and what parameters that are classified as efficient. In order to have a true parameter deviation that is smaller than the false prior level, a maximum of eight parameters should be used according to the $\bar{\varepsilon}_x^t$ -column. For the motored case, this number was as low as three according to table 7.4. The $\bar{\varepsilon}_x^t$ -column also shows that $\bar{\varepsilon}_x^t$ is minimized by seven parameters, which is also the minimizer of the Akaike FPE for this particular cycle. This is more of a coincidence than a pattern.

If the individual estimates are considered, it is notable that the C_1 -estimate has the largest normalized bias in general, which was also the case for the motored cycles. Until C_1 is fixed the other parameters, especially T_{IVC} and b , and to some extent Q_{in} , K_p , and T_w , compensate for the bad C_1 -estimates. This results in biased estimates for these parameters as well. When C_1 is fixed, the pressure gain K_p and the mean wall temperature T_w still have considerable biases.

The two parameters γ_{300} and V_c was shown to be important in the sensitivity analysis in table 3.2. If the estimation accuracy of these two parameters would decide how many parameters to use, the answer would be eight parameters. This motivates why eight parameters are used for compression ratio estimation on firing cycles in chapter 5.

Due to the unsuccessful results of applying method 1 to setup 1 without a preferred ordering of the parameters, as well as the unsuccessful results for a preferred ordering for the motored case in section 7.1.3, the investigations concerning a preferred parameter ordering as well as setup 2 are left out.

Summary of method 1

To summarize, the usage of method 1 for estimating all the parameters in the presence of a false prior has not been successful, which confirms

$d^\#$	V_c [cm ³]	C_1 [-]	T_{IVC} [K]	p_{IVC} [kPa]	γ_{300} [-]	b [K ⁻¹]	T_w [K]	V_{cr} [cm ³]	Δp [kPa]	$\Delta\theta$ [deg]	K_p [-]	C_2 [m/(s K)]	Q_{in} [J]	θ_{ig} [deg ATDC]	$\Delta\theta_d$ [deg]	$\Delta\theta_b$ [deg]	$\bar{\varepsilon}_x^t$ [%]	$\bar{\varepsilon}_x^\#$ [%]
16	57.3	3.15	561	51.0	1.33	$-5.42 \cdot 10^{-5}$	552	0.27	2.5	0.08	1.02	$2.85 \cdot 10^{-4}$	544	-16.1	21.3	20.0	20.5	20.7
15	57.5	3.13	486	48.6	1.34	$-6.25 \cdot 10^{-5}$	524	0.5	3.5	0.06	1.05	$3.40 \cdot 10^{-4}$	513	-16.0	21.2	20.0	12.0	11.5
14	57.8	2.39	445	47.7	1.34	$-6.86 \cdot 10^{-5}$	396	0.5	3.7	0.07	1.07		488	-16.1	21.2	20.0	7.3	9.0
13	58.0		423	48.4	1.35	$-7.21 \cdot 10^{-5}$	390	0.5	4.1	0.08	1.05		493	-16.1	21.2	20.0	6.9	8.6
12	57.1		700	50.7	1.32	$-4.35 \cdot 10^{-5}$	549	0.12	1.4	0.11			540	-16.1	21.4	20.1	28.6	29.0
11	57.2		607	49.8	1.33	$-5.07 \cdot 10^{-5}$	504	0.32	2.4				523	-16.1	21.4	20.0	18.2	18.7
10	57.4		531	48.6	1.34	$-5.78 \cdot 10^{-5}$		0.62	3.7				506	-16.1	21.3	20.0	9.2	8.9
9	58.3		474	47.4	1.36	$-6.57 \cdot 10^{-5}$			5.3				488	-16.2	21.4	20.0	5.7	5.5
8	58.6		435	47.2	1.35	$-6.88 \cdot 10^{-5}$							484	-16.0	21.2	20.0	4.2	4.4
7	58.4			47.3	1.35	$-6.83 \cdot 10^{-5}$							485	-15.8	20.9	20.0	3.9	4.5
6	59.1			46.7	1.37	$-7.35 \cdot 10^{-5}$							478		20.9	19.9	4.3	4.3
5	54.8			47.1	1.32								528		21.4	19.6	4.8	4.7
4	59.9			52.5	1.32										20.9	18.9	4.4	3.3
3	61.5				1.32										20.0	21.0	4.3	2.1
2	61.7				1.32										20.0		4.4	2.1
1					1.33										21.0		4.5	1.6
$x^\#$	61.7	2.39	435	52.5	1.42	$-7.35 \cdot 10^{-5}$	504	0.62	5.3	0.11	1.05	$3.40 \cdot 10^{-4}$	528	-15.8	21.0	21.0	5.0	0.0
x^t	58.8	2.28	414	50.0	1.35	-7e-005	480	0.59	5.0	0.10	1.00	$3.24 \cdot 10^{-4}$	503	-15.0	20.0	20.0	0.0	5.0

Table 8.3: Method 1: Parameter estimates at OP1 for $d^\# \in [1, 16]$ parameters when using no preferred ordering and a false prior level of 5%. The true and nominal parameter deviations $\bar{\varepsilon}_x^t$ and $\bar{\varepsilon}_x^\#$ are given as RMSE-s of their relative values, i.e. $\bar{\varepsilon}_x^t = RMSE(\varepsilon_x^t)$ and $\bar{\varepsilon}_x^\# = RMSE(\varepsilon_x^\#)$.

the results found for the motored cycles in chapter 7. Minimizing the Akaike FPE criterion gives a recommended number of parameters between 3 and 16, which fluctuates with both operating point and noise realization and therefore hardly gives any guidance at all. If we instead just consider the true parameter deviation, a maximum of eight parameters can be used in order to yield a true parameter deviation that is less than the applied false prior level. For a specific application, like compression ratio estimation in section 5.3.4, eight parameters are recommended to be used.

Method 1 has also given valuable insight in which parameters that are most efficient. For instance it has been shown that γ_{300} is the most efficient parameter, given the structure of the standard model in section 3.8.

8.1.4 Method 2– Results and evaluation

Now the focus is turned to evaluating method 2. First the results are presented and then the performance of the three versions M2:1, M2:2 and M2:3 are evaluated using the two setups described previously in section 7.1.2.

Implementation details

The implementation details described in section 7.1.4 for motored cycles apply here as well and are therefore only repeated in a summarized manner. The interesting search region Δ_x for the regularization parameter δ_x is again chosen as $\delta_x \in [10^{-11}, 10^5]$, see figure 7.5, to assure that the L-shaped corner is included for all examined cases. When it comes to the three versions of method 2, the constants m_ε and m_δ for M2:1 and a_ε for M2:2 are computed in the same manner for both fired and motored cycles, see section 6.4.2 for details. Version M2:3 requires no choices to be made.

Results for setup 1

The results of method 2 are now given for setup 1, where the nominal values are given by $x^\# = (1 + \text{FP})x^t$ for $\text{FP} \in \{0, 1, 2.5, 5\}$ % and the assigned standard deviation $\sigma = 0.01x^t$ is equal for all parameters, yielding equal regularization elements δ_i , i.e. case 1 of δ_i ($\delta_i = c$).

An example of an L-curve is given in figure 8.3 for one engine cycle at OP1 and $\text{FP} = 5$ %. It also shows the true parameter deviation $\bar{\varepsilon}_x^t$ and the false prior level, as well as the results from the three versions of method 2 and the optimal choice of δ_x . As before, the optimal δ_x^* is determined as the one minimizing $\bar{\varepsilon}_x^t = \text{RMSE}(\varepsilon_x^t)$, for the δ_x :s used in the computation.

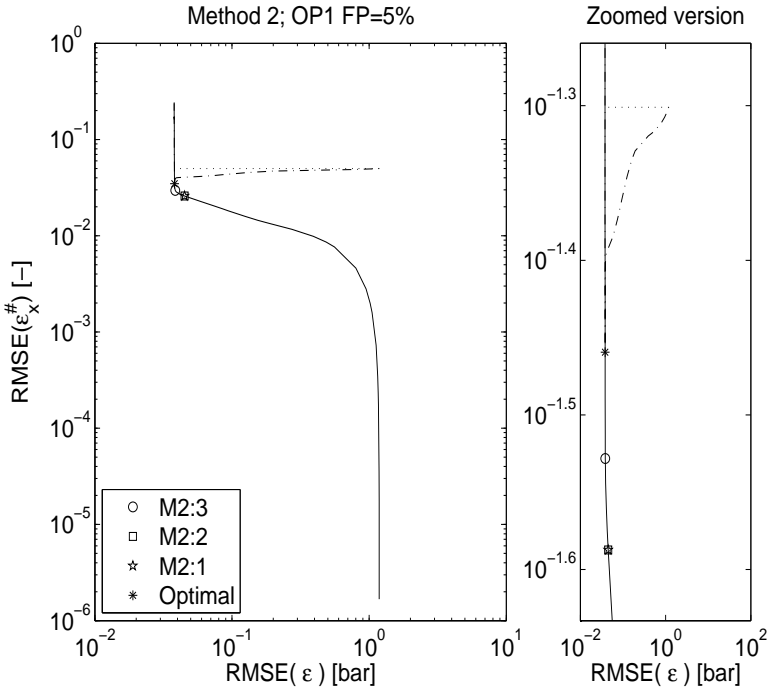


Figure 8.3: L-curve (solid line) for one engine cycle at OP1 with FP=5 % (dotted line) for setup 1. The results for the three versions of method 2 and the optimal choice of regularization parameter are indicated by the legend. The mean true parameter deviation $\bar{\varepsilon}_x^t$ (dash-dotted line) is also given.

The optimal δ_x^* is given in table 8.4 for all operating points and false prior levels used in setup 1. The corresponding true parameter deviations $\bar{\varepsilon}_x^t$ are summarized in table 8.5. The numerical values in both tables are given as mean values for the ten cycles.

Table 8.6 summarizes the results for all six operating points in terms of the true parameter deviation $\bar{\varepsilon}_x^t$ in percent as mean values of ten cycles at FP=5 %. The results are similar for the other false prior levels used. The mean and maximum difference compared to δ_x^* are also given, together with the mean computational time for completing the estimation of one engine cycle.

Table 8.7 shows the individual parameter estimates and the corresponding mean true and nominal parameter deviations $\bar{\varepsilon}_x^t$ and $\bar{\varepsilon}_x^{\#}$ at OP1 for FP = 5 %. The corresponding table for OP6 is given in table 8.8. These parameter values are computed as mean values for ten

FP [%]	1	2	3	4	5	6
0	$1 \cdot 10^5$					
1	0.085	0.091	0.095	0.56	0.15	0.0081
2.5	0.0062	0.011	0.051	0.0013	0.02	0.0033
5	0.002	0.0044	0.008	0.00098	0.019	0.0044

Table 8.4: Value of optimal regularization parameter δ_x^* , for setup 1 and operating points OP1 to OP6. For FP = 0 %, δ_x^* is the highest value used in the computation.

FP [%]	1	2	3	4	5	6
0	10^{-7}	10^{-7}	10^{-7}	10^{-7}	10^{-7}	10^{-7}
1	0.8	0.8	0.8	0.8	0.8	0.7
2.5	1.9	1.9	1.9	1.6	1.8	1.6
5	3.4	3.5	3.4	3.0	3.3	3.2

Table 8.5: Mean true parameter deviation $\bar{\varepsilon}_x^t$ [%] corresponding to optimal δ_x^* in table 8.4, for setup 1 and operating points OP1 to OP6.

consecutive cycles. The tables also entail the relative mean estimation error (RME) in percent, as well as numerical values for the true and (emphasized) nominal values.

Evaluation for setup 1

Evaluation for OP1: Figure 8.3 is very similar to figure 7.6 in that $\bar{\varepsilon}_x^t$ becomes smaller for a decreasing δ_x until it reaches its optimal value, and that all three versions of method 2 visually find positions close to the corner of the “L”. Note that the estimate lies in between the true value and the nominal (false) value, and therefore is a compromise between the data and the prior knowledge.

The placement order on the L-curve in figure 8.3 in which the versions occur is however somewhat altered compared to the motored case. As for the motored case, the approximative versions are a little more conservative than the optimal δ_x^* , resulting in higher values of δ_x and estimates that are closer to the nominal values. This is however preferable to a situation where δ_x is too low, which would result in parameter estimates that have drifted away from the nominal ones.

Just as for the motored case, the optimal regularization parameter δ_x^* is approximately the same for different noise realizations, but depends upon the operating point and false prior level used. Concerning the estimation accuracy, the true parameter deviation $\bar{\varepsilon}_x^t$ is fairly constant from cycle-to-cycle and different operating points, for a given FP

OP	δ_x^*	δ_x (M2:1)	δ_x (M2:2)	δ_x (M2:3)	$\text{mv}(\delta_x)$
1	3.4	4.1	4.1	4.0	4.0
2	3.5	4.0	4.0	3.9	3.9
3	3.4	4.1	4.1	4.0	4.0
4	3.0	4.0	4.0	4.0	4.0
5	3.3	4.0	4.0	3.9	4.0
6	3.2	3.9	3.9	3.6	3.8
Max Diff	0	0.98	1	0.95	0.95
Mean Diff	0	0.69	0.69	0.58	0.65
Time [s]	21275	296	9109	21275	358

Table 8.6: True parameter deviation $\bar{\varepsilon}_x^t$ for the optimal δ_x^* in table 8.4, the three versions of method 2 and as mean value for the optimal δ_x^* corresponding to table 8.4. The numerical values are given in percent and are evaluated for $FP = 5\%$ for setup 1. The mean computational time for completing the estimation for one engine cycle is also given, where the assumptions made are the same as for the motored cycles in section 7.1.4.

level. These statements are not shown, but are in accordance with the motored cycles and are based on the similarity of figures 7.8 and 7.9 for the motored cycles.

Evaluation for all OP:s. The focus is now turned to evaluating method 2 for all operating points. Table 8.4 shows that the optimal δ_x^* changes with the FP level and operating point, and the effect is most pronounced for changes in the FP level. However the estimation accuracy is approximately the same although the optimal δ_x^* varies depending on the operating point at a given FP level, as shown in table 8.5. The table also shows that the true parameter deviation $\bar{\varepsilon}_x^t$ is less than the false prior level used for $FP > 0\%$. This is all in accordance with what was concluded earlier for motored cycles.

Table 8.6 shows that the true parameter deviation is larger for the approximative versions of δ_x as compared to the optimal choice δ_x^* . However all estimates are a compromise between the true and nominal (false) values, and are somewhat biased towards the nominal ones. As illustrated earlier for figure 8.3, the approximative versions resulted in conservative δ_x :s, which in turn results in estimates that are close to the nominal ones, i.e. estimates that are over-smoothed by the regularization. The mean difference in $\bar{\varepsilon}_x^t$ compared to δ_x^* is in the order of 0.6-0.7% as indicated in the table. The difference in between the approximative versions is however relatively small. Compared to the corresponding motored case in table 7.10 the estimation accuracy for δ_x^* is higher for fired cycles, while the approximative versions yield approx-

imatively the same accuracy. Algorithm M2:3 however has the overall highest accuracy of the three versions, and is in the mean 0.1 % more accurate than M2:1 and M2:2 for all the examined operating points. These two versions yield approximately the same estimate and they could both be trimmed to give better estimates, which would however require ad-hoc tuning. This is therefore not pursued here since the goal has been to compute the values for the constants m_ε , m_δ and a_ε in the same way, regardless of operating point.

As pointed out in section 7.1.4, M2:1 (and M2:2) could have a disadvantage compared to M2:3 when changing operating conditions which could either result in some loss in estimation accuracy or requires an ad-hoc tuning of the parameters in M2:1. The former effect is seen in table 8.6 by comparing the columns for M2:1 and M2:3, especially for OP6. For the motored cycles this effect did not show up, which could be due to the simpler model of cylinder pressure, but is more likely due to that the changes in thermodynamic properties are larger when an operating point is changed for the firing cycles.

The computational time given in table 8.6 again shows that algorithm M2:1 and $mv(\delta_x^*)$ are the fastest and they differ merely due to that they use a different number of iterations to minimize the loss function W_N . Compared to M2:3, M2:1 is approximately 70 times faster according to table 8.6, while M2:2 is approximately 30 times slower than M2:1. As expected the computational time increases significantly for fired cycles as compared to motored, the increase is approximately a factor eight in the mean. The increase is due to the more complex model, more parameters to estimate and more iterations performed before convergence of the local optimizer for each specific δ_x .

Estimation accuracy for x_i : Now the focus is turned to the estimation accuracy for the individual parameters x_i . Tables 8.7 and 8.8 show that the estimates for C_1 , T_{IVC} , b , T_w , Δp , and especially for V_{cr} , $\Delta\theta$ and C_2 , are regularized to the vicinity of their respective nominal value $x_i^\#$, indicated by an RME close to 5 %. These eight parameters correspond fairly well with the order in which the parameters are set spurious for method 1 when no preferred ordering is used, compare (8.1). The difference is K_p , otherwise it corresponds to the eight most spurious parameters. The estimates for the other parameters, except for θ_{ig} and K_p , yield estimates that are in between the true and (false) nominal value. For all examined operating points the estimation accuracy is highest for γ_{300} , which has an overall RME within 1.5 %, closely followed by $\Delta\theta_b$ (1.6 %), p_{IVC} and Q_{in} (within 1.8 %). The accuracy for V_c is within 3.2 %.

The estimation accuracy also depends upon the routine used to determine the regularization parameter δ_x . From table 8.6 it was found that routine M2:3 gave the smallest overall mean error, followed by

δ_x :	V_c [cm^3]	C_1 [-]	T_{IVC} [K]	p_{IVC} [kPa]	γ_{300} [-]	b [K^{-1}]	T_w [K]	V_{cr} [cm^3]	Δp [kPa]	$\Delta \theta$ [deg]	K_p [-]	C_2 [$m/(sK)$]	Q_m [J]	θ_{ig} [deg ATDC]	$\Delta \theta_I$ [deg]	$\Delta \theta_b$ [deg]	$\bar{\varepsilon}_x^t$ [%]	$\bar{\varepsilon}_x^\#$ [%]
δ_x^*	59.0	2.40	422	50.3	1.356	$-7.02 \cdot 10^{-5}$	496	0.613	5.2	0.10	0.984	$3.41 \cdot 10^{-4}$	512	-15.7	20.8	20.0	3.3	3.3
RME	0.4	5.4	1.9	0.7	0.5	0.2	3.2	4.3	4.9	4.1	-1.6	5.2	1.7	4.8	3.9	-0.1	3.3	3.3
$\delta_x(M/2:1)$	60.7	2.40	435	50.9	1.366	$-7.31 \cdot 10^{-5}$	502	0.617	5.2	0.11	0.986	$3.40 \cdot 10^{-4}$	513	-15.9	20.8	20.2	4.1	2.5
RME	3.2	5.3	5.1	1.8	1.2	4.5	4.7	5.0	4.8	5.0	-1.4	5.1	1.8	6.0	3.8	1.2	4.1	2.5
$\delta_x(M/2:2)$	60.5	2.40	435	50.8	1.369	$-7.3 \cdot 10^{-5}$	502	0.617	5.2	0.11	0.982	$3.40 \cdot 10^{-4}$	512	-15.9	20.8	20.2	4.1	2.6
RME	3.0	5.3	5.0	1.6	1.4	4.3	4.6	4.9	4.8	5.0	-1.8	5.1	1.6	5.9	3.9	0.8	4.1	2.6
$\delta_x(M/2:3)$	59.7	2.40	433	50.5	1.369	$-7.25 \cdot 10^{-5}$	501	0.617	5.2	0.10	0.975	$3.41 \cdot 10^{-4}$	512	-15.9	20.9	20.0	3.9	2.9
RME	1.6	5.4	4.5	1.0	1.4	3.5	4.5	4.9	4.9	5.0	-2.5	5.1	1.7	5.7	4.6	-0.1	3.9	2.9
$x^\#$	61.7	2.39	435	52.5	1.418	$-7.35 \cdot 10^{-5}$	504	0.617	5.3	0.11	1.050	$3.40 \cdot 10^{-4}$	528	-15.8	21.0	21.0	5.0	0.0
RME($x^\#$)	5.0	5.0	5.0	5.0	5.0	5.0	5.0	5.0	5.0	5.0	5.0	5.0	5.0	5.0	5.0	5.0	5.0	0.0
x^t	58.8	2.28	414	50.0	1.350	$-7 \cdot 10^{-5}$	480	0.588	5.0	0.10	1.000	$3.24 \cdot 10^{-4}$	503	-15.0	20.0	20.0	0.0	5.0

Table 8.7: Parameter estimates and corresponding relative mean estimation error (RME) for OP1 at FP = 5 %, using method 2, setup 1 and case 1 ($\delta_i = c$).

δ_i :	V_c [cm ³]	C_1 [-]	T_{IVC} [K]	p_{IVC} [kPa]	γ_{IVC} [-]	b [K ⁻¹]	T_w [K]	V_{c^*} [cm ³]	Δp [kPa]	$\Delta \theta$ [deg]	K_p [-]	C_2 [m/(s K)]	Q_{in} [J]	θ_{ig} [deg AIDC]	$\Delta \theta_t$ [deg]	$\Delta \theta_b$ [deg]	$\frac{\varepsilon^t}{\varepsilon^*}$ [%]	$\frac{\varepsilon^t}{\varepsilon^*}$ [%]	
δ^*	59.7	2.40	375	101.3	1.358	-6.97 · 10 ⁻⁵	414	0.620	5.3	0.10	0.980	3.40 · 10 ⁻⁴	1210	-25.2	15.2	29.8	3.2	3.7	
RME	1.5	5.3	1.2	1.3	0.6	-0.4	3.5	5.4	5.3	4.9	-2.0	4.8	1.4	0.7	1.2	-0.6	3.2	3.7	
$\delta_x (M2 : 1)$	60.4	2.40	386	101.2	1.370	-7.24 · 10 ⁻⁵	418	0.617	5.2	0.10	0.975	3.40 · 10 ⁻⁴	1211	-25.8	15.8	29.5	3.9	3.1	
RME	2.7	5.4	4.2	1.2	1.5	3.4	4.6	4.9	4.9	4.9	-2.5	5.0	1.5	3.3	5.3	-1.6	3.9	3.1	
$\delta_x (M2 : 2)$	60.4	2.40	386	101.1	1.368	-7.26 · 10 ⁻⁵	419	0.617	5.2	0.10	0.978	3.40 · 10 ⁻⁴	1214	-25.9	15.8	29.6	3.9	3.0	
RME	2.7	5.3	4.3	1.1	1.4	3.7	4.6	4.9	4.9	5.0	-2.2	5.0	1.8	3.6	5.4	-1.2	3.9	3.0	
$\delta_x (M2 : 3)$	60.5	2.41	383	101.3	1.369	-7.15 · 10 ⁻⁵	417	0.617	5.3	0.10	0.975	3.40 · 10 ⁻⁴	1206	-25.6	15.5	29.5	3.6	3.2	
RME	2.9	5.6	3.4	1.3	1.4	2.2	4.2	4.9	5.1	4.9	-2.5	5.1	1.2	2.3	3.6	-1.6	3.6	3.2	
$x^{\#}$	61.7	2.39	389	105.0	1.418	-7.35 · 10 ⁻⁵	420	0.617	5.3	0.11	1.050	3.40 · 10 ⁻⁴	1252	-26.3	15.8	31.5	5.0	0.0	
RME($x^{\#}$)	5.0	5.0	5.0	5.0	5.0	5.0	5.0	5.0	5.0	5.0	5.0	5.0	5.0	5.0	5.0	5.0	5.0	0.0	0.0
x^t	58.8	2.28	370	100.0	1.350	-7 · 10 ⁻⁵	400	0.588	5.0	0.10	1.000	3.24 · 10 ⁻⁴	1193	-25.0	15.0	30.0	0.0	0.0	5.0

Table 8.8: Parameter estimates and corresponding relative mean estimation error (RME) for OP6 at FP = 5 %, using method 2, setup 1 and case 1 ($\delta_i = c$).

M2:1 and M2:2. When considering the individual estimates of the five parameters, the same relative ordering is found if all six operating points are considered. In the case for M2:3 the accuracy of the estimates for the five parameters is within 3 %. This value is larger than the 0.5 % which was found for the corresponding motored case, and is probably due to the more complex model structure and harder estimation problem in the fired case. The other estimates end up as a compromise in between the true value and the (false) nominal value, except for θ_{ig} and K_p . In the case of the two parameters Δp and C_2 , these two estimates coincide with the nominal values for all cases of δ_x in table 8.7. For the two parameters V_{cr} and $\Delta\theta$ the estimates coincide with the nominal ones for the approximative versions, but not for the optimal choice of δ_x .

As pointed out for the motored case, in the presence of a false prior of 5 % the estimates for method 2 are equally or more accurate compared to method 1 for all number of, except seven, efficient parameters, as shown by comparing the $\bar{\varepsilon}_x^t$ -columns in tables 8.3 and 8.7. This again illustrates that method 2 is more robust to a false prior than method 1 and this results in better estimates. The difference between method 1 and method 2 are however smaller in the fired case.

Results for setup 2

The results for method 2 is now presented for setup 2, where the nominal values are given by $x_i^\# = (1 + \sigma_i)x_i^t$, for which the standard deviations are given in table 8.1. The assigned regularization elements are given for the two cases $\delta_i = c$ and $\delta_i \neq c$. The first case is $\delta_i = \frac{1}{2N} \frac{1}{(0.01x_i^t)^2}$, i.e. all elements are equal, and in the second case $\delta_i = \frac{1}{2N\sigma_i^2}$. The tables and figures follow the same structure as for the corresponding motored case in section 7.1.4.

The L-curves based on one engine cycle for each case at OP1 are given in figures 8.4 and 8.5 respectively. The individual parameter estimates are given in tables 8.10–8.13, and corresponds to the form used in table 8.7. Tables 8.10 and 8.11 represent case 1 ($\delta_i = c$) for OP1 and OP6, while the corresponding tables for case 2 ($\delta_i \neq c$) are given in tables 8.12 and 8.13. It is worth to mention again that the second case uses the weighted versions of the nominal parameter deviation $RMSE(L^\delta \varepsilon_x^\#)$ and so on in the tables and figures. Therefore the optimal regularization parameter δ_x^* is now determined as the one minimizing the weighted true parameter deviation, i.e. $RMSE(L^\delta \varepsilon_x^t)$. The nominal and true parameter deviations $\bar{\varepsilon}_x^t$ and $\bar{\varepsilon}_x^\#$ for both cases at OP1 and OP6 are then summarized in table 8.9.

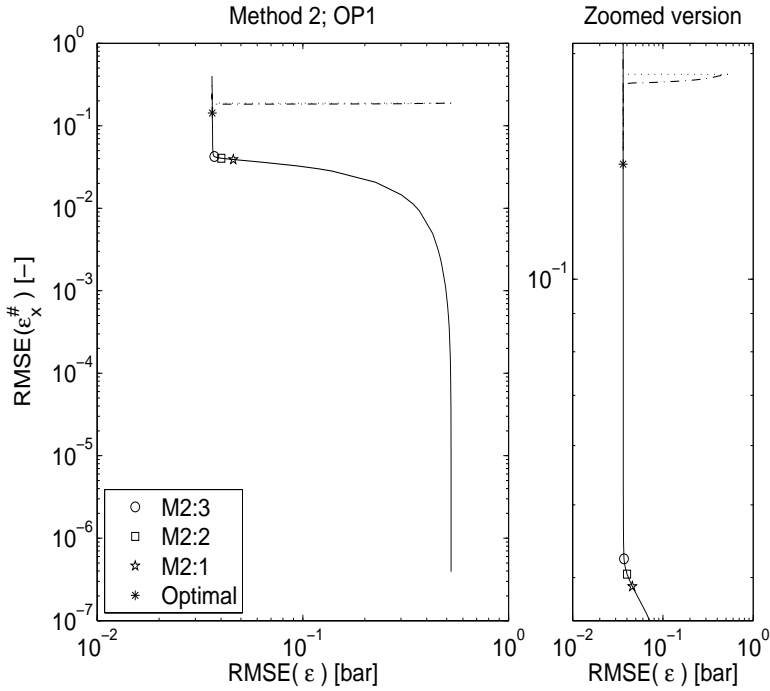


Figure 8.4: L-curve (solid line) for one engine cycle at OP1 with false prior $\bar{\varepsilon}_x^{\#-t}$ (dotted line), when using setup 2 and case 1 of the δ_i ($\delta_i = c$). The results for the three versions of method 2 and the optimal choice of regularization parameter are indicated by the legend. The true parameter deviation $\bar{\varepsilon}_x^t$ (dash-dotted line) is also given.

Evaluation for setup 2

Evaluation for OP1: Figures 8.4 and 8.5 both illustrate the L-shaped curve which was also found for the corresponding motored case. The three approximative versions of method 2 all yield estimates that are close to the corner of the “L”. This is however not the case for the optimal regularization parameter. Figure 8.4 ($\delta_i = c$) shows that the optimal δ_x^* is not as close to the corner as in the approximative versions. This is directly reflected in the parameter estimates for δ_x^* that are close to the true values. They are closer than the estimates from the approximative versions, as seen in the $\bar{\varepsilon}_x^t$ - and $\bar{\varepsilon}_x^{\#}$ -columns in tables 8.10 and 8.11. For $\delta_i \neq c$ the optimal δ_x^* is closer to the corner as shown in figure 8.5, which is also reflected in a better consistency between the optimal and approximative versions. It also reflects a better

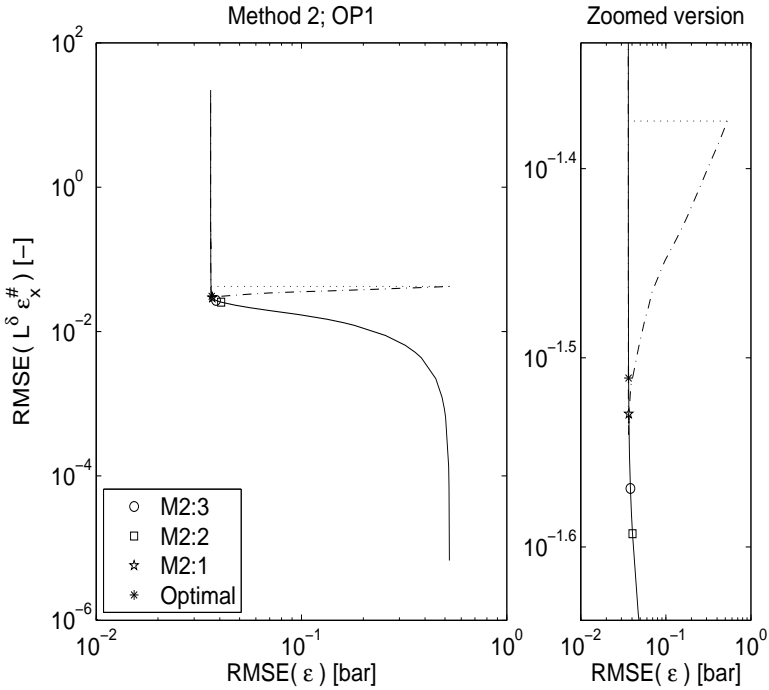


Figure 8.5: L-curve (solid line) for one engine cycle at OP1 with weighted false prior $RMSE(L^\delta \varepsilon_x^{\#-t})$ (dotted line), when using setup 2 and case 2 of the δ_i ($\delta_i \neq c$). The results for the three versions of method 2 and the optimal choice of regularization parameter are indicated by the legend. The weighted true parameter deviation $RMSE(L^\delta \varepsilon_x^t)$ (dash-dotted line) is also given.

δ_x :	$\delta_i = c$				$\delta_i \neq c$			
	OP1		OP6		OP1		OP6	
	$\bar{\varepsilon}_x^t$ [%]	$\bar{\varepsilon}_x^\#$ [%]	$\bar{\varepsilon}_x^t$ [%]	$\bar{\varepsilon}_x^\#$ [%]	$\bar{\varepsilon}_x^t$ [%]	$\bar{\varepsilon}_x^\#$ [%]	$\bar{\varepsilon}_x^t$ [%]	$\bar{\varepsilon}_x^\#$ [%]
δ_x^*	6.5	16.6	6.2	17.7	5.8	15.2	11.2	16.0
$\delta_x(M2:1)$	18.3	3.8	18.3	3.2	11.1	12.7	14.3	11.7
$\delta_x(M2:2)$	18.3	4.1	18.3	3.3	12.8	10.4	13.8	8.6
$\delta_x(M2:3)$	18.2	4.3	18.2	3.9	11.4	12.5	12.6	11.9
$x^\#$	18.8	0.0	18.7	0.0	18.8	0.0	18.7	0.0
x^t	0.0	18.8	0.0	18.7	0.0	18.8	0.0	18.7

Table 8.9: Mean true and nominal parameter deviation for method 2 using two cases of δ_i at OP1 and OP6 for setup 2.

(weighted) compromise between $L^\delta \varepsilon_x^t$ and $L^\delta \varepsilon_x^\#$, as they are equal in size in tables 8.12 and 8.13. This speaks in favor of using $\delta_i \neq c$.

Evaluation for the individual estimates x_i : Now consider the estimation accuracy of the individual parameters x_i , and especially the estimates produce by M2:1, M2:2 and M2:3. Tables 8.10 and 8.11 show that the estimates for the parameters C_1 , b , and especially for V_{cr} , Δp , $\Delta\theta$ and C_2 are regularized to the vicinity of their respective nominal value $x_i^\#$, indicated by an RME that is close to the one for the nominal parameter values. Most of the remaining parameters end up in the region between the true and nominal values, except for the estimates of C_1 , V_c , γ_{300} and K_p . These parameters end up just outside of the region with estimates that are within 6 % for the worst case (K_p).

For $\delta_i \neq c$, tables 8.12 and 8.13 show that C_1 , T_{IVC} , γ_{300} , T_w , V_{cr} , $\Delta\theta$ and C_2 end up near their respective nominal value, while the burn angle parameters θ_{ig} , $\Delta\theta_d$ and $\Delta\theta_b$, and the released energy Q_{in} yield estimates within 2.3 %. The estimates of the four parameters V_c , γ_{300} , Q_{in} and $\Delta\theta_b$ are again better for $\delta_i \neq c$ than $\delta_i = c$, while the accuracy of p_{IVC} is approximately the same.

The conclusion from tables 8.10-8.13 is that the regularization is used to pull parameters that are hard to estimate toward their nominal values, while the efficient parameters are free to fit the data. This was the drive for using method 2, and it works as intended.

Evaluation for all OP:s: Table 8.9 shows that for $\delta_i = c$ the true parameter deviation $\bar{\varepsilon}_x^t$ is almost as large as the false prior level used, while for $\delta_i \neq c$ the true and nominal parameter deviations $\bar{\varepsilon}_x^t$ and $\bar{\varepsilon}_x^\#$ are approximately equal in size. This is also illustrated in the weighted true and nominal parameter deviations, $L^\delta \varepsilon_x^t$ and $L^\delta \varepsilon_x^\#$, in tables 8.12 and 8.13. As pointed out earlier, it reflects a better compromise between prior knowledge and measurement data for the second case. From table 8.9 it can also be concluded that the true parameter deviation $\bar{\varepsilon}_x^t$ is smaller for the second case for all three versions of method 2, which also was the case for evaluation based upon motored cycles, see table 7.13. As for the corresponding motored case the mean nominal parameter deviation $\bar{\varepsilon}_x^\#$ is relatively small for $\delta_i = c$ and significantly higher for $\delta_i \neq c$. This together with the smaller $\bar{\varepsilon}_x^t$ reflects that the second case is more robust to a false prior, which of course is preferable. Note that the false prior level for the fired cycles is smaller than for the motored cycles, which is due to the larger number of parameters and that the RME of the false prior in setup 2 for Δp and $\Delta\theta$ are 50 %, see table 8.1.

Now the attention is turned to finding which version of method 2 that performs the best. In the case of $\delta_i = c$ all three versions are restrictive and yield estimates close to the nominal values. This is, as pointed out previously, reflected by a relatively low value of $\bar{\varepsilon}_x^\#$ in

δ_x :	V_c [cm^3]	C_1 [-]	T_{IVC} [K]	p_{IVC} [kPa]	γ_{300} [-]	b [K^{-1}]	T_w [K]	V_{cr} [cm^3]	Δp [kPa]	$\Delta\theta$ [deg]	K_p [-]	C_2 [$m/(sK)$]	Q_{in} [J]	θ_{ig} [deg ATDC]	$\Delta\theta_d$ [deg]	$\Delta\theta_b$ [deg]	ε_x^t [%]	$\varepsilon_x^\#$ [%]
δ_x^*	58.4	2.68	436	49.3	1.349	$-6.77 \cdot 10^{-5}$	505	0.71	5.1	0.11	1.011	$3.49 \cdot 10^{-4}$	509	-15.5	20.6	20.0	6.5	16.6
RME	-0.6	17.5	5.2	-1.4	-0.1	-3.2	5.2	21.4	1.9	14.1	1.1	7.6	1.2	3.4	3.2	0.1	6.5	16.6
$\delta_x(M2:1)$	58.6	2.40	422	50.3	1.375	$-7.92 \cdot 10^{-5}$	487	0.74	7.5	0.15	0.956	$3.57 \cdot 10^{-4}$	527	-14.9	20.3	20.4	18.3	3.8
RME	-0.3	5.3	1.9	0.5	1.9	13.1	1.5	25.4	49.9	50.0	-4.4	10.1	4.6	-0.5	1.3	2.0	18.3	3.8
$\delta_x(M2:2)$	58.8	2.40	421	50.2	1.379	$-7.89 \cdot 10^{-5}$	487	0.74	7.5	0.15	0.949	$3.57 \cdot 10^{-4}$	524	-14.9	20.2	20.1	18.3	4.1
RME	-0.0	5.4	1.7	0.4	2.1	12.7	1.4	25.5	49.9	50.0	-5.1	10.1	4.1	-0.4	1.2	0.7	18.3	4.1
$\delta_x(M2:3)$	59.2	2.41	418	50.4	1.381	$-7.8 \cdot 10^{-5}$	485	0.74	7.5	0.15	0.946	$3.57 \cdot 10^{-4}$	520	-15.0	20.3	20.0	18.2	4.3
RME	0.7	5.6	0.9	0.8	2.3	11.5	1.0	25.5	49.9	50.0	-5.4	10.1	3.4	0.2	1.5	-0.1	18.2	4.3
$x^\#$	59.3	2.39	424	52.5	1.355	$-8 \cdot 10^{-5}$	490	0.74	7.5	0.15	1.005	$3.56 \cdot 10^{-4}$	528	-14.0	22.0	22.0	18.8	0.0
RME($x^\#$)	0.9	5.0	2.4	5.0	0.4	14.3	2.1	25.5	50.0	50.0	0.5	10.0	5.0	-6.7	10.0	10.0	18.8	0.0
x^t	58.8	2.28	414	50.0	1.350	$-7 \cdot 10^{-5}$	480	0.59	5.0	0.10	1.000	$3.24 \cdot 10^{-4}$	503	-15.0	20.0	20.0	0.0	18.8

Table 8.10: Parameter estimates and corresponding relative mean estimation error (RME) for OP1 when $\delta_i = c$, using method 2 and setup 2.

δ_x :	V_c [cm^3]	C_1 [-]	T_{IVC} [K]	p_{IVC} [kPa]	γ_{300} [-]	b [K^{-1}]	T_w [K]	V_{cr} [cm^3]	Δp [kPa]	$\Delta \theta$ [deg]	K_p [-]	C_2 [$m/(sK)$]	Q_{in} [J]	θ_{ig} [deg ATDC]	$\Delta \theta_d$ [deg]	$\Delta \theta_h$ [deg]	$\bar{\varepsilon}_x$ [%]	$\bar{\varepsilon}_x^\#$ [%]
δ_x^*	58.9	2.28	369	101.8	1.352	$-6.91 \cdot 10^{-5}$	386	0.86	5.0	0.11	0.980	$3.28 \cdot 10^{-4}$	1217	-24.9	15.0	29.9	6.2	17.7
RME		-0.2	-0.2	1.8	0.2	-1.3	-3.4	46.1	-0.9	12.8	-2.0	1.4	2.1	-0.4	-0.3	-0.2	6.2	17.7
$\delta_x(M2:1)$	58.1	2.40	376	98.6	1.373	$-7.89 \cdot 10^{-5}$	408	0.74	7.5	0.15	0.970	$3.57 \cdot 10^{-4}$	1221	-25.5	16.1	29.9	18.3	3.2
RME		5.4	1.7	-1.4	1.7	12.7	2.1	25.4	50.0	50.0	-3.0	10.1	2.4	2.1	7.3	-0.3	18.3	3.2
$\delta_x(M2:2)$	58.7	2.41	375	99.0	1.375	$-7.85 \cdot 10^{-5}$	407	0.74	7.5	0.15	0.969	$3.57 \cdot 10^{-4}$	1216	-25.5	16.0	29.8	18.3	3.3
RME		5.5	1.3	-1.0	1.9	12.1	1.9	25.4	50.1	50.0	-3.1	10.1	2.0	2.1	6.6	-0.8	18.3	3.3
$\delta_x(M2:3)$	60.1	2.42	369	99.9	1.377	$-7.67 \cdot 10^{-5}$	405	0.74	7.5	0.15	0.969	$3.57 \cdot 10^{-4}$	1203	-25.4	15.6	29.6	18.2	3.9
RME		2.3	5.9	-0.3	2.0	9.6	1.1	25.5	50.3	49.9	-3.1	10.1	0.8	1.8	4.2	-1.4	18.2	3.9
$x^\#$	59.3	2.39	380	102.5	1.355	$-8 \cdot 10^{-5}$	410	0.74	7.5	0.15	1.005	$3.56 \cdot 10^{-4}$	1218	-24.0	17.0	32.0	18.7	0.0
RME($x^\#$)		0.9	5.0	2.7	0.4	14.3	2.5	25.5	50.0	50.0	0.5	10.0	2.1	-4.0	13.3	6.7	18.7	0.0
x^t	58.8	2.28	370	100.0	1.350	$-7 \cdot 10^{-5}$	400	0.59	5.0	0.10	1.000	$3.24 \cdot 10^{-4}$	1193	-25.0	15.0	30.0	0.0	18.7

Table 8.11: Parameter estimates and corresponding relative mean estimation error (RME) for OP6 when $\delta_i = c$, using method 2 and setup 2.

δ_x :	V_c [cm ³]	C_1 [-]	T_{IVC} [K]	p_{IVC} [kPa]	γ_{300} [-]	b [K ⁻¹]	T_w [K]	V_{cr} [cm ³]	Δp [kPa]	$\Delta\theta$ [deg]	K_p [-]	C_2 [m/(sK)]	Q_{in} [J]	θ_{ig} [deg.ATDC]	$\Delta\theta_d$ [deg]	$\Delta\theta_b$ [deg]	$L^{\delta} \epsilon_x^t$ [%]	$L^{\delta} \epsilon_x^{\#}$ [%]
δ_x^*	58.8	2.38	421	49.5	1.352	-6.89 · 10 ⁻⁶	491	0.74	5.1	0.12	1.004	3.54 · 10 ⁻⁴	504	-15.3	20.4	20.0	2.5	3.2
RME	0.1	4.5	1.8	-0.9	0.2	-1.5	2.2	25.5	2.5	20.2	0.4	9.3	0.2	1.8	1.9	0.1	2.5	3.2
$\delta_x(M2:1)$	59.0	2.40	423	49.5	1.355	-6.96 · 10 ⁻⁶	490	0.74	5.3	0.14	1.004	3.58 · 10 ⁻⁴	503	-15.0	20.1	20.0	2.9	2.9
RME	0.4	5.3	2.1	-1.1	0.4	-0.6	2.1	25.5	5.2	42.5	0.4	10.5	-0.0	-0.0	0.6	0.1	2.9	2.9
$\delta_x(M2:2)$	59.2	2.40	424	49.7	1.355	-7.18 · 10 ⁻⁶	490	0.74	5.7	0.15	1.004	3.58 · 10 ⁻⁴	507	-14.7	19.8	19.9	3.1	2.6
RME	0.7	5.4	2.3	-0.6	0.4	2.5	2.0	25.5	14.0	47.6	0.4	10.5	0.8	-2.3	-0.9	-0.3	3.1	2.6
$\delta_x(M2:3)$	59.1	2.40	423	49.5	1.355	-6.98 · 10 ⁻⁶	490	0.74	5.3	0.14	1.004	3.58 · 10 ⁻⁴	504	-14.8	20.0	20.0	3.0	2.8
RME	0.5	5.4	2.2	-0.9	0.4	-0.3	2.0	25.5	5.6	43.5	0.4	10.5	0.1	-1.0	-0.1	0.1	3.0	2.8
$x^{\#}$	59.3	2.39	424	52.5	1.355	-8 · 10 ⁻⁶	490	0.74	7.5	0.15	1.005	3.56 · 10 ⁻⁴	528	-14.0	22.0	22.0	4.2	0.0
RME($x^{\#}$)	0.9	5.0	2.4	5.0	0.4	14.3	2.1	25.5	50.0	50.0	0.5	10.0	5.0	-6.7	10.0	10.0	4.2	0.0
x^t	58.8	2.28	414	50.0	1.350	-7 · 10 ⁻⁵	480	0.59	5.0	0.10	1.000	3.24 · 10 ⁻⁴	503	-15.0	20.0	20.0	0.0	4.2

Table 8.12: Parameter estimates and corresponding relative mean estimation error (RME) for OP1 when $\delta_i \neq c$, using method 2 and setup 2.

δ_x :	V_c [cm ³]	C_1 [-]	T_{IVC} [K]	p_{IVC} [kPa]	γ_{300} [-]	b [K ⁻¹]	T_w [K]	V_{c_p} [cm ³]	Δp [kPa]	$\Delta\theta$ [deg]	K_p [-]	C_2 [m/(s K)]	Q_{in} [J]	θ_{ig} [deg ATDC]	$\Delta\theta_d$ [deg]	$\Delta\theta_b$ [deg]	$L^{\delta} \varepsilon_x^t$ [%]	$L^{\delta} \varepsilon_x^{\#}$ [%]
δ^*	59.1	2.35	381	99.8	1.350	-6.61 · 10 ⁻⁵	407	0.74	4.6	0.14	1.003	3.38 · 10 ⁻⁴	1196	-25.0	15.0	30.0	2.4	3.3
RME	0.6	3.0	2.9	-0.2	0.0	-5.6	1.8	25.5	-8.1	43.4	0.3	4.3	0.3	-0.2	0.2	0.1	2.4	3.3
$\delta_x(M/2; 1)$	59.2	2.41	380	99.2	1.354	-6.75 · 10 ⁻⁵	409	0.74	5.5	0.15	1.003	3.58 · 10 ⁻⁴	1193	-25.0	15.1	30.0	3.0	3.0
RME	0.7	5.8	2.6	-0.8	0.3	-3.6	2.3	25.5	9.8	54.7	0.3	10.5	0.1	-0.2	0.5	-0.0	3.0	3.0
$\delta_x(M/2; 2)$	59.2	2.41	380	99.7	1.354	-7 · 10 ⁻⁶	409	0.74	6.2	0.15	1.003	3.57 · 10 ⁻⁴	1200	-24.7	14.9	29.8	3.0	2.6
RME	0.7	5.7	2.7	-0.3	0.3	-0.0	2.3	25.5	23.2	48.3	0.3	10.3	0.6	-1.3	-0.7	-0.7	3.0	2.6
$\delta_x(M/2; 3)$	59.2	2.41	380	99.2	1.354	-6.75 · 10 ⁻⁵	409	0.74	5.4	0.15	1.003	3.58 · 10 ⁻⁴	1193	-25.0	15.1	30.0	2.9	3.0
RME	0.7	5.8	2.6	-0.8	0.3	-3.6	2.3	25.5	8.8	47.9	0.3	10.4	0.1	-0.1	0.6	-0.0	2.9	3.0
$x^{\#}$	59.3	2.39	380	102.5	1.355	-8 · 10 ⁻⁵	410	0.74	7.5	0.15	1.005	3.56 · 10 ⁻⁴	1218	-24.0	17.0	32.0	4.2	0.0
RME($x^{\#}$)	0.9	5.0	2.7	2.5	0.4	14.3	2.5	25.5	50.0	50.0	0.5	10.0	2.1	-4.0	13.3	6.7	4.2	0.0
x^t	58.8	2.28	370	100.0	1.350	-7 · 10 ⁻⁵	400	0.59	5.0	0.10	1.000	3.24 · 10 ⁻⁴	1193	-25.0	15.0	30.0	0.0	4.2

Table 8.13: Parameter estimates and corresponding relative mean estimation error (RME) for OP6 when $\delta_i \neq c$, using method 2 and setup 2.

table 8.9. Out of these three, M2:3 performs best, but the difference is small and the estimation bias is still significant as reflected by the $\bar{\varepsilon}_x^t$ -columns.

In the case of $\delta_i \neq c$, all three versions render weighted parameter deviations $RMSE(L^\delta \varepsilon_x^t)$ and $RMSE(L^\delta \varepsilon_x^\#)$ that are approximately the same and fairly close to the optimal, see tables 8.12 and 8.13. Table 8.9 shows that $\bar{\varepsilon}_x^t$ is smallest for M2:1 at OP1 and for M2:3 at OP6. However when considering $\bar{\varepsilon}_x^t$ for all investigated operating points, it is lowest for M2:3 followed by M2:2 and M2:1 for all six operating points except OP1.

8.1.5 Summary for simulation results

Method 1 resulted in parameter estimates that are significantly biased in the presence of a false prior, since the bias is larger than the false prior level used. It is therefore in itself not recommended to use for estimation of all parameters in the given formulation. When the true parameter deviation is available, the number of efficient parameters can be determined for a specific application such as for example compression ratio estimation.

Method 2 outperforms method 1 since it is more robust to a false prior level and yields more accurate parameter estimates. The drive for method 2 was to regularize the solution such that the parameters that are hard to determine are pulled towards their nominal values, while the efficient parameters are free to fit the data. This has shown to be the case in the simulations for both fired and motored cycles.

The user can chose between two cases of the parameter uncertainty, namely $\delta_i = c$ and $\delta_i \neq c$. The former is directly applicable once nominal values of the parameters are determined and yields good estimates. The second case is however more robust to false prior as seen in setup 2, and it is therefore recommended since it pays off in better estimates.

Method 2 is given three versions; For the fired cycles it has been shown that M2:3 yields the best estimates in terms of estimation accuracy. For motored cycles it was shown that M2:1 could be used in all the examined operating points without any noticeable loss in estimation accuracy. This has not been the case for the fired cycles, where a change in operating conditions changes the thermodynamic properties more significantly and results in larger biases for M2:1 than for M2:3. The difference in estimation accuracy between M2:1 and M2:3 is however small, within 0.3 % and 2 % for setup 1 and 2 respectively, while the difference in computational time is more significant. Thus if time is available the recommendation is to use M2:3, while if computational time is an important feature M2:1 is recommended.

8.2 Experimental results – fired cycles

The methods will now be evaluated on experimental engine data. The structure of the section is similar to the corresponding motored case, i.e. section 7.2. Thus first the experimental engine data will be described, followed by a discussion on the parameter prior knowledge used. The focus is then turned to evaluating the performance of method 1, followed by method 2.

8.2.1 Experimental engine data

Data is collected during stationary operation at engine speeds $N \in [1200, 3500]$ rpm, intake manifold pressures $p_{man} \in [32, 130]$ kPa and ignition angle $\theta_{ig} \in [-33, -5]$ deg ATDC, altogether forming six different operating points. These operating points are defined in the upper part of table 8.14, and are also given in table C.9 in appendix C.7.

For each operating point 101 consecutive fired cycles were sampled for two cylinders with a crank-angle resolution of 1 degree, using an AVL GU21D cylinder pressure sensor. But due to the longer computational time for firing cycles as compared to motored, especially for M2:3 as shown in table 8.6, only the first 40 cycles will be considered in the evaluation. Figure 8.6 displays one measured cycle for each operating point. The operating points are numbered in an ascending order of their maximum cylinder pressure.

8.2.2 Parameter prior knowledge

The parameter prior knowledge used in the experimental evaluation is based on different strategies to set the nominal parameter values $x^\#$ and the regularization elements δ_i .

Nominal parameter values $x^\#$

The nominal parameter values $x^\#$ are set based on a combination of the parameter initial methods described in chapter 3 and expert prior knowledge of what the numerical value of $x^\#$ should be. The values for $x^\#$ for each operating point are given as the emphasized values in table 8.15. The nominal values are also given in table C.10 in appendix C.7. Of these parameters it is only the nominal values for Δp , $\Delta\theta_d$ and $\Delta\theta_b$ that are updated for each cycle, and therefore for these three, their respective mean value is given in the table. The other parameters are updated for each operating condition.

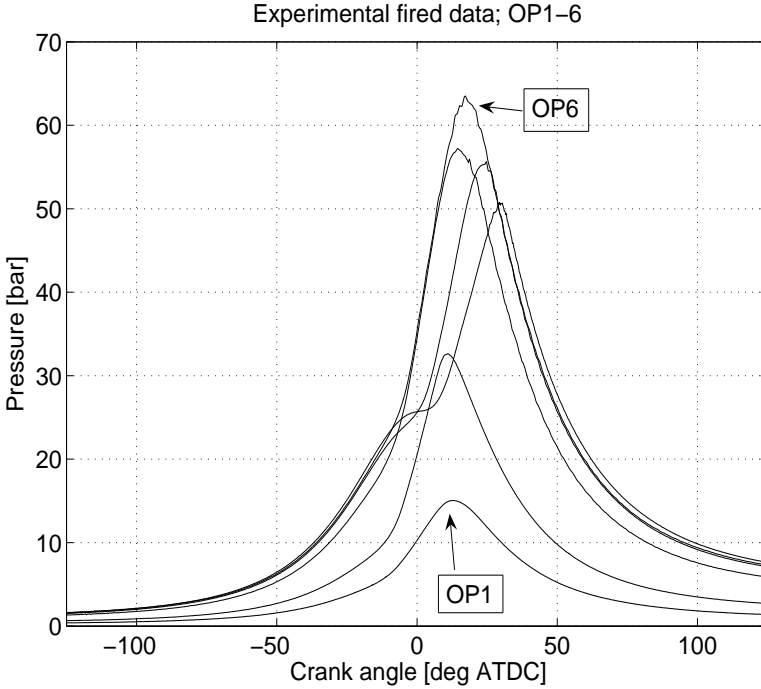


Figure 8.6: Experimentally measured fired cylinder pressures at operating conditions OP1–6.

Regularization elements δ_i

Two cases of regularization parameter elements are used for method 2 and they correspond to the two cases used in the simulation-based evaluation done previously. The first case ($\delta_i = c$) sets the standard deviation σ_i for each parameter as $\sigma_i = 0.01\bar{x}_i^\#$, where $\bar{x}_i^\#$ is the mean value of $x_i^\#$ for one operating point. It is used to assure that σ_i does not fluctuate in size from cycle-to-cycle. In the simulation-based evaluation x^t was used instead of $\bar{x}^\#$.

The second case ($\delta_i \neq c$) is based on expert knowledge of the uncertainty for each parameter and it is therefore subjectively chosen by the user. The standard deviation used here in the experimental evaluation coincides with the one used for the simulation-based evaluation in table 8.1.

The first case is updated for each operating point, while this is not required for the second case.

	OP1	OP2	OP3	OP4	OP5	OP6
N [rpm]	1200	1500	1500	2000	3000	3500
p_{man} [kPa]	32	55	130	123	103	120
θ_{ig} [deg ATDC]	-33	-26	-5	-12	-28	-24
mean(d^*)	13.2	13.2	13.1	11.8	13.6	14.3
$d^* \in$	[11, 16]	[12, 16]	[9, 16]	[10, 15]	[11, 16]	[11, 16]

Table 8.14: Mean number and region of d^* for 40 experimental cycles at OP1–6.

8.2.3 Method 1– Results and evaluation

Method 1 is evaluated without a preferred ordering, since no gain was found in the simulation-based evaluation by using one in section 7.1.3. The parameter order for all six operating points is given by

$$\begin{aligned} \Delta p < C_2 < T_w < p_{IVC} < \Delta\theta < V_{cr} < C_1 < T_{IVC} \\ < \Delta\theta_d < b < Q_{in} < K_p < \Delta\theta_b < V_c < \theta_{ig} < \underline{\gamma_{300}}, \end{aligned} \quad (8.2)$$

which reflects the most common case. This parameter order differs somewhat from the corresponding order found in simulations (8.1), for instance θ_{ig} and $\Delta\theta_d$ have changed places, but γ_{300} is still the most efficient parameter and invariant in position for the investigated operating conditions and cycle-to-cycle variations. The other parameters differ in order at most instances as permutations of the three groups $[b, C_1, C_2, T_{IVC}, p_{IVC}, T_w, V_{cr}]$, $[K_p, p_{IVC}, Q_{in}, \Delta\theta_b]$ and $[\theta_{ig}, \Delta\theta_d]$. The same groups were found in the simulation-based evaluation in section 8.1.3 except for V_{cr} and $\Delta\theta_b$ that are now included in the first and second group respectively.

The minimizing number of parameters d^* using algorithm 6.2 are given in table 8.14 as a mean over the 40 cycles at all six operating points. The range of d^* for each operating point is also given. The table shows that the mean values of d^* are more stable between operating points and that the variation is smaller in the experimental case, compared to the simulation given in table 8.2. The trend of more efficient parameters for high loads seen in table 8.2 does not show up in table 8.14.

The mean value, standard deviation, and relative mean error for the individual estimates are given in table 8.15. The relative mean error is computed relative to the nominal parameter value at each cycle and is given in percent. All parameters give reasonable values except for T_w and V_{cr} that yield unreasonably large parameter values, while T_{IVC} and to some extent also V_c yield small values. The parameter C_1 yields estimates that are either too small, reasonable or too large. Especially for OP3 and OP4 the C_1 -estimate becomes too small, while at the same

	V_c [cm^3]	C_1 [-]	T_{IVC} [K]	p_{IVC} [kPa]	γ_{300} [-]	b [K^{-1}]	T_w [K]	V_{cr} [cm^3]	Δp [kPa]	$\Delta \theta$ [deg]	K_p [-]	C_2 [$m/(s \cdot K)$]	Q_{in} [J]	θ_{ig} [deg ATDC]	$\Delta \theta_d$ [deg]	$\Delta \theta_b$ [deg]	$\varepsilon_x^\#$ [%]
OP1 mean	56.7	3.60	304	39.0	1.253	$-3.12 \cdot 10^{-5}$	606	2.72	0.1	0.06	1.071	$3.13 \cdot 10^{-4}$	345	-31.0	25.7	20.3	79.7
σ_{est}	4.7	2.08	56	4.0	0.050	$3.18 \cdot 10^{-5}$	203	2.11	1.4	0.03	0.107	$0.81 \cdot 10^{-4}$	31	3.9	3.6	1.4	79.7
RME	-3.5	58.1	-30.6	-3.7	-6.6	-57.9	27.6	208.8	-17.5	-86.7	7.1	-3.2	-1.6	-4.8	-6.9	-0.9	79.7
$x^\#$	58.8	2.28	450	40.8	1.336	$-7.42 \cdot 10^{-5}$	475	0.882	0.5	0.47	1.000	$3.24 \cdot 10^{-4}$	373	-32.6	27.5	20.3	0.0
OP2 mean	51.4	3.24	271	68.4	1.211	$-1.13 \cdot 10^{-5}$	677	2.46	0.2	0.34	1.037	$3.12 \cdot 10^{-4}$	732	-28.5	22.7	15.7	74.8
σ_{est}	1.7	1.60	1	3.3	0.017	$1.3 \cdot 10^{-5}$	175	2.18	0.3	0.39	0.046	$0.41 \cdot 10^{-4}$	60	5.4	5.5	0.8	74.8
RME	-12.5	42.2	-34.7	-0.6	-9.6	-84.7	42.5	179.1	-0.1	-28.3	3.7	-3.8	5.9	9.7	15.4	-2.4	74.8
$x^\#$	58.8	2.28	425	68.6	1.395	$-7.42 \cdot 10^{-5}$	475	0.882	0.6	0.47	1.000	$3.24 \cdot 10^{-4}$	731	-26.0	19.9	16.0	0.0
OP3 mean	54.7	0.02	335	171.0	1.293	$-2.22 \cdot 10^{-5}$	371	3.12	-2.9	0.09	1.002	$2.86 \cdot 10^{-4}$	1085	-13.3	25.3	18.3	95.7
σ_{est}	3.8	0.02	66	9.7	0.013	$0.754 \cdot 10^{-5}$	85	2.49	1.3	0.08	0.058	$0.61 \cdot 10^{-4}$	124	4.6	4.4	0.9	95.7
RME	-6.9	-99.1	-15.0	5.1	-5.5	-70.1	-22.0	254.3	-8.7	-80.4	0.2	-11.8	-7.7	153.4	63.2	-4.5	95.7
$x^\#$	58.8	2.28	407	162.5	1.336	$-7.42 \cdot 10^{-5}$	475	0.882	-2.3	0.47	1.000	$3.24 \cdot 10^{-4}$	1864	-5.3	15.4	19.3	0.0
OP4 mean	57.0	0.95	270	154.9	1.288	$-2.33 \cdot 10^{-5}$	631	2.8	-2.8	0.18	1.014	$3.16 \cdot 10^{-4}$	1562	-17.9	24.4	18.5	79.1
σ_{est}	3.7	1.12	0	5.1	0.019	$1.32 \cdot 10^{-5}$	238	3.32	0.5	0.22	0.048	$0.25 \cdot 10^{-4}$	100	3.5	3.2	1.1	79.1
RME	-3.0	-58.2	-31.4	1.7	-5.3	-68.6	32.8	217.6	-1.0	-62.7	1.4	-2.6	-9.0	45.2	39.7	-4.2	79.1
$x^\#$	58.8	2.28	394	152.3	1.336	$-7.42 \cdot 10^{-5}$	475	0.882	-2.8	0.47	1.000	$3.24 \cdot 10^{-4}$	1756	-12.3	17.3	19.1	0.0
OP5 mean	54.2	2.16	292	131.6	1.269	$-2.22 \cdot 10^{-5}$	772	3.92	-3.9	0.05	1.011	$3.18 \cdot 10^{-4}$	1400	-32.8	27.8	17.7	102.9
σ_{est}	4.1	1.66	46	3.8	0.034	$2.02 \cdot 10^{-5}$	282	2.62	2.6	0.00	0.032	$0.09 \cdot 10^{-4}$	52	5.0	4.2	1.2	102.9
RME	-7.8	-5.2	-26.8	-0.2	-7.8	-70.1	62.5	344.3	-16.7	-80.8	1.1	-1.8	-4.3	17.2	24.0	-5.6	102.9
$x^\#$	58.8	2.28	400	132.2	1.335	$-7.42 \cdot 10^{-5}$	475	0.882	-3.8	0.47	1.000	$3.24 \cdot 10^{-4}$	1502	-28.0	22.0	18.7	0.0
OP6 mean	54.5	2.00	338	142.6	1.284	$-2.55 \cdot 10^{-5}$	754	3.55	-3.0	0.06	1.021	$3.10 \cdot 10^{-4}$	1566	-29.5	26.2	17.7	91.8
σ_{est}	4.7	1.77	113	12.4	0.043	$1.79 \cdot 10^{-5}$	304	1.95	1.6	0.02	0.062	$0.26 \cdot 10^{-4}$	180	5.8	4.8	1.4	91.8
RME	-7.3	-12.2	-14.2	-1.2	-6.9	-65.6	58.8	302.1	-8.7	-87.7	2.1	-4.3	-4.7	13.9	19.5	-6.6	91.8
$x^\#$	58.8	2.28	392	153.3	1.334	$-7.42 \cdot 10^{-5}$	475	0.882	-2.7	0.47	1.000	$3.24 \cdot 10^{-4}$	1797	-24.4	21.1	19.1	0.0

Table 8.15: Mean value, standard deviation σ_{est} , relative mean error (RME) and nominal parameter deviation $\varepsilon_x^\#$ of the estimate for method 1, evaluated at d^* for 40 experimental cycles at OP1-6.

time a high p_{IVC} , an advanced ignition angle θ_{ig} and a prolonged burn delay angle $\Delta\theta_d$ as compared to the nominal values is notable. The lack of accuracy for the estimates is due to the high mean number of efficient parameters found in table 8.14. These high numbers are probably due to that the Akaike FPE assumes that the system considered is covered by the model structure used. All models are approximations and this is the case here, especially for firing cycles, since not every physical process influencing the measured cylinder pressure is modeled. The combination of modeling error and the measurement noise makes the Akaike criterion become minimized for a high value of d^* .

In accordance with the simulation-based evaluation in section 8.1.3, method 1 is not recommended to use for parameter estimation in the given formulation. The attention is therefore turned to method 2.

8.2.4 Method 2– Results and evaluation

In the experimental evaluation of method 2 for motored cycles in section 7.2.4, a fourth version called M2:3+ was included. The algorithm was motivated and fully described in appendix C.3, and it will also be studied here in the experimental evaluation for firing cycles.

First the results are presented for the two cases of δ_i :s, $\delta_i = c$ and $\delta_i \neq c$, and then the performance of the four versions M2:1, M2:2, M2:3 and M2:3+ are evaluated. The same implementation settings, as for the simulation-based evaluation in section 8.1.4, are used and are therefore not repeated here.

Results for case 1 ($\delta_i = c$) and case 2 ($\delta_i \neq c$)

The results are first described for case 1. An example of an L-curve is given in figure 8.7. Table 8.16 summarizes the mean value and standard deviation of the computed regularization parameter δ_x for 40 experimental cycles. This is done for all six operating points and for each of the four versions of method 2. The individual parameter estimates are given as mean values for 40 cycles at each OP in table 8.18, as well as the corresponding (emphasized) nominal values $x^\#$ and the nominal parameter deviation $\bar{\varepsilon}_x^\#$.

The corresponding figures and tables for case 2 are given in figure 8.8, table 8.17, table 8.19 that now also include the weighted nominal parameter deviation $RMSE(L^\delta \varepsilon_x^\#)$.

Evaluation for case 1 ($\delta_i = c$)

Case 1 is considered first. Figure 8.7 illustrates that the L-curve does not have as sharp transition as in the corresponding simulated case given in figure 8.4. The difference is believed to be due to that the

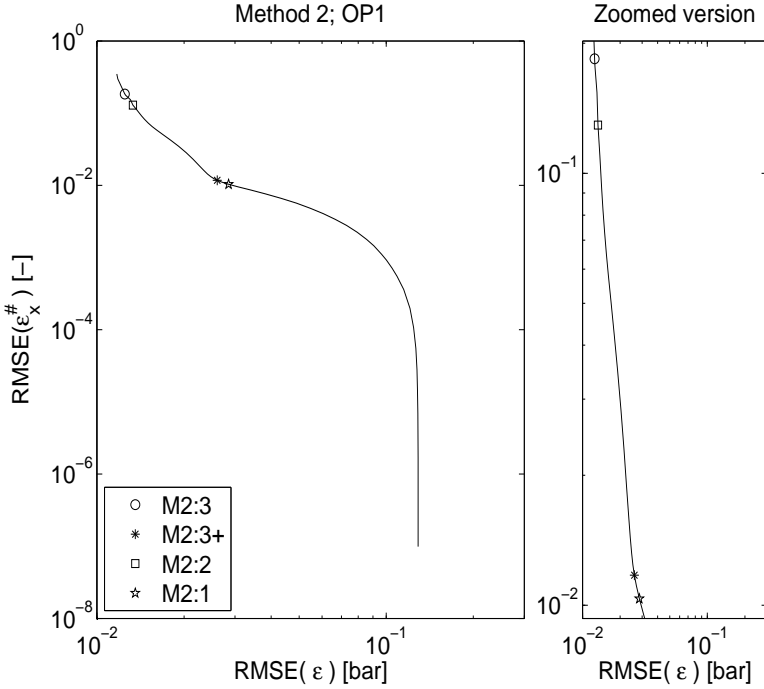


Figure 8.7: L-curve (solid line) for one engine cycle at OP1, when using case 1 of the δ_i ($\delta_i = c$). The results for the four versions of method 2 are indicated by the legend.

δ_x :		OP1	OP2	OP3	OP4	OP5	OP6
$\delta_x(M2:1)$	mean	$1.8 \cdot 10^{-2}$	$4.0 \cdot 10^{-1}$	$3.9 \cdot 10^0$	$6.7 \cdot 10^{-1}$	$7.3 \cdot 10^{-1}$	$1.1 \cdot 10^0$
	σ_{est}	$2.0 \cdot 10^{-2}$	$8.8 \cdot 10^{-2}$	$1.4 \cdot 10^0$	$1.5 \cdot 10^0$	$7.1 \cdot 10^{-1}$	$4.2 \cdot 10^{-1}$
$\delta_x(M2:2)$	mean	$4.9 \cdot 10^{-7}$	$2.9 \cdot 10^{-7}$	$9.5 \cdot 10^{-6}$	$1.1 \cdot 10^{-6}$	$3.4 \cdot 10^{-6}$	$8.8 \cdot 10^{-7}$
	σ_{est}	$2.2 \cdot 10^{-6}$	$1.2 \cdot 10^{-7}$	$1.0 \cdot 10^{-5}$	$1.2 \cdot 10^{-5}$	$3.7 \cdot 10^{-4}$	$2.0 \cdot 10^{-6}$
$\delta_x(M2:3)$	mean	$2.8 \cdot 10^{-5}$	$7.3 \cdot 10^{-6}$	$7.3 \cdot 10^{-6}$	$6.2 \cdot 10^{-6}$	$8.0 \cdot 10^{-6}$	$1.5 \cdot 10^{-6}$
	σ_{est}	$4.9 \cdot 10^{-4}$	$3.3 \cdot 10^{-5}$	$1.3 \cdot 10^{-4}$	$2.6 \cdot 10^{-5}$	$1.5 \cdot 10^{-4}$	$1.2 \cdot 10^{-5}$
$\delta_x(M2:3+)$	mean	$3.2 \cdot 10^{-3}$	$9.7 \cdot 10^{-3}$	$8.8 \cdot 10^{-2}$	$6.3 \cdot 10^{-2}$	$4.1 \cdot 10^{-2}$	$4.8 \cdot 10^{-2}$
	σ_{est}	$3.8 \cdot 10^{-3}$	$2.0 \cdot 10^{-3}$	$3.1 \cdot 10^{-2}$	$1.8 \cdot 10^{-2}$	$1.1 \cdot 10^{-2}$	$1.1 \cdot 10^{-2}$

Table 8.16: Mean value and standard deviation (σ_{est}) of δ_x for the four versions of method 2 using case 1, evaluated for 40 experimental cycles at OP1–6.

model structure is not correct. Figure 8.7 also shows that the four versions yield different regularization parameters δ_x . Version M2:1 is the most conservative of them all and yields the highest δ_x , closely followed by M2:3+. Then there is a gap to the two versions M2:2 and M2:3, which in turn render approximately the same δ_x . Both M2:3 and M2:3+ correspond to corners on the L-curve, although the corner for M2:3 is hardly visible to the eye.

For all six operating points table 8.16 shows that the regularization parameter for the four versions are ordered in size according to

$$\delta_x(M2 : 1) > \delta_x(M2 : 3+) > \delta_x(M2 : 3) > \delta_x(M2 : 2), \quad (8.3)$$

except for OP3 where it is the other way around for M2:2 and M2:3. As expected the difference between $\delta_x(M2 : 1)$ and $\delta_x(M2 : 3+)$ is smaller than between $\delta_x(M2 : 1)$ and $\delta_x(M2 : 3)$. Version M2:3+ is more flexible to changes in operating condition than M2:1, since it finds a convex corner of the L-curve. For the examined operating points, M2:1 yields a higher δ_x than M2:3+. Using M2:3 in its original form or M2:2 results in lower values of δ_x . For M2:3 this corresponds to the high value of the curvature found in figure C.2. Table 8.16 also shows that the mean value of δ_x depends upon operating condition, and that for a given version of method 2 δ_x is in the same order of magnitude for all six operating points.

The different δ_x :s result in different nominal parameter deviations and individual estimates, as shown in table 8.18 for OP1-6. The $\bar{\varepsilon}_x^\#$ -column shows that M2:1 yields the smallest nominal parameter deviation of all versions, closely followed by M2:3+. The nominal deviations $\bar{\varepsilon}_x^\#$ are within 2.2 % and 4.4 % respectively for all operating points considered. The other two versions, M2:2 and M2:3, render a significantly larger $\bar{\varepsilon}_x^\#$, where the parameters b , γ_{300} and T_{IVC} give unreasonable values. Of these parameters, b is the largest contributor to the nominal deviations. At some instances the ignition angle θ_{ig} is advanced compared to the nominal value, and this is compensated by a longer flame development angle $\Delta\theta_d$, see e.g. OP2. In the experimental evaluation for motored cycles it was found that K_p yielded unreasonable estimates, see table 7.21, but this is not the case for the firing cycles. Of the other parameters p_{IVC} , K_p , C_2 , Q_{in} and $\Delta\theta_b$ all end up within 5 % of their nominal values for all operating points.

The individual estimates for M2:1 and M2:3+ are all reasonable, which is expected since they end up close to their nominal values. The maximum deviation occurs for the parameters θ_{ig} and $\Delta\theta_d$ for both versions, the others are all within 5 %.

To summarize the evaluation for $\delta_i = c$, using M2:1 or M2:3+ yield estimates that deviate less than 3 and 5 percent in the mean.

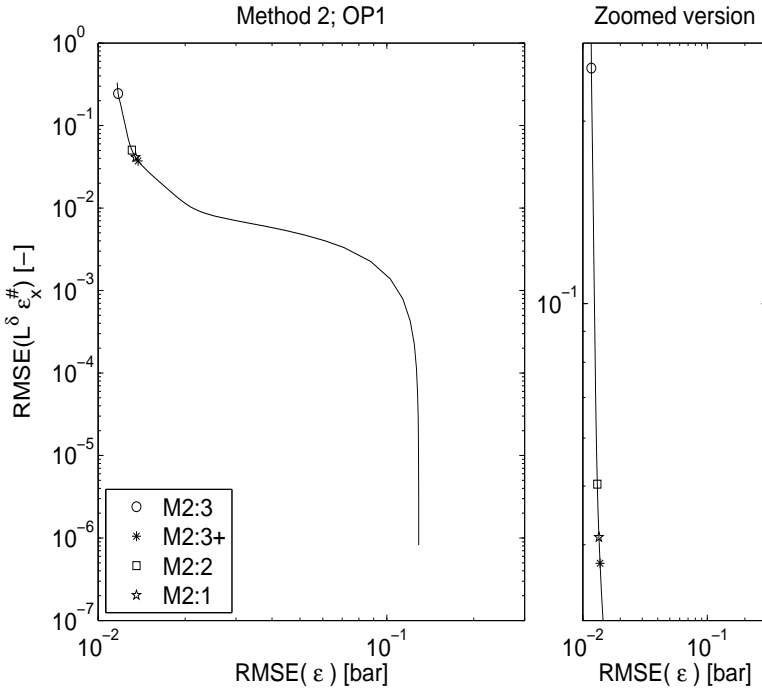


Figure 8.8: L-curve (solid line) for one engine cycle at OP1, when using case 2 of the δ_i ($\delta_i \neq c$). The results for the four versions of method 2 are indicated by the legend.

δ_x :		OP1	OP2	OP3	OP4	OP5	OP6
$\delta_x(M2:1)$	mean	$7.7 \cdot 10^{-4}$	$1.4 \cdot 10^{-2}$	$1.7 \cdot 10^{-1}$	$3.5 \cdot 10^{-2}$	$3.2 \cdot 10^{-2}$	$5.3 \cdot 10^{-2}$
	σ_{est}	$6.1 \cdot 10^{-4}$	$3.0 \cdot 10^{-3}$	$3.8 \cdot 10^{-2}$	$5.2 \cdot 10^{-2}$	$2.1 \cdot 10^{-2}$	$2.3 \cdot 10^{-2}$
$\delta_x(M2:2)$	mean	$4.3 \cdot 10^{-5}$	$5.6 \cdot 10^{-5}$	$3.8 \cdot 10^{-3}$	$1.4 \cdot 10^{-4}$	$1.9 \cdot 10^{-3}$	$7.1 \cdot 10^{-4}$
	σ_{est}	$3.4 \cdot 10^{-4}$	$3.0 \cdot 10^{-5}$	$2.9 \cdot 10^{-3}$	$8.0 \cdot 10^{-4}$	$6.7 \cdot 10^{-3}$	$1.5 \cdot 10^{-2}$
$\delta_x(M2:3)$	mean	$1.5 \cdot 10^{-6}$	$5.8 \cdot 10^{-7}$	$8.5 \cdot 10^{-5}$	$7.3 \cdot 10^{-6}$	$1.2 \cdot 10^{-4}$	$8.7 \cdot 10^{-6}$
	σ_{est}	$1.8 \cdot 10^{-5}$	$6.4 \cdot 10^{-7}$	$1.3 \cdot 10^{-3}$	$9.5 \cdot 10^{-5}$	$1.9 \cdot 10^{-3}$	$3.6 \cdot 10^{-4}$
$\delta_x(M2:3+)$	mean	$2.2 \cdot 10^{-4}$	$4.6 \cdot 10^{-4}$	$1.3 \cdot 10^0$	$7.1 \cdot 10^{-4}$	$1.6 \cdot 10^{-3}$	$1.8 \cdot 10^{-2}$
	σ_{est}	$7.9 \cdot 10^{-4}$	$3.0 \cdot 10^{-4}$	$2.4 \cdot 10^0$	$1.8 \cdot 10^{-3}$	$1.5 \cdot 10^{-3}$	$1.1 \cdot 10^{-1}$

Table 8.17: Mean value and standard deviation (σ_{est}) of δ_x for the four versions of method 2 using case 2, evaluated for 40 experimental cycles at OP1–6.

Evaluation for case 2 ($\delta_i \neq c$)

Now the second case will be evaluated. The L-curve in figure 8.8 is similar to the corresponding L-curve for the simulated case in figure 8.5, although it is not as sharp in the transition. As for case 1, both M2:3 and M2:3+ correspond to corners on the L-curve, although the corner for M2:3 is hardly visible to the eye. Figure 8.8 also displays that the three versions M2:1, M2:2 and M2:3+ yield approximately the same δ_x for OP1, while M2:3 yields a smaller δ_x . This observation is confirmed by table 8.17. However the variation in δ_x for M2:1, M2:2 and M2:3+ is larger for the other five operating points, and thus reflect that the versions typically are a little more spread out on the L-curve as compared to OP1.

Table 8.17 shows that for all six operating points the regularization parameter for the four versions are ordered in size according to

$$\delta_x(M2 : 1) > \delta_x(M2 : 3+) > \delta_x(M2 : 2) > \delta_x(M2 : 3), \quad (8.4)$$

except for OP3 where it is the other way around for M2:1 and M2:3+. Compared to (8.3), the ordering is the same apart from M2:2 and M2:3 which now have changed places. As for the first case, M2:3 results in low values of δ_x , due to the same reason. It is also found that the mean value of δ_x depends upon operating conditions, and that for a given version of method 2 δ_x is in the same order of magnitude for almost all six operating points. The only exception is OP3 for version M2:3+.

As expected, the different δ_x :s result in different nominal parameter deviations and individual estimates, as shown in table 8.19 for OP1-6. The column for weighted parameter deviation, $L^\delta \varepsilon_x^\#$, shows that M2:1 and then M2:3+ yield the smallest nominal parameter deviations of all versions, except for OP3 where it is the other way around. This corresponds to the ordering given in (8.4). The other two versions, M2:2 and M2:3, render a significantly larger $L^\delta \varepsilon_x^\#$, mainly due to low estimates of γ_{300} and T_{IVC} as seen for OP2. Considering the $\bar{\varepsilon}_x^\#$ -column, these values are larger than the corresponding column for $\delta_i = c$, see table 8.18. This is mainly due to the relatively large contribution of nominal deviation in $\Delta\theta$ for $\delta_i \neq c$. The nominal deviations $\bar{\varepsilon}_x^\#$ for M2:1 and M2:3+ are within 67 % and 76 % respectively for all operating points considered.

Now consider the individual estimates in table 8.19; Just as for $\delta_i = c$, the ignition angle θ_{ig} is advanced compared to the nominal value, and this is compensated by a longer flame development angle $\Delta\theta_d$. Another trend is that $\Delta\theta$ is larger than the nominal value for all operating points. For M2:2 and M2:3 the parameters p_{IVC} , V_{cr} , K_p , C_2 , Q_{in} and $\Delta\theta_b$ all end up within 5 % of their nominal values. These parameters are the same as for $\delta_i = c$, but now also includes V_{cr} . For M2:3+ the estimates of C_1 , p_{IVC} , γ_{300} , T_w , V_{cr} , K_p , C_2 , Q_{in} , $\Delta\theta_b$ and

δ_x :	V_c [cm ³]	C_1 [-]	T_{IVC} [K]	p_{IVC} [kPa]	γ_{3000} [-]	b [K ⁻¹]	T_{c0} [K]	V_{c0} [cm ³]	Δp [kPa]	$\Delta\theta$ [deg]	K_p [-]	C_5 [m/(s K)]	Q_{in} [J]	θ_{ig} [deg ATDC]	$\Delta\theta_I$ [deg]	$\Delta\theta_0$ [deg]	$\varepsilon_{\#}$ [%]
OP1 $\delta_x(M2:1)$ $\delta_x(M2:2)$ $\delta_x(M2:3)$ $\delta_x(M2:3+)$ $x_{\#}$	58.2	2.29	449	40.8	1.344	$-7.38 \cdot 10^{-5}$	474	0.881	0.5	0.47	0.987	$3.24 \cdot 10^{-4}$	368	-32.2	27.9	20.0	1.1
	58.2	2.13	325	42.0	1.299	$-5.01 \cdot 10^{-5}$	443	1.56	0.4	0.81	0.978	$2.99 \cdot 10^{-4}$	366	-31.8	27.2	20.0	38.9
	57.9	2.42	362	40.8	1.296	$-5.22 \cdot 10^{-5}$	479	0.916	0.5	0.52	1.002	$3.23 \cdot 10^{-4}$	364	-31.6	27.0	20.3	10.7
	58.2	2.29	449	40.9	1.346	$-7.34 \cdot 10^{-5}$	473	0.881	0.5	0.47	0.984	$3.24 \cdot 10^{-4}$	365	-32.1	27.9	19.7	1.6
OP2 $\delta_x(M2:1)$ $\delta_x(M2:2)$ $\delta_x(M2:3)$ $\delta_x(M2:3+)$ $x_{\#}$	58.8	2.28	450	40.8	1.336	$-7.42 \cdot 10^{-5}$	475	0.882	0.5	0.47	1.000	$3.24 \cdot 10^{-4}$	373	-32.6	27.5	20.3	0.0
	57.8	2.28	424	68.6	1.349	$-7.37 \cdot 10^{-5}$	474	0.881	0.6	0.47	0.988	$3.24 \cdot 10^{-4}$	721	-25.3	20.4	15.9	1.1
	50.4	2.42	270	69.0	1.215	$-3.16 \cdot 10^{-5}$	478	0.89	0.6	0.57	1.041	$3.24 \cdot 10^{-4}$	744	-34.8	30.0	15.7	24.2
	50.3	2.41	281	68.9	1.218	$-3.39 \cdot 10^{-5}$	477	0.89	0.6	0.56	1.041	$3.24 \cdot 10^{-4}$	745	-34.7	30.0	15.6	23.4
OP3 $\delta_x(M2:1)$ $\delta_x(M2:2)$ $\delta_x(M2:3)$ $\delta_x(M2:3+)$ $x_{\#}$	52.1	2.29	413	68.1	1.326	$-7.12 \cdot 10^{-5}$	472	0.879	0.6	0.47	0.974	$3.24 \cdot 10^{-4}$	715	-24.9	21.2	15.1	4.1
	58.8	2.28	425	68.6	1.335	$-7.42 \cdot 10^{-5}$	475	0.882	0.6	0.47	1.000	$3.24 \cdot 10^{-4}$	731	-26.0	19.9	16.0	0.0
	59.4	2.28	406	162.7	1.341	$-7.39 \cdot 10^{-5}$	475	0.882	-2.2	0.47	1.001	$3.24 \cdot 10^{-4}$	1864	-5.2	16.0	19.2	1.2
	52.7	1.80	270	165.9	1.231	$-0.0864 \cdot 10^{-5}$	488	1.07	-2.4	1.11	1.020	$3.07 \cdot 10^{-4}$	1914	-12.0	24.3	18.9	58.4
OP4 $\delta_x(M2:1)$ $\delta_x(M2:2)$ $\delta_x(M2:3)$ $\delta_x(M2:3+)$ $x_{\#}$	53.4	1.72	270	165.4	1.256	$-1.83 \cdot 10^{-5}$	418	1.07	-2.4	1.00	1.007	$3.09 \cdot 10^{-4}$	1878	-9.8	22.2	18.8	46.3
	59.0	2.29	397	161.9	1.378	$-7.14 \cdot 10^{-5}$	471	0.882	-2.2	0.47	0.963	$3.24 \cdot 10^{-4}$	1802	-5.0	17.7	18.6	4.4
	58.8	2.28	407	162.5	1.339	$-7.42 \cdot 10^{-5}$	475	0.882	-2.2	0.47	1.000	$3.24 \cdot 10^{-4}$	1864	-5.3	15.4	19.0	0.0
	59.0	2.28	390	151.9	1.359	$-7.31 \cdot 10^{-5}$	474	0.881	-2.8	0.47	0.987	$3.24 \cdot 10^{-4}$	1738	-11.8	18.5	18.9	2.2
OP5 $\delta_x(M2:1)$ $\delta_x(M2:2)$ $\delta_x(M2:3)$ $\delta_x(M2:3+)$ $x_{\#}$	53.7	1.80	270	155.2	1.254	$-1.21 \cdot 10^{-5}$	519	1.55	-3.4	1.61	0.995	$3.10 \cdot 10^{-4}$	1827	-20.2	27.6	18.9	74.8
	54.9	2.17	270	156.4	1.262	$-2.65 \cdot 10^{-5}$	503	1.05	-3.0	0.88	0.998	$3.21 \cdot 10^{-4}$	1779	-17.6	24.7	18.6	36.9
	58.2	2.29	384	151.3	1.375	$-7.14 \cdot 10^{-5}$	471	0.882	-2.8	0.47	0.963	$3.24 \cdot 10^{-4}$	1701	-11.6	19.2	18.3	3.7
	58.8	2.28	394	152.9	1.339	$-7.42 \cdot 10^{-5}$	475	0.882	-2.8	0.47	1.000	$3.24 \cdot 10^{-4}$	1756	-12.9	17.3	19.1	0.0
OP6 $\delta_x(M2:1)$ $\delta_x(M2:2)$ $\delta_x(M2:3)$ $\delta_x(M2:3+)$ $x_{\#}$	57.9	2.28	396	131.5	1.358	$-7.34 \cdot 10^{-5}$	474	0.881	-3.8	0.47	0.984	$3.24 \cdot 10^{-4}$	1485	-27.2	22.5	18.3	1.4
	56.4	1.86	290	134.0	1.293	$-4.37 \cdot 10^{-5}$	566	1.2	-4.3	0.77	0.989	$2.99 \cdot 10^{-4}$	1449	-31.1	26.5	18.0	33.1
	56.1	2.08	291	134.3	1.296	$-5.25 \cdot 10^{-5}$	469	1.12	-4.1	0.74	0.992	$3.06 \cdot 10^{-4}$	1467	-32.0	27.5	17.9	26.8
	55.8	2.29	391	131.3	1.356	$-7.19 \cdot 10^{-5}$	472	0.88	-3.8	0.47	0.969	$3.24 \cdot 10^{-4}$	1465	-26.9	23.0	17.5	2.9
OP6 $\delta_x(M2:1)$ $\delta_x(M2:2)$ $\delta_x(M2:3)$ $\delta_x(M2:3+)$ $x_{\#}$	58.8	2.28	400	132.2	1.335	$-7.42 \cdot 10^{-5}$	475	0.882	-3.8	0.47	1.000	$3.24 \cdot 10^{-4}$	1502	-28.0	22.0	18.7	0.0
	58.4	2.28	389	152.4	1.357	$-7.35 \cdot 10^{-5}$	474	0.881	-2.7	0.47	0.991	$3.24 \cdot 10^{-4}$	1790	-23.7	21.6	18.7	1.3
	57.9	2.13	270	157.4	1.295	$-5.4 \cdot 10^{-5}$	578	0.96	-2.8	0.62	0.982	$3.24 \cdot 10^{-4}$	1780	-28.2	26.1	18.1	20.5
	58.0	1.82	270	154.2	1.296	$-4.95 \cdot 10^{-5}$	606	1.04	-2.9	0.73	0.999	$3.12 \cdot 10^{-4}$	1728	-27.5	25.5	18.1	28.9
$\delta_x(M2:3)$ $\delta_x(M2:3+)$ $x_{\#}$	56.9	2.29	382	152.2	1.356	$-7.2 \cdot 10^{-5}$	472	0.881	-2.7	0.47	0.979	$3.24 \cdot 10^{-4}$	1771	-23.5	22.1	17.8	2.8
	58.8	2.28	392	153.9	1.335	$-7.42 \cdot 10^{-5}$	475	0.882	-2.7	0.47	1.000	$3.24 \cdot 10^{-4}$	1797	-24.4	21.1	19.1	0.0

Table 8.18: Mean value of the estimate for the four versions of method 2 using case 1, evaluated for 40 experimental cycles at OP1-6. The nominal values $x_{\#}$ are also included.

for M2:1 also the parameters V_c and T_{IVC} , are all within 5 % of their nominal value. Compared to $\delta_i = c$, fewer parameters are within this limit, but as before all the estimates are still reasonable.

To summarize the evaluation for $\delta_i \neq c$, using M2:1 or M2:3+ yield weighted nominal parameter deviations that are less than 10 and 17 percent respectively.

Summary of method 2

To summarize, case 1 and 2 yield different estimates and for the versions M2:2 and M2:3 almost the same parameters are close (within 5 %) of their nominal values. For M2:1 and M2:3+ more parameters are within this limit, especially for case 1. It can however not be determined which case that gives the best estimates, since the true values are unknown. But it has been shown that the extension of M2:3 to M2:3+ has resulted in a more robust algorithm. It has also been shown that M2:1 and M2:3+ give more reasonable estimates, compared to M2:2 and M2:3. This is in line with the results from the simulation study. The simulation study also showed that case 2 ($\delta_i \neq c$) is to be preferred, and therefore this is the recommended choice.

Unlike M2:1, M2:3+ finds a convex corner of the L-curve. This makes M2:3+ more flexible to changes in operating condition. Therefore if time is available, M2:3+ is preferable to M2:1.

8.3 Summary of results for fired cycles

For method 1 the same conclusions as for the motored cycles in section 7.3 can be drawn; Both the simulation and experimental studies showed that method 1 did not render accurate estimates. It was even hard to decide upon the number of efficient parameters to use. However, method 1 allows for the parameters to be ordered in how efficient they are for the given estimation problem and data. It was also shown that γ_{300} is the most efficient parameter.

According to the simulation-based evaluation, method 2 is more robust to an introduced false prior than method 1 since it yields more accurate parameter estimates. The difference in accuracy is however smaller between method 1 and 2 for firing cycles compared to the motored case. Just as for the motored case, the simulation study showed that the regularization pulls some of the parameters towards their nominal values, while the efficient parameters are free to fit the data.

Method 2 was originally formulated for three variants. For the simulation-based evaluation variant M2:3 is the most accurate one, followed by M2:2 and M2:1. From the experimental evaluation it was found that an extension of variant M2:3, called M2:3+, was needed to

cope with unreasonably high curvature for low δ_x that can occur for experimental data. With this extension, the two variants M2:1 and M2:3+ both give reasonable estimates, and where M2:3+ is more flexible to changes in operating condition of the two.

Considering the two cases of parameter uncertainty, $\delta_i = c$ and $\delta_i \neq c$, it was found in the simulations that the second case was recommended since it pays off in better estimates that are more robust to a false nominal parameter value. The experimental evaluation can neither confirm or decline this observation, since both cases yield reasonable estimates, at least for variants M2:1 and M2:3+.

Thus if computational time is available, variant M2:3+ of method 2 is recommended due to its accuracy. However if computational time is an important feature variant M2:1 is the best choice. The chosen variant should preferably be combined with case 2 ($\delta_i \neq c$), i.e. individually set parameter uncertainty.

The compiled conclusions from the evaluations of motored and fired data are given in section 9.3.

8.4 Future Work

It would be interesting to include a multi-zone cylinder pressure model as a reference model in the simulation study done in section 8.1. Such a study would shed more light on what happens when the chosen model structure is not covered by the cylinder pressure data, while the true value of the parameters are known. It would therefore resemble the situation for the experimental firing cycles better. The study could also include the model of the specific heat ratio developed in chapter 4. This extended model, in chapter 4 named model \mathcal{D}_1 , is simulated by using (3.36)–(3.43), (4.28), (A.9) and algorithm A.1. This inclusion would allow for a direct performance comparison of the standard and extended cylinder pressure models.

SUMMARY AND CONCLUSIONS

The theme of the thesis is cylinder pressure modeling and estimation. The results from part I are given in section 9.1, which repeats the conclusions from section 4.7. In the same way, the results for part II are given in section 9.2, which repeats the conclusions from section 5.6. The compiled conclusions for part III are then given in section 9.3.

9.1 A specific heat ratio model for single-zone heat release models

The first part of the thesis is on single-zone heat release modeling, where the specific heat ratio model constitutes a key part. Chapter 2 gives an overview of single-zone heat release models, while chapter 3 gives a more thorough description of the model components. In chapter 4 various specific heat ratio models are investigated. The conclusions from chapter 4 are now given here.

Based on assumptions of frozen mixture for the unburned mixture and chemical equilibrium for the burned mixture, the specific heat ratio is calculated, using a full equilibrium program, for an unburned and a burned air-fuel mixture, and compared to several previously proposed models of γ . It is shown that the specific heat ratio and the specific heats for the unburned mixture are captured to within 0.25 % by a linear function in mean charge temperature T for $\lambda \in [0.8, 1.2]$. Furthermore the burned mixture is captured to within 1 % by the higher-

order polynomial in cylinder pressure p and temperature T developed in Krieger and Borman (1967) for the major operating range of a spark ignited (SI) engine. If a linear model is preferred for computational reasons for the burned mixture, then the temperature region should be chosen with care which can reduce the modeling error in γ by 25 %.

With the knowledge of how to describe γ for the unburned and burned mixture respectively, the focus is turned to finding a γ -model during the combustion process, i.e. for a partially burned mixture. This is done by interpolating the specific heats for the unburned and burned mixture using the mass fraction burned x_b . The objective was to find a model of γ , which results in a cylinder pressure error that is lower than or in the order of the measurement noise. It is found that interpolating the linear specific heats for the unburned mixture and the higher-order polynomial specific heats for the burned mixture, and then forming the specific heat ratio

$$\gamma(T, p, x_b) = \frac{c_p(T, p, x_b)}{c_v(T, p, x_b)} = \frac{x_b c_{p,b}^{KB} + (1 - x_b) c_{p,u}^{lin}}{x_b c_{v,b}^{KB} + (1 - x_b) c_{v,u}^{lin}} \quad (9.1)$$

results in a small enough modeling error in γ . This modeling error results in a cylinder pressure error that is lower than 6 kPa in mean, which is in the same order as the cylinder pressure measurement noise.

It was also shown that it is important to evaluate the model error in γ to see what impact it has on the cylinder pressure, since a small error in γ can yield a large cylinder pressure error. This also stresses that the γ -model is an important part of the heat release model.

Applying the proposed model improvement \mathcal{D}_1 (9.1) of the specific heat ratio to the Gatowski et al. (1984) single-zone heat release model is simple, and it does not increase the computational burden immensely. Compared to the original setting, the computational burden increases with 40 % and the modeling error introduced in the cylinder pressure is reduced by a factor 15 in mean.

9.2 Compression ratio estimation

Four methods for compression ratio estimation based on cylinder pressure traces are developed and evaluated for both simulated and experimental cycles in chapter 5. The conclusions are given here.

Conclusions from the simulation results

The first three methods rely upon the assumption of a polytropic compression and expansion. It is shown that this is sufficient to get a rough estimate of the compression ratio r_c for motored cycles, especially for a low r_c and by letting the polytropic exponent become small. For a high

r_c it is important to take the heat transfer into account, and then only method 4 is accurate to within 0.5 % for all operating points. Method 4 is however slow and not suitable for on-line implementation. Method 2 on the other hand is substantially faster and still yields estimates that are within 1.5 %. The formulation of the residual is also important, since it influences the estimated r_c . For fired cycles, methods 1-3 yield poor estimates and therefore only method 4 is recommended.

A sensitivity analysis, with respect to crank angle phasing, cylinder pressure bias, crevice volume, and heat transfer, shows that the third and fourth method are more robust. They therefore deal with these parameter deviations better than methods 1 and 2. Of the latter two, method 2 has the best performance for all parameter deviations except for an additive pressure bias.

Conclusions from the experimental results

All methods yield approximately the same confidence intervals for the simulated and experimental data. The confidence intervals resulting from method 4 are smallest of all methods, but it suffers from a high computational time. Method 2 yields smaller confidence intervals than methods 1 and 3, and is outstanding regarding convergence speed. The effects and trends shown in the simulation evaluation are also present in the experimental data. Therefore the conclusions made in the simulation evaluation with respect to models, residuals, methods, heat transfer and crevice effects are the same for the experimental evaluation. For diagnostic purposes, all methods are able to detect if the compression ratio is stuck at a too high or too low level.

Concluding recommendations

The accuracy of the compression ratio estimate is higher for motored cycles with high initial pressures. Thus if it is possible to choose the initial pressure, it should be as high as possible. Using motored cycles assures that all pressure information available is utilized and the high initial pressure improves the signal-to-noise ratio, while the effects of heat transfer and crevice flows remain the same.

Two methods are recommended; If estimation accuracy has the highest priority, and time is available, method 4 should be used. Method 4 yields the smallest confidence intervals of all investigated methods for both simulated and experimental data. In the simulation case where the true value of the compression ratio is known, method 4 gave estimates with smallest bias. If computational time is the most important property, method 2 is recommended. It is the most computationally efficient of all investigated methods, and yields the smallest confidence intervals out of methods 1-3.

9.3 Prior knowledge based heat release analysis

The objective in part III, as stated in the beginning of chapter 6, was to develop an estimation tool that is accurate, systematic and efficient. For this purpose two methods that incorporate parameter prior knowledge in a systematic manner are presented in chapter 6. Method 1 is based on using a singular value decomposition (SVD) of the estimated hessian, to reduce the number of estimated parameters one-by-one. Then the suggested number of parameters to use is found as the one minimizing the Akaike final prediction error. Method 2 uses a regularization technique to include the prior knowledge in the criterion function. The compiled conclusions from the evaluation of the methods on motored (chapter 7) and fired (chapter 8) are given here.

Method 1 restrains the estimation problem, since not all parameters are estimated simultaneously. More importantly, it introduces an estimation bias in the efficient parameters since the uncertain parameters are almost unavoidably false. Method 2 enables estimation of all parameters simultaneously, which is an important feature when a parameter's prior knowledge is false. Compared to method 2, method 1 yields more biased parameter estimates in the case of a false prior.

It has also been shown by using method 1 that, given the Gatowski et al. cylinder pressure model, the constant γ_{300} in the linear γ -model is the most important parameter.

The drive for method 2 was to regularize the solution such that the parameters that are hard to determine are pulled towards their nominal values, while the efficient parameters are free to fit the data. This has shown to be the case in the simulations for both fired and motored cycles.

The user can chose between two cases of the parameter uncertainty, either equal (in a normalized sense) or individually chosen. The former is directly applicable once nominal values of the parameters are determined and yields good estimates in the simulations. For experimental motored cycles it has been shown that the second case gives more accurate and reasonable parameter estimates, while this can not be determined from the firing cycles. The conclusion is still to use the second case. It requires more effort to decide upon the uncertainty for each parameter, but pays off in better estimates that are more robust to a false nominal parameter value. Once a choice of parameter uncertainty has been done, no user interaction is needed.

Method 2 was originally formulated for three versions. The versions differ in how they determine how strong the regularization should be. For the simulation-based evaluation version M2:1 and M2:3 where found to be the most accurate one for motored and fired cycles respectively.

From the experimental evaluation it was found that an extension of version M2:3, called M2:3+, was needed. With this extension, the two versions M2:1 and M2:3+ both give reasonable estimates, and where M2:3+ is more flexible to changes in operating condition of the two, a feature which is more required for firing cycles than for motored cycles. Method 2 can therefore be said to be systematic and accurate, and therefore fulfills two of the requirements for the estimation tool.

Thus if computational time is available, version M2:3+ of method 2 is recommended due to its accuracy. However if computational time is an important feature version M2:1 is the best choice. The chosen version should preferably be combined with individually set parameter uncertainties, i.e. case 2. In this formulation the third requirement is also fulfilled.

To summarize, the proposed tool for heat release analysis is efficient, systematic and accurate, and can be used for engine calibration, as a diagnostic tool or as an analyzing tool for future engine designs.

BIBLIOGRAPHY

- H. Akaike. Fitting autoregressive models for prediction. *Ann. Inst. Stat. Math.*, (21):243–347, 1969.
- C.A. Amann. Cylinder pressure measurement and its use in engine research. 1985. SAE Technical Paper 852067.
- M. Anatone and R. Cipollone. A contribution in calculating the thermal fields in internal combustion engines components. Number 961127 in SAE Technical paper series, SAE World Congress, Detroit, USA, 1996.
- I. Andersson. Cylinder pressure and ionization current modeling for spark ignited engines. Technical report, Vehicular Systems, 2002. LiUTEK-LIC-2002:35, Thesis No. 962.
- I. Andersson. *Ion Current and Torque Modeling for Combustion Engine Control*. PhD thesis, Chalmers University, December 2005. ISBN 91-7291-706-7.
- W. J. D. Annand. Heat transfer in the cylinders of reciprocating internal combustion engines. *Proc. Instn. Mechanical Engineers*, Vol. 177, 1963. 36.
- I. Arsie, G. Flauti, C. Pianese, and G. Rizzo. Cylinder thermal state detection from pressure cycle in SI engine. 4th International Conference on Internal Combustion Engines: Experiments and Modeling, Capri, Italy, 1999.

E. Bergstedt. A sliding mode observer for a nonlinear temperature estimation in a cylinderhead of a diesel engine. Master's thesis, Linköping University, SE-581 83 Linköping, 2002. LiTH-ISY-EX-3255-2002.

Å. Björck. *Numerical Methods for Least Squares Problems*. Siam, 1996.

M.F.J. Brunt and A.L. Emtage. Evaluation of IMEP routines and analysis errors. In *Spark-Ignition Engine Combustion and Emissions (SP-1157)*, 1996. SAE Technical Paper 960609.

M.F.J. Brunt and A.L. Emtage. Evaluation of burn rate routines and analysis errors. In *Spark-Ignition Engine Combustion and Emissions (SP-1267)*, 1997. SAE Technical Paper 970037.

M.F.J. Brunt and C.R. Pond. Evaluation of techniques for absolute cylinder pressure correction. In *Spark-Ignition Engine Combustion and Emissions (SP-1267)*, 1997. SAE Technical Paper 970036.

M.F.J. Brunt, A. Rai, and A.L. Emtage. The calculation of heat release energy from engine cylinder pressure data. In *SI Engine Combustion*, 1998. SAE Technical Paper 981052.

H.M. Cheung and J.B. Heywood. Evaluation of a one-zone burn-rate analysis procedure using production SI engine pressure data. 1993. SAE Technical Paper 932749.

K. M. Chun and J. B. Heywood. Estimating heat-release and mass-of-mixture burned from spark-ignition engine pressure data. *Combustion Sci. and Tech.*, Vol. 54:133–143, 1987.

Y.A. Çengel and M.A. Boles. *Thermodynamics: An Engineering Approach*. McGraw-Hill, 4th edition, 2002. <http://highered.mcgraw-hill.com>.

H.W. Engl, M. Hanke, and A. Neubauer. *Regularization of inverse problems*. Kluwer Academic Publishers, London, 1996. ISBN 0-7923-4157-0.

L. Eriksson. CHEPP –a chemical equilibrium program package for matlab. volume SP-1830, 2004. SAE Technical Paper 2004-01-1460.

L. Eriksson. Requirements for and a systematic method for identifying heat-release model parameters. *Modeling of SI and Diesel Engines*, SP-1330:19–30, 1998. SAE Technical Paper no.980626.

L. Eriksson. *Spark Advance Modeling and Control*. PhD thesis, Linköping University, May 1999. ISBN 91-7219-479-0, ISSN 0345-7524.

J.W. Fox, W.K. Cheng, and J.B. Heywood. A model for predicting residual gas fraction in spark ignition engines. 1993. SAE Technical Paper 931025.

J.A. Gatowski, E.N. Balles, K.M. Chun, F.E. Nelson, J.A. Ekchian, and J.B. Heywood. Heat release analysis of engine pressure data. 1984. SAE Technical Paper 841359.

P.E. Gill, W. Murray, and M.H. Wright. *Practical Optimization*. Academic Press, 1981.

S. Gordon and B.J. McBride. Computer program for the calculation of complex chemical equilibrium composition, rocket performance, incident and reflected shocks, and chapman-jouguet detonations. Technical Report NASA Publication SP-273, NASA Lewis Research Center, 1971.

Y.G. Guezennec and W. Hamama. Two-zone heat release analysis of combustion data and calibration of heat transfer correlation in an I.C. engine. 1999. SAE Technical paper 1999-01-0218.

P.C. Hansen. *Rank-deficient and discrete ill-posed problems: numerical aspects of linear inversion*. Society for Industrial and Applied Mathematics, Philadelphia, PA, USA, 1998. ISBN 0-89871-403-6.

P.C. Hansen. Regularization tools; a matlab package for analysis and solution of discrete ill-posed problems. *Numerical Algorithms*, 6(1): 1–35, 1994.

P.C. Hansen and D.P. O’Leary. The use of the l-curve in the regularization of discrete ill-posed problems. *SIAM Journal on Scientific Computing*, 14(6):1487–1503, 1993. doi: 10.1137/0914086. URL <http://link.aip.org/link/?SCE/14/1487/1>.

T.K. Hayes, R.A. White, and J.E. Peters. Combustion chamber temperature and instantaneous local heat flux measurements in a spark ignition engine. 1993. SAE Technical Paper 930217.

J. B. Heywood. *Internal Combustion Engine Fundamentals*. McGraw-Hill series in mechanical engineering. McGraw-Hill, 1988. ISBN 0-07-100499-8.

G.F. Hohenberg. Advanced approaches for heat transfer calculations. 1979. SAE Technical Paper 790825.

B. Johansson. *On Cycle to Cycle Variations in Spark Ignition Engines*. PhD thesis, Lund Institute of Technology, 1995.

- M. Klein. A specific heat ratio model and compression ratio estimation. Licentiate thesis, Vehicular Systems, Linköping University, 2004. LiU-TEK-LIC-2004:33, Thesis No. 1104, <http://www.fs.isy.liu.se/Publications/>.
- M. Klein and L. Eriksson. A specific heat ratio model for single-zone heat release models. *SAE 2004 Transactions Journal of Engines*, 2004-01-1464, 2005a.
- M. Klein and L. Eriksson. A comparison of specific heat ratio models for cylinder pressure modeling. CCSSE, Norrköping, Sweden, October 2004a.
- M. Klein and L. Eriksson. Utilizing cylinder pressure data for compression ratio estimation. IFAC World Congress, Prague, Czech Republic, 2005b.
- M. Klein and L. Eriksson. Models, methods and performance when estimating the compression ratio based on the cylinder pressure. Fourth conference on Computer Science and Systems Engineering in Linköping (CCSSE), 2002.
- M. Klein and L. Eriksson. A comparison of specific heat ratio models for cylinder pressure modeling. CCSSE, Norrköping, Sweden, October 2004b.
- M. Klein and L. Eriksson. A specific heat ratio model for single-zone heat release models. *Modeling of SI Engines*, SP-1830, 2004c. SAE Technical Paper 2004-01-1464.
- M. Klein and L. Eriksson. Methods for cylinder pressure based compression ratio estimation. In *Electronic Engine Control*, number 2006-01-0185 in SAE Technical paper series SP-2003, SAE World Congress, Detroit, USA, 2006.
- M. Klein and L. Nielsen. Evaluating some gain scheduling strategies in diagnosis of a tank system. IFAC Fault Detection, Supervision and Safety for Technical Processes, pages 902–907, Budapest, Hungary, 2000.
- M. Klein, L. Eriksson, and Y. Nilsson. Compression estimation from simulated and measured cylinder pressure. In *Electronic Engine Controls*, SP-1704, 2002. SAE Technical Paper 2002-01-0843.
- M. Klein, L. Eriksson, and Y. Nilsson. Compression estimation from simulated and measured cylinder pressure. *SAE 2002 Transactions Journal of Engines*, 111(3), 2003. SAE Technical Paper 2002-01-0843.

- M. Klein, L. Eriksson, and J. Åslund. Compression ratio estimation based on cylinder pressure data. 2004. In proceedings of IFAC symposium on Advances in Automotive Control, Salerno, Italy.
- M. Klein, L. Eriksson, and J. Åslund. Compression ratio estimation based on cylinder pressure data. *Control Engineering Practice*, 14(3): 197–211, 2006.
- R.B. Krieger and G.L. Borman. The computation of apparent heat release for internal combustion engines. *ASME*, 1967.
- D. R. Lancaster, R. B. Krieger, and J. H. Lienesch. Measurement and analysis of engine pressure data. 1975. SAE Technical Paper 750026.
- P. Lindskog. *Methods, algorithms and tools for system identification based on prior knowledge*. PhD thesis, Linköping University, 1996.
- L. Ljung. *System Identification Theory for the User*. Prentice Hall, 2nd edition, 1999.
- F.A. Matekunas. Modes and measures of cyclic combustion variability. 1983. SAE Technical Paper 830337.
- K. Miller. Least squares methods for ill-posed problems with a prescribed bound. *SIAM Journal on Mathematical Analysis*, 1(1):52–74, 1970. doi: 10.1137/0501006. URL <http://link.aip.org/link/?SJM/1/52/1>.
- M. Mladek and C.H. Onder. A model for the estimation of inducted air mass and residual gas fraction using cylinder pressure measurements. 2000. SAE Technical Paper 2000-01-0958.
- M. Morishita and T. Kushiyama. An improved method for determining the TDC position in a pv-diagram (first report). *SAE Technical Paper 970062*, 1997.
- V.A. Morozov. *Methods for solving incorrectly posed problems*. Springer Verlag, New York, USA, 1984.
- Y. Nilsson and L. Eriksson. A new formulation of multi-zone combustion engine models. IFAC Workshop: Advances in Automotive Control, pages 629–634, Karlsruhe, Germany, 2001.
- Y. Nilsson and L. Eriksson. Determining TDC position using symmetry and other methods. *Modeling of SI Engines*, SP-1830, 2004. SAE Technical Paper 2004-01-1458.
- M. Nyberg. *Model Based Fault Diagnosis: Methods, Theory, and Automotive Engine Applications*. PhD thesis, Linköpings Universitet, June 1999.

M. Nyberg. A general framework for model based diagnosis based on statistical hypothesis testing (revised version). 12:th International Workshop on Principles of Diagnosis, pages 135–142, Sansicario, Via Lattea, Italy, 2001.

P. Öberg and L. Eriksson. Control oriented modeling of the gas exchange process in variable cam timing engines. Number SAE Technical Paper 2006-01-0660, 2006.

R. Pivec, T. Sams, and A. Wimmer. Wärmeübergang im ein- und auslasssystem. pages 658–663, 1998. MTZ Motortechnische Zeitschrift 59 (1998) Nr. 10.

F. Ponti, J. C. Pianai, and R. Suglia. Residual gas model for on-line estimation for inlet and exhaust continuous VVT engine configuration. *In proceedings of IFAC symposium on Advances in Automotive Control, Salerno, Italy, 2004.*

A.L. Randolph. Methods of processing cylinder-pressure transducer signals to maximize data accuracy. 1990. SAE Technical Paper 900170.

G.M. Rassweiler and L. Withrow. Motion pictures of engine flames correlated with pressure cards. *SAE Technical Paper 800131*, 1938.

F. Schmidt, R. Henderson, and C. Wolgemuth. *Introduction to thermal sciences*. John Wiley & Sons, Inc., 2nd edition, 1993.

P.J. Shayler, S.A. May, and T. Ma. The determination of heat transfer from the combustion chambers of SI engines. 1993. SAE Technical Paper 931131.

J. Sjöberg, Q. Zhang, L. Ljung, A. Benveniste, B. Deylon, P-Y. Glorennec, H. Hjalmarsson, and A. Juditsky. Nonlinear black-box modeling in system identification: a unified overview. *Automatica*, 31: 1691–1724, Dec 1995.

M.J. Staś. Thermodynamic determination of T.D.C. in piston combustion engines. 1996. SAE Technical Paper 960610.

M.J. Staś. A universally applicable thermodynamic method for T.D.C. determination. 2000. SAE Technical Paper 2000-01-0561.

R. Stone. *Introduction to Internal Combustion Engines*. SAE International, 3rd edition, 1999.

R.A. Svehla and B.J. McBride. Fortran IV computer programs for calculation of thermodynamic and transport properties of complex chemical systems. Technical Report NASA Technical Note TND-7056, NASA Lewis Research Center, 1973.

I.I. Vibe. *Brennverlauf und Kreisprozess von Verbrennungsmotoren*. VEB Verlag Technik Berlin, 1970. German translation of the russian original.

N. Watson and M.S. Janota. *Turbocharging the Internal Combustion Engine*. The Macmillan Press Ltd, 1982. ISBN 0-333-24290-4.

A. Wimmer, R. Pivec, and T. Sams. Heat transfer to the combustion chamber and port walls of IC engines – measurement and prediction. 2000. SAE Technical Paper 2000-01-0568.

G. Woschni. A universally applicable equation for the instantaneous heat transfer coefficient in the internal combustion engine. 1967. SAE Technical Paper No. 670931.

A SPECIFIC HEAT RATIO MODEL – FURTHER DETAILS

Additional details and argumentation for the results in chapter 4 are given in this appendix. Each section is referenced from various sections in chapter 4, and this appendix is therefore a complement.

A.1 Temperature models

Two models for the in-cylinder temperature will be described, the first is the mean charge single-zone temperature model. The second is a two-zone mean temperature model, used to compute the single-zone thermodynamic properties as mean values of the properties in a two-zone model.

A.1.1 Single-zone temperature model

The mean charge temperature T for the single-zone model is found from the ideal state equation $pV = m_{tot}RT$, assuming the total mass of charge m_{tot} and the mass specific gas constant R to be constant. These assumptions are reasonable since the molecular weights of the reactants and the products are essentially the same (Gatowski et al., 1984). If all thermodynamic states $(p_{ref}, T_{ref}, V_{ref})$ are known/evaluated at a given reference condition *ref*, such as IVC, the mean charge temperature T is computed as

$$T = \frac{T_{IVC}}{p_{IVC}V_{IVC}}pV. \quad (\text{A.1})$$

This model has already been described in section 3.3.1.

A.1.2 Two-zone mean temperature model

A two-zone model is divided into two zones; one containing the unburned gases and the other containing the burned gases, separated by an infinitesimal thin divider representing the flame front. Each zone is homogeneous considering temperature and thermodynamic properties, and the pressure is the same throughout all zones, see e.g. (Nilsson and Eriksson, 2001). Here a simple two-zone model will be used to find the burned zone temperature T_b and the unburned zone temperature T_u , in order to find a more accurate value of $\gamma(T)$ as an interpolation of the thermodynamic properties for burned and unburned mixtures. The model is called temperature mean value approach (Andersson, 2002), and is based on a single-zone combustion model and polytropic compression of the unburned charge. The single-zone temperature can be seen as a mass-weighted mean value of the two zone temperatures.

Prior to start of combustion (SOC), the unburned zone temperature T_u equals the single-zone temperature T :

$$T_{u,SOC} = T_{SOC}. \quad (\text{A.2})$$

The unburned zone temperature T_u after SOC is then computed assuming polytropic compression (2.11) of the unburned charge according to:

$$T_u = T_{u,SOC} \left(\frac{p}{p_{SOC}} \right)^{1-1/n} = T_{SOC} \left(\frac{p}{p_{SOC}} \right)^{1-1/n}. \quad (\text{A.3})$$

The crank angle position for ignition θ_{ig} is assumed to coincide with SOC, and then the unburned zone temperature T_u is given by:

$$T_u(\theta) = \begin{cases} T(\theta) & \theta \leq \theta_{ig} \\ T(\theta_{ig}) \left(\frac{p}{p(\theta_{ig})} \right)^{1-1/n} & \theta > \theta_{ig}. \end{cases} \quad (\text{A.4})$$

Energy balance between the single-zone and the two-zone models yields:

$$(m_b + m_u)c_v T = m_b c_{v,b} T_b + m_u c_{v,u} T_u. \quad (\text{A.5})$$

In order to have a fast computation it is assumed that $c_v = c_{v,b} = c_{v,u}$, i.e. a caloric perfect gas, which ends up in

$$T = \frac{m_b T_b + m_u T_u}{m_b + m_u} = x_b T_b + (1 - x_b) T_u, \quad (\text{A.6})$$

where x_b is the mass fraction burned. The single-zone temperature T can be seen as the mass-weighted mean temperature of the two zones. If a temperature and pressure dependent model of c_v would be used, the weight of T_b in (A.6) would increase, resulting in a lower value for T_b since $c_{v,b} > c_{v,u}$. From (A.6), T_b is found as

$$T_b = \frac{T - (1 - x_b) T_u}{x_b}. \quad (\text{A.7})$$

The burned zone temperature is sensitive to low values of the mass fraction burned, x_b . Therefore T_b is set to the adiabatic flame temperature for $x_b < 0.01$. The adiabatic flame temperature T_{ad} for a constant pressure process is found from:

$$h_u(T_u) = h_b(T_{ad}, p) \quad (\text{A.8})$$

where h_u and h_b are the enthalpy for the unburned and burned mixture respectively. An algorithm for computing the zone temperatures is summarized as:

Algorithm A.1 – Temperature mean value approach

1. Compute the single-zone temperature T in (A.1).
 2. Compute the mass fraction burned x_b by using the Matekunas pressure ratio concept (2.21)–(2.22).
 3. Compute the unburned zone temperature T_u using (A.4).
 4. If $x_b \geq 0.01$ then; Compute the burned zone temperature T_b from (A.7).
else; Compute the burned zone temperature T_b from (A.8).
 5. Return T , T_u and T_b .
-

In step 2 the Matekunas pressure ratio concept could be exchanged for any of the single-zone heat-release models given in chapter 2, but the Matekunas concept is used due to its computational efficiency.

As an illustration, the zone temperatures for the cylinder pressure trace displayed in figure 4.8 are shown in figure A.1.

A.2 SAAB 2.3L NA – Geometric data

A SAAB 2.3L NA engine is for simulated and experimental data in chapters 2–4. The geometric data for the crank and piston movement are given in the following table:

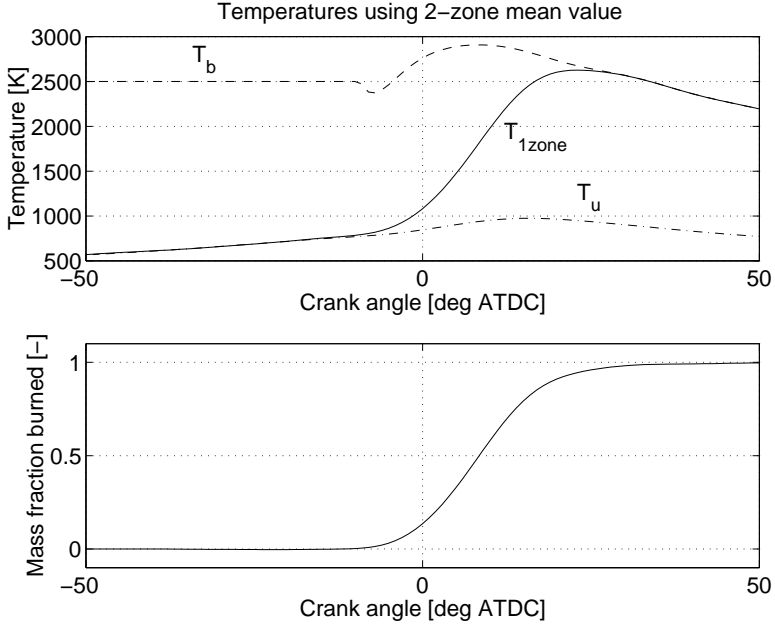


Figure A.1: *Upper*: Single-zone temperature T ($=T_{1zone}$), unburned T_u and burned T_b zone temperatures for the cylinder pressure given in figure 4.8. *Bottom*: Corresponding mass fraction burned trace calculated using Matekunas pressure ratio.

Property	Abbrev.	Value	Unit
Bore	B	90	[mm]
Stroke	S	90	[mm]
Crank radius	$a_r = \frac{S}{2}$	45	[mm]
Connecting rod	l	147	[mm]
No. of cylinders	n_{cyl}	4	[-]
Displacement volume	V_d	2290	[cm ³]
Clearance volume	V_c	62.9	[cm ³]
Compression ratio	r_c	10.1	[-]

A.3 Parameters in single-zone model

The nominal parameters used in the single-zone model (3.36)–(3.45) are summarized in table A.1 for operating point 2. The parameter values for Q_{in} , p_{IVC} and T_{IVC} differ for all the nine operating points according to table A.2. All the other parameters remain the same.

The difference between the γ -models is expected to be largest during

Par.	Description	Value
γ_{300}	constant ratio of specific heat [-]	1.3678
b	slope for ratio of specific heat [K^{-1}]	$-8.13 \cdot 10^{-5}$
C_1	Woschni heat transfer parameter [-]	2.28
C_2	Woschni heat transfer parameter [$m/(s K)$]	$3.24 \cdot 10^{-4}$
$\Delta\theta$	crank angle phasing [deg]	0
θ_{ig}	ignition angle [deg ATDC]	-15
θ_d	flame development angle [deg]	20
θ_b	rapid burn angle [deg]	40
V_c	clearance volume [cm^3]	62.9
V_{cr}	single aggregate crevice volume [% V_c]	1.5%
Δp	pressure bias in measurements [kPa]	0
T_w	mean wall temperature [K]	440
T_{IVC}	mean charge temperature at IVC [K]	341
p_{IVC}	cylinder pressure at IVC [kPa]	50
Q_{in}	released energy from combustion [J]	760
K_p	pressure sensor gain [-]	1

Table A.1: Nominal parameter values for OP2 in the single zone model.

OP	p_{IVC} [kPa]	T_{IVC} [K]	Q_{in} [J]
1	25	372	330
2	50	341	760
3	100	327	1620
4	150	326	2440
5	200	325	3260
1	25	372	330
6	50	372	700
7	100	372	1420
8	150	372	2140
9	200	372	2850

Table A.2: Operating points (OP) for the simulated cylinder pressure.

combustion, therefore a slow burn rate is used to extend the period when the models differ. Compared to table 3.1 the following parameters are changed; The burn related angles θ_{ig} , θ_d and θ_b are changed, to reflect a slower burn rate. The offsets $\Delta\theta$ and Δp are both set to zero since they do not have an effect on the investigation.

A.4 Crevice energy term

The energy term $u' - u$ in (2.26) describes the energy required to heat up a unit mass that enters the cylinder from the crevice volume. The term depends on which γ -model is used and therefore has to be stated for every γ -model except \mathcal{B}_1 , which is already done in (2.32) for the original setting in the Gatowski et al.-model.

For model \mathcal{D}_1 , the energy term $u' - u$ in (2.32) is:

$$\begin{aligned} u' - u &= \int_T^{T'} c_v dT \\ &= x_b \int_{T_b}^{T'} c_{v,b}^{KB} dT + (1 - x_b) \int_{T_u}^{T'} c_{v,u}^{lin} dT \\ &= x_b (u^{KB}(T', p) - u^{KB}(T_b, p)) + (1 - x_b) \frac{R}{b^u} \ln \left(\frac{\gamma_{lin}^u(T') - 1}{\gamma_{lin}^u(T_u) - 1} \right), \end{aligned} \quad (\text{A.9})$$

where we have used that $c_v = x_b c_{v,b}^{KB} + (1 - x_b) c_{v,u}^{lin}$ in the second equality, and in the third equality that $c_v = \left(\frac{\partial u}{\partial T} \right)_V$ for the burned mixture and equation (2.31) for the linear approximation of the unburned mixture. The first term in (A.9) is given directly by the Krieger-Borman polynomial in its original form (4.9). The second term is easily computed when knowing the coefficient values γ_{300}^u and b^u for the linear unburned mixture model, i.e.

$$\gamma_{lin}^u = \gamma_{300}^u + b^u (T_u - 300), \quad (\text{A.10})$$

where the coefficients γ_{300}^u and b^u are given in table 4.2.

Different modeling assumptions in terms of single-zone or two-zone models result in different temperatures T' . In these cases the temperature T' is as follows: For the single-zone model

$$T' = \begin{cases} T_w & dm_{cr} < 0 \\ T & dm_{cr} \geq 0, \end{cases} \quad (\text{A.11})$$

for the burned zone

$$T' = \begin{cases} T_w & dm_{cr} < 0 \\ T_b & dm_{cr} \geq 0, \end{cases} \quad (\text{A.12})$$

and according to

$$T' = \begin{cases} T_w & dm_{cr} < 0 \\ T_u & dm_{cr} \geq 0 \end{cases} \quad (\text{A.13})$$

for the unburned zone. Note that (A.9) is zero whenever $T' = T$, i.e. when the mass flows to the crevice volume.

Now the attention is turned to the crevice energy term $u' - u$ for the γ -models (4.19)–(4.31). For \mathcal{C}_1 , \mathcal{C}_3 and \mathcal{C}_4 approximations are made during the combustion phase. In order to see if a modeling error in $u' - u$ has a large impact on the cylinder pressure, a sensitivity analysis will be performed after all models have been described. Model \mathcal{B}_1 (4.19):

$$u' - u = \frac{R}{b} \ln \left(\frac{\gamma_{lin}(T') - 1}{\gamma_{lin}(T) - 1} \right), \quad (\text{A.14})$$

according to (2.32). Model \mathcal{B}_2 (4.20):

$$u' - u = u_{\mathcal{B}_2}(T') - u_{\mathcal{B}_2}(T). \quad (\text{A.15})$$

Model \mathcal{B}_3 (4.21):

$$u' - u = u_{\mathcal{B}_3}(T', p) - u_{\mathcal{B}_3}(T, p). \quad (\text{A.16})$$

Model \mathcal{B}_4 (4.22):

$$u' - u = (T' - T) \frac{R}{\gamma_{\mathcal{B}_4}}. \quad (\text{A.17})$$

Model \mathcal{C}_1 (4.23):

$$\begin{aligned} u' - u &= \int_T^{T'} \frac{R}{\gamma_{\mathcal{C}_1}} dT \\ &= R \int_T^{T'} \frac{R}{x_b \gamma_{300}^b + (1-x_b) \gamma_{300}^u + x_b b^b (T_b - 300) + (1-x_b) b^u (T_u - 300)} dT \\ &\approx R \int_T^{T'} \frac{R}{x_b \gamma_{300}^b + (1-x_b) \gamma_{300}^u + (x_b b^b + (1-x_b) b^u) (T - 300)} dT \\ &= \frac{R}{x_b b^b + (1-x_b) b^u} \ln \left(\frac{\gamma_{\mathcal{C}_1}(T') - 1}{\gamma_{\mathcal{C}_1}(T_b, T_u) - 1} \right), \end{aligned} \quad (\text{A.18})$$

where the approximation is an equality whenever $x_b = 0$, $x_b = 1$ or $dm_{cr} \geq 0$. The coefficients for the unburned mixture γ_{300}^u and b^u are given in table 4.2 and the values for γ_{300}^b and b^b are taken from table 4.3 for temperature region E ($T \in [1200, 3000]$ K).

Model \mathcal{C}_2 (4.24):

$$u' - u = u_{\mathcal{C}_2}(T') - u_{\mathcal{C}_2}(T). \quad (\text{A.19})$$

Model \mathcal{C}_3 (4.25):

$$\begin{aligned} u' - u &= \int_T^{T'} \frac{R}{\gamma_{\mathcal{C}_3}} dT \\ &= R \int_T^{T'} \frac{R}{x_b \gamma_{KB} + (1-x_b) \gamma_{in}^u} dT \\ &\approx R(x_b \int_{T_b}^{T'} \frac{R}{\gamma_{KB}} dT + (1-x_b) \int_{T_u}^{T'} \frac{R}{\gamma_{in}^u} dT) \\ &\quad x_b (u^{KB}(T', p) - u^{KB}(T_b, p)) + (1-x_b) \frac{R}{b^u} \ln \left(\frac{\gamma_{in}^u(T') - 1}{\gamma_{in}^u(T_u) - 1} \right), \end{aligned} \quad (\text{A.20})$$

where the approximation is an equality whenever $x_b = 0$, $x_b = 1$ or $dm_{cr} \geq 0$. The approximation made for \mathcal{C}_3 yields the same energy term as for \mathcal{D}_1 (A.9).

For model \mathcal{C}_4 (4.26) the energy term is approximated in the same way as for \mathcal{C}_3 , i.e.

$$\begin{aligned} u' - u &= \int_T^{T'} \frac{R}{\gamma_{\mathcal{C}_4}} dT \\ &\approx x_b (u_b(T', p) - u_b(T_b, p)) + (1-x_b) (u_u(T') - u_u(T_u)) \end{aligned} \quad (\text{A.21})$$

where the internal energies for burned, u^b , and unburned mixture, u^u , are computed from CHEPP (4.3), and the approximation is an equality whenever $x_b = 0$, $x_b = 1$ or $dm_{cr} \geq 0$. The approximation made for \mathcal{C}_4 yields the same energy term as for the reference model \mathcal{D}_4 (A.25).

Model \mathcal{C}_5 (4.27):

$$\begin{aligned} u' - u &= \int_T^{T'} \frac{R}{\gamma_{c_5}(T, x_b)} dT \\ &= \begin{cases} \frac{R}{b^{comp}} \ln \left(\frac{\gamma_{c_5}(T', 0) - 1}{\gamma_{c_5}(T, 0) - 1} \right) & x_b < 0.01 \\ (T' - T) \frac{R}{\gamma_{c_5} - 1} & 0.01 \leq x_b \leq 0.99 \\ \frac{R}{b^{exp}} \ln \left(\frac{\gamma_{c_5}(T', 1) - 1}{\gamma_{c_5}(T, 1) - 1} \right) & x_b > 0.99 \end{cases} \quad (\text{A.22}) \end{aligned}$$

The energy term corresponding to $x_b < 0.01$ is at most instances equal to zero, but not when the start of combustion occurs after TDC.

Model \mathcal{D}_2 (4.29):

$$u' - u = x_b(u^{KB}(T', p) - u^{KB}(T_b, p)) + (1 - x_b)(u_u(T') - u_u(T_u)). \quad (\text{A.23})$$

Model \mathcal{D}_3 (4.30):

$$u' - u = x_b(u_b(T', p) - u_b(T_b, p)) + (1 - x_b) \frac{R}{b^u} \ln \left(\frac{\gamma_{in}^u(T') - 1}{\gamma_{in}^u(T_u) - 1} \right). \quad (\text{A.24})$$

Model \mathcal{D}_4 (4.31):

$$u' - u = x_b(u_b(T', p) - u_b(T_b, p)) + (1 - x_b)(u_u(T') - u_u(T_u)). \quad (\text{A.25})$$

Crevice term sensitivity

An investigation of what impact a modeling error in the crevice term has on the cylinder pressure is now performed. The same sensitivity analysis as in section 3.9 is made, but this time the crevice volume V_{cr} is set to 0 in the nominal cylinder pressure. The results from the simulations are summarized in table A.3.

The investigation shows that the $\text{RMSE}(p)$ is higher for all parameters except T_w , T_{IVC} and Δp when $V_{cr} = 0$, suggesting that the crevice volume has a dampening effect on the cylinder pressure error. The change in all the measures RMSE, maximum residual value and sensitivity S are small, when compared to table 3.2. Although the sensitivity analysis is performed in a specific operating point and therefore only valid locally, this result indicates that a correct crevice-term modeling is not crucial for the single-zone heat-release models. It also indicates that the crevice effect has a small impact on the resulting cylinder pressure. Therefore a modeling error in $u' - u$ such as for models \mathcal{C}_1 , \mathcal{C}_3 and \mathcal{C}_4 will not have not a crucial effect on the final result and conclusions

Par.	Nominal & perturbation value			RMSE	Max Res	S
				[kPa]	[kPa]	[-]
γ_{300}	1.3678	0.137	[-]	542.0	1471.10	5.40
$\Delta\theta_d$	15	5	[deg]	282.5	1081.2	0.60
θ_{ig}	-20	5	[deg ATDC]	248.3	904.0	0.74
V_c	62.9	6.29	[cm^3]	217.5	632.2	1.80
K_p	1	0.1	[-]	188.4	477.2	1.56
T_w	440	44	[K]	108.7	283.5	0.86
Q_{in}	1500	150	[J]	103.6	271.9	0.81
$\Delta\theta_b$	30	5	[deg]	105.2	412.7	0.46
p_{IVC}	100	10	[kPa]	97.5	221.5	0.77
T_{IVC}	340	44	[K]	62.8	175.2	0.35
b	$-8.13 \cdot 10^{-5}$	$-8.13 \cdot 10^{-6}$	[K^{-1}]	27.0	82.7	0.20
$\Delta\theta$	0.4	0.2	[deg]	10.6	32.7	0.2
Δp	30	10	[kPa]	10.0	10.0	0.2
C_2	$3.24 \cdot 10^{-3}$	$3.24 \cdot 10^{-4}$	[$m/(s K)$]	4.1	8.8	0.3
C_1	2.28	0.228	[-]	1.7	2.10	0.1

Table A.3: Nominal and perturbation values, where the perturbations are performed by adding or subtracting the perturbation from the nominal value. The root mean square error (RMSE), maximal residual (Max Res) and sensitivity function S (3.46) are computed for the worst case for each parameter.

drawn. It is important to note that the γ -model is very important for the cylinder pressure model. This is primarily through its direct influence by coupling the pressure, temperature and volume changes to each other. The crevice effect is also directly dependent on the γ -model, but here γ only has a secondary effect on the total cylinder pressure model.

A.5 Simple residual gas model

An approximative model for finding the residual gas fraction $x_r = \frac{m_r}{m_{tot}}$ and temperature T_r cited in Heywood (1988, p.178) is used to find T_{IVC} . The residual gas mass is given by m_r and the total cylinder gas mass by m_{tot} . The residual gas is left behind from the exhaust process and fills the clearance volume V_c at pressure p_{exh} and temperature T_6 , where p_{exh} is the exhaust manifold pressure and T_6 is the mean charge temperature at $\theta = 360$ [deg ATDC], i.e. at the end of the exhaust stroke. The intake manifold contains a fresh air-fuel charge at pressure p_{man} and temperature T_{man} . As the intake valve opens, the residual gases expand according to the polytropic relation (2.11) to volume V_r and temperature T_r according to

$$V_r = V_c \left(\frac{p_{exh}}{p_{man}} \right)^{1/n}, \quad (\text{A.26a})$$

$$T_r = T_6 \left(\frac{p_{man}}{p_{exh}} \right)^{\frac{n}{n-1}}. \quad (\text{A.26b})$$

The rest of the cylinder volume V_{af} is filled with fresh air-fuel charge, i.e. $V_{af} = V - V_r$. The ideal gas law is then used to compute the residual gas fraction x_r as

$$\begin{aligned} x_r &= \frac{m_r}{m_{af} + m_r} = \frac{\frac{p_{man} V_r}{RT_r}}{\frac{p_{man} V_{af}}{RT_{man}} + \frac{p_{man} V_r}{RT_r}} = \dots \\ &= \left(1 + \frac{T_r}{T_{man}} \left(r_c \frac{p_{man}}{p_{exh}} - \left(\frac{p_{man}}{p_{exh}} \right)^{(n-1)/n} \right) \right)^{-1}, \quad (\text{A.27}) \end{aligned}$$

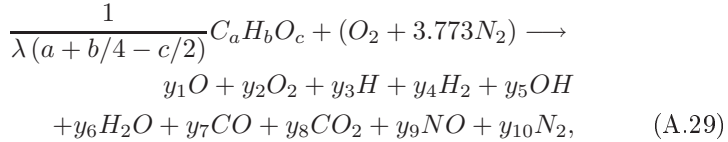
and the mean charge temperature at IVC is then computed as

$$T_{IVC} = T_r r_c x_r \left(\frac{p_{man}}{p_{exh}} \right), \quad (\text{A.28})$$

where $T_r = 1400$ K and $(n-1)/n = 0.24$ are appropriate average values to use for initial estimates (Heywood, 1988, p.178).

A.6 Fuel composition sensitivity of γ

So far, the focus has only been on iso-octane C_8H_{18} as the fuel used. Since the actual fuel composition can differ over both region of country and time of year, it is interesting to see what happens with the specific heat ratios when the fuel composition is changed. Consider the general fuel $C_a H_b O_c$, which is combusted according to



where a , b and c are positive integers.

First our attention is turned to the properties of hydrocarbons and then to a few alcohols, when considering burned mixtures. Then a similar investigation is made for unburned mixtures. Finally the properties of partially burned mixtures and their influence on the cylinder pressure are examined.

A.6.1 Burned mixture – Hydrocarbons

Considering hydrocarbons $C_a H_b$ only ($c = 0$), the hydrocarbon ratio $y = b/a$ will determine the properties of the air-fuel mixture, since the a and b are only relative proportions on a molar basis (Heywood,

1988)[p.69]. The specific heat ratio is computed using CHEPP for the fuels given in table A.4. Gasoline 1 and 2 are commercial fuels listed in Heywood (1988)[p.133]. The fuels methane and gasoline 2 are extreme points for the hydrocarbon ratio y in the study, a region which covers most hydrocarbon fuels. In the upper plot of figure A.2 the specific heat ratio for the fuels at $\lambda = 1$ and $p = 7.5$ bar are displayed. They are computed using model \mathcal{D}_4 (4.31). The difference between the fuels is hardly visible. Therefore, the fuels are compared to iso-octane, and the difference in γ is plotted in the lower part of figure A.2.

The difference is small, and smallest for the commercial gasoline as expected, since the hydrocarbon ratio y is closest to that of iso-octane. The NRMSE(γ) are found in table A.4, for $p_1 = 7.5$ and $p_2 = 35$ bar respectively. Compared to table 4.5, the fuel composition introduces a smaller error in γ than the Krieger-Borman polynomial. Therefore the iso-octane γ can be used as a good approximation for a burned mixture for the hydrocarbon fuels used in this study.

A.6.2 Burned mixture – Alcohols

Considering more general fuels such as alcohols, the specific heat ratio of methanol CH_3OH is computed and compared to the ones found for iso-octane and methane respectively. The comparison with methane shows what influence the extra oxygen atom brings about, and the comparison with iso-octane yields the difference to the fuel used here as a reference fuel. The specific heat ratios are computed using \mathcal{D}_4 (4.31). The results are displayed in figure A.3, where the upper plot shows γ for the three fuels listed in table A.5. The lower plot shows the difference in γ for methanol when compared to iso-octane and methane respectively. In figure A.3 and table A.5 the results for the fuels are compared to methanol instead of iso-octane due to three reasons; First of all this allows for a direct comparison of the results for methane and methanol. Secondly, it allows for a comparison of methanol and iso-octane. Thirdly γ for methane and iso-octane have already been compared in figure A.2 and table A.4.

Surprisingly, the difference in γ is smaller between iso-octane and methanol than between methane and methanol as shown in figure A.3, which is also concluded by comparing the NRMSE:s from table A.5. These NRMSE:s are in fact quite large, which is found by comparing them to the ones found in table 4.4. This suggests that the error introduced by using iso-octane γ to describe methanol γ is almost as large the error introduced by the linear model γ_{lin}^b . If a better approximation of the methanol γ is needed, one should use CHEPP (Eriksson, 2004) to compute the thermodynamic properties for methanol and then estimate the coefficients in the Krieger-Borman polynomial (4.9) in a least squares sense.

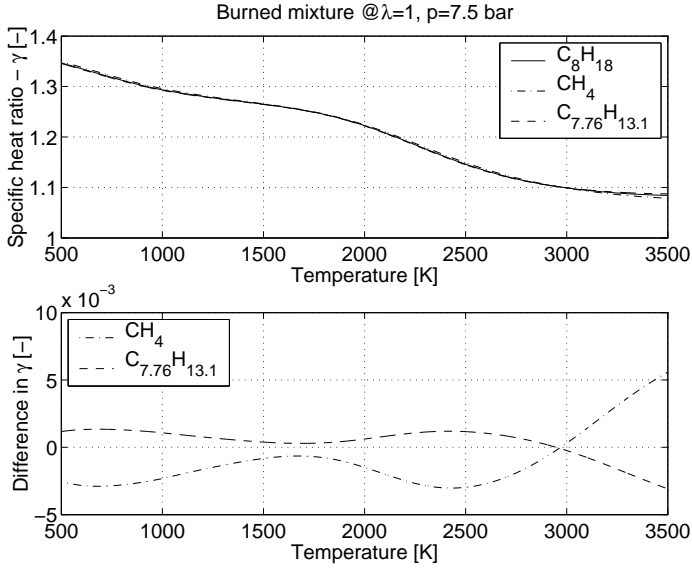


Figure A.2: *Upper*: Specific heat ratio for various fuels. *Lower*: Difference in γ for methane CH_4 and gasoline 2 $C_{7.76}H_{13.1}$, compared to iso-octane C_8H_{18} .

Fuel	C_aH_b	y	NRMSE @ p_1		NRMSE @ p_2	
			A	B	A	B
Methane	CH_4	4	0.19 %	0.17 %	0.16 %	0.15 %
Iso-octane	C_8H_{18}	2.25	0	0	0	0
Gasoline 1	$C_{8.26}H_{15.5}$	1.88	0.06 %	0.05 %	0.05 %	0.04 %
Gasoline 2	$C_{7.76}H_{13.1}$	1.69	0.09 %	0.07 %	0.07 %	0.07 %

Table A.4: Burned mixtures: Different fuels and their chemical composition. The NRMSE(γ) is formed as the difference compared to iso-octane, and evaluated at $\lambda = 1$ and temperature regions A and B, for $p_1 = 7.5$ and $p_2 = 35$ bar respectively.

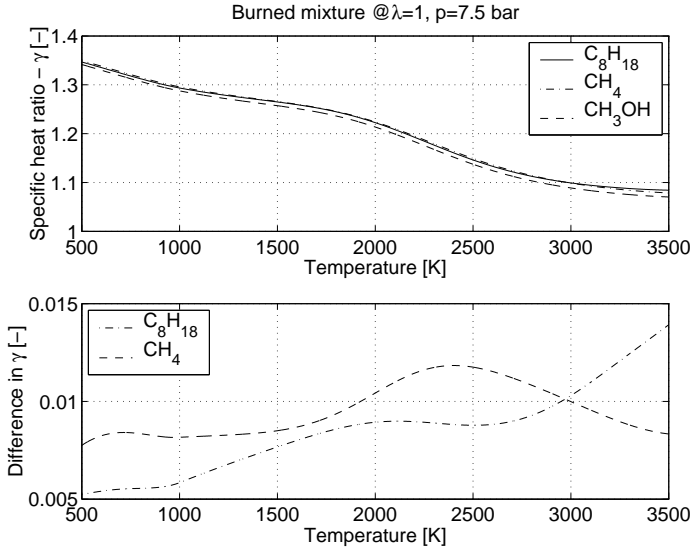


Figure A.3: *Upper*: Specific heat ratio for various fuels. *Lower*: Difference in γ for methanol CH_3OH compared to iso-octane C_8H_{18} and methane CH_4 .

Fuel	$C_aH_bO_c$	NRMSE @ p_1		NRMSE @ p_2	
		A	B	A	B
Methanol	CH_4O	0	0	0	0
Methane	CH_4	0.80 %	0.75 %	0.81 %	0.72 %
Iso-octane	C_8H_{18}	0.73 %	0.60 %	0.70 %	0.60 %

Table A.5: Burned mixtures: Different fuels and their chemical composition. The NRMSE is formed as the difference for methanol compared to methane and iso-octane respectively, and evaluated at $\lambda = 1$ and temperature regions A and B, for $p_1 = 7.5$ and $p_2 = 35$ bar respectively.

A.6.3 Unburned mixtures

The specific heat ratios for both unburned hydrocarbons and alcohols are analyzed in a similar manner as for the burned mixtures presented earlier. The results are summarized in table A.6. All fuels but methane are captured fairly well by the reference fuel iso-octane. Comparing gasoline 1 with the linear model of the unburned mixture given in table 4.2, one see that it introduces an NRMSE which is of the same order. A trend in the results shows that for hydrocarbons, the specific heat ratio is more accurately determined for burned mixtures than unburned. This conclusion can be drawn by comparing tables A.4 and A.6. For the alcohol methanol it is the other way around, compare tables A.5 and A.6.

Fuel	$C_aH_bO_c$	$y = b/a$	NRMSE
Methane	CH_4	4	2.57 %
Iso-octane	C_8H_{18}	2.25	0
Gasoline 1	$C_{8.26}H_{15.5}$	1.88	0.18 %
Gasoline 2	$C_{7.76}H_{13.1}$	1.69	0.39 %
Methanol	CH_3OH	4	0.50 %

Table A.6: Unburned mixtures: Different fuels and their chemical composition. The $NRMSE(\gamma)$ is formed as the difference compared to iso-octane, and evaluated at $\lambda = 1$ for temperature region $T \in [300, 1000]$ K.

A.6.4 Partially burned mixture – influence on cylinder pressure

The cylinder pressure at OP 2 given in figure 4.8 is used to exemplify the impact a certain fuel has on the cylinder pressure, given that all the other operating conditions are the same. The reference model (4.18) is used to model γ for each fuel. The impact is displayed as the RMSE for the pressure in table A.7, as well as the NRMSE and MRE for γ . Iso-octane is used as the reference fuel. Compared to table 4.6, the cylinder pressure impact ($RMSE(p)$) of the fuels listed in table A.7 are larger than the impact of \mathcal{D}_1 , see the $RMSE(p)$ column in table 4.6, for all fuels except gasoline 1. However for all fuels but methane, the $RMSE(p)$ introduced is increased with less than 75 % compared to iso-octane, which is acceptable.

The goal is to find a model that approximates the actual γ well. Model \mathcal{D}_1 is computationally efficient and will therefore be used in the evaluation. Table A.8 evaluates the impact the use of the polynomials in model \mathcal{D}_1 has on a specific fuel, in terms of $MRE(\gamma)$, $NRMSE(\gamma)$

Fuel	MRE: γ [%]	NRMSE: γ [%]	RMSE: p [kPa]
Methane	2.8	2.0	36.6
Iso-octane	0.0	0.0	0.0
Gasoline 1	0.20	0.12	2.2
Gasoline 2	0.40	0.29	5.3
Methanol	0.85	0.63	5.1

Table A.7: Evaluation of the impact on cylinder pressure and specific heat ratio for various fuels using iso-octane as reference fuel, for the simulated cylinder pressure at OP 2 in figure 4.8.

Fuel	MRE: γ [%]	NRMSE: γ [%]	RMSE: p [kPa]
Methane	2.7	1.9	34.3
Iso-octane	0.27	0.10	2.8
Gasoline 1	0.27	0.15	1.5
Gasoline 2	0.47	0.29	3.3
Methanol	1.1	0.70	5.4

Table A.8: Evaluation of the impact on cylinder pressure and specific heat ratio for various fuels by using model \mathcal{D}_1 , for the simulated cylinder pressure at OP 2 in figure 4.8.

and $\text{RMSE}(p)$. In the evaluation model \mathcal{D}_4 has been used for a specific fuel to generate the thermodynamic properties of the mixture, from which a cylinder pressure simulation has been performed. This reference pressure and specific heat ratio has then been compared to the ones given by model \mathcal{D}_1 for the same operating conditions at OP 2. The table shows that the $\text{RMSE}(p)$ for gasolines 1 and 2 are close to the one found for iso-octane. In fact, the $\text{RMSE}(p)$ is only increased by 20 %. It can therefore be concluded that model \mathcal{D}_1 can be used for fuels that have a hydrocarbon ratio close to 2, at least within [1.69, 2.25] and still have a modeling error in the order of the noise. Note that the closer y is to 2, the smaller $\text{RMSE}(p)$ is. This is due to that the hydrocarbon ratio for the Krieger-Borman polynomial used in \mathcal{D}_1 is 2. This also explains why the $\text{RMSE}(p)$ are smaller in table A.8 compared to table A.7.

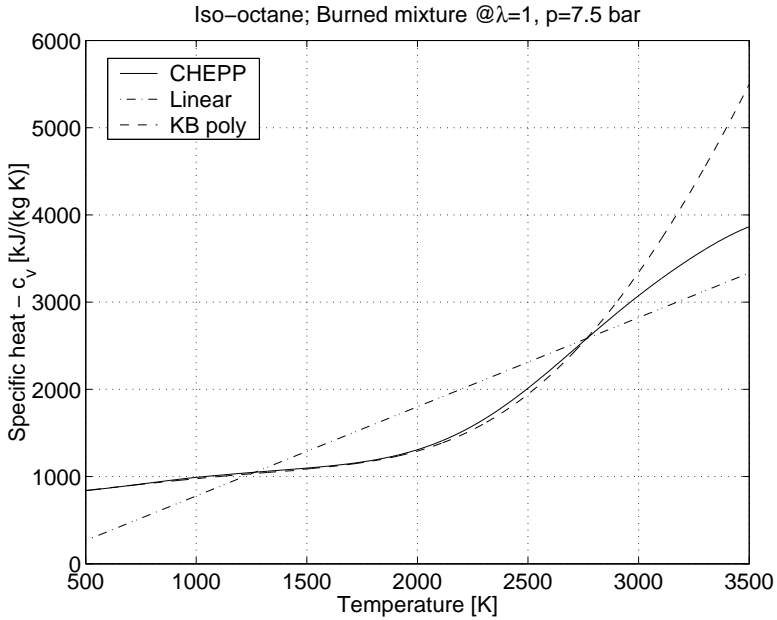


Figure A.4: Specific heat $c_{v,b}$ for burned stoichiometric mixture using CHEPP, the corresponding linear function $c_{v,b}^{lin}$ and $c_{v,b}^{KB}$ found using the Krieger-Borman polynomial.

Region	$T \in$	$c_{v,b}^{lin}$		$c_{v,b}^{KB}$	
		MRE	NRMSE	MRE	NRMSE
A	[500, 3500]	0.68 %	0.20 %	0.42 %	0.21 %
B	[500, 3000]	0.68 %	0.23 %	0.09 %	0.03 %
C	[500, 2700]	0.68 %	0.27 %	0.04 %	0.02 %
D	[500, 2500]	0.68 %	0.30 %	0.04 %	0.02 %
E	[1200, 3000]	0.38 %	0.20 %	0.09 %	0.04 %

Table A.9: Maximum relative error (MRE) and normalized root mean square error (NRMSE) of specific heat $c_{v,b}$ for different temperature regions at $\lambda = 1$ and $p = 7.5$ bar.

A.7 Thermodynamic properties for burned mixture

This section entails further details on thermodynamic properties for the burned mixture. The focus is on approximative models for the specific heats. As mentioned in section 4.6, there is a potential of improving the Krieger-Borman polynomial. Here it will be shown why. Figure A.4 displays the reference specific heat $c_{v,b}$ as well as the two approximations, i.e. the linear and the Krieger-Borman model respectively. The linear approximation has poor performance over the entire temperature region, and does not capture non-linear behavior of the reference model very well. The Krieger-Borman polynomial fits the reference model quite well for $T < 2800$ K, but for higher temperatures the fit is worse. This is reflected in table A.9, which displays the maximum relative error (MRE) and normalized root mean square error (NRMSE) for a number of temperature regions.

For temperature regions B–E, the NRMSE for $c_{v,b}^{KB}$ is immensely lower than for region A, which verifies that the Krieger-Borman polynomial works well for temperatures below 3000 K. Actually the Krieger-Borman polynomial has poorer performance than the linear model for high temperatures, as seen by comparing the NRMSE:s for temperature region A. This shows that there is a potential of enhancing the Krieger-Borman polynomial, at least for temperatures above 3000 K. If a better model approximation is sought, one should first increase the polynomial order in T of (4.10) with at least 1, to better catch the behavior for $T > 3000$ K in figure A.4. The thermodynamic properties can then be computed using CHEPP (Eriksson, 2004), and all coefficients estimated in a least squares sense.

The corresponding results for specific heat $c_{p,b}$ are shown in figure A.5 and table A.10, from which the same conclusions as for $c_{v,b}$ can be drawn.

Region	$T \in$	$c_{p,b}^{lin}$		$c_{p,b}^{KB}$	
		MRE	NRMSE	MRE	NRMSE
A	[500, 3500]	0.51 %	0.17 %	0.39 %	0.19 %
B	[500, 3000]	0.51 %	0.19 %	0.08 %	0.03 %
C	[500, 2700]	0.51 %	0.23 %	0.03 %	0.02 %
D	[500, 2500]	0.51 %	0.25 %	0.03 %	0.02 %
E	[1200, 3000]	0.31 %	0.17 %	0.08 %	0.03 %

Table A.10: Maximum relative error (MRE) and normalized root mean square error (NRMSE) of specific heat $c_{p,b}$ for different temperature regions at $\lambda = 1$ and $p = 7.5$ bar.

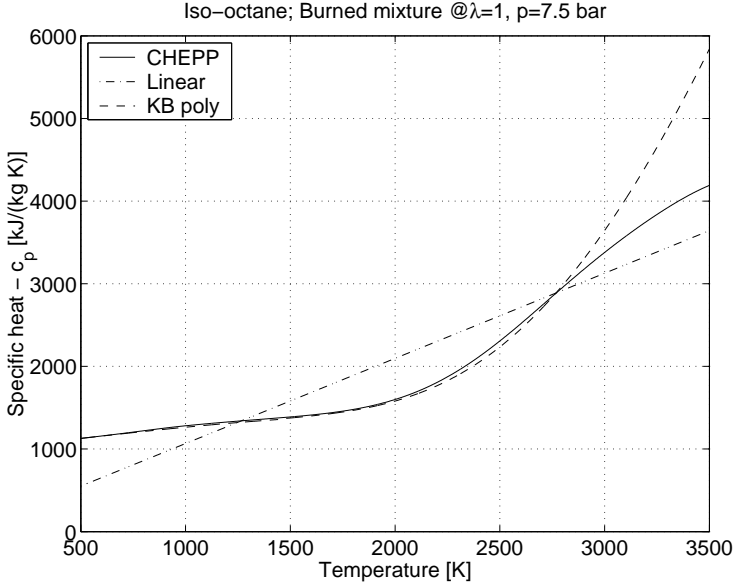


Figure A.5: Specific heat $c_{p,b}$ for burned stoichiometric mixture using CHEPP, the corresponding linear function $c_{p,b}^{lin}$ and $c_{p,b}^{KB}$ found using the Krieger-Borman polynomial.

A.8 Thermodynamic properties for partially burned mixture

The operating points (OP) for the simulated cylinder pressure traces used to evaluate the proposed γ -models are given in table A.2. In operating points 1-9 the mean charge temperature at IVC, T_{IVC} , is computed as a function of exhaust pressure p_{exh} (A.28), see appendix A.5. The released energy Q_{in} is computed as in (3.27), where the residual gas ratio x_r is determined from (A.27). The cylinder pressure at IVC, p_{IVC} , here ranges from 25 kPa up to 200 kPa, i.e. from low intake pressure to a highly supercharged pressure. The values of the parameters in the single-zone heat release model are given in tables A.1 and A.2. The corresponding cylinder pressures during the closed part of the cycle are shown in figure A.6, where the upper figure shows the cylinder pressure for operating points 1-5, and the lower plot displays operating point 1 and 6-9.

The results from applying operating points 1-9 to the approximate γ -models are summarized in the following tables and figures; Tables A.11 and A.12 summarizes the maximum relative error and nor-

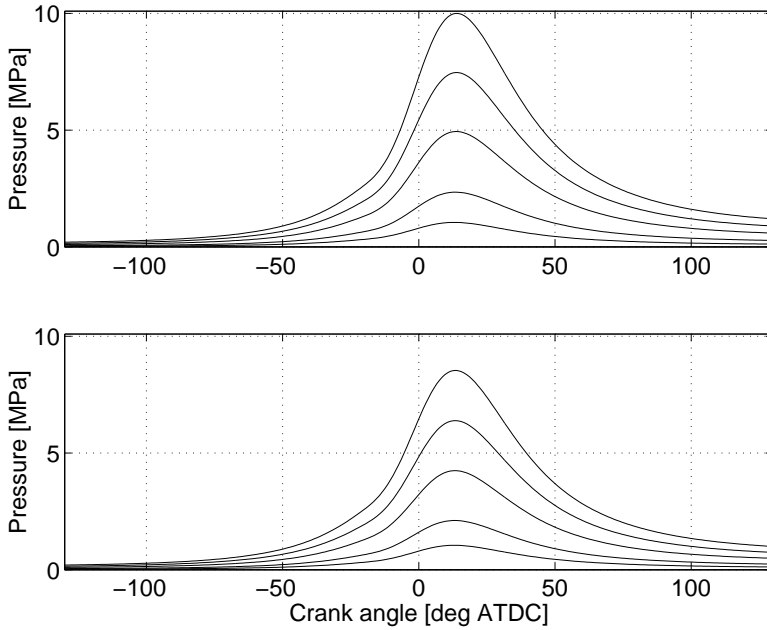


Figure A.6: *Upper:* Simulated cylinder pressure for operating points 1-5. *Lower:* Simulated cylinder pressure for operating points 1 and 6-9.

malized root mean square error in specific heat ratio γ , table A.13 summarizes the root mean square error for the cylinder pressure p . Figures A.7 to A.10 display the approximative γ -models and the reference γ -model as function of crank angle degree and single zone temperature respectively, for the cylinder pressure trace given in figure 4.8. In those figures, the reference model γ_{CE} is the dashed line and the solid line corresponds to each specific model. Figures A.11 and A.12 illustrates the corresponding cylinder pressure errors introduced by the model error each γ -model brings along.

OP	B_1	B_2	B_3	B_4	C_1	C_2	C_3	C_4	C_5	D_1	D_2	D_3
1	4.1	5.9	5.2	7.7	2.3	7.3	2.2	2.1	8.1	0.29	0.28	0.049
2	4.1	5.9	5.2	7.8	2.3	7.3	2.4	2.3	8.4	0.27	0.26	0.039
3	3.6	5.5	4.7	7.4	1.9	6.9	2.3	2.1	8.6	0.26	0.25	0.036
4	3.3	5.1	4.4	7.2	1.8	6.5	2.1	1.9	8.6	0.26	0.25	0.036
5	3.1	4.9	4.1	7	2.1	6.3	2	1.8	8.7	0.26	0.25	0.036
1	4.1	5.9	5.2	7.7	2.3	7.3	2.2	2.1	8.1	0.29	0.28	0.049
6	3.5	5.3	4.6	7.2	1.7	6.7	1.8	1.7	8.1	0.26	0.25	0.049
7	3	4.8	4.1	6.7	1.4	6.2	1.5	1.5	8.1	0.24	0.24	0.05
8	2.7	4.5	3.8	6.4	1.7	5.9	1.4	1.3	8.1	0.24	0.23	0.05
9	2.5	4.2	3.6	6.2	2	5.7	1.3	1.2	8.1	0.23	0.22	0.05
Mean	3.4	5.2	4.5	7.1	1.9	6.6	1.9	1.8	8.3	0.26	0.25	0.044

Table A.11: Maximum relative error (MRE) [%] for γ .

OP	B_1	B_2	B_3	B_4	C_1	C_2	C_3	C_4	C_5	D_1	D_2	D_3
1	1.4	2.6	1.8	4.2	0.62	4.1	0.59	0.52	1.5	0.11	0.1	0.016
2	1.3	2.7	1.8	4.5	0.69	4.1	0.65	0.58	1.5	0.098	0.094	0.014
3	1.2	2.6	1.7	4.6	0.82	4	0.62	0.55	1.6	0.095	0.091	0.014
4	1.2	2.4	1.6	4.5	0.93	3.9	0.58	0.5	1.7	0.096	0.091	0.014
5	1.1	2.4	1.6	4.4	1	3.8	0.56	0.47	1.7	0.097	0.092	0.014
1	1.4	2.6	1.8	4.2	0.62	4.1	0.59	0.52	1.5	0.11	0.1	0.016
6	1.2	2.4	1.7	4.1	0.57	4	0.51	0.44	1.6	0.098	0.092	0.017
7	1.1	2.3	1.6	4	0.69	3.8	0.44	0.38	1.6	0.094	0.088	0.017
8	1.1	2.2	1.5	3.9	0.81	3.8	0.4	0.34	1.7	0.092	0.086	0.017
9	1	2.1	1.5	3.9	0.91	3.7	0.38	0.32	1.8	0.092	0.086	0.017
Mean	1.2	2.4	1.7	4.2	0.77	3.9	0.53	0.46	1.6	0.097	0.092	0.016

Table A.12: Normalized root mean square error (NRMSE) [%] for γ -models.

OP	B_1	B_2	B_3	B_4	C_1	C_2	C_3	C_4	C_5	D_1	D_2	D_3
1	26.1	37.3	33.3	29.5	17.2	61.6	9.7	8.6	34.2	1.3	1.2	0.1
2	52.3	85.8	76.0	62.8	39.8	140.7	25.4	22.8	82.9	2.8	2.6	0.3
3	98.4	172.5	152.9	125.7	74.1	289.4	53.3	47.3	192.3	5.9	5.3	0.7
4	135.1	248.8	221.0	180.3	98.4	427.0	76.7	67.3	305.4	9.2	8.2	1.0
5	168.1	321.7	286.3	232.3	118.9	561.7	99.0	86.0	422.8	12.5	11.2	1.4
1	28.7	37.3	33.3	29.5	17.2	61.6	9.7	8.6	34.2	1.3	1.2	0.1
6	42.0	70.0	62.7	49.6	28.5	120.0	17.5	15.2	75.2	2.5	2.2	0.3
7	73.1	130.9	117.7	91.5	45.3	233.2	31.4	26.9	163.5	4.9	4.3	0.7
8	100.3	188.4	169.8	130.7	58.0	343.9	44.3	37.5	256.4	7.4	6.4	1.1
9	125.1	243.7	220.2	168.4	68.2	453.0	56.6	47.4	352.2	9.9	8.5	1.5
Mean	84.9	153.6	137.3	110.0	56.6	269.2	42.4	36.7	191.9	5.8	5.1	0.7

Table A.13: Root mean square error (RMSE) [kPa] for cylinder pressure.

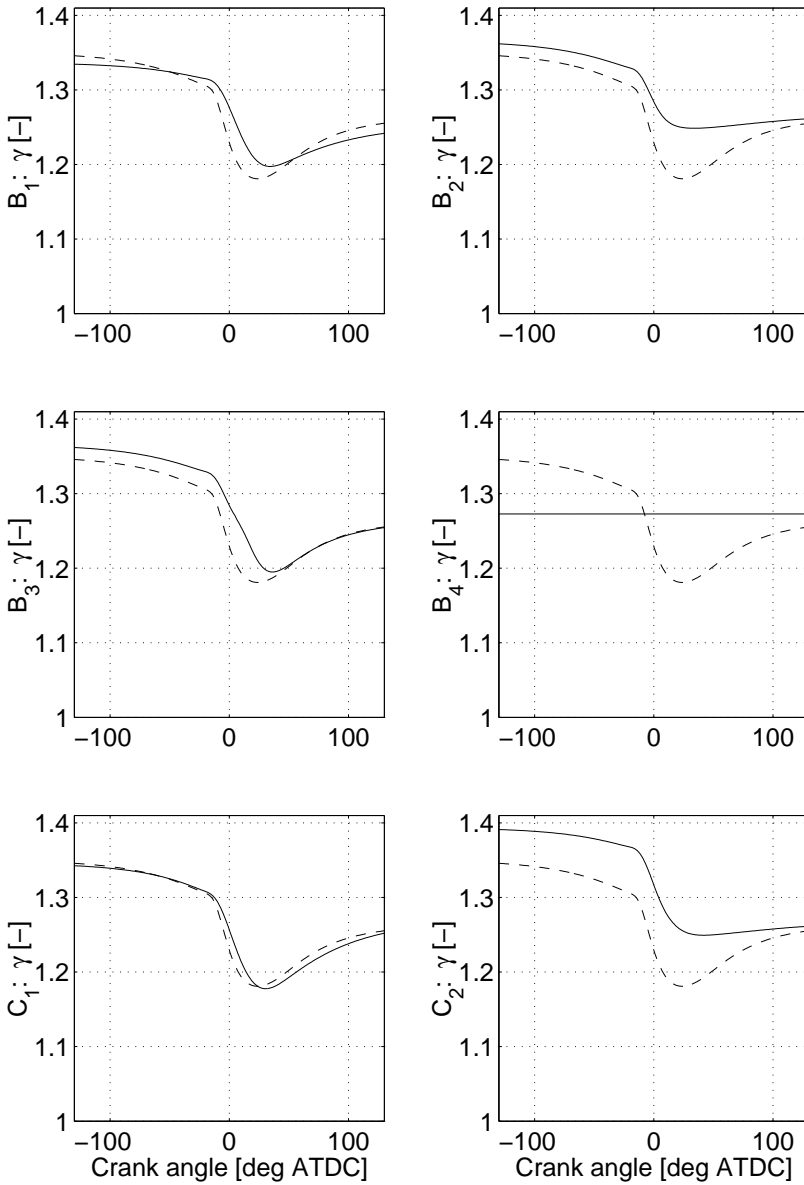


Figure A.7: Specific heat ratio γ for models B_1 to C_2 (solid line) at operating point 2 given in table A.2. The dashed line corresponds to the reference model \mathcal{D}_4 found by CHEPP.

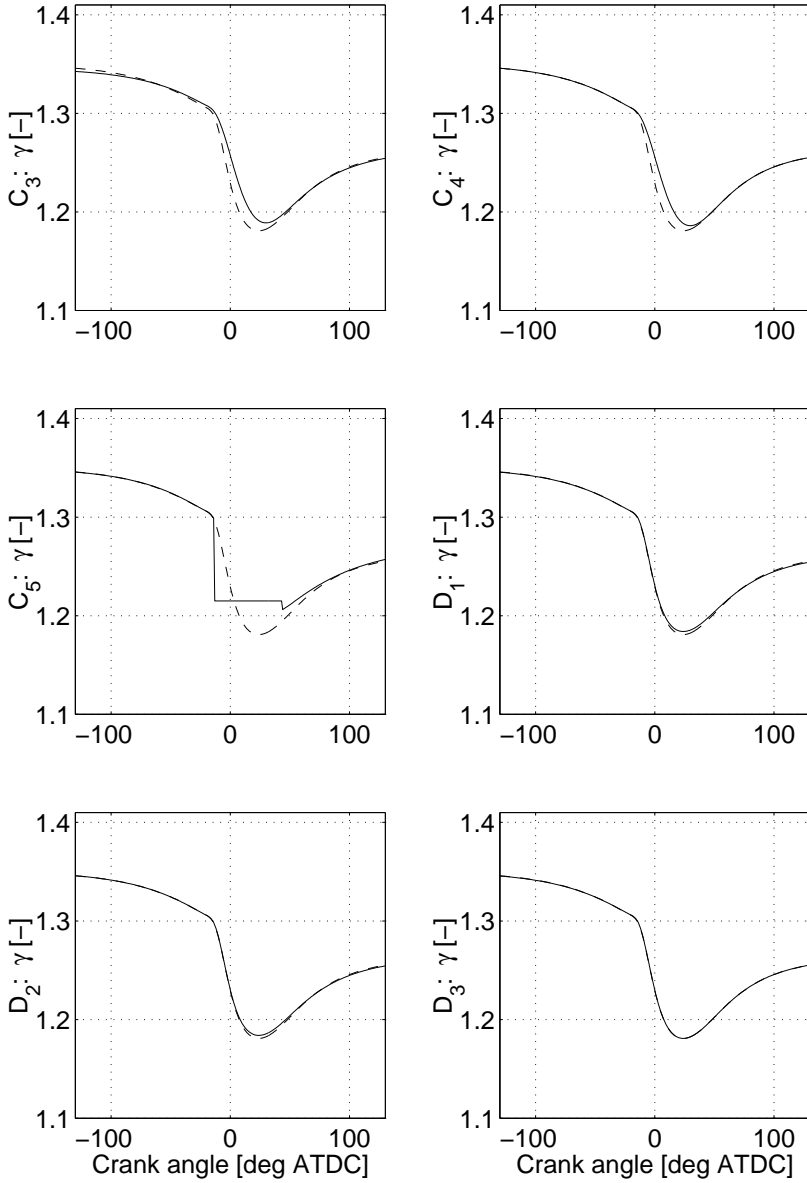


Figure A.8: Specific heat ratio γ for models C_3 to D_3 (solid line) at operating point 2 given in table A.2. The dashed line corresponds to the reference model D_4 found by CHEPP.

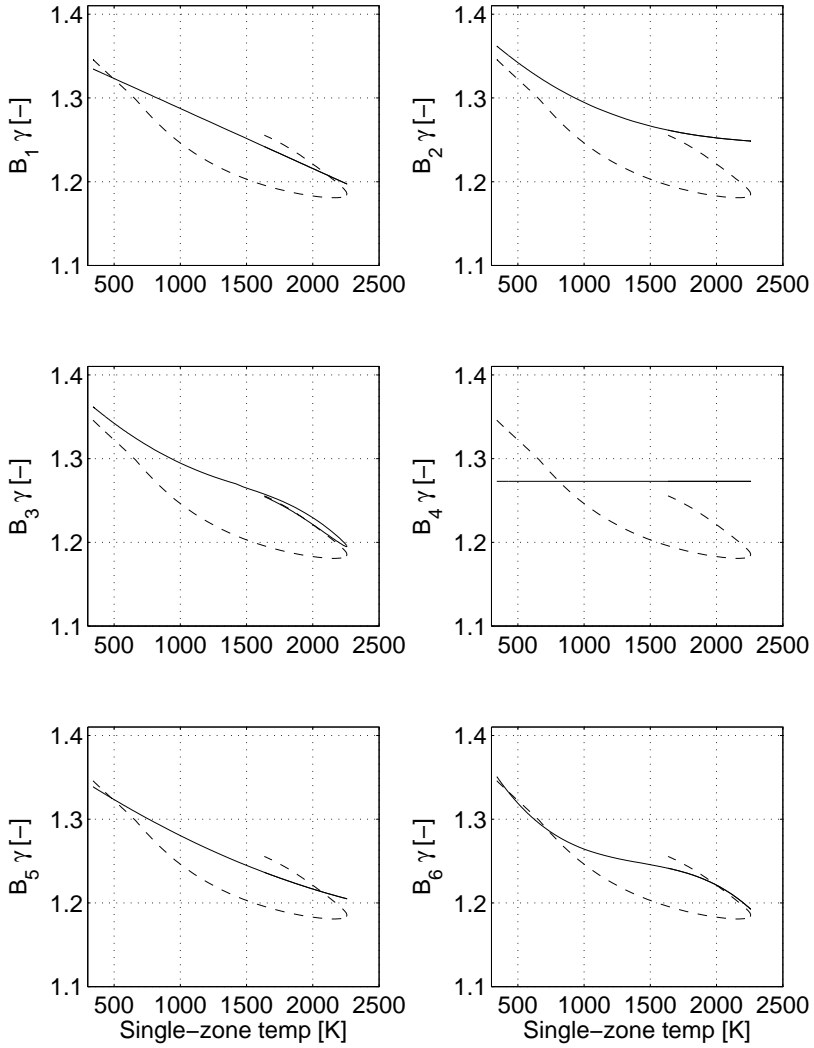


Figure A.9: Specific heat ratio γ for models \mathcal{B}_1 to \mathcal{C}_2 (solid line) at operating point 2 given in table A.2. The dashed line corresponds to the reference model \mathcal{D}_4 found by CHEPP.

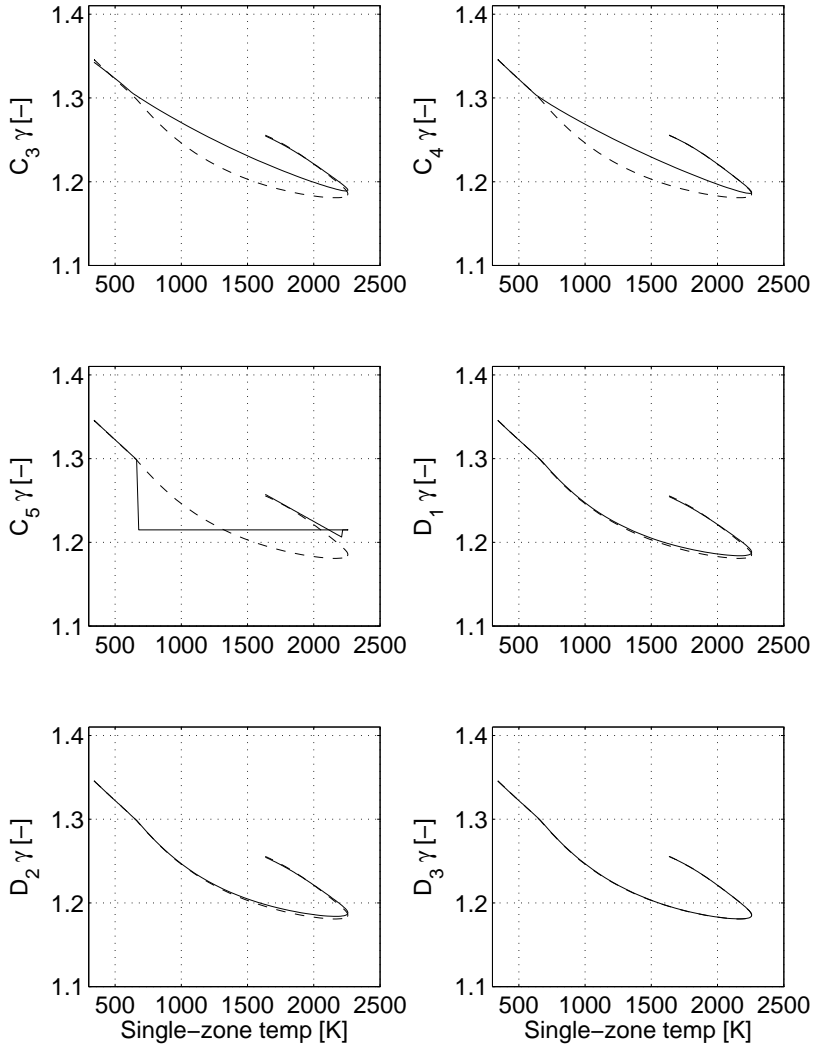


Figure A.10: Specific heat ratio γ for models C_3 to D_3 (solid line) at operating point 2 given in table A.2. The dashed line corresponds to the reference model D_4 found by CHEPP.

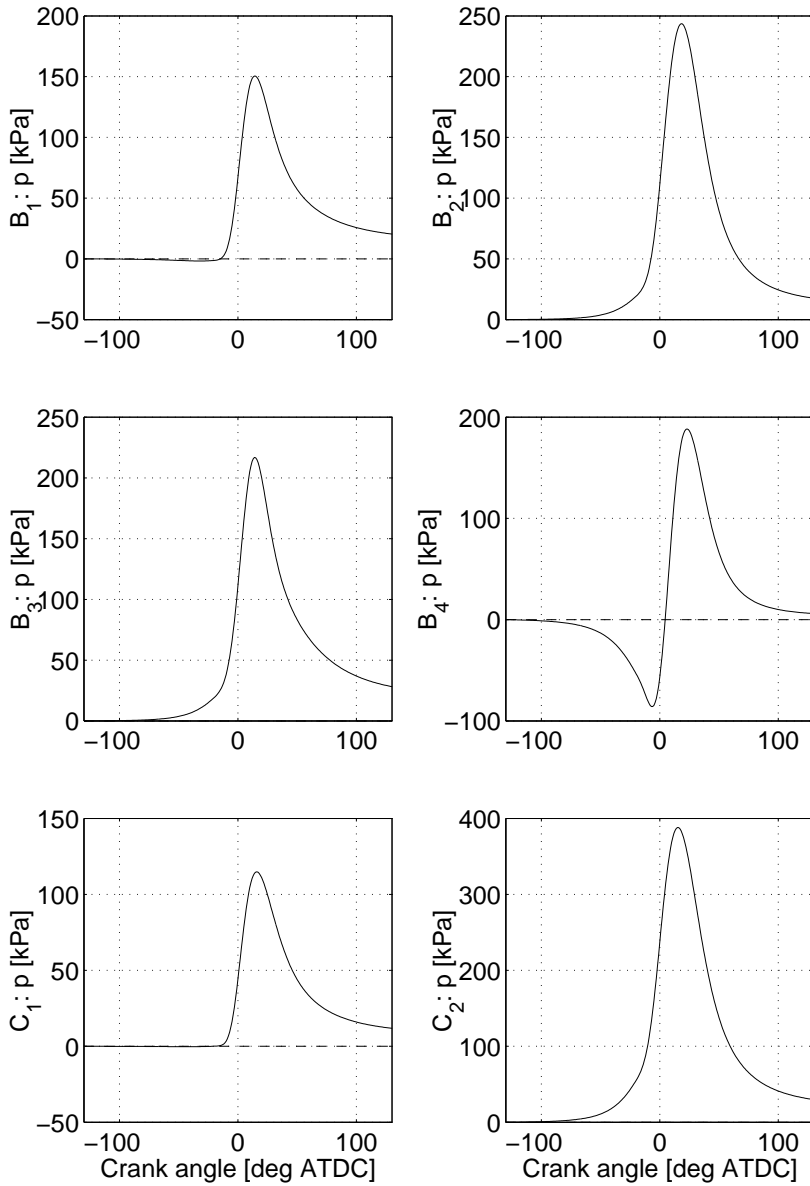


Figure A.11: Cylinder pressure error for models B_1 to C_2 (solid line) at operating point 2 given in table A.2, as compared to the reference model. The reference cylinder pressure is given in figure 4.8.

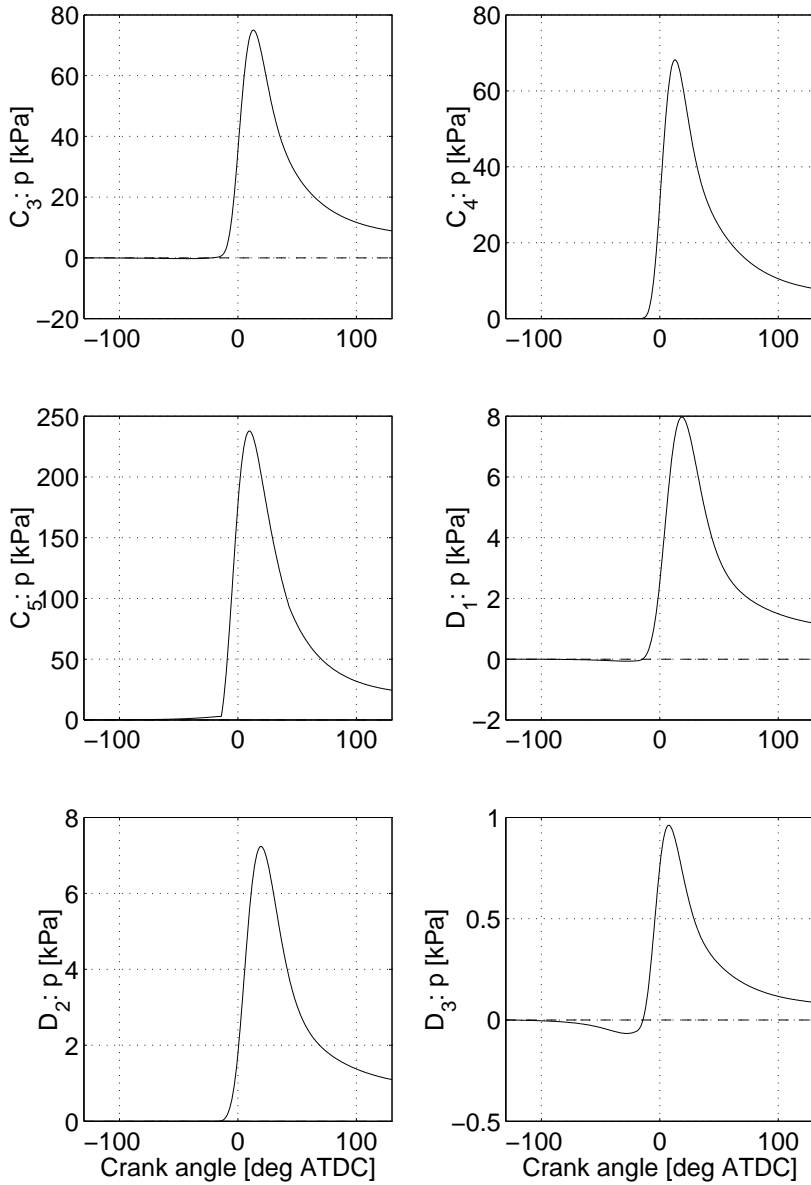


Figure A.12: Cylinder pressure error for models C_3 to D_3 (solid line) at operating point 2 given in table A.2, as compared to the reference model. For convenience, the sign of the pressure error for model C_5 is changed.

COMPRESSION RATIO ESTIMATION – FURTHER DETAILS

Further details and argumentation for the results found in chapter 5 are given in this appendix. Each section is referenced from various sections in chapter 5 and this appendix is therefore a complement.

B.1 Taylor expansions for sublinear approach

This section presents the calculations that support the algorithm development in section 5.3. In particular the relation between the two residuals

$$\varepsilon_{1a}(C_1, n) = \ln p(\theta) - (C_1 - n \ln(V_{id}(\theta) + V_c)) \quad (\text{B.1})$$

and

$$\varepsilon_{1b}(C_2, V_c) = V_{id}(\theta) - (C_2 p(\theta)^{-1/n} - V_c) \quad (\text{B.2})$$

is investigated. By using that $C_1 = \ln C$ and $C_2 = C^{1/n}$, the following relation is obtained

$$\begin{aligned} \varepsilon_{1a} &= n \ln p^{1/n} - \ln C_2^n + n \ln(V_{id}(\theta) + V_c) \\ &= -n \ln \left(\frac{C_2 p(\theta)^{-1/n}}{V_{id}(\theta) + V_c} \right) \\ &= -n \ln \left(1 - \frac{V_{id}(\theta) - (C_2 p(\theta)^{-1/n} - V_c)}{V_{id}(\theta) + V_c} \right) \\ &= -n \ln \left(1 - \frac{\varepsilon_{1b}}{V_{id}(\theta) + V_c} \right). \end{aligned}$$

If the residuals are small, i.e. $\varepsilon_{1b} \ll V_c \leq V_{id}(\theta) + V_c$, then the Taylor expansion gives

$$-n \ln \left(1 - \frac{\varepsilon_{1b}}{V_{id}(\theta) + V_c} \right) \approx \frac{n}{V_{id}(\theta) + V_c} \varepsilon_{1b}. \quad (\text{B.3})$$

It then follows that

$$\varepsilon_{1a}(\theta, x) \approx \frac{n}{V_{id}(\theta) + V_c} \varepsilon_{1b}(\theta, x), \quad (\text{B.4})$$

which is the sought relation.

B.2 Variable Projection Algorithm

A computationally efficient algorithm described in Björck (1996, p. 352) is summarized here.

Algorithm B.1 – Variable projection

Partition the parameter vector x such that $x = (y \ z)^T$, where $\varepsilon(y, z)$ is linear in y . Rewrite $\varepsilon(y, z)$ as

$$\varepsilon(y, z) = F(z)y - g(z) \quad (\text{B.5})$$

Let $x_k = (y_k, z_k)$ be the current approximation.

1. Solve the linear subproblem

$$\min_{\delta y_k} \|F(z_k)\delta y_k - (g(z_k) - F(z_k)y_k)\|_2^2 \quad (\text{B.6})$$

and set $x_{k+1/2} = (y_k + \delta y_k, z_k)$.

2. Compute the Gauss-Newton direction p_k at $x_{k+1/2}$, i.e. solve

$$\min_{p_k} \|C(x_{k+1/2})p_k + \varepsilon(y_{k+1/2}, z_k)\|_2^2 \quad (\text{B.7})$$

where $C(x_{k+1/2}) = (F(z_k), \frac{\partial}{\partial z}\varepsilon(y_{k+1/2}, z_k))$ is the Jacobian matrix.

3. Set $x_{k+1} = x_{k+1/2} + \alpha_k p_k$, do a convergence test and return to step 1 if the estimate has not converged. Otherwise return x_{k+1} .

The polytropic model in (5.8) is rewritten as

$$\ln p(\theta) = C_2 - n \ln(V_d(\theta) + V_c). \quad (\text{B.8})$$

This equation is linear in the parameters $C_2 = \ln C$ and n and nonlinear in V_c and applies to the form given in (B.5). With the notation from the

algorithm above, the parameters are $x = (C_2 \ n \ V_c)^T$, with $y = (C_2 \ n)^T$ and $z = V_c$. The measurement vector is formed as $g = -\ln p$ and the regression vector as $F = [-I \ \ln(V_c + V_d(\theta))]$.

Another possibility is to rewrite the polytropic model (5.8) to the following

$$V_d(\theta) = C_1 p(\theta)^{-1/n} - V_c. \quad (\text{B.9})$$

This equation does also fit into the form of (B.5). However this formulation is not as appropriate as (B.8), due to that the parameters $C_1 = C^{1/n}$ and n are coupled.

B.3 SVC – Geometric data

The SVC engine is used for simulated and experimental data in chapter 5. The geometric data for the crank and piston movement are given in the following table:

Property	Abbrev.	Value	Unit
Bore	B	68	[mm]
Stroke	S	88	[mm]
Crank radius	$a_r = \frac{S}{2}$	44	[mm]
Connecting rod	l	158	[mm]
No. of cylinders	n_{cyl}	5	[-]
Displacement volume	V_d	1598	[cm ³]
Maximum compression ratio	r_c^{max}	14.66	[-]
Minimum compression ratio	r_c^{min}	8.13	[-]
Pin-off	x_{off}	[-2.2, 4.7]	[mm]
Tilting angle	v	[0, 4]	[deg]

B.4 Parameters in single-zone model

The nominal parameters used in the single-zone model (5.4) are summarized in the table B.1. For motored cycles the numerical values of T_w and T_{IVC} are 400 K and 310 K respectively, while for fired cycles $T_w = 440$ K and $T_{IVC} = 340$ K have been used. Compared to table 3.1 the following parameters are changed; The clearance volume V_c is altered since a different engine is simulated. The crank angle offset $\Delta\theta$ and pressure offset Δp are both set to zero since their effect is investigated explicitly in section 5.4.4. The pressure at IVC $p_{IVC} \in \{0.5, 1.0, 1.8\}$ bar depends on the operating point.

Par.	Description	Value
γ_{300}	constant ratio of specific heat [-]	1.3678
b	slope for ratio of specific heat [K^{-1}]	$-8.13 \cdot 10^{-5}$
C_1	Woschni heat transfer parameter [-]	2.28
C_2	Woschni heat transfer parameter [m/(s K)]	$3.24 \cdot 10^{-4}$
$\Delta\theta$	crank angle phasing [deg]	0
θ_{ig}	ignition angle [deg ATDC]	-20
$\Delta\theta_d$	flame development angle [deg]	15
$\Delta\theta_b$	rapid burn angle [deg]	30
V_c	clearance volume [cm^3]	22.8–45.7
V_{cr}	single aggregate crevice volume [cm^3]	1.5% $V_c(r_c = 11)$
Δp	pressure bias in measurements [kPa]	0
T_w	mean wall temperature [K]	440
T_{IVC}	mean charge temperature at IVC [K]	340
p_{IVC}	cylinder pressure at IVC [kPa]	100
Q_{in}	released energy from combustion [J]	500
K_p	pressure sensor gain [-]	1

Table B.1: Nominal parameter values in the single-zone model.

PRIOR KNOWLEDGE APPROACH – FURTHER DETAILS

Further details and argumentation for the results found in chapters 6–8 are given in this appendix.

C.1 Levenberg-Marquardt method

The parameters x are estimated by minimizing the difference between the measured cylinder pressure and the modeled cylinder pressure, i.e. by minimizing the prediction error. A Gauss-Newton method called the Levenberg-Marquardt procedure is used to find the parameter estimate \hat{x} for methods 3 and 4 in chapter 5 and for methods 1 and 2 in chapters 6–8 for any given number of parameters.

A thorough presentation of system identification is given in Ljung (1999), from which most of the material presented in the subsequent subsections are from. The material is included here for two reasons: First to describe how the parameter estimation is performed when using the Levenberg-Marquardt procedure. Secondly as a comparison to the expressions given in section 6.4.2 for method 2, where a regularization term is included in the criterion function. The first subsection states the equations used when minimizing the prediction error for a nonlinear estimation problem. The Levenberg-Marquardt procedure is then presented as a special case. The next subsection concerns issues such as stopping criteria, local minima, scaling of the parameters and asymptotic variance of the estimate.

C.1.1 Minimizing prediction errors using a local optimizer

When the estimation problem is non-linear in the parameters, typically the minimum of the loss function can not be computed analytically as in the linear case. Instead, numerical search routines must be used (Björck, 1996). Given an observed data set $Z^N = [y(1), u(1), y(2), u(2), \dots, y(N), u(N)]$ of inputs $u(t)$ and outputs $y(t)$, a good model $\mathcal{M}(x)$ describing the data set Z^N is found by minimizing the prediction error

$$\varepsilon(t, x) = y(t) - \hat{y}(t|x), \quad t = 1, 2, \dots, N \quad (\text{C.1})$$

where $y(t)$ is the output of the system and $\hat{y}(t|x)$ is the predicted output of the model $\mathcal{M}(x)$. The prediction error is also termed residual. The prediction error is minimized by using a norm on $\varepsilon(t, x)$ and minimize the size of it. A quadratic norm is our choice here and it can be written as

$$V_N(x, Z^N) = \frac{1}{N} \sum_{t=1}^N \frac{1}{2} \varepsilon^2(t, x). \quad (\text{C.2})$$

The term V_N is a measure of the validity of $\mathcal{M}(x)$ and is often called loss function or criterion function. A problem on this form is known as *the nonlinear least-squares problem* in numerical analysis (Ljung, 1999, pp.327) and can be solved by an iterative search for minimum, a number of methods are described in e.g. (Björck, 1996). The estimate \hat{x} is defined as the minimizing argument of (C.2):

$$\hat{x}(Z^N) = \arg \min_x V_N(x, Z^N). \quad (\text{C.3})$$

Minimizing the criterion function $V_N(x, Z^N)$

To find the solution to (C.3) numerical methods are employed and these methods use the gradient and hessian, or approximations of them. The gradient of (C.2) is

$$V'_N(x, Z^N) = \frac{1}{N} \sum_{t=1}^N \psi(t, x) \varepsilon(t, x), \quad (\text{C.4})$$

where $\psi(t, x)$ is the jacobian vector given by

$$\psi(t, x) = \frac{d}{dx} \varepsilon(t, x) = -\frac{d}{dx} \hat{y}(t|x) = \left[-\frac{\partial \hat{y}(t|x)}{\partial x_1} \quad \dots \quad -\frac{\partial \hat{y}(t|x)}{\partial x_d} \right]^T, \quad (\text{C.5})$$

where d are the number of parameters. For our problem, the jacobian $\psi(t, x)$ is computed numerically with a forward difference approximation, as

$$\frac{\partial \varepsilon(t, x)}{\partial x_j} \approx \frac{\varepsilon(t, x + \Delta x_j) - \varepsilon(t, x)}{\Delta x_j}. \quad (\text{C.6})$$

Computing the central difference approximation instead of the forward one, would double the amount of computations. Differentiating the gradient with respect to x yields the hessian of (C.2) as

$$V_N''(x, Z^N) = \frac{1}{N} \sum_{t=1}^N \psi(t, x) \psi^T(t, x) + \frac{1}{N} \sum_{t=1}^N \psi'(t, x) \varepsilon^T(t, x), \quad (\text{C.7})$$

where $\psi'(t, x) = -\frac{d^2}{dx^2} \hat{y}(t|x)$. It is however computationally heavy to compute all d^2 terms in $\psi'(t, x)$. An approximation is therefore desirable and it is made reasonable by the following assumption; Assume that at the global minimum x^* , the prediction errors are independent. Thus close to x^* the second sum in (C.7) will be close to zero, and the following approximation can be made close to optimum (Ljung, 1999, p.328):

$$V_N''(x, Z^N) \approx \frac{1}{N} \sum_{t=1}^N \psi(t, x) \psi^T(t, x) = H_N(x, Z^N). \quad (\text{C.8})$$

By omitting the second sum in (C.7), the estimate $H_N(x, Z^N)$ is assured to be positive semidefinite, which guarantees convergence to a stationary point.

The estimate \hat{x} can be found numerically by updating the estimate of the minimizing point \hat{x}^i iteratively as

$$\begin{aligned} \hat{x}^{i+1}(Z^N) &= \hat{x}^i(Z^N) - \mu_N^i [R_N^i(\hat{x}^i, Z^N)]^{-1} V_N'(\hat{x}^i, Z^N) \\ &= \hat{x}^i(Z^N) + d^i(\hat{x}^i, Z^N), \end{aligned} \quad (\text{C.9})$$

where i is the i th iterate, in which d^i is the search direction and R_N^i is the approximate hessian H_N in (C.8). Finding the estimate \hat{x} in this manner is known as a Gauss-Newton method.

Regularization – Levenberg-Marquardt procedure

If the model $\mathcal{M}(x)$ is over-parameterized or the data Z^N is not informative enough, this causes an ill-conditioned jacobian which results in that the approximative hessian $H_N(x, Z^N)$ may be singular or close to singular. This causes numerical problems when computing the iterative estimates in (C.9), when inverting H_N . One way to avoid this is the Levenberg-Marquardt procedure, which uses

$$R_N^i(\hat{x}^i, Z^N, \nu) = H_N^i(\hat{x}^i, Z^N) + \nu I \quad (\text{C.10})$$

to regularize the approximation of the hessian. The iterative parameter estimate \hat{x}^i then becomes

$$\begin{aligned}\hat{x}^{i+1}(Z^N, \nu) &= \hat{x}^i(Z^N) - \mu_N^i [R_N^i(\hat{x}^i, Z^N, \nu)]^{-1} V'_N(\hat{x}^i, Z^N) \\ &= \hat{x}^i(Z^N) + d^i(\hat{x}^i, Z^N, \nu).\end{aligned}\tag{C.11}$$

For $\nu > 0$, the hessian approximation $R_N^i(\hat{x}^i, Z^N, \nu)$ is guaranteed to be positive definite. With $\nu = 0$ this is the Gauss-Newton method and by increasing ν the step size is reduced and the search direction d^i is turned towards the gradient, resulting in the steepest descent direction as $\nu \rightarrow \infty$.

Generally it can not be guaranteed that $d^i(\hat{x}^i, Z^N, \nu)$ in (C.11) is a descent direction. This can happen if the prediction errors are large or if (C.6) is not a good approximation (close to the optimum) (Eriksson, 1998). The approach here is to start up with a $\nu > 0$, and if $V_N(\hat{x}^{i+1}, Z^N) > V_N(\hat{x}^i, Z^N)$ occurs, ν is increased and new values of d^{i+1} and \hat{x}^{i+1} are computed until d^{i+1} is a descent direction.

Stopping criteria

A stopping criterion must be stated in order for the optimization procedure to terminate. In theory this should be done when the gradient V'_N is zero, so an obvious practical test is to terminate once $\|V'_N\|$ is small enough. Another useful test is to compute the relative difference in loss function V_N between two iterations, and terminate if this difference is less than a given tolerance level. The algorithm can also terminate after a given maximum number of iterations.

Local minima and initial parameter values

Generally, the optimization procedures converge to a local minimum of $V_N(x, Z^N)$. This is due to that although the stated optimization problem may only have one local minimum, i.e. the global one, the function $V_N(x, Z^N)$ can have several local minima due to the noise in the data Z^N . To find the global minimum, there is usually no other way than to start the iterative optimization routine at different feasible initial values x^{init} and compare the results (Ljung, 1999, p.338). Therefore, the initial values should be chosen with care by e.g. using prior knowledge. Good initial values generally pays off in fewer iterations and a faster convergence of the optimization procedure. For instance the Newton-type methods have good local convergence rates, but not necessarily far from optimum.

Scaling of parameters

The optimization procedure works best when the size of the unknown parameters are all in the same order (Gill et al., 1981, p.346). From

table 3.1, where the unknown parameters are summarized, it can be concluded that the nominal parameter values range over 10 decades. Therefore a scaling in terms of a linear transformation of the parameters is introduced,

$$x^s = Dx, \quad (\text{C.12})$$

where D is a diagonal matrix with $D_{i,i} = 1/x_i$, $x_i \neq 0$. It is of importance for the implementation that the initial guess of x_i , x_i^{init} , is assured to be non-zero. The gradient of $V_N(x^s, Z^N)$ in the scaled parameters is given by

$$V'_N(x^s, Z^N) = D^{-T} \psi(x) \varepsilon^T(x) = D^{-T} V'_N(x, Z^N), \quad (\text{C.13})$$

since $\psi(t, x^s) = D^{-T} \psi(t, x)$. The linear transformation matrix D is diagonal and invertible, and therefore $D^{-T} = D^{-1}$. The hessian of $V_N(x^s, Z^N)$ is given by

$$V''_N(x^s, Z^N) = D^{-T} V''_N(x, Z^N) D^{-1}, \quad (\text{C.14})$$

since $\psi'(t, x^s) = D^{-T} x D^{-1}$.

Scaling of parameters – regularized case

This subsection deals with the issue of scaling the parameters when using method 2 in section 6.4.2, i.e. regularization using prior knowledge. Whenever the parameters x are rescaled with D from (C.12), the nominal values $x^\#$ and the regularization matrix must be rescaled as well. The rescaled nominal values $x^{\#,s}$ are defined by

$$x^{\#,s} = Dx^\#, \quad (\text{C.15})$$

where D is a diagonal matrix with $D_{i,i} = 1/x_i$, $x_i \neq 0$. The elements δ_i^s in the diagonal scaled regularization matrix δ^s is thereby defined by

$$\delta_i^s = \frac{1}{2N \left(\frac{\sigma_i}{D_{i,i}}\right)^2} = \frac{D_{i,i}^2}{2N \sigma_i^2}. \quad (\text{C.16})$$

Asymptotic variance and parameter confidence interval

Consider the case when our model $\mathcal{M}(x)$ has the correct model structure and is provided with data Z^N , such that the measured output can be predicted correctly by the model. This would mean that there is no bias in the parameter estimate \hat{x} , and thus $\hat{x} \rightarrow \hat{x}^*$ asymptotically as the number of data N goes to infinity. It can then be shown (Ljung, 1999, pp.282) that the probability distribution of the random variable $\sqrt{N}(\hat{x} - \hat{x}^*)$ converges asymptotically to a Gaussian distribution with zero mean and covariance matrix P . This is formalized as

$$(\hat{x} - \hat{x}^*) \in \text{AsN}\left(0, \frac{P}{N}\right). \quad (\text{C.17})$$

For a quadratic prediction-error criterion the covariance matrix P is estimated by

$$\hat{P}_N = \hat{\lambda}_N \left(\frac{1}{N} \sum_{t=1}^N \psi(t, \hat{x}) \psi^T(t, \hat{x}) \right)^{-1} = \hat{\lambda}_N (H_N(\hat{x}, Z^N))^{-1}, \quad (\text{C.18a})$$

$$\hat{\lambda}_N = \frac{1}{N} \sum_{t=1}^N \varepsilon^2(t, \hat{x}), \quad (\text{C.18b})$$

for the parameter estimate \hat{x} and N data points, where $\hat{\lambda}_N$ is the estimated noise variance and $H_N(\hat{x}, Z^N)$ is the approximated hessian in (C.8). When using scaled parameters according to (C.12), one has to re-scale the hessian using (C.14) in a straight forward manner.

The result in (C.18) has a natural interpretation. The more data or the less noisier measured output, the more accurate the estimate. Also, since ψ is the gradient of \hat{y} , the asymptotic accuracy of a certain parameter is related to how sensitive the prediction is with respect to this parameter. Therefore, the more or less a parameter affects the prediction, the easier or harder respectively it will be to determine its value (Ljung, 1999, p.284).

The asymptotic covariance in (C.18) can be used to compute confidence intervals for the parameter estimates \hat{x} , and thereby give a reliability measure of a particular parameter \hat{x}^i . When (C.17) is valid, the $(1 - \alpha)$ -confidence interval for the true parameter \hat{x}^{*i} is formed as (Ljung, 1999, p.302)

$$P(|\hat{x}^i - \hat{x}^{*i}| > \alpha) \approx \frac{\sqrt{N}}{\sqrt{2\pi \hat{P}_N^{ii}}} \int_{|y| > \alpha} \exp(-y^2 N / 2 \hat{P}_N^{ii}) dy, \quad (\text{C.19})$$

where \hat{P}_N^{ii} is the i -th diagonal element of \hat{P}_N . From this, it can be stated that the true parameter value \hat{x}^{*i} lies in the interval around the parameter estimate \hat{x}^i with a certain significance $1 - \alpha$. The size of the interval is determined by α , and for a 95 % confidence interval the limits for parameter \hat{x}^i are

$$\hat{x}^i \pm 1.96 \sqrt{\frac{\hat{P}_N^{ii}}{N}}. \quad (\text{C.20})$$

C.2 Linear example

According to Hansen (1998), a rank-deficient or an ill-posed estimation problem can be solved by the same methods. Therefore, the main difficulties with an ill-posed problem is illustrated by the following rank-deficient example partly from Hansen (1994);

Example C.1 – Linear rank-deficient problem

Consider the following least-squares problem

$$\min_x \|Ax - b\|_2, \quad (\text{C.21})$$

where A and b are given by

$$A = \begin{bmatrix} 0.16 & 0.10 \\ 0.17 & 0.11 \\ 2.02 & 1.29 \end{bmatrix}, \quad b = \begin{bmatrix} 0.27 \\ 0.25 \\ 3.33 \end{bmatrix}. \quad (\text{C.22})$$

The true solution is $x^t = [1 \ 1]^T$, and the measurement vector b is found by adding a small noise perturbation according to:

$$b = \begin{bmatrix} 0.16 & 0.10 \\ 0.17 & 0.11 \\ 2.02 & 1.29 \end{bmatrix} \begin{bmatrix} 1.00 \\ 1.00 \end{bmatrix} + \begin{bmatrix} 0.01 \\ -0.03 \\ 0.02 \end{bmatrix}. \quad (\text{C.23})$$

The A -matrix of this linear problem has a condition number of $1.1 \cdot 10^3$, i.e. it is ill-conditioned and thus potentially sensitive to noise. Indeed, solving the ordinary least-squares problem as it is formulated in (C.21) ends up in an estimate $x_{LS} = [7.01 \ -8.40]^T$, which is far from the true solution $x^t = [1 \ 1]^T$.

The large condition number implies that the columns of A are nearly linearly dependent. One approach could therefore be to merge the two parameters into one, and replace $A = [a_1 \ a_2]$ with either $[a_1 \ 0]$ or $[0 \ a_2]$, since they are well-conditioned independently. This results in the two solutions

$$x_{a_1} = [1.65 \ 0]^T, \quad x_{a_2} = [0 \ 2.58]^T, \quad (\text{C.24})$$

which are better than x_{LS} but still far from the true solution.

Introducing constraints on the parameters results could result in better estimates, however the difficulty now lies in how to choose the constraints. When setting the constraints to $|x - x^t| \leq \alpha$, for α equal to 0.02, 1 and 10, the estimates becomes

$$x_{0.02} = [1.02 \ 0.98]^T, \quad x_1 = [1.65 \ 0.00]^T, \quad x_{10} = [7.01 \ -8.40]^T = x_{LS}, \quad (\text{C.25})$$

i.e. the solution lies on the boundary as long as x_{LS} is not included in the interval.

This example illustrates three main difficulties with ill-posed problems (Hansen, 1994):

1. The condition number of A is large.

2. Replacing A with a well-conditioned matrix derived from A does not necessarily lead to a useful solution.
3. Care must be taken when imposing additional constraints.

C.2.1 Linear example for methods 1 and 2

We now return to example C.2 for the two methods presented in section 6.4.

Example C.2 – Linear rank-deficient problem, cont.

Methods 1 and 2 are now applied to the estimation problem described in Example C.1 by using prior knowledge of the parameters x . The true values are given by $x^t = [1 \ 1]^T$, and the nominal values $x^\#$ are given in four cases; $x^\# = [1 \ 1]^T$, $x^\# = [1.05 \ 1]^T$, $x^\# = [1 \ 1.05]^T$ and $x^\# = [1.05 \ 1.05]^T$. The first case corresponds to a true prior knowledge and the remaining three involves a false prior knowledge. The results of the estimations are given in table C.1. For method 1, either x_1 or x_2 could be set spurious and therefore both cases are given. For method 2, the estimate is a function of the regularization parameter δ_x . This is illustrated in figure C.1, where the compromise between the residual error V_N and the nominal parameter error V_N^δ is obvious. The estimate corresponding to the L-corner of the curve, which is the best compromise between V_N and V_N^δ , is the one given in table C.1.

Nominal $x^\#$	M1 (x_1 fixed)	M1 (x_2 fixed)	M2
$[1 \ 1]^T$	$[1 \ 1.01]^T$	$[1.01 \ 1]^T$	$[1.01 \ 1.00]^T$
$[1.05 \ 1]^T$	$[1.05 \ 0.94]^T$	$[1.01 \ 1]^T$	$[1.02 \ 0.98]^T$
$[1 \ 1.05]^T$	$[1 \ 1.01]^T$	$[0.98 \ 1.05]^T$	$[1.01 \ 1.01]^T$
$[1.05 \ 1.05]^T$	$[1.05 \ 0.94]^T$	$[0.98 \ 1.05]^T$	$[1.00 \ 1.01]^T$

Table C.1: Parameter estimates for methods 1 and 2, in four cases of prior knowledge. The true values are $[1 \ 1]$.

Table C.1 shows that when the prior is true, the estimate is close to the true estimate and approximately the same for methods 1 and 2. This is also the case for method 1, as long as the prior is true for all spurious parameters, in which case a better estimate is found than for method 2. However, in the presence of a false prior in the spurious parameters, method 2 yields a smaller estimation bias than method 1. This highlights one of the features with method 2, namely the compromise between the data fitting and the parameter prior knowledge.

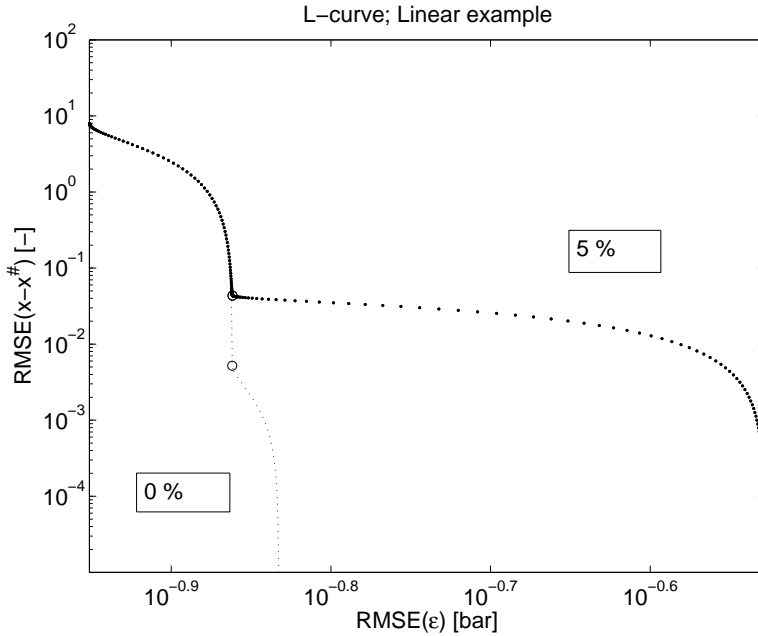


Figure C.1: L-curves for linear example corresponding to true prior (0 %) and false prior (5 %), i.e. case 1 and 4 in table C.1. The circles correspond to the estimates in the corners of the L-function.

Note also that the bias depends upon which parameter that has the false prior, as illustrated by comparing rows 2 and 3 for method 2. In this case the false prior in x_2 results in a smaller estimation bias, compared to if the false prior is in x_1 .

C.3 Motivation for M2:3+

This section gives a motivation for why the version M2:3 needs to be extended, or at least handled with care. Note that the focus of the section is on firing cycles, while the results and conclusions are valid for the motored cycles as well.

Consider figure C.2 where the upper plot displays the L-curve corresponding to OP1 for experimental firing cycles using method 2 and $\delta_i = c$, i.e. the same L-curve as in figure 8.7. In the lower plot the corresponding positive, i.e. convex, curvature τ (6.23) from algorithm 6.5 is given. The corresponding figures for a simulated fired cycle and an experimental motored cycle are given in figures C.3 and C.4. They correspond to the L-curves presented earlier in figure 8.4 and figure 7.12.

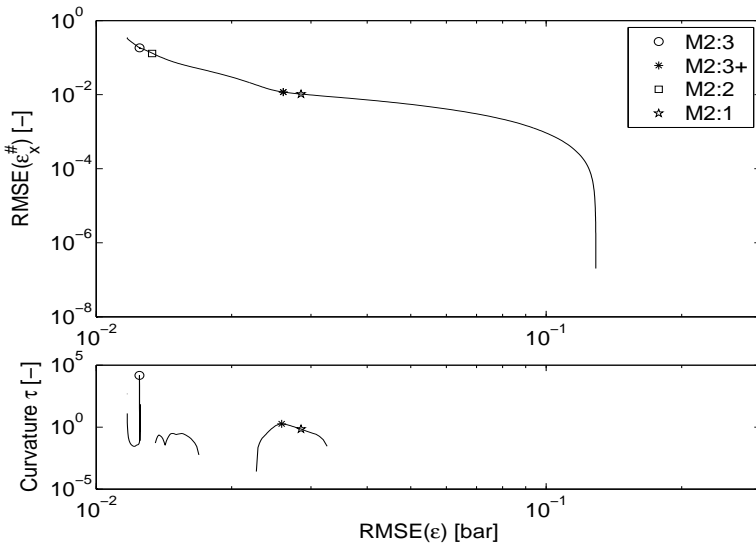


Figure C.2: *Upper*: L-curve for *experimental* firing cycles using method 2 and $\delta_i = c$ at OP1. The four versions are indicated by the legend. *Lower*: Corresponding positive curvature τ from (6.23).

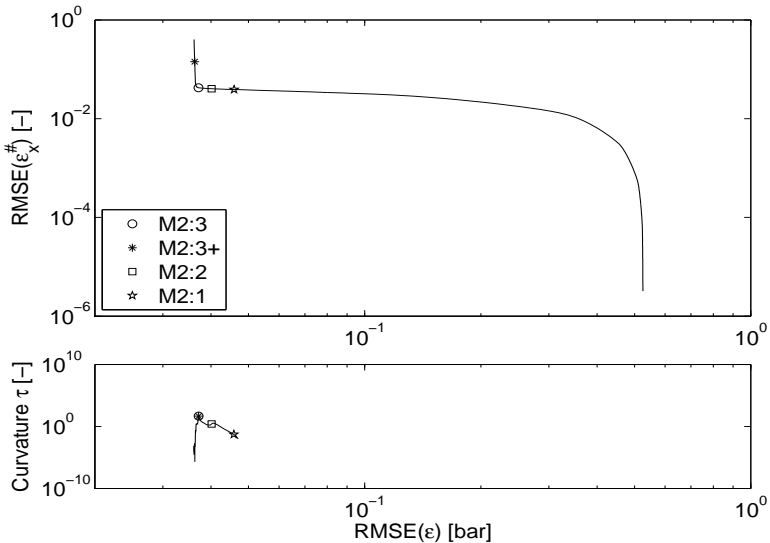


Figure C.3: *Upper*: L-curve for *simulated* firing cycles using method 2 and $\delta_i = c$ at OP1. *Lower*: Corresponding positive curvature τ from (6.23).

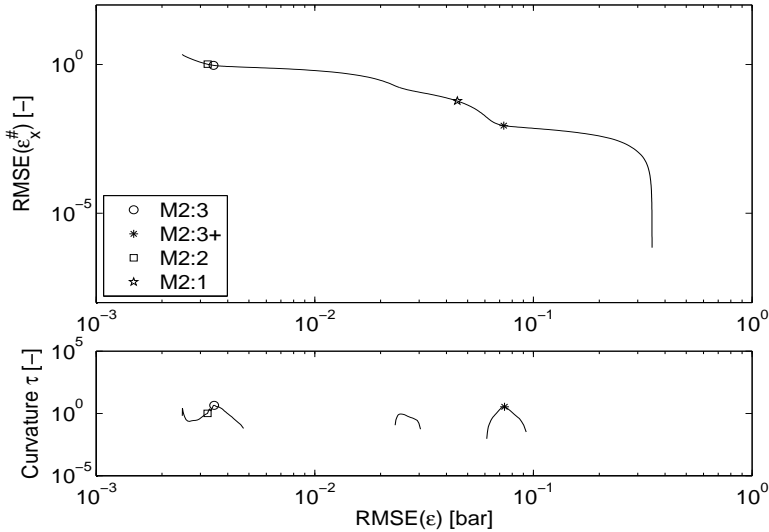


Figure C.4: *Upper*: L-curve for *experimental* motored cycles using method 2 and $\delta_i = c$ at OP1. The four versions are indicated by the legend. *Lower*: Corresponding positive curvature τ from (6.23).

Figure C.2 shows that the curvature τ is maximized for a relatively low value of δ_x , as shown for M2:3. The corresponding curvature does not show up in the simulated case in figure C.3, and is thus believed to correspond to a “false” corner. Such a corner is believed to be due to that the measurement noise causes a jump in $RMSE(\epsilon)$ between two different local minima. The same behavior occurs for case 2. It will be shown in the evaluation of case 1 and 2 for experimental fired cycles, see section 8.2.4, that the estimates for experimental cycles for M2:3 are less accurate than the estimates for M2:1. This is shown in tables 8.18 and 8.19 for case 1 and 2.

The correct corner is instead close to M2:1, here exemplified by both figure C.2 and figure C.3. Therefore the extension of M2:3 is to use a smaller region Δ_x of δ_x . Since M2:1 is both fast and close to the correct corner in the L-curve, the regularization parameter δ_x from M2:1 is used as a mid-value for this region. The lower and upper limit of this region Δ_x is then chosen as to assure that a convex curvature is included. This is done by assuring that the curvature τ is positive for at least one sample of δ_x , and that the position for maximum τ is an interior point of the region Δ_x .

For this application the δ_x :s are distributed according to the 69 samples in figure 7.5, and it has proved to be sufficient to use ± 12 samples of δ_x , starting from $\delta_x(M2 : 1)$. This typically yields a region of δ_x that covers four orders of magnitude. This choice of Δ_x also reduces the computational time approximately by a factor $\frac{69}{25}$ for M2:3+ as compared to M2:3. Applying these modifications to M2:3 renders the corner shown for M2:3+ in figure 8.7, and therefore M2:3+ performs as intended for both case 1 and 2.

The algorithm for M2:3+ is given by:

Algorithm C.1 – Hansen’s L-curve with Miller initialization (M2:3+)

1. Assign a prior $x_i^\#$ and δ_i to each of the parameters $x \in \mathbf{R}^{d \times 1}$. The regularization matrix is then formed as $\delta = \delta_x \text{diag}(\delta_i)$.
2. Compute boundaries m_ε and m_δ in (6.20), that give δ_x from (6.21).
3. Compute the region Δ_x with δ_x from step 2 as the mid-value, and the upper and lower limit as chosen relative to the same δ_x .
4. Minimize the criterion function W_N (6.7) for the discrete points $\delta_x \in \Delta_x$, equally spaced in a logarithmic scale.
5. Find the δ_x for which (6.22) is fulfilled, by using a cubic spline interpolation.
6. Minimize W_N (6.7) w.r.t. x using δ_x from step 5.
7. Return the estimate $x^{\delta,*}$.

Steps 1 and 2 in algorithm C.1 correspond to steps 1 and 2 in algorithm 6.3 (M2:1), step 3 computes the region Δ_x , while steps 4–7 correspond to steps 2–5 in algorithm 6.5 (M2:3).

C.4 L850 – Geometric data

The L850 engine is used for simulated and experimental data in chapters 6–8. The geometric data for the crank and piston movement are given in the following table:

Property	Abbrev.	Value	Unit
Bore	B	86	[mm]
Stroke	S	86	[mm]
Crank radius	$a_r = \frac{S}{2}$	43	[mm]
Connecting rod	l	145.5	[mm]
No. of cylinders	n_{cyl}	4	[-]
Displacement volume	V_d	1998	[cm ³]
Clearance volume	V_c	58.8	[cm ³]
Pin-off	x_{off}	0.8	[mm]
Compression ratio	r_c	9.5	[-]

C.5 Parameters in single-zone model – motored cycles

The nominal parameters used in the single-zone model (3.36)–(3.45) are summarized in table C.2 for operating point 1. The parameter values for N , p_{IVC} and T_{IVC} differs for all the eight operating points according to table C.3. All the other parameters remain the same.

Compared to table 3.1 the following parameters are changed; The constant γ_{300} is set to 1.40, since this is the value for pure air. The slope coefficient b is changed accordingly. The crank angle offset $\Delta\theta$ is set to 0.1 CAD, a smaller value than in table 3.1, since 0.1 CAD is the approximate value for a well-calibrated measurement system. The clearance volume V_c is altered due to the changed engine geometry. The crevice volume is now altered to 1 cm^3 , which is approximately the same V_{cr} as for table 3.1 in absolute numbers. The pressure offset is now set to 5 kPa.

C.6 Parameters in single-zone model – fired cycles

The nominal parameters used in the single-zone model (3.36)–(3.45) are summarized in table C.4 for operating point 1. The parameter values for Q_{in} , p_{IVC} , T_{IVC} , T_w and the burn related parameters θ_{ig} , $\Delta\theta_d$ and $\Delta\theta_b$ differs for all the eight operating points according to table C.5. All the other parameters remain the same.

Par.	Description	Value
γ_{300}	constant ratio of specific heat [-]	1.40
b	slope for ratio of specific heat [K^{-1}]	$-1 \cdot 10^{-4}$
C_1	Woschni heat transfer parameter [-]	2.28
$\Delta\theta$	crank angle phasing [deg]	0.1
V_c	clearance volume [cm^3]	58.8
V_{cr}	single aggregate crevice volume [cm^3]	1
Δp	pressure sensor bias [kPa]	5
T_w	mean wall temperature [K]	400
T_{IVC}	mean charge temperature at IVC [K]	370
p_{IVC}	cylinder pressure at IVC [kPa]	50
K_p	pressure sensor gain [-]	1

Table C.2: Nominal parameter values for motored cycles at OP1 in the single-zone model.

OP	T_{IVC} [K]	p_{IVC} [kPa]	N [rpm]
1	370	50	1500
2	310	50	1500
3	370	100	1500
4	310	100	1500
5	370	50	3000
6	310	50	3000
7	370	100	3000
8	310	100	3000

Table C.3: Operating points (OP) for the simulated motored cylinder pressure.

Out of these, the following parameters are changed compared to table 3.1; The constant γ_{300} and the slope coefficient b are set to lower values, although the difference is small. The crank angle offset $\Delta\theta$ is set to 0.1 CAD, a smaller value than in table 3.1, since 0.1 CAD is the approximate value for a well-calibrated measurement system. The clearance volume V_c is altered due to the changed engine geometry. The crevice volume is now altered to 0.588 cm^3 . The pressure offset is now set to 5 kPa.

Par.	Description	Value
γ_{300}	constant ratio of specific heat [-]	1.35
b	slope for ratio of specific heat [K^{-1}]	$-7 \cdot 10^{-5}$
C_1	Woschni heat transfer parameter [-]	2.28
C_2	Woschni heat transfer parameter [m/(s K)]	$3.24 \cdot 10^{-4}$
$\Delta\theta$	crank angle phasing [deg]	0.1
θ_{ig}	ignition angle [deg ATDC]	-15
$\Delta\theta_d$	flame development angle [deg]	20
$\Delta\theta_b$	rapid burn angle [deg]	20
V_c	clearance volume [cm^3]	58.8
V_{cr}	single aggregate crevice volume [cm^3]	0.588
Δp	pressure sensor bias [kPa]	5
T_w	mean wall temperature [K]	480
T_{IVC}	mean charge temperature at IVC [K]	414
p_{IVC}	cylinder pressure at IVC [kPa]	50
Q_{in}	released energy from combustion [J]	503
K_p	pressure sensor gain [-]	1

Table C.4: Nominal parameter values for fired cycles at OP1 in the single-zone model.

Parameter	OP1	OP2	OP3	OP4	OP5	OP6
N [rpm]	1500	3000	1500	3000	1500	3000
p_{IVC} [kPa]	50	100	50	100	50	100
T_{IVC} [K]	414	370	414	370	414	370
T_w [K]	480	400	480	400	480	400
Q_{in} [J]	503	1192	503	1192	503	1192
θ_{ig} [deg ATDC]	-15	-15	-20	-20	-25	-25
$\Delta\theta_d$ [deg]	20	20	15	15	15	15
$\Delta\theta_b$ [deg]	20	20	30	30	30	30

Table C.5: Operating points (OP) for the simulated fired cylinder pressure.

C.7 Complementary results for prior knowledge approach

This section contains the complementary figures and tables that are referenced from chapters 7 and 8.

Complementary results for simulations – motored cycles

Figures C.5 and C.6 show the L-curve for one motored cycle at operating point OP8 for setup 2 using $\delta_i = c$ and $\delta_i \neq c$ respectively.

Complementary results for experiments – motored cycles

Tables C.6 and C.7 show the mean value, standard deviation, and relative mean error for the individual estimates at OP1 for method 2, using $\delta_i = c$ and $\delta_i \neq c$ respectively. The relative mean error is computed relative to the nominal parameter value at each cycle and is given in percent.

Complementary results for simulations – fired cycles

Table C.8 shows the individual parameter estimates for the entire range of $d^\#$, i.e. from 16 to 1 parameter. The numerical values are given for one engine cycle at OP1 in the presence of a false prior level of 0 %.

Complementary results for experiments – fired cycles

Table C.9 defines the operating points used in experimental evaluation. The corresponding nominal values are given in table C.10.

δ_x :	V_c [cm^3]	C_1 [-]	T_{IVC} [K]	p_{IVC} [kPa]	γ_{300} [-]	b [K^{-1}]	T_w [K]	V_{cr} [cm^3]	Δp [kPa]	$\Delta\theta$ [deg]	K_p [-]	$\bar{\varepsilon}_x^\#$ [%]
$\delta_x(M2:1)$	58.0	2.70	358	53.8	1.396	$-8.8 \cdot 10^{-5}$	370	0.883	1.1	4.48	0.998	5.8
σ_{est}	0.7	0.11	6	0.4	0.009	$2.5 \cdot 10^{-6}$	10	0.00511	0.9	0.14	0.005	5.8
RME	2.0	5.9	12.4	-3.2	1.1	-0.6	-12.7	1.8	-0.7	-89.9	-1.6	5.8
$\delta_x(M2:2)$	59.0	6.27	550	34.1	1.370	$-3.0 \cdot 10^{-7}$	712	0.64	-0.4	0.15	1.596	103.9
σ_{est}	0.7	0.32	18	1.5	0.002	$1.2 \cdot 10^{-7}$	34	0.393	0.2	0.03	0.071	103.9
RME	0.3	175.0	75.0	-39.6	-2.1	-99.7	78.1	-27.4	-76.7	-67.7	103.9	
$\delta_x(M2:3)$	59.1	6.54	567	32.8	1.371	$-2.1 \cdot 10^{-7}$	741	0.597	-0.3	0.11	1.658	73.5
σ_{est}	0.1	0.09	5	0.4	0.002	$3.4 \cdot 10^{-8}$	11	0.0528	0.1	0.01	0.020	73.5
RME	0.5	149.6	64.4	-33.9	-2.0	-79.8	68.1	-25.8	-64.3	-78.7	73.5	
$\delta_x(M2:3+)$	57.8	2.70	357	53.8	1.393	$-8.7 \cdot 10^{-5}$	373	0.882	1.3	0.47	0.999	0.8
σ_{est}	0.4	0.11	11	0.6	0.007	$2.9 \cdot 10^{-6}$	8	$4.48 \cdot 10^{-5}$	0.8	0.10	0.003	0.8
RME	0.6	0.0	0.3	-1.3	-1.8	0.0	-0.2	0.0	0.0	-90.0	-1.3	0.8
$x^\#$	58.8	2.28	314	56.4	1.400	$-9.3 \cdot 10^{-5}$	400	0.882	-1.4	0.47	1.000	0.0

Table C.6: Mean value, standard deviation (σ_{est}) and RME of the estimate for the four versions of method 2 using case 1 ($\delta_i = c$), evaluated for 101 experimental motored cycles at OPI.

δ_x :	V_c [cm^3]	C_1 [-]	T_{IVC} [K]	p_{IVC} [kPa]	γ_{300} [-]	b [K^{-1}]	T_w [K]	V_{cr} [cm^3]	Δp [kPa]	$\Delta\theta$ [deg]	K_p [-]	$L^{\delta} \varepsilon_x^{\#}$ [%]	$\varepsilon_x^{\#}$ [%]
$\delta_x(M2:1)$	57.7	2.73	359	53.7	1.394	$-8.7 \cdot 10^{-5}$	372	0.882	1.4	0.49	1.000	14.7	34.4
σ_{est}	0.2	0.07	5	0.3	0.004	$2.1 \cdot 10^{-6}$	6	$4 \cdot 10^{-7}$	0.4	0.02	0.000	14.7	34.4
RME	-1.8	19.7	14.2	-4.8	-0.5	-6.2	-7.1	0.0	-414.9	5.0	0.0	14.7	34.4
$\delta_x(M2:2)$	57.5	3.54	368	53.8	1.389	$-8.8 \cdot 10^{-5}$	406	0.882	1.0	0.46	1.002	21.0	36.7
σ_{est}	0.4	0.84	12	0.4	0.007	$9.7 \cdot 10^{-6}$	37	$3.61 \cdot 10^{-6}$	0.6	0.04	0.002	21.0	36.7
RME	-2.1	55.5	17.2	-4.6	-0.8	-5.8	1.4	0.0	-387.6	-2.8	0.2	21.0	36.7
$\delta_x(M2:3)$	57.7	2.72	359	53.7	1.394	$-8.7 \cdot 10^{-5}$	371	0.882	1.4	0.49	1.000	15.8	35.4
σ_{est}	0.3	0.05	6	0.4	0.006	$2.6 \cdot 10^{-6}$	5	$3.6 \cdot 10^{-7}$	0.5	0.02	0.000	15.8	35.4
RME	-1.7	23.7	14.8	-4.8	-0.5	-9.0	-6.0	0.0	-401.2	3.6	0.0	15.8	35.4
$\delta_x(M2:3+)$	57.7	2.72	359	53.7	1.394	$-8.7 \cdot 10^{-5}$	371	0.882	1.4	0.49	1.000	14.7	34.5
σ_{est}	0.3	0.05	5	0.4	0.005	$2.6 \cdot 10^{-6}$	5	$3.73 \cdot 10^{-7}$	0.5	0.02	0.000	14.7	34.5
RME	-1.8	19.1	14.2	-4.8	-0.4	-6.5	-7.2	0.0	-403.3	5.0	-0.0	14.7	34.5
$x^{\#}$	58.8	2.28	314	56.4	1.400	$-9.3 \cdot 10^{-5}$	400	0.882	-1.4	0.47	1.000	0.0	0.0

Table C.7: Mean value, standard deviation (σ_{est}) and RME of the estimate for the four versions of method 2 using case 2 ($\delta_i \neq c$), evaluated for 101 experimental motored cycles at OPI.

$d^\#$	V_c [cm^3]	C_1 [-]	T_{IVC} [K]	p_{IVC} [kPa]	γ_{300} [-]	b [K^{-1}]	T_w [K]	V_{cr} [cm^3]	Δp [kPa]	$\Delta \theta$ [deg]	K_p [-]	C_2 [$m/(s K)$]	Q_{in} [J]	θ_{ig} [deg ATDC]	$\Delta \theta_d$ [deg]	$\Delta \theta_b$ [deg]	ε_x^t [%]	$\varepsilon_x^\#$ [%]
16	57.3	3.15	561	51.0	1.33	$-5.42 \cdot 10^{-5}$	552	0.27	2.5	0.08	1.02	$2.85 \cdot 10^{-4}$	544	-16.1	21.3	20.0	20.5	20.5
15	57.5	3.04	499	49.0	1.34	$-6.1 \cdot 10^{-5}$	525	0.49	3.5	0.09	1.05	$3.24 \cdot 10^{-4}$	516	-16.1	21.3	20.0	11.8	11.8
14	57.5	3.45	537	52.1	1.32	$-5.6 \cdot 10^{-5}$	561	0.14	2.4	0.07	1.00		559	-16.0	21.3	20.1	25.4	25.4
13	57.4	3.78	414	52.5	1.32	$-7.3 \cdot 10^{-5}$	393	0.2	2.1	0.05			554	-16.0	21.2	20.0	24.1	24.1
12	56.8	4.43		51.6	1.32	$-7.21 \cdot 10^{-5}$	476	0.59	2.9	0.05			556	-15.9	21.1	20.0	24.0	24.0
11	57.8	2.28		51.3	1.34	$-7.2 \cdot 10^{-5}$	373		3.4	0.01			518	-15.8	20.8	20.0	6.5	6.5
10	58.6			50.4	1.35	$-6.95 \cdot 10^{-5}$	480		4.3	0.01			508	-15.6	20.7	19.9	2.8	2.8
9	58.8			49.8	1.35	$-7.12 \cdot 10^{-5}$			5.0	0.06			503	-15.8	20.9	19.9	2.2	2.2
8	58.8			49.8	1.35	$-7.05 \cdot 10^{-5}$							504	-15.9	21.0	20.0	2.0	2.0
7	58.2			49.9	1.35	$-6.84 \cdot 10^{-5}$				0.10			508	-15.0	20.1	20.0	0.7	0.7
6	58.4			49.7	1.35	$-7 \cdot 10^{-5}$							506		20.2	20.0	0.3	0.3
5	58.7			49.7	1.35								503		20.1	20.0	0.2	0.2
4	58.9			50.0	1.35										20.1	20.0	0.2	0.2
3	59.0				1.35										20.1	20.0	0.1	0.1
2	58.8				1.35										20.1	20.0	0.2	0.2
1					1.35										20.0		0.0	0.0
$x^\#$	58.8	2.28	414	50.0	1.35	$-7 \cdot 10^{-5}$	480	0.59	5.0	0.10	1.00	$3.24 \cdot 10^{-4}$	503	-15.0	20.0	20.0	5.0	0.0
x^t	58.8	2.28	414	50.0	1.35	-7e-005	480	0.59	5.0	0.10	1.00	$3.24 \cdot 10^{-4}$	503	-15.0	20.0	20.0	0.0	5.0

Table C.8: Method 1: Parameter estimates at OP1 (firing cycles) for $d^\# \in [1, 16]$ parameters when using no preferred ordering and a false prior level of 0 %. The true and nominal parameter deviations ε_x^t and $\varepsilon_x^\#$ are given as RMSE:s of their relative values, i.e. $\varepsilon_x^t = RMSE(\varepsilon_x^t)$ and $\varepsilon_x^\# = RMSE(\varepsilon_x^\#)$.

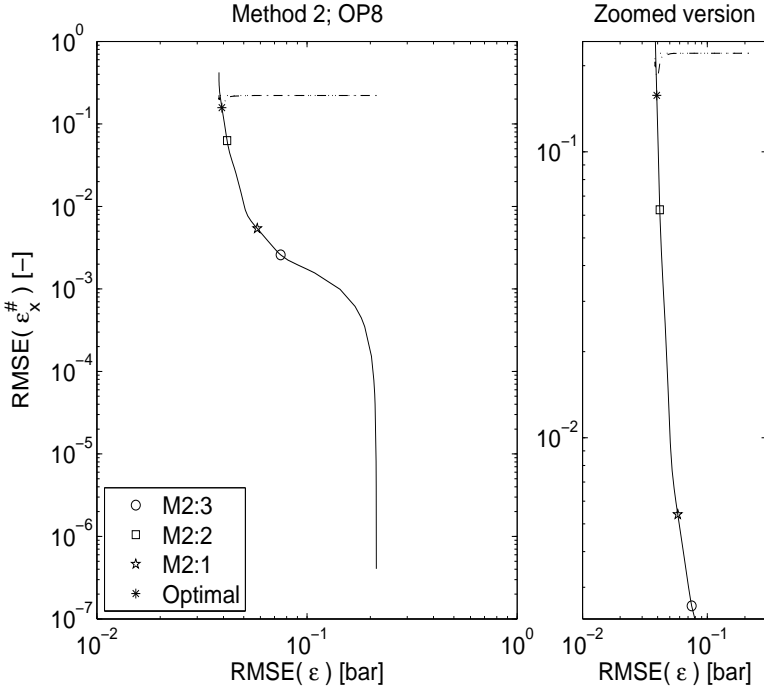


Figure C.5: L-curve (solid line) for one (motored) engine cycle at OP8 with false prior $RMSE(\varepsilon_x^{\#-t})$ (dotted line), when using setup 2 and case 1 of the δ_i ($\delta_i = c$). The results for the three versions of method 2 and the optimal choice of regularization parameter are indicated by the legend. The true parameter deviation $RMSE(\varepsilon_x^t)$ (dash-dotted line) is also given.

	OP1	OP2	OP3	OP4	OP5	OP6
N [rpm]	1200	1500	1500	2000	3000	3500
p_{man} [kPa]	32	55	130	123	103	120
θ_{ig} [deg ATDC]	-33	-26	-5	-12	-28	-24

Table C.9: Operating point conditions for experimental cycles at OP1–6.

	V_c [cm^3]	C_1 [-]	T_{IVC} [K]	p_{IVC} [kPa]	γ_{300} [-]	b [K^{-1}]	T_w [K]	V_{cr} [cm^3]	Δp [kPa]	$\Delta \theta$ [deg]	K_p [-]	C_2 [$m/(s K)$]	Q_{in} [J]	θ_{ig} [deg-ATDC]	$\Delta \theta_d$ [deg]	$\Delta \theta_b$ [deg]
OP1	58.8	2.28	450	40.8	1.336	$-7.42 \cdot 10^{-5}$	475	0.882	0.5	0.47	1.000	$3.24 \cdot 10^{-4}$	373	-32.6	27.5	20.3
OP2	58.8	2.28	425	68.6	1.335	$-7.42 \cdot 10^{-5}$	475	0.882	0.6	0.47	1.000	$3.24 \cdot 10^{-4}$	731	-26.0	19.9	16.0
OP3	58.8	2.28	407	162.5	1.339	$-7.42 \cdot 10^{-5}$	475	0.882	-2.2	0.47	1.000	$3.24 \cdot 10^{-4}$	1864	-5.3	15.4	19.0
OP4	58.8	2.28	394	152.3	1.339	$-7.42 \cdot 10^{-5}$	475	0.882	-2.8	0.47	1.000	$3.24 \cdot 10^{-4}$	1756	-12.3	17.3	19.1
OP5	58.8	2.28	400	132.2	1.335	$-7.42 \cdot 10^{-5}$	475	0.882	-3.8	0.47	1.000	$3.24 \cdot 10^{-4}$	1502	-28.0	22.0	18.7
OP6	58.8	2.28	392	153.3	1.335	$-7.42 \cdot 10^{-5}$	475	0.882	-2.7	0.47	1.000	$3.24 \cdot 10^{-4}$	1797	-24.4	21.1	19.1

Table C.10: Nominal parameter values for experimental firing cycles at operating points OP1–6.

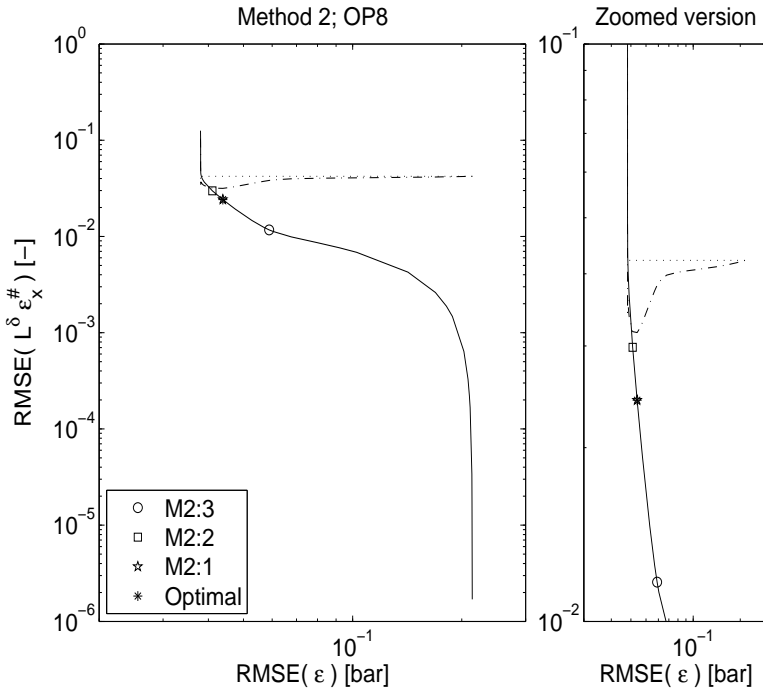


Figure C.6: L-curve (solid line) for one (motored) engine cycle at OP8 with weighted false prior $RMSE(L^\delta \varepsilon_x^{\#-t})$ (dotted line), when using setup 2 and case 2 of the δ_i ($\delta_i \neq c$). The results for the three versions of method 2 and the optimal choice of regularization parameter are indicated by the legend. The weighted true parameter deviation $RMSE(L^\delta \varepsilon_x^t)$ (dash-dotted line) is also given.

 NOTATION

The parameters are given in appendix D.1, and the abbreviations are summarized in appendix D.2. In the thesis various evaluation criteria are used, and they are summarized in appendix D.3.

D.1 Parameters

In system identification literature, e.g. (Ljung, 1999), the convention is to name the parameters by θ . However throughout this thesis, the parameters are instead named x . This in order to assign θ as the crank angle degree, which is common in engine literature, see e.g. (Heywood, 1988).

D.1.1 Heat transfer

C_1	constant in Woschni's correlation	[-]
C_2	constant in Woschni's correlation	[$m/(s K)$]
h_c	convection heat transfer coefficient	[$W / (m^2 K)$]
p	cylinder pressure for firing cycle	[Pa]
p_0	cylinder pressure for motored cycle	[Pa]
T	mean gas temperature	[K]
T_0	mean gas temperature for motored cycle	[K]
T_w	wall temperature	[K]
u_p	mean piston speed	[m/s]
w	characteristic velocity	[m / s]

D.1.2 Engine geometry

A	instantaneous surface area	$[m^2]$
A_{ch}	cylinder head surface area	$[m^2]$
A_{lat}	instantaneous lateral surface area	$[m^2]$
A_{pc}	piston crown surface area	$[m^2]$
a_r	crank radius	$[m]$
B	cylinder bore	$[m]$
l	connecting rod length	$[m]$
r_c	compression ratio index	$[-]$
S	piston stroke	$[m]$
θ	crank angle	$[\text{rad}]$
V	instantaneous cylinder volume	$[m^3]$
V_c	clearance volume	$[m^3]$
V_{cr}	aggregate crevice volume	$[m^3]$
V_d	displacement volume	$[m^3]$
V_{id}	instantaneous displacement volume	$[m^3]$
v	tilt angle	$[\text{deg}]$
x_{off}	pin-off	$[m]$

D.1.3 Engine cycle

K_p	pressure measurement gain	$[-]$
N	engine speed	$[\text{rpm}]$
p	cylinder pressure	$[\text{Pa}]$
Δp	pressure bias	$[\text{Pa}]$
p_{exh}	exhaust manifold pressure	$[\text{Pa}]$
p_m	measured cylinder pressure	$[\text{Pa}]$
p_{man}	intake manifold pressure	$[\text{Pa}]$
T_{man}	intake manifold temperature	$[\text{K}]$
T_w	mean wall temperature	$[\text{K}]$
θ	crank angle	$[\text{rad}]$
$\Delta\theta$	crank angle offset	$[\text{rad}]$
θ_{ig}	ignition angle	$[\text{rad}]$
θ_{ppp}	peak pressure position	$[\text{rad}]$

D.1.4 Thermodynamics and combustion

$(\frac{A}{F})_s$	stoichiometric air-fuel ratio	[-]
a	Vibe parameter	[-]
b	slope in linear model of γ (2.30)	[1/K]
c_v	mass specific heat at constant volume	$[\frac{J}{kgK}]$
c_p	mass specific heat at constant pressure	$[\frac{J}{kgK}]$
dm_i	mass flow into zone i	$[\frac{kg}{s}]$
dm_{cr}	mass flow into crevice region	$[\frac{kg}{s}]$
h_i	mass specific enthalpy	$[\frac{J}{kg}]$
M_i	molar mass of specie i	[kg/mole]
m	Vibe parameter	[-]
m_a	air mass	[kg]
m_{af}	air-fuel charge mass	[kg]
m_b	burned charge mass	[kg]
m_f	fuel mass	[kg]
m_r	residual gas mass	[kg]
m_{tot}	total mass of charge	[kg]
n	polytropic exponent	[-]
Q	transported heat	[J]
Q_{ch}	chemical energy released as heat	[J]
Q_{ht}	heat transfer to the cylinder walls	[J]
Q_{in}	released energy from combustion	[J]
q_{HV}	specific heating value of fuel	$[\frac{J}{kg}]$
R	specific gas constant	$[\frac{J}{kgK}]$
T_b	temperature in burned zone	[K]
T_r	residual gas temperature	[K]
T_u	temperature in unburned zone	[K]
U	internal energy	[J]
V_r	residual gas volume	$[m^3]$
W	mechanical work	[J=Nm]
x_b	mass fraction burned	[-]
x_i	mass fraction of specie i	[-]
\tilde{x}_i	mole fraction of specie i	[-]
x_r	residual gas fraction $x_r = m_r/m_c$	[-]
y_i	CHEPP coefficient for specie i	[-]
γ	specific heat ratio	[-]
γ_{300}	constant value in linear model of γ (2.30)	[-]
γ_b	γ for burned mixture	[-]
γ_u	γ for unburned mixture	[-]
η_f	combustion efficiency	[-]
$\Delta\theta_b$	rapid burn angle	[rad]
$\Delta\theta_{cd}$	total combustion duration	[rad]
$\Delta\theta_d$	flame development angle	[rad]
λ	(gravimetric) air-fuel ratio	[-]
$\phi = \lambda^{-1}$	(gravimetric) fuel-air ratio	[-]

D.1.5 Parameter estimation

a_ε	Morozov coefficient (6.22)
d	number of parameters in $\mathcal{M}(x)$
d^k	descent direction for iteration k
FP	false prior level
H_N	approximative Hessian in (C.8)
L^δ	weighting matrix, $L^\delta = (\delta)^{1/2}$
$\mathcal{M}(x)$	model for x
m_δ	Miller coefficient (6.20b)
m_ε	Miller coefficient (6.20a)
P	covariance matrix
\hat{P}_N	estimate of covariance at \hat{x}
$V_N(x, Z^N)$	loss (criterion) function based on residual error
V_N^δ	penalty term based on nominal parameter deviation
v	eigenvector
W_N	loss function using prior knowledge
x	vector used to parameterize model
\hat{x}	parameter estimate
\hat{x}^*	parameter estimate at optimum
x^δ	parameter estimate when using regularization
$x^{\delta,*}$	regularized parameter estimate at optimum
x^{eff}	efficient parameter
\hat{x}^{eff}	estimate for the efficient parameters
x_i	parameter i
\hat{x}^k	estimate of parameter k
x^{init}	initial values of parameters
x^s	scaled parameters $x^s = Dx$
x^{sp}	spurious parameters
x^t	true value of the parameters
$x^\#$	nominal value of parameters
$x^{\#,s}$	scaled nominal value of parameters
$y(t)$	measured output
$\hat{y}(t x)$	predicted model output
Z^N	data set $[y(1), u(1), y(2), u(2), \dots, y(N), u(N)]$
α	significance level
δ	regularization matrix
δ_i	diagonal element in δ
δ_x	regularization parameter
Δ_x	search region for δ_x
ε	prediction error $y(t) - \hat{y}(t x)$ or residual
ε_x^t	true parameter deviation (D.8)
$\bar{\varepsilon}_x^t$	mean true parameter deviation (D.9)
$\varepsilon_x^\#$	nominal parameter deviation (D.10)
$\bar{\varepsilon}_x^\#$	mean nominal parameter deviation (D.11)

$\varepsilon_x^{\#-t}$	nominal parameter deviation from true values (D.12)
η	noise level
λ_0	noise variance
$\hat{\lambda}_N$	estimated noise variance
μ	step size for optimization algorithm
ν	regularization parameter for Levenberg-Marquardt
ς	singular value
σ	standard deviation
τ	curvature of L-curve
ψ	Jacobian vector, defined in (C.5)

D.2 Abbreviations

AFR	Air-Fuel equivalence Ratio
AHR	Accumulated Heat Release
ATDC	After TDC
CAD	Crank Angle Degree
CHEPP	CHEMical Equilibrium Program Package(Eriksson, 2004)
CI	Compression Ignited
PDF	Probability Density Function
ECU	Electronic Control Unit
EVO	Exhaust Valve Opening
FAP	False Alarm Probability
FAR	Fuel-Air equivalence Ratio
FP	(level of) False Prior
FPE	Final Prediction Error
GDI	Gasoline Direct Injected
IVC	Inlet Valve Closing
MAP	Maximum A Posteriori
MDP	Missed Detection Probability
MFB	Mass Fraction Burned
MRE	Maximum Relative Error
NRMSE	Normalized Root Mean Square Error
RCI	Relative (95 %) Confidence Interval
RE	Relative estimation Error
RME	Relative Mean estimation Error
RMSE	Root Mean Square Error
SI	Spark Ignited
SOC	Start Of Combustion
SVC	Saab Variable Compression
SVD	Singular Value Decomposition
TDC	Top Dead Center, engine crank position at 0 CAD
TWC	Three-Way Catalyst

D.3 Evaluation criteria

The evaluation criteria used in the thesis are summarized here, and given in a general form. Here y^t denotes the true value, \hat{y} denotes the estimated or modeled value, $y^\#$ is the nominal value and j is the sample number.

Root mean square error (RMSE):

$$RMSE = \sqrt{\frac{1}{M} \sum_{j=1}^M (y_j^t - \hat{y}_j)^2}. \quad (\text{D.1})$$

Normalized root mean square error (NRMSE):

$$NRMSE = \sqrt{\frac{1}{M} \sum_{j=1}^M \left(\frac{y_j^t - \hat{y}_j}{y_j^t} \right)^2}. \quad (\text{D.2})$$

Maximum relative error (MRE):

$$MRE = \max_j \left| \frac{y_j^t - \hat{y}_j}{y_j^t} \right|. \quad (\text{D.3})$$

The relative mean error (RME):

$$RME = \frac{1}{M} \sum_{j=1}^M \frac{y_j^t - \hat{y}_j}{y_j^t}. \quad (\text{D.4})$$

Mean 95 % relative confidence interval (RCI):

$$RCI = \frac{1}{M} \sum_{j=1}^M \frac{1.96\sigma_j}{y_j^t}, \quad (\text{D.5})$$

where σ is computed using (C.18) and (C.20) in appendix C.1.
False alarm probability (FAP):

$$FAP = P(\text{reject } H^0 | r_c^{est} \in \mathbf{NF}) = P(T \geq J | r_c^{est} \in \mathbf{NF}). \quad (\text{D.6})$$

The variables and nomenclature used are defined in example 5.1.
Missed detection probability (MDP):

$$MDP = P(\text{not reject } H^0 | r_c^{est} \notin \mathbf{NF}) = P(T < J | r_c^{est} \notin \mathbf{NF}). \quad (\text{D.7})$$

The variables and nomenclature used are defined in example 5.1.

True parameter deviation ε_x^t :

$$\varepsilon_x^t = \hat{y} - y^t, \quad (\text{D.8})$$

which is closely related to the mean true parameter deviation:

$$\bar{\varepsilon}_x^t = RMSE(\varepsilon_x^t) = \sqrt{\frac{1}{M} \sum_{j=1}^M (\hat{y}_j - y_j^t)^2}. \quad (\text{D.9})$$

Nominal parameter deviation $\varepsilon_x^\#$:

$$\varepsilon_x^\# = \hat{y} - y^\#, \quad (\text{D.10})$$

which is closely related to the mean nominal parameter deviation:

$$\bar{\varepsilon}_x^\# = RMSE(\varepsilon_x^\#) = \sqrt{\frac{1}{M} \sum_{j=1}^M (\hat{y}_j - y_j^\#)^2}. \quad (\text{D.11})$$

Nominal parameter deviation from true values $\varepsilon_x^{\#-t}$:

$$\varepsilon_x^{\#-t} = y^\# - y^t. \quad (\text{D.12})$$

Linköping Studies in Technology and Science
Department of Electrical Engineering
Dissertations, Vehicular Systems

- No. 8 *Modelling for Fuel Optimal Control of a Variable Compression Engine*
Ylva Nilsson, Dissertation No. 1119, 2007
- No. 7 *Fault Isolation in Distributed Embedded Systems*
Jonas Biteus, Dissertation No. 1074, 2007
- No. 6 *Design and Analysis of Diagnosis Systems Using Structural Methods*
Mattias Krysander, Dissertation No. 1033, 2006
- No. 5 *Air charge Estimation in Turbocharged Spark Ignition Engines*
Per Andersson, Dissertation No. 989, 2005
- No. 4 *Residual Generation for Fault Diagnosis*
Erik Frisk, Dissertation No. 716, 2001
- No. 3 *Model Based Fault Diagnosis: Methods, Theory, and Automotive Engine Applications*, Mattias Nyberg, Dissertation No. 591, 1999
- No. 2 *Spark Advance Modeling and Control*
Lars Eriksson, Dissertation No 580, 1999
- No. 1 *Driveline Modeling and Control*
Magnus Petterson, Dissertation No. 484, 1997